FLUID-ASSISTED FRACTURING IN GEOLOGICAL MATERIALS

A Dissertation
Presented to
The Academic Faculty

by

Devon C. Gwaba

In Partial Fulfillment
of the Requirements for the Degree
Doctor of Philosophy in the
School of Civil and Environmental Engineering

Georgia Institute of Technology
May, 2017

FLUID-ASSISTED FRACTURING IN GEOLOGICAL MATERIALS

Approved by:

Dr. Leonid Germanovich, Advisor
School of Civil and Environmental Engineering
Georgia Institute of Technology

Dr. Paul Mayne
School of Civil and Environmental Engineering
Georgia Institute of Technology

Dr. Haiying Huang
School of Civil and Environmental Engineering
Georgia Institute of Technology

Dr. Zhigang Peng
School of Earth and Atmospheric Sciences
Georgia Institute of Technology

Dr. Sheng Dai
School of Civil and Environmental Engineering
Georgia Institute of Technology

Mr. Joseph Ayoub
DCM Production and Completion Engineering Discipline Manager
Schlumberger

Date Approved: January 3, 2017

ACKNOWLEDGEMENTS

First of all, I would like to thank my advisor, Dr. Leonid Germanovich, for his paramount guidance and support throughout my research and study at Georgia Tech. Without his endless support and confidence at all levels, I could not have accomplished the research reported in this dissertation. His imaginative perspective into the scientific research and optimistic attitude towards the challenges in daily life has set up a good example for me to follow in my future career.

I would also like to thank Dr. Sheng Dai, Dr. Haiying Huang, Dr. Paul Mayne, Dr. Zhigang Peng and Mr. Joseph Ayoub for serving on my thesis committee. I have benefited greatly from their comments and suggestions. In particular, discussions with Dr. Dai and Dr. Peng on the interpretations of acoustic data were very helpful. Dr. Huang's work at Georgia Tech exposed me to the fundamental physics of hydraulic fracturing of particulate materials. Dr. Mayne's geotechnical insights and suggestions were extremely insightful. Last but not least, Mr. Ayoub's encouragement and numerous advises on all aspects of my experiments starting from design and through the analysis of experimental data were critical for the success of this work.

The completion of this research was possible due to the contributions of many other people. Specifically, I really appreciate Dr. Sergey Stanchits, Dr. Eduard Siebrits, Mr. Nick Whitney and other members of the TerraTek team who assisted me with my industrial experiments in Salt Lake City, Utah. I also thank Mr. Andy Udell, Mr. Blake Baklini, Mr. Billy Plum, Mr. Dennis Brown, Mr. Cole Borton and Mr. Jeff Wilkie for helping to fabricate various tools for my experiments in their machine shops at Georgia Tech. I greatly appreciate the assistance and encouragement from past and present graduate students of the Geosystems engineering program at the Georgia Institute of Technology: Robert Hurt, Sihyun Kim, Cem Ozan, Pierre Ramondenc, Fengshou Zhang, Chanin Ruangthaveekoon, Tahiru Mawia, Lucas Curry, Josh Smith, Yixuan Sun, and Longde Jin. I am particularly in debt to Robert Hurt for his kind help with training me on the use of the Rock and Fracture Mechanics laboratory equipment and for regular follow-ups with my progress after that. I am also grateful to Ms. Allison Keefer, P.G., for the assistance she rendered in proofreading and editing the manuscript of this dissertation.

I cannot forget to thank my wife, Charlotte Chintu Gwaba, RN, for her enduring and unconditional love, encouragement, trust, and support. I should also express my deep gratitude to my beloved mother, Ms. Ethel Mutinta Gwaba and my dear elder brother, Malambo Moonga Gwaba who taught me a lot about hard work. I dedicate this dissertation to four very special people in my life: Mwiinga Joseph Gwaba, Elisabeth Michelo Gwaba, Amoache Juliet Adonle and Charlotte Butala Gwaba.

Finally, I would like to thank Schlumberger, Schlumberger Client Advisory Board members (BG Group, BP, Chevron, Conoco-Phillips, Statoil, and Total), the U.S. National Science Foundation and the Georgia Tech Foundation for the financial support provided during my Ph.D. study.

TABLE OF CONTENTS

LIST OF TABLES

LIST OF FIGURES

SUMMARY

We have developed and advanced novel experimental techniques to study, in the laboratory and in-situ, fluid-assisted fracturing in geological materials. Fractures and fluids influence numerous mechanical processes in the earth's crust, but many aspects of these processes remain poorly understood; in large part, because of a scarcity of controlled field experiments at appropriate scales.

Faulting processes are a good example. In the laboratory, faults are typically simulated at the centimeter to decimeter (cm-to-dm) scale using load cells. Laboratory results are then routinely up-scaled by several orders of magnitude to understand faulting and earthquakes in a wide range of conditions. We show, however, that a scale of at least a few meters is required to adequately simulate earthquake nucleation processes. For this reason, we developed an experimental approach that aims to induce new faults or reactivate existing faults in-situ at scales of 10 to 100 meters. The approach uses thermal techniques and fluid injection to modify in situ stresses and the fault strength to the point where the rock fails. Mines where the modified in-situ stresses are sufficient to drive faulting, present an opportunity to conduct such experiments.

Another example is hydraulic fracturing in unconsolidated sediments and soils, which is important for many applications ranging from compensation grouting to sand control in petroleum reservoirs to sand diking in shallow formations. In this work, we advance experimental methods of hydraulic fracturing of cohesionless particulate media. The hydraulic fracturing behavior in natural sands, obtained from a production well, is compared and contrasted with that in synthetic sands. Conventional wisdom suggests that it is not possible to monitor hydraulic fracturing in cohesionless materials using passive acoustic emission and active ultrasonic measurements. Yet, we show that not only is this possible but it is an effective monitoring technique allowing for important insights into the fracturing process and fracture geometry mapping. Also, this technique gives a reference for interpreting microseismic data recorded in the field.

1. GOALS AND OBJECTIVES

Fractures and fluids influence virtually all mechanical processes in the earth's crust, but many aspects of these processes remain poorly understood largely because of a lack of controlled experiments at appropriate scales. In this work, we have developed and advanced novel experimental techniques to study, in the laboratory and in-situ, fluid-assisted fracturing in geological materials. The methods developed in this work are suitable for (1) fluid-induced earthquake nucleation field experiments in a deep mine, (2) fluid-induced hydraulic fracturing in cohesionless sediments and soils, and (3) acoustic monitoring of fluid-induced fracturing in particulate cohesionless materials.

Faults are typically simulated at the centimeter to decimeter (cm-to-dm) scale in the laboratory using load cells. Laboratory results are then routinely up-scaled by several orders of magnitude to investigate faulting and earthquakes in a wide range of conditions. One of the main conclusions of the first part of this work is that a scale of at least a few meters is required to adequately simulate earthquake nucleation processes. We describe an experimental approach that aims to induce new faults or reactivate existing faults in-situ at scales of 10 to 100 m. The approach uses thermal techniques and fluid injection to modify in situ stresses and the fault strength to the point where the rock fails. Mines where the modified in-situ stresses are sufficient to drive faulting present an opportunity to conduct such experiments. The former Homestake gold mine in the Black Hills of South Dakota presents an opportunity for conducting these experiments. It has a large fault extending at least 1.5 km along the strike and dip and is accessible at several mine levels. The fault strikes at 340 degrees and dips 60 degrees NE. The gouge thickness is approximately 0.4 m and it contains crushed host rock and graphite. Our results are also important for understanding and interpreting other mine experiments or faulting and earthquake nucleation [e.g., *Reches and Ito,* 2007; *Germanovich et al.,* 2010; *Durrheim et al.,* 2012; *Ogasawara et al.,* 2009; *Gischig,* 2015; *Guglielmi et al.,* 2015].

The second part of this work discusses hydraulic fracturing in cohesionless particulate materials. Hydraulic fracturing has been used in the petroleum industry as a production

enhancement technique for over six decades. Hydraulic fracturing in unconsolidated materials has also been used in such applications as sand control in unconsolidated petroleum reservoirs [*Ayoub et al.,* 1992; *Hainey and Troncoso*, 1992; *Wedman et al.,* 1999], compensation grouting [e.g. *Soga et al.,* 2004; *Au et al.,* 2006], evaluating in-situ stresses [*Al-Shaikh-Ali et al.,* 1981; *Zhou et al.,* 2010b], and in soil fracturing, for environmental reasons [*Murdoch,* 1993c; *Murdock and Slack*, 2002; *Murdoch et al.,* 2006a], and climate control [*Germanovich and Murdoch*, 2010]. Understanding hydraulic fracturing in unconsolidated reservoirs is important for enhancing production by water flooding [*Jones and Soler,* 1999; *Khodaverdian et al.,* 2010b] and for cuttings reinjection [*Chin and Montgomery,* 2004; *Ji et al.,* 2009; *Van Den Hoek,* 1993]. In this work, we advance experimental methods in hydraulic fracturing of cohesionless particulate media. Fracturing behavior in a natural sand, for example, the Bromide formation sand obtained from a production well, is compared to that in synthetic sands such as quartz sand USM100, quartz sand F110 [*Chang,* 2004; *Hurt,* 2012], silica flour SIL-CO-SIL 106 [*Chang,* 2004; *Hurt,* 2012], and their mixtures [*Hurt,* 2012]. Over 45 hydraulic fracturing experiments were conducted in the natural sand and the synthetic materials in triaxial loading conditions and low stress regimes (up to 160 psi). The main question we sought to answer was whether hydraulic fracturing behavior in natural sand was similar to that in synthetic sands in terms of fracture geometries, pressure signatures, leakoff thickness, and fracture initiation and propagation mechanisms. Our finding was that hydraulic fracturing behavior in the natural Bromide formation sand is similar to that in man-made cohesionless particulate materials. Therefore, it appears that hydraulic fracturing laboratory experiments, with synthetic sands, are sufficiently representative. This is significant as prior to this work, nearly all experiments had been done with synthetic sands [*Chang et al.,* 2003; *Chang*, 2004; *Hurt et al.,* 2005; *Germanovich and Hurt*, 2007; *Huang et al.,* 2011; *Zhang and Huang,* 2011; *Callahan,* 2011; *Huang et al.,* 2012; *Zhang,* 2012; *Germanovich et al.,* 2012; *Hurt and Germanovich,* 2012; *Hurt,* 2012; *Zhang et al.,* 2012; *Jaworski et al.,* 1981; *Panah and Yanagisawa,* 1989; *Murdoch,* 1993; *Andersen et al.,* 1994; *Vallejo,* 1993; *Khodaverdian and Mcelfresh,* 2000; *Soga et al.,* 2004; *de Pater and Dong,* 2007; 2009; *Golovani et al.,* 2010; *Jasarevic et al.,* 2010].

This work also advances the study of hydraulic fracturing in particulate, cohesionless media in true-triaxial loading conditions and large confining stress regimes (up to 1600 psi), and the use of passive acoustic emissions and active ultrasonic transmissions to monitor the fracturing process. Four hydraulic fracturing tests were conducted in cohesionless particulate block samples in an industrial laboratory. The goals and objectives of this experimental series were:

1. To verify that plastic deformation is a dominant mechanism in fluid-assisted fracturing of cohesionless, sediment-like particulate materials.
2. To study the effect of scale and high confining stresses on hydraulic fracturing behavior of cohesionless, sediment-like particulate materials.
3. To investigate the plausibility of using acoustic emission and ultrasonic transmission measurement techniques to monitor hydraulic fracture evolution in cohesionless, sediment-like particulate materials.

At least four major sources of acoustic emissions (AE) in granular media are identified in the literature [e.g., *Michlmayr et al.,* 2012; *Reiweger et al.,* 2014; *Akay*, 2002; *Yabe,* 2008; *Goren et al.,* 2010, 2011]. These are grain contact network rearrangement, grain friction, crack formation, and pore fluid motion. The characteristics and statistics of AE from these sources can be used to identify deformation events such as hydraulic fracturing. Thus far, however, the conventional wisdom has been that it is not possible to monitor hydraulic fracturing in cohesionless materials using acoustic monitoring techniques. Yet we show that not only is this possible, but that it is an effective monitoring technique allowing for important insights into the fracturing process and fracture geometry mapping. This technique also gives a reference for interpreting microseismic data recorded in the field.

Another important contribution of this work is the observation of strain localization features, termed shear bands, in hydraulic fracturing experiments in particulate materials, using computed tomography (CT) imaging.

The detailed structure of this thesis is as follows:

Chapter 2 provides a literature review of fault slip nucleation studies both in the laboratory and in the field. Three laboratory experiments simulating fault slip are discussed at length. The use of deep mines as a stage for monitoring seismic events are then presented. Finally, the use of deep boreholes at KTB, Rangely, and SAFOD are presented and discussed.

Chapter 3 presents a design of a field experiment at appropriate scales for investigating earthquake nucleation. The prevailing use of small scale laboratory tests to simulate the earthquake nucleation process is tested. It is shown that in order to adequately simulate earthquake nucleation, a slip patch size of 1 – 10 m is needed. This requires an experimental configuration of 10-100 m. This is outside the range of laboratory experiments. Therefore, field scale experiments are required.

Chapter 4 describes hydraulic fracturing experiments conducted in triaxial loading conditions and low stress regimes (up to 160 psi), including the introduction of natural sands as experimental sample materials. The experimental procedure, materials, and results are discussed.

Chapter 5 describes hydraulic fracturing experiments in true-triaxial loading conditions and high stress regimes (up to 1600 psi). The experimental setup, procedure, materials used, and results are discussed in detail.

Chapter 6 presents the use of acoustic monitoring techniques to study the hydraulic fracturing process. Acoustic emission and ultrasonic transmission results are analyzed and discussed.

Chapter 7 summarizes main results obtained in this thesis.

Some of the results of this work (Chapter 3, Chapter 5 and Chapter 6) have been presented by *Gwaba et al.* [2014], *Germanovich et al.* [2010], and *Germanovich et al.* [2016].

2. FAULT SLIP NUCLEATION EXPERIMENTS – A REVIEW

2.1. INTRODUCTION

The study of fault processes and earthquake source mechanics has been of central interest to many researchers for several decades. Topics of localization, nucleation, growth, and propagation of single faults and the development of fault systems have been studied in the laboratory and the field. In this chapter, a review of laboratory experiments on fault slip nucleation, field studies of seismicity in deep mines and deep boreholes, and studies of human induced seismicity, is presented. The purpose of this review, is to present what knowledge and ideas have been established on the topic of earthquake triggering, as a foundation for the earthquake nucleation techniques that we propose in Chapter 3. The strengths and weaknesses of these established experimental methods are discussed and the advantages of our proposed experimental techniques are also offered.

Advancing the understanding of faulting processes and earthquake nucleation is important to many fields of earth science and engineering, including seismology, resource recovery and environmental remediation, structural geology, disposal of radioactive wastes, carbon dioxide sequestration, and civil engineering and building construction. Earthquake nucleation is a complicated topic with many questions that still remain unanswered. To understand an earthquake preparation process or rock mass behavior during the earthquake process, we should get closer to the hypocenter [*Ogasawara et al.,* 2002a]. However, this is not easy with natural earthquakes because hypocenters are usually located very deep in the earth's crust. Over the last thirty years, some researchers have attempted to bridge the gap in science between laboratory experimental data and natural fault mechanisms by methods of direct seismic observations [*Ogasawara et al.,* 2002a]. In Section 2.2, a review of laboratory experiments on fault slip nucleation is presented. Specifically, three examples of triaxial experiments to study fault growth are discussed. In section 2.3, field studies on earthquake nucleation are discussed. These include studies in the deep gold mines of South Africa, fluid injection studies at Rangely, Colorado, direct seismic observations in the deep borehole at KTB, Germany, and the San Andreas Fault Observatory at Depth (SAFOD). Hydraulic fracturing and

fluid injection induced seismic events are discussed in Section 2.4. followed by a summary discussion in Section 2.5.

2.2. LABORATORY EXPERIMENTS ON FAULT SLIP NUCLEATION

Lockner et al. [1991] conducted lab experiments to study quasi-static fault growth in Westerly granite and Berea sandstone. They utilized acoustic emission (AE) monitoring, to study the faulting processes. An array of piezoelectric transducers was used to record arrival times of acoustic signals, which indicate the growth of microcracks. The arrival times were then used to locate, in three dimensions, the micro events that occurred during fault nucleation and growth.

The study of fault growth using triaxial experiments of the fracture of brittle rock are difficult because of the tendency for fault growth to proceed violently, at near shear wave velocity, in an uncontrolled manner after fault initiation. *Lockner et al.* [1991] were able to develop a fast acting axial control system that adjusts the load applied to the sample to maintain a constant AE rate. They stabilized the axial loading through a feedback looping technique in which a pulse counter-generated output voltage, proportional to the AE rate occurring in the sample, was used. In this manner, they were able to follow, quasi-statically, the growth of the fracture plane typically extending the fault formation phase so that it would last a matter of minutes or even hours [*Lockner and Byerlee*, 1993].

Figure 2.1 shows the locations of the largest-amplitude AE events during the Lockner experiments. In the bottom projection, the sample is viewed along the strike, while in the top projection the sample is viewed perpendicular to the strike. Each dot represents a location of an AE event. *Lockner et al.* [1991] state that the bottom projection shades light on the plane of the fault as it grows while the top projection places emphasis on the event density. In all their granite experiments, the fault plane nucleated abruptly at a point on the sample surface soon after reaching peak stress. This is clearly seen in the accompanying curve to the plot of the AE.

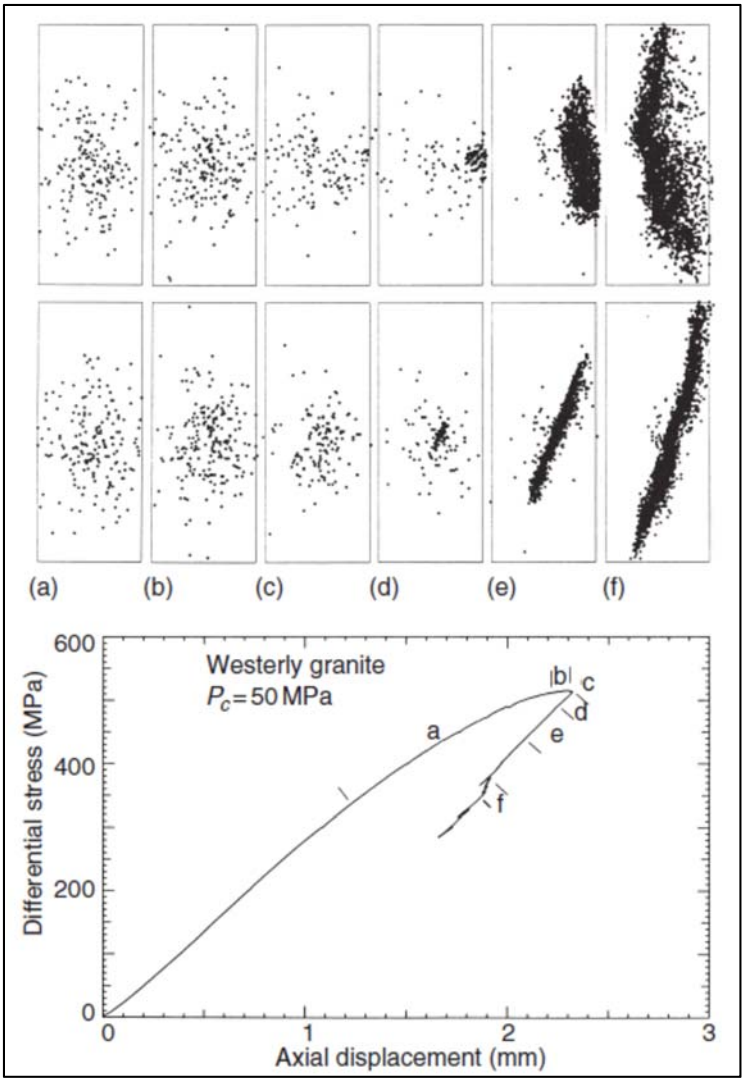

Figure 2.1: Sequential plots of locations of acoustic emission (AE) sources during fault formation in initially intact Westerly granite [*Lockner et al.,* 1991]. Time progress from left to right. Middle: Figures show events viewed along-strike of eventual fault plane, which appears as diagonal feature in (e) and (f). Top: Figures show same AE events when fault plane is viewed face-on (Perpendicular to strike). Fault nucleation occurs in (d). Bottom: Accompanying stress-displacement curve indicates segments of the experiment from which acoustic emission plots are made.

In earlier publications, it was often argued that the eventual fault plane began forming as a region of high micro-crack damage, well before peak strength. For example, *Hallbauer et al.* [1973] reported the localization of micro-crack damage onto an emerging fracture plane as between 95 and 98 percent of peak strength. *Spetzler et al.* [1981] observed localized surface dilatancy preceding peak strength of about 2 percent in a pyrophyllite sample.

It can be seen from **Figure 2.1** that prior to fault nucleation, micro-crack growth is distributed evenly throughout the central portion of the granite samples (**Figures 2.1a, 2.1b** and **2.1c**). This is a reflection of the uniform dilatancy occurring during this portion of the experiment, and no clustering of AE locations is observed that is comparable to clustering seen in the later stages of the experiment. After peak stress, a zone of intense AE activity forms on the surface, near the sample mid-plane. The nucleation site, with a volume of approximately 2 cm^3, rapidly evolved into the nascent fault, narrowing into a half-disk shape that defined the position and orientation of the fracture [*Lockner et al.,* 1991]. *Lockner et al.* [1991] also observed that a rapid drop in stress accompanied this nucleation process.

The observation was made in these experiments that the newly formed fault grew by developing a characteristic zone of intense AE activity that was interpreted as a fracture front propagating across the sample [*Lockner and Byerlee,* 1993]. This process zone was 10 – 50 mm wide and 1-5 mm thick. As the fracture front passed, the AE from a given region would drop to a low level. If allowed to progress to completion, stress eventually dropped to the frictional sliding strength [*Lockner et al.,* 1991].

From these observations, *Lockner et al.* [1991] proposed the following model for the nucleation and growth of faults in intact brittle rocks. They proposed that faults in granite nucleate and propagate by the interaction of tensile microcracks in the following style. First, under overburden loading, tensile microcracking occurs randomly, with no significant crack interaction and with no relation to the location or inclination of the future fault [*Lockner et al.,* 1991]. Then nucleation initiates when a few tensile microcracks interact and enhance the dilation of one another. The stress field associated with crack dilation is such that the region of maximum tension induced by an open crack is not in the crack plane but is inclined at an angle of 20 – 30 degrees with respect to the crack. The interacting tensile microcracks create a process zone that

is a region with closely spaced microcracks. As the process zone lengthens, its central part yields by shear and a fault nucleus forms. The fault nucleas grows in the wake of the propagating process zone. The stress fields associated with shear along the fault further enhance the microcrack dilation in the process zone [*Lockner et al.,* 1991]. This model explains how faults grow in their own plane and why they often make an angle of 20-30 degrees with the maximum compression axis.

The understanding of faulting processes is of obvious importance to our understanding of earthquakes and to our ability to predict earthquakes. Lockner's model needs further validation at appropriate scales. Fault growth under artificially slowed down conditions may not be completely representative of the dynamic loading conditions in the earth. We have designed a field experiment that can verify the model and findings of the above observations. Chapter 3 gives a detailed description of this field experiment.

Lei et al. [2000] have also investigated fault nucleation and quasi-static fault growth in intact brittle rocks (Hornblende Schist) under triaxial compression in experiments that utilized AE monitoring. Rather than stabilize the failure process by controlling axial stress to maintain a constant rate of AE as in the works of *Lockner and Byerlee* [1993]; *Lockner et al.* [1991], they developed a rapid 32 channel data collection system. This enabled them to monitor the dynamics of fault nucleation using AE hypocenters under conditions of constant stress loading and low strain. These laboratory conditions are better approximations of subsurface conditions and allow both quasi-static and dynamic crack growth to occur. *Lei et al.* [2000] were also able to locate AE events during unstable dynamic failure after fault initiation. They report that the waveforms of more than 8000 AE events, which occurred mainly during a 15 s period, were recorded on 32 channels, with a sampling rate of 50 nanoseconds and mask time of 200 microseconds. Using Focal mechanism solutions, four types of mechanism solutions were distinguished using the distribution of P wave first motions. These were categorized as type T, type S, type TS, and type TTS, respectively. Type T corresponded to tensile cracking, type S corresponded to shear cracking, while types TS and TTS are combinations containing tensile and shear cracking modes. *Reches and Lockner* [1994] proposed a model based on the mutual enhancement of cracking due to stress induction and pointed out the propagation of faults occurred through the interaction of

tensile cracks. On the other hand, *Lei et al.* [2000] report that tensile cracking was dominant only in the process zone, based on their focal mechanisms solution types. When the density of the damage zone increased or when fault growth was accelerated, shear mode or other modes containing a shear component became the major modes of cracking, in agreement with a suggestion by *Cox and Scholz* [1988] based on microstructural examination. Thus we here have another discrepancy that can be clarified by a controlled field experiment.

There is a large discrepancy between slip weakening distances, Dieterich's parameter D_c, inferred from conventional laboratory faulting experiments and those evidenced from seismological studies. This discrepancy is commonly referred to as "the D_c paradox." Coventional friction experiments have produced values of D_c, in the range of 10^{-5} – 10^{-3} m [*Dieterich,* 1978, 1979, 1981; *Tullis and Weeks,* 1986] while recent seismological studies have revealed D_c values in the range of 10^{-1} – 10^{0} m [*Fukuyama et al.,* 2003]. *Hirose and Shimamoto* [2005] conducted laboratory experiments to try and explain the D_c paradox. Frictional melting experiments were conducted with a rotary-shear, high-velocity frictional testing machine to determine the order of D_c values for natural faults containing pseudotachylytes based on a comparison between experimental and natural pseudotachylytes. This machine was equipped with a precise torque gauge and could measure mechanical properties (shear resistance) of simulated faults during frictional melting [*Hirose and Shimamoto,* 2005]. This machine typically has two cylindrical or hollow-cylindrical samples pressed together with one sample being allowed to rotate while the other is held stationary. *Hirose and Shimamoto* [2005] used hollow cylindrical specimens with external and internal diameters of 25 mm and 15 mm, respectively. A maximum rate of revolution of 1,500 revolutions per minute (rpm) gave slip rates of 2.0 m/sec and 1.2 m/sec and an equivalent velocity of 1.6 m/sec [*Hirose and Shimamoto,* 2005]. Their experiments at a constant slip velocity of 0.85 m/sec and a normal stress of 1.4 MPa on gabbro from India revealed that the progressive growth of a molten layer causes marked slip weakening (a reduction in frictional strength with displacement). *Hirose and Shimamoto* [2005] observed that the growth rate of a molten layer with increasing displacement can be correlated with the slip-weakening behavior of a simulated fault with about the same characteristic distances. They stated that this comparison suggests the order of D_c can be estimated from the relationship between pseudotachylyte

thickness along its generation fault and fault displacement. Further, they compared this with *Sibson's* [1975] data from the Outer Hebrides and found that they exhibited a similar pseudotachylyte-thickness-versus-fault-displacement curve with a characteristic distance of 0.38 m, which is the same order of magnitude as those from seismological studies. Therefore, *Hirose and Shimamoto* [2005] conclude that the effect of frictional melting may be a possible solution for the D_c paradox, although they point out it is not the only possible solution, since frictional melting along large faults is rather uncommon.

In Chapter 3 of this work, we present an experimental technique that can be used to resolve such questions as the Dietrich's parameter paradox. We also show, by dimensionless (scaling) analyses, that a slip patch size of the order of magnitude of 1 – 10 m is required to adequately study earthquake nucleation.

2.3. FIELD EXPERIMENTS ON EARTHQUAKE NUCLEATION

2.3.1. Studies in South African deep mines

Most earthquake investigations are based on data collected at or near the earth surface and on analyses of earthquake rupture zones observed in soils or soft sediments [*Reches and Ito,* 2007]. In-situ stresses and pore pressures associated with earthquakes are often not measured directly. A major drawback of these methods is that they do not provide a complete picture of the processes controlling faulting and earthquake source mechanics. Therefore, direct field experiments close to the hypocenter are needed. Deep underground mines provide an opportunity for such experiments. The following is a brief summary of earthquake process studies that have been conducted in deep mines in South Africa.

The mining operations in the deep gold mines of South Africa generate thousands of earthquakes per day, and some of these events approach magnitudes of M 5 [*Reches and Ito*, 2007]. When underground drifts are excavated in the highly stressed rock mass of these deep mines, the stress field in the vicinity of these openings is locally re-distributed and a new set of stresses are induced in the surrounding rock mass. There is a seismogenic zone that forms ahead of the advancing stope face during the mining process. If faults are present near the openings, these induced stresses can trigger earthquakes and tremors. Therefore, these deep mines

provide an opportunity to study the entire lifespan of an earthquake at close proximity. To study earthquake source mechanisms, seismic monitoring instruments can be placed in the path of the future seismogenic zone.

There are quantifiable changes in some or all of the following physical parameters that can be used to predict the time and location of mining-induced ruptures: stress, strain rate, tilt rate, acoustic emission rate, seismic source parameters, electromagnetic emission rate, and micro-crack density. In the past decade, several research projects have been initiated to build earthquake laboratories in the deep gold mines of South Africa. These include SATREPS (Science and Technology Research Partnership for Sustainable Development) initiative, and the linked DAFSAM (Drilling Active Faults Laboratory in South African Mines) and NELSAM (Natural Earthquake Laboratory in South African Mines) projects. Under SATREPS, a five year Japan-South Africa joint project captioned "Observational studies to mitigate seismic risks in mines" was launched in August 2010 [*Durrheim et al.,* 2012]. The project had three main objectives, namely:

1. To learn more about earthquake preparation and nucleation mechanisms by deploying arrays of sensitive instruments within rock volumes where mining is likely to induce seismic activity. The knowledge gained will help upgrade schemes of seismic hazard assessment and limit the seismic risks in deep and highly stressed mines and in areas vulnerable to natural earthquakes [*Durrheim et al.,* 2010].
2. To learn more about earthquake rupture and rockburst damage phenomena by deploying robust strong ground motion sensors close to potential fault planes and within mining excavations.
3. To upgrade the South African surface national seismic network in the mining districts.

A total of 70 boreholes, totaling more than 2 km in length, were drilled for the purpose of locating faults accurately and to deploy seismic monitoring instruments. Over 110 sensors were installed at sites in Ezulwini, Moab-Khotsong and Drietontein gold mines. Accelerometers, acoustic emission sensors, strain meters, tilt meters, geophones, controlled seismic sources and electromagnetic sensors were all installed to monitor the deformation of the rock mass, the

accumulation of damage during the earthquake preparation process, and the changes in stress produced by the propagation of the rupture front.

According to *Ogasawara et al.* [2009], a pilot experiment was conducted at Western Holdings mine in 1995. They state that a very sensitive borehole strainmeter [*Ishii,* 1997], was used to detect fine details of rock mass deformation and to record large, sudden changes associated with large events.

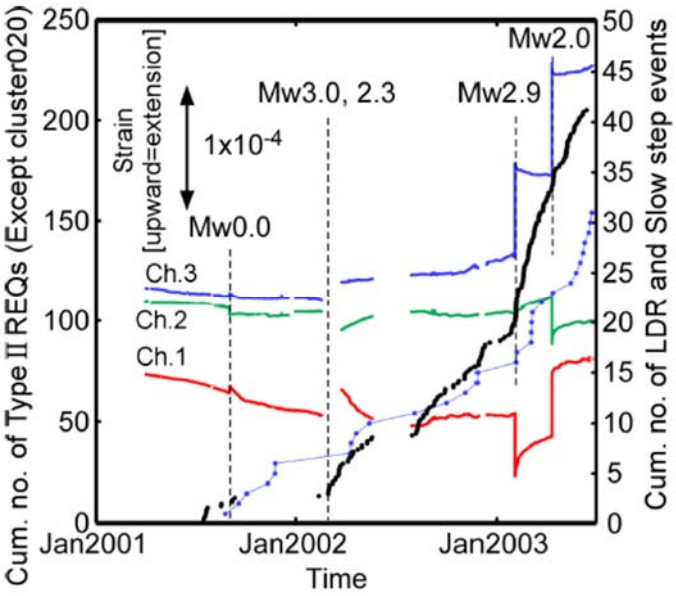

Figure 2.2: Strain change recorded over a 3-year period at a fault in the Bambanani mine[*Ogasawara et al.,* 2009]. Connect-dots: cumulative number of slow events. Thick line: cumulative number of repeating earthquakes close to the Mw2.9 event in February 2003.

Figure 2.2 shows mining associated accumulation and earthquake associated release of strain followed by relaxation corresponding to a 10 MPa stress change. *Ogasawara et al.* [2009] further note that examples of strain changes with clear forerunners were observed at Pretorius fault zones at Mponeng mine as shown in the **Figure 2.3**. They also note that two strainmeters near to the slow events showed that they were caused by slip on the distinctive fracture zones in the faults.

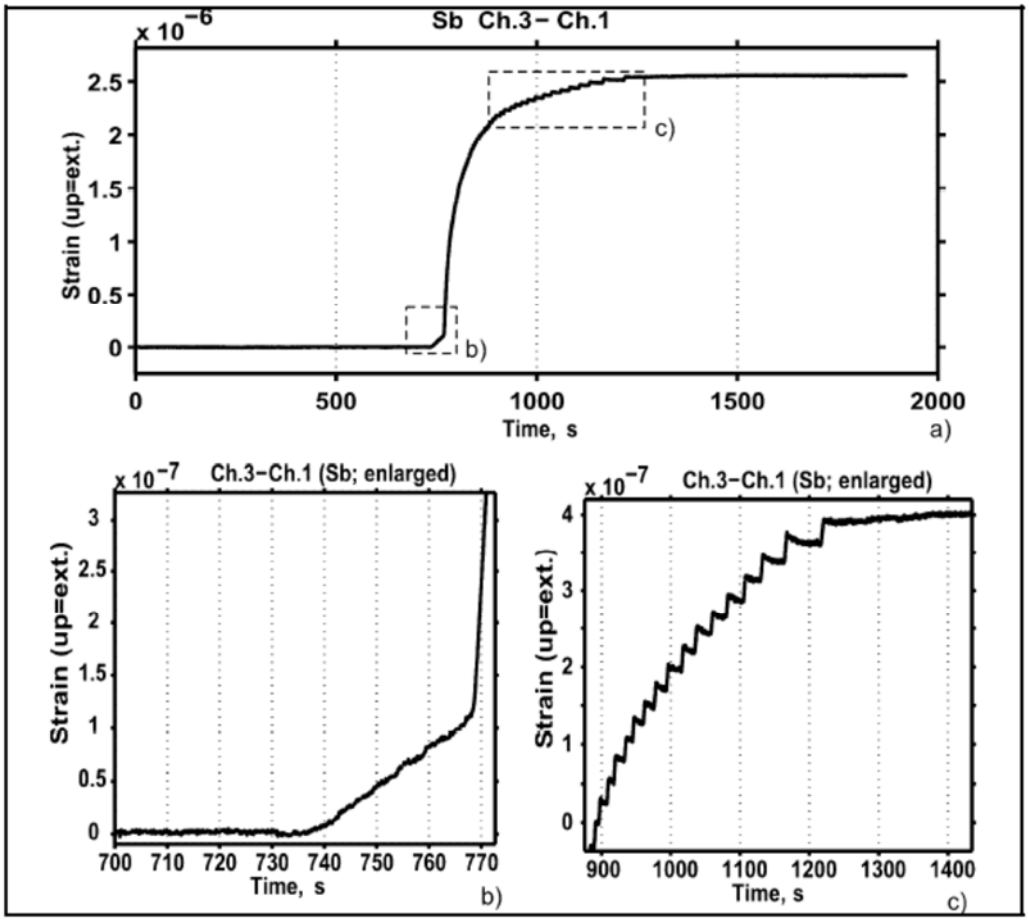

Figure 2.3: An example of slow strain changes with clear forerunner after 735 s observed at the Pretorius fault zone, Mponeng mine [*Ogasawara et al.,* 2009].

This project also implemented an acoustic monitoring network to delineate the source faults of major seismic events. *Nakatani et al.* [2007] deployed a small network (approx. 40 m span) of eight acoustic emission (AE) sensors covering a frequency range up to 200 kHz in a seismically active hard rock pillar at 3300 m below surface in the Mponeng gold mine. The network recorded an M 2.1 event on 27 December 2007 [*Durrheim et al.,* 2010]. Tilt-meters were installed at two underground sites in Mponeng mine. *Ogasawara and Durrheim* [2009] report that both the rate of tilt, defined as quasi-static deformations, and the ground motion, defined as dynamic deformations, were analyzed in order to understand the rock mass behavior around deep level mining. **Figure 2.4** shows some results of the distribution of coseismic and aseismic tilt during a typical work day. Notice that the daily blasting time at this mine was between 19:30 and 21:00 (7:30 pm and 9:00 pm).

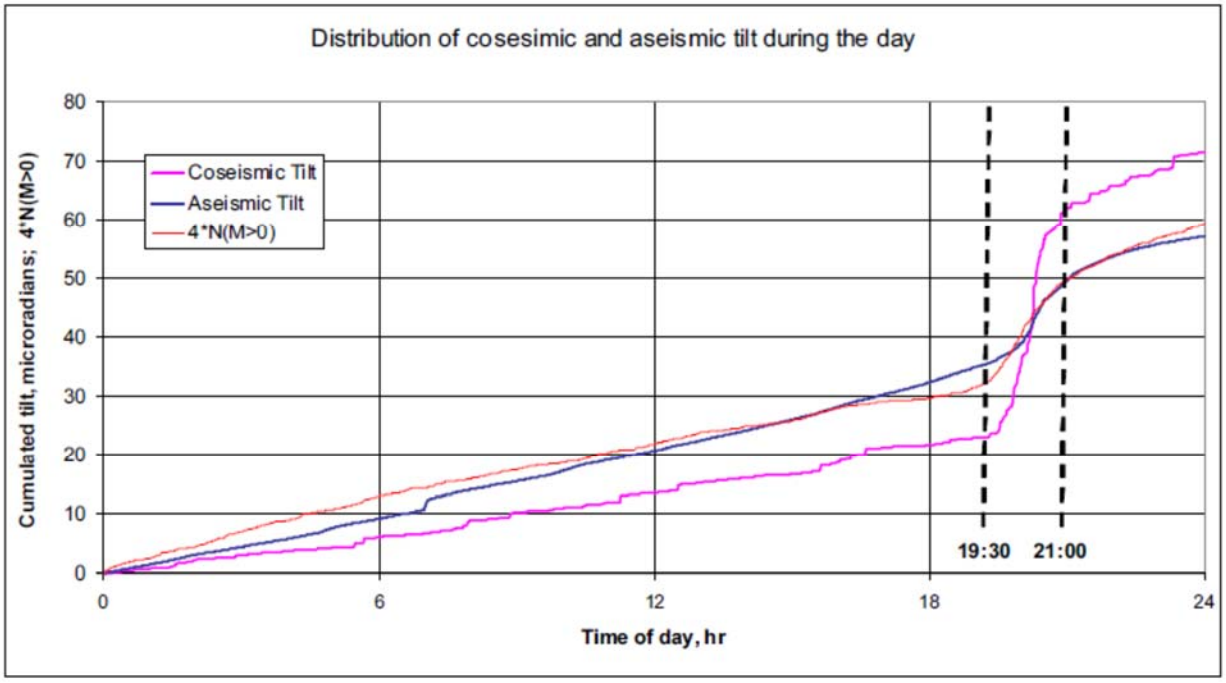

Figure 2.4: Distribution of coseismic and aseismic tilt during the day at Mponeng mine [*Ogasawara et al.,* 2009].

It was found that the rate of coseismic and aseismic tilt, as well as seismicity recorded by the mine seismic network, were approximately constant until the daily blasting time [*Ogasawara et al.,* 2009]. *Durrheim et al.* [2010] also report that tilt changes associated with a M 2.1 seismic event at Mponeng on 27 December 2007 (**Figure 2.5**) had well pronounced after-tilt, probably due to the aftershock sequence or the aseismic expansion of the source.

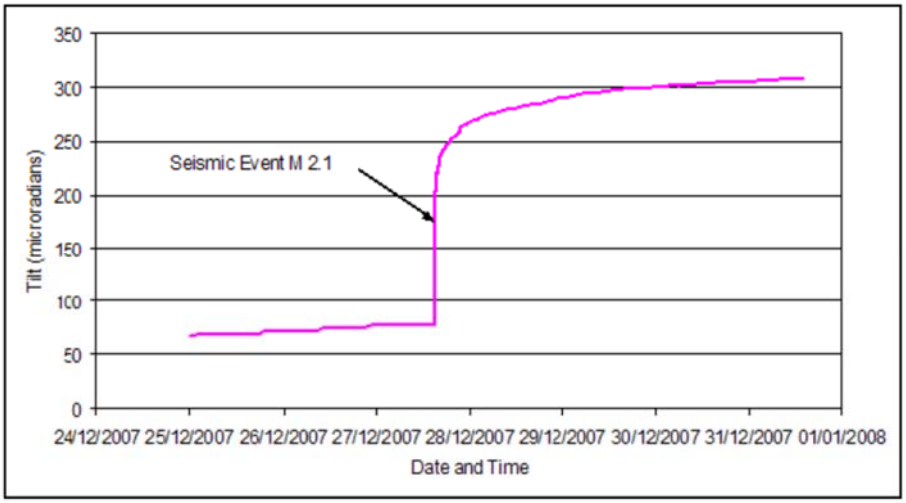

Figure 2.5: Tilt associated with the M_w1.9 (M 2.1) event on 27 December 2007 at Mponeng gold mine, South Africa [*Ogasawara et al.,* 2009].

The disadvantage of the approach used in the deep mines of South Africa to study seismic nucleation is that one does not know the timing of the earthquake nucleation events. The earthquake nucleation experiment that we propose in Chapter 3 allows us to control the time and location for earthquake nucleation and therefore makes it more robust in the study of earthquake triggering mechanisms.

2.3.2. Fluid Injection studies in Rangely, Colorado

Between 1969 and 1973, a series of fluid-injection and extraction experiments were conducted in an oil field of Rangely, Colorado with the objective of assessing whether earthquake control was possible. *Raleigh et al.* [1976] reported that earlier in 1966, it had been discovered that injection of fluids at high pressure, deep underground, was responsible for triggering of earthquakes near Denver, Colorado. The mechanism of earthquake triggering is such that the injection of fluids at high pressure in pre-existing fault zones results in an increase of local pore pressure in the fault, which, in turn, results in a decrease in the shear strength of the fault. At great depths, the ambient stresses are high enough to cause fault slip, which can generate an earthquake. In September of 1969, Raleigh, *Healy* and *Bredehoeft* in conjunction with the Chevron oil company and the support of the Defense Advanced Research Projects Agency (DARPA), began a field experiment to control the seismicity of an existing fault zone by controlled variations in pore pressure [*Raleigh et al.,* 1976]. They report that the experiment was conducted in four stages as follows:

1. The seismicity of the vicinity of the injection wells was recorded for a year from a local network of seismographs. Approximately 40 small earthquakes were recorded in a 10-day period during this stage of the experiment.
2. In stage II, the fluid pressure was reduced by withdrawing fluid from the injection wells and monitoring the seismic reaction of this action. It is reported that this resulted in a reduction in seismic activity in the vicinity.
3. In stage III, fluid pressure was increased by injecting high pressure fluid in the injection wells. Concurrent measurements of reservoir pressure in nearby observation wells were also conducted.

4. The cycle of fluid extraction and injection was repeated while monitoring the bottom hole pressure in the injection wells and nearby test wells.

Measuring the stresses in situ and the frictional properties of the reservoir rock in the laboratory, the observations can be compared with the predicted fluid pressure for triggering earthquakes. For an adequate field experiment, it was necessary to know the following:

1. The pore pressure in the vicinity of the hypocenter of the earthquake. The reservoir virgin pore pressure was calculated to be 17 MPa (2466 psi).
2. The absolute state of stress and the orientation of the fault planes and slip directions in the vicinity of the hypocenter. Hydraulic fracturing of rock in boreholes was used to measure the stress state. *Haimson* [1972], carried out hydraulic fracturing at a depth of 2 km in the Weber sandstone at Rangely and reported values of σ_1 = 55.2 MPa, σ_2 = 42.7 MPa (Overburden stress) and σ_3 = 31.4 MPa. *Raleigh et al.* [1976] report that, based on focal solutions derived from the radiation pattern of compressional wave arrivals, the subsurface faults correspond to fault planes with a right-lateral sense of shear, having a slip direction plunging 10° to 20° to the southwest. The fault can therefore be considered to be a right-lateral, approximately strike-slip fault [*Raleigh et al.,* 1976]. It appears the fault is not a single, large fracture surface, but a broad zone composed of sub-parallel fractures. From the orientation of the fault and slip direction determined from focal plane solutions of nearby earthquakes, the shear and normal stresses resolved into the slip direction and normal to the fault plane, respectively, are τ = 7.2 MPa and σ_n = 34.2 MPa [*Raleigh et al.,* 1976]. Based on laboratory measurements, the coefficient of static friction, μ, for faulted specimens of Weber sandstone is 0.81 [*Byerlee,* 1975]. Applying the Hubert-Rubey failure criterion:

$$\tau_c = \mu\,(\sigma_n - p_c) \tag{2.1}$$

where τ_c, is the shear stress at failure, σ_n is the normal stress, and p_c is the critical pore pressure required to trigger earthquakes. Therefore, p_c = 25.7 MPa (3728 psi) is the critical pore pressure above which earthquakes should be triggered.

3. The precise hypo central locations and focal plane solutions for the earthquakes.
4. To be certain that the active stage of the test would not substantially increase the likelihood of a damaging earthquake.

Raleigh et al. [1976] reported that from October 1969 to 10 November 1970, four designated wells were injected with fluid at high pressure. There were more than 900 earthquakes in the field during this period of time. On November 10 these four wells were shut in for 3 days and then fluid withdraw was conducted. Seismic activity within 1 km of the wells dropped from the previous year's average of 28 earthquakes per month to about 1 per month. It is further reported that on 26 May 1971 reinjection was initiated and the seismic activity remained at less than 1 earthquake per month. Between September 1971 and August 1972 the bottom-hole pressure declined. Then the pressure was raised up again. In October 1972 the bottom-hole pressure exceeded the predicted critical value of 25.7 MPa and in January 1973 the pressure reached 27.5 MPa. During this time space the monthly average of earthquakes near the wells rose to 6. From January to the end of April, with the pressure standing at about 28 MPa, the monthly average of earthquakes near the wells was 26. Then the wells were shut in and fluid withdraw was began on 6 May 1973. Since that day, no earthquakes have been recorded within 1 km of the bottom of the four injection wells, and only one earthquake per month has been recorded along the fault zone to the southwest [*Raleigh et al.,* 1976]. **Figure 2.6** shows the correlation between the fluid injection/withdrawal cycle and the earthquake seismic activity frequency.

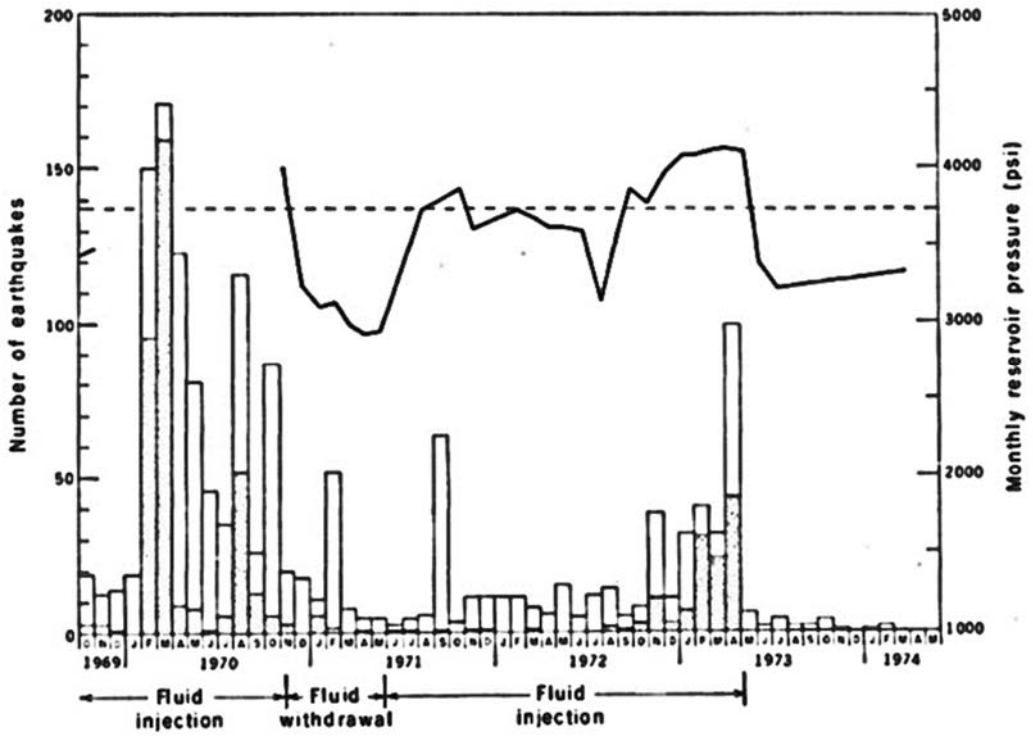

Figure 2.6: Frequency of earthquakes at Rangely [*Raleigh et al*., 1976]. Stippled bars indicate earthquakes within 1 km of experimental wells. The clear parts of the bars indicate all others. Pressure history in well Fee 69 is shown by the heavy line. Predicted critical pressure is shown by the dashed line.

Raleigh et al. [1976] reported that the largest earthquakes, both of which occurred on 21 April 1970, were M 3.1. The results showed that there was a strong correlation between the variations in fluid pressure in the fault zone and the frequency of the seismicity in the field vicinity. They also confirmed the hypothesis that earthquakes may be nucleated by pore pressure perturbation, which is well accounted for by the Hubbert-Rubey principle of effective stress. It was especially significant that successful prediction of the approximate pore pressure required for nucleating fault slip in accordance with the Hubbert-Rubey theory was possible. We can surmise from these findings that the following parameters are important when selecting an existing fault for similar field experiments:

1. The size and orientation of the fault.
2. The permeability of the fault gouge and parent rock including permeability anisotropy.
3. The complete state of stress in the fault zone.

Another important finding from the Rangely experiment was the short time scale within which seismicity was arrested by fluid withdrawal. *Raleigh et al*. [1976] report cessation of seismic activity occurring within one day of the initiation of fluid extraction from the experimental wells in May 1973. It is hoped that by making use of the strengthening effect of a reduction of fluid pressure in a major fault zone, it may be ultimately possible to control the timing and the size of major earthquakes [*Raleigh et al.,* 1976]. This conclusion is important for the experimental techniques that we design and propose in Chapter 3.

Raleigh et al. [1976] proposed a scheme of how the strength of a major fault like the San Andreas Fault can be reduced so as to avoid a major earthquake. An earthquake of magnitude 4.5 requires a fault length of about 5 km and yields about 2 cm of slip [*Wallace,* 1970]. *Raleigh et al.* [1976] explain that in this hypothetical scheme of controlling earthquakes, two 5 km deep wells are drilled 5 km apart on an existing fault line. Fluids are removed from these two wells to increase the frictional strength of the fault. Then a third well is drilled in half way between the first two wells and fluid is injected into this well (while fluid is still being withdrawn from the other wells) to trigger an earthquake [*Raleigh et al.,* 1976]. The stress drops at this well and increases towards the two outer wells were the earthquake rupture is arrested. In the next phase, fluid is then extracted from the middle well while withdraw in the outer wells is stopped, resulting in an increase in the frictional fault strength. Finally, fluid is injected at the outer wells to trigger earthquakes and produce a stress drop. It is proposed that the procedures be alternated at intervals of 6 months to accommodate the required slip rate [*Raleigh et al.,* 1976]. **Figure 2.7** summarizes the proposed scheme.

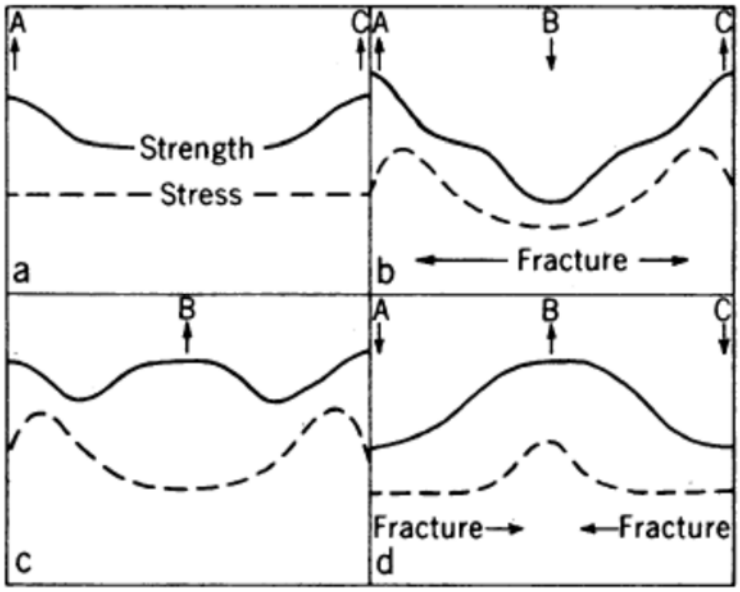

Figure 2.7: Hypothetical scheme for controlling Earthquakes [*Raleigh et al.,* 1976].

(a) Fluid removed from wells A and C to increase frictional strength along fault.
(b) Fluid injection into well B Triggering Earthquake and resulting in stress drop at B and increase at A and C where rupture is arrested.
(c) Fluid is extracted at B, resulting in increase in strength at B.
(d) Fluid is injected at A and C, producing earthquakes, with rupture arrest at B.

To get a better handle on the feasibility of this scheme, a more complete study of the fault properties and in situ stresses is necessary. Not the least among these properties would be the permeability of the fault zone, including the permeability anisotropy.

2.3.3. Deep borehole at KTB, Germany

One of the best investigated deep drilling boreholes in the world is the 9.1 km deep KTB (Kontinentale Tiefbohrung, Germany) drilling hole. This superdeep drill hole was designed for two objectives: The first objective was to verify the most widely used hypothesis of crustal stress and strength that the lithosphere is in failure equilibrium, with the state of stress in the upper crust being controlled by its frictional strength [*e.g., Brace and Kohldtedt,* 1980]. This was done by verifying that small pore pressure perturbations can trigger seismicity at great depths (~7.7 km) and temperatures (300 ^{o}C). The second objective was to extend knowledge about the crustal stress profile and brittle faulting to depths and temperatures approaching the brittle-ductile transition zone [*Zoback and Harjes,* 1997]. Two short term fluid injection experiments inducing

microseismicity were conducted at the KTB in 1994 and 2000 [*Zoback and Harjes,* 1997; *Baisch et al.,* 2002]. A long-term experiment was conducted from 2002 to 2005 during which fluid extraction was conducted for one year from 2002 to 2003 followed by one year of injection from 2004 to 2005 [*Shapiro et al.,* 2006].

The superdeep KTB site is located in south east Germany near the western margin of Bohemian massif at the contact zone of the Saxo-Thuringian and the Moldanubian. Natural seismicity is meager in the region with approximately one event per year [*Zoback and Harjes,* 1997]. *Shapiro et al*. [2006] report that two boreholes were drilled into a crustal segment mainly composed of metabasites and gneisses. They state that a 4 km deep pilot hole was completed in 1989, and the 9.1 km deep main hole was completed in 1994. A total volume of 22,300 m^3 of saline crustal fluids was extracted from the pilot hole during the first phase of the experiment from June 2002 to June 2003. There was no evidence of induced seismicity during this phase of fluid extraction [*Shapiro et al.,* 2006]. *Baisch and Harjes* [2003] report that the fluid level in the main hole dropped about 50 m as fluid was being extracted from the pilot hole located about 200 m away. They conclude that this was due to the highly fractured crust between the two holes with a permeable fault network between the 9.1 km depth and the surface of the earth. Hydraulic permeability was estimated to be approximately 2 x 10^{-15} m^2 [*Baisch and Harjes,* 2003] One year of fluid extraction was followed by one year of fluid injection from 2004 to 2005. *Shapiro et al.* [2006] report that over 84,600 m^3 of water was injected into the open hole section (uncased) at the 4 km depth of the pilot hole, where a fault intersects the borehole. They also state that the injection rate was kept at an average of 200 l/min while the well head injection pressure was kept below 30 MPa with a mean value of 28 MPa. They observed that induced seismicity commenced in September 2004 and increased thereafter. **Figures 2.8** shows the changes in seismicity recorded at the surface stations from the day the water injection was started (27th May, 2004) to the day the injection was stopped (1st June, 2005).

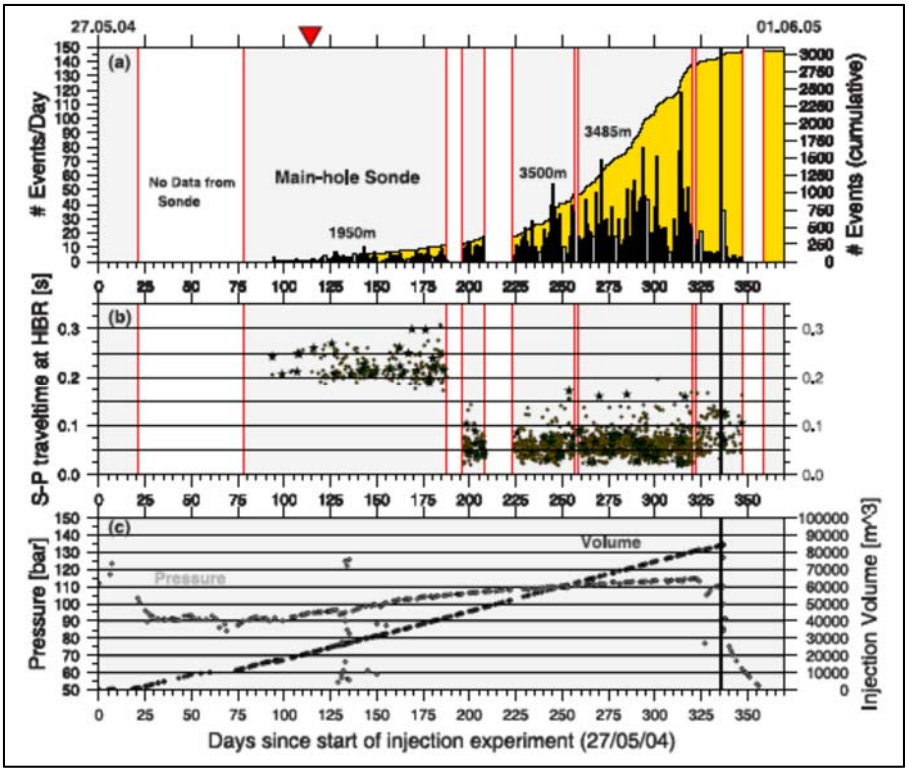

Figure 2.8: Results of the 2004/2005 KTB injection experiment [*Shapiro et al.,* 2006]. (a) Microseismic events as recorded by the surface stations. (b) Changes in the locations of the borehole geophone are evident from the plot of differences of the S and P waves arrival times. (c) The injection pressure along with the cumulative volume of the injected water. The time when the amount of previously extracted fluid was re-injected is marked in part (a) (red inverse triangle on the top).

The cumulative volume of injected water and the well head injection pressure are shown in **Figure 2.8**. The mean elevated pore pressure of 28 MPa was well below the minimum principal stress near the borehole and therefore was too small to cause hydraulic opening of existing fractures or to cause new fractures. Therefore, seismicity was only induced by pore pressure perturbations. *Baisch and Harjes* [2003] also observed that seismicity initiated at the point when the injected fluid volume equaled the previously withdrawn water volume of 22,300 m^3. They also observed that seismicity only occurred when the elevated pore pressure exceeded the critical value to cause Coulomb-failure, i.e., the ratio of shear to normal effective stress becomes larger than the coefficient of friction. *Shapiro et al*. [2006] also observed that seismicity only occurred during periods of positive pore pressure perturbation (injection) and not during periods of fluid withdraw.

Zoback and Harjes [1997] estimated the pore pressure at which earthquakes were triggered by modeling the pressure record of the 1994 injection experiment. They estimated the

pore pressure as a function of time and distance from the borehole in order to determine the approximate magnitude of the pore pressure changes associated with earthquake nucleation. **Figure 2.9** shows estimates of pore pressure perturbations as a function of time at four distances away from the borehole: 7, 16, 33, and 66 m. These pressures were calculated by obtaining the bulk permeability of the fracture zone into which fluid was diffusing and then using the time variation of injection to estimate how pressure in the fracture zone was changing with time [*Zoback and Harjes,* 1997]. *Zoback and Harjes* [1997] observed from this modeling that at distances of only a few tens of meters from the borehole, the changes of pressure in the fault zone appears to be small. The Figure also shows that the pressure in the formation took several hours to build up and was possibly a function of the coefficient of diffusivity. They also state that this figure illustrates that pressure in the fracture zone persists long after injection ceased, and is consistent with the occurrence of seismicity during the later stages of the experiment. The fact that very small pore pressure perturbations were able to induce seismicity confirms the hypothesis that the crust is in brittle failure equilibrium at great depths and temperatures approaching the brittle-ductile transition.

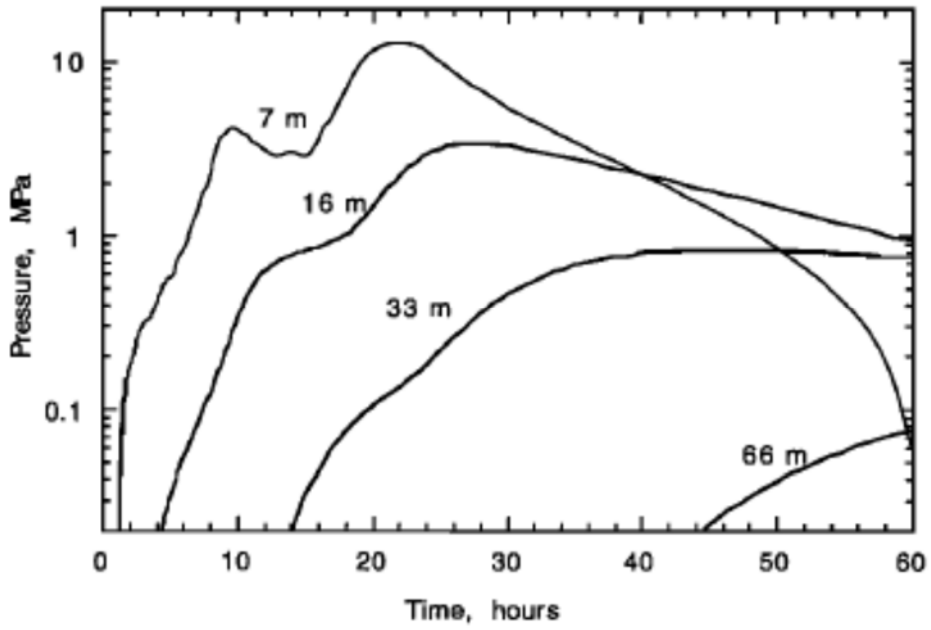

Figure 2.9: Theoretical pore pressure perturbation in the fault and fracture zone into which injected brine was diffusing as a function of time [*Zoback and Harjes,* 1997]. Modeled pressures are shown at 7 m, 16 m, 33 m, and 66 m. Note that even at small distances, the change of pressure in the fault zone appears to be small.

2.3.4. San Andreas Fault Observatory at Depth (SAFOD)

The San Andreas Fault Observatory at Depth (SAFOD) is a scientific drilling project whose objective is to directly study the physical and chemical processes that control faulting and earthquake generation within the San Andreas Fault (SAF) at seismogenic depth. This is a comprehensive project in which drilling has been conducted into the hypocenter zone of earthquakes that have been repeating on the SAF at a depth of approximately 3 km. A comprehensive suite of downhole measurements has been conducted in order to analyze the physical and chemical conditions under which earthquakes occur. Rock and fluid samples have also been exhumed and will be used for extensive laboratory studies across the world. According to *Hickman and Zoback* [2004], intensive downhole geophysical measurements and long-term monitoring are also being implemented within and adjacent to the active fault zone. They go on to say that the observatory-mode monitoring activities include near-field, wide-dynamic-range seismological observations of earthquake nucleation and rupture as well as continuous monitoring of pore pressure, temperature and strain during the earthquake cycle.

The SAFOD project site is located near Parkfield, California about 1.8 km southwest of the SAF and was drilled in such a way that the inclined borehole penetrates the entire fault-zone at seismogenic depth [*Zoback et al.,* 2011]. The fault is seismically active around SAFOD with numerous sites of repeating micro-earthquakes, M ≈ 3 and smaller, occurring on the fault at a depth of 3 - 12 km. A 2.2 km deep vertical pilot hole was drilled and instrumented at the SAFOD project in 2002. *Hickman and Zoback* [2004] present an overview of the pilot hole experiment at SAFOD. The SAFOD main borehole was drilled in 3 phases from 2004 to 2007. *Zoback et al.* [2011] reports that phase 1 was carried out in the summer of 2004 and started with the vertical drilling of the main hole to a depth of ≈ 1.5 km followed by the use of directional drilling techniques to deviate the borehole at an angle of ~60^{o} from the vertical to drill through the entire width of the fault near the repeating micro-earthquakes hypocenters at a vertical depth of ≈ 2.7 km. **Figure 2.10,** shows a simplified cross-section parallel to the trajectory of the SAFOD borehole. It is also reported by *Zoback et al.* [2011] that during phase 2, a large diameter (≈ 22 cm) hole was rotary drilled across the SAF zone in the summer of 2005. Although no core samples can be obtained during rotary drilling, it is more robust than core drilling and allows for bigger size boreholes than

core drilling would allow. A relatively larger diameter hole for SAFOD was required in order to allow for the deployment of the observatory instrumentation in the fault zone after drilling was completed.

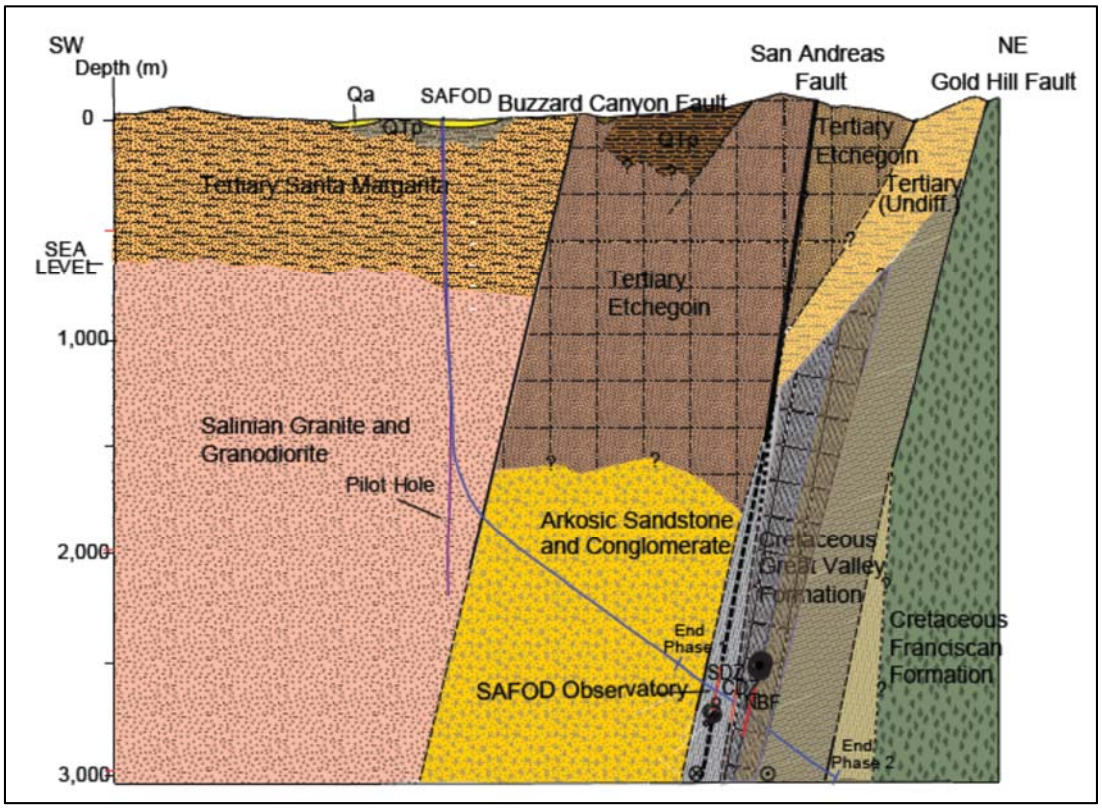

Figure 2.10: Simplified Geological cross-section showing the flight of the SAFOD borehole at subsequent phases of the project [*Zoback et al.,* 2011]. The geologic units are constrained by surface mapping and the rock units encountered along both the main borehole and the pilot hole. The black circles represent repeating micro-earthquakes. The depth at which the SAFOD observatory is deployed is shown.

During phase 3, in the summer of 2007, several sidetracks were drilled laterally off the phase 2 main hole to obtain core samples from two actively deforming traces of the SAF [www.earthscope.org]. Thus, the scientific community has been able to obtain core samples from an active major fault zone for the first time and access to these samples will now end decades of speculation about the fault's composition.

Drill cuttings were collected in real time as drilling was taking place during phase 1 and 2 of the project. The soft, slippery mineral, talc was discovered in cuttings of serpentinite collected in 2005. Talc was produced by the reaction of serpentine with silica-bearing ground water that

migrated up the fault. If talc is widespread in the fault zone, it could explain both the weakness of the SAF and its creeping behavior.

One of the most important findings at SAFOD is the observation by *Zoback et al.* [2011] that the San Andreas Fault is a weak fault in a strong crust. This is an issue that had generated a myriad of debate for decades in the past. *Zoback et al.* [2011] found that the direction of maximum horizontal stress was at a high angle to the SAF at depth, indicating that fault slip occurs in response to low resolved shear stress. They also noted that temperature measurements in the main hole at depth show no evidence of frictionally generated heat and that there was no evidence of elevated fluid pressure. They conclude that all this information and measurements are consistent with the strong crust/weak fault model of the SAF proposed over 40 years ago that had not been confirmed by direct observations.

Installation of the long-term SAFOD observatory was completed on September 28, 2008 [www.earthscope.org]. Borehole seismometers, accelerometers, and tiltmeters were deployed to observe variations in deformation, fluid pressure, microseismicity, and radiated seismic energy within and adjacent to repeating earthquake nucleation patches over multiple earthquake cycles. The schematic in **Figure 2.11** shows the observatory instrumentation consisting of five pods containing different types of sensors. *Zoback et al.* [2011], report that pods 1 and 3 each contained a 3-component seismometer and a 3-component accelerometer, pods 2 and 4 each contained a 2-axis tiltmeter, and pod 5 contained a 3-component seismometer, accelerometer as well as a passive electromagnetic (EM) coil. The objective of the EM test was to establish if electromagnetic waves are radiated by the earthquake source [*Zoback et al.,* 2011]. To isolate them from contact with wellbore fluids, all instruments were housed in sealed steel pods. The tilt and seismic systems were independent of each other, with separate power and data telemetry lines.

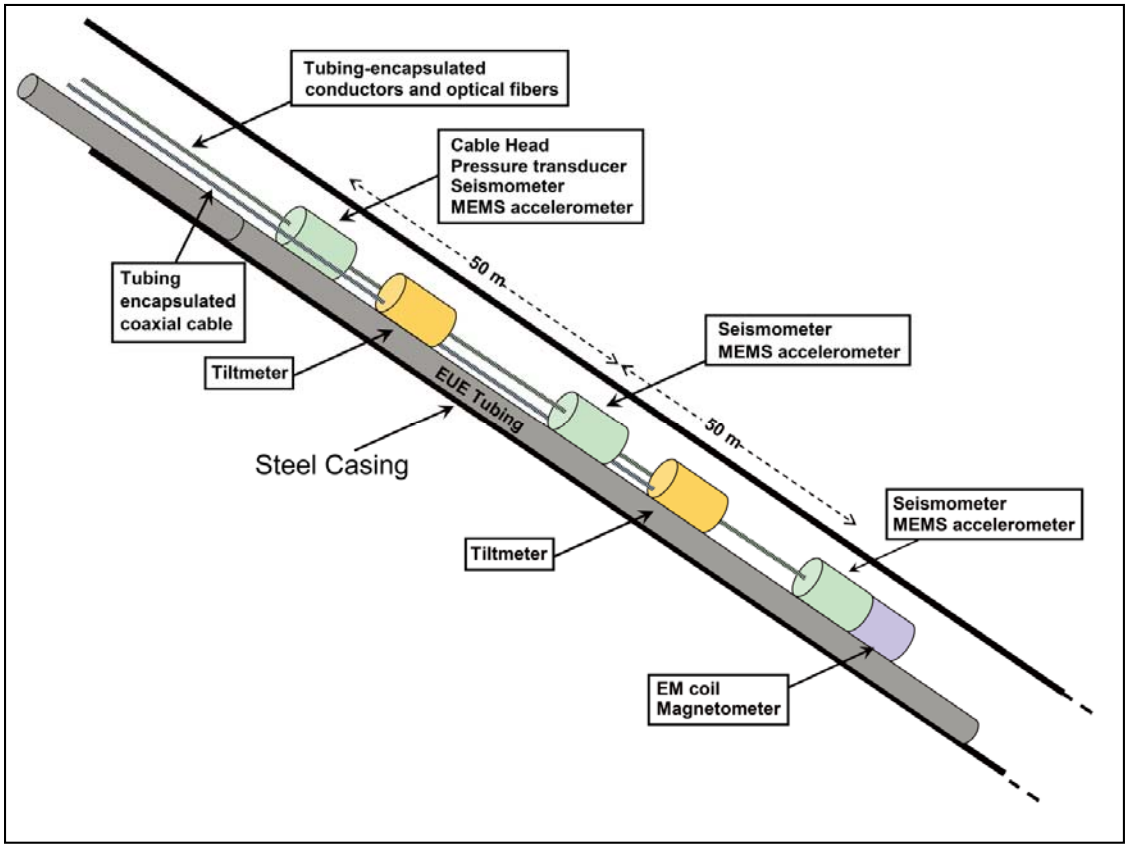

Figure 2.11: Schematic diagram of the instrumentation deployed in the SAFOD observatory above the location of the HI repeating earthquake sequence [*Zoback et al.,* 2011].

Figure 2.12 is an example of the data produced by the SAFOD observatory instrumentation for an earthquake that occurred on September 30th, 2008 [*Zoback et al.,* 2011]. According to *Zoback et al.* [2011], the hypocenter of the earthquake was located ~2.5 km from the assortment and the earthquake was an M 1.3 micro-earthquake. They state that the EM signal appeared at the same time as the seismic waves because it was the result of shaking of the coil within the earth's magnetic field by the seismic waves as they passed the instrument.

The Observatory suffered a major setback in that some of the instruments developed electronic problems shortly after installation. It is speculated that this may have been caused by water leakage into the pods [*Zoback et al.,* 2011].

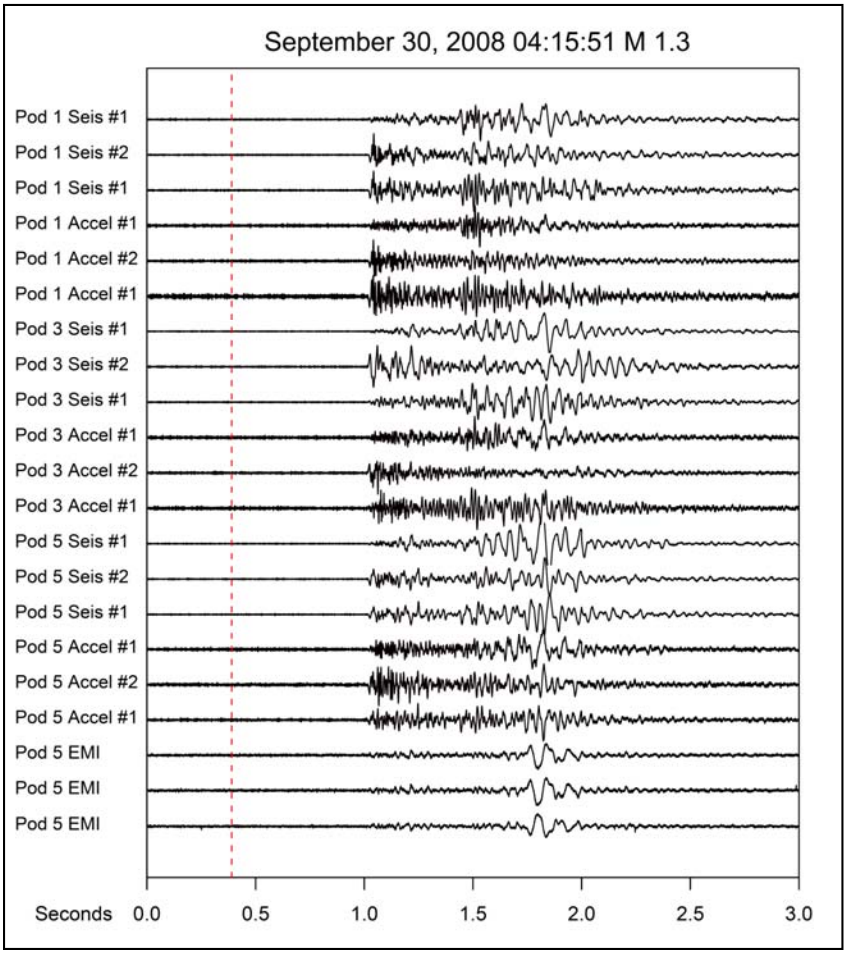

Figure 2.12: Example of seismograms produced by SAFOD observatory seismometers. The origin time of the M 1.3 microearthqauke is shown by the dashed line in red. The lower 3 traces are the output of the passive electromagnetic coil [*Zoback et al.,* 2011].

The drilling of deep boreholes such as KTB and SAFOD observatory for studying earthquake processes is prohibitively expensive. Another disadvantage of studying earthquake source processes in the manner applied at KTB and SAFOD observatory is the luck of control on the timing of the earthquakes. Further, in a situation where instruments are not operational due to malfunction, there is usually no opportunity to fix the instruments in time for the next earthquake. In the following chapter, we discuss some earthquake triggering methods that will allow controlling of the timing, location and size of an artificial earthquake for research purposes. The techniques we propose in Chapter 3, also allows for better control of instrumentation, including corrections in cases where the instruments malfunction.

2.3.5. Fault-injection experiment in southeastern France

Guglielmi et al. [2015] recently conducted a field experiment in which they stimulated a previously inactive fault through a high-pressure injection of water. They used a newly designed instrument, the phase-rate injection method for fracture in situ properties (SIMFIP) probe displacement sensor [*Guglielmi et al.,* 2015] that allows detection of 3-D motions on the fault as well as monitoring fluid pressures. They injected the preexisting fault in an underground experimental facility in southeastern France at a depth of 282 m below the earth's surface. *Guglielmi et al.* [2015] observed a highly dilatant and slow ($\simeq$ 4 μm/s) aseismic slip associated with a twenty-fold increase of permeability, which transitioned to faster slip ($\simeq$ 10 μm/s) associated with reduced dilatancy and micro-earthquakes. No seismic event was detected until about 0.3 mm of fault slip, about 1100 s into the experiment. This author reports that the seismicity consisted of impulsive micro-earthquakes and tremors. About 80 seismic events were generated at an average rate of 15 events per min [*Guglielmi et al.,* 2015, 2016]. The experimental design that we propose in Chapter 3 would be conducted at greater depths than the southeastern France experiment and therefore will be more likely to produce seismic events.

2.4. SEISMIC EVENTS CORRELATED TO FLUID INJECTION

This section is a brief review of induced seismicity that has been correlated to the injection of waste fluids into wastewater disposal wells in deep geologic basement rock and to hydraulic fracturing associated with oil and gas production. More comprehensive reviews of injection and hydraulic fracturing induced seismicity have been presented by other researchers [e.g. *Ellworth,* 2013; *Folger and Tiemann,* 2015]. *Folger and Tiemann* [2015] report that the number of earthquakes of magnitude 3.0 or greater in the central and eastern United States has increased dramatically since about 2009 from an average of approximately 20 per year between 1970 and 2000 to over 100 events per year in the period 2010-2013. **Figure 2.13** shows the dramatic rise in the earthquake count in the central and eastern United States from 1967 to 2014. There appears to be a correlation between the sharp rise in seismicity in the recent years and the rise in deep-well injections and hydraulic fracturing in these areas. *Ellsworth* [2013] reports that the states experiencing elevated levels in seismic activity include Arkansas, Colorado, New Mexico,

Ohio, Oklahoma, Texas, and Virginia. The M 4.0 earthquake of December 2011 in Youngstown, Ohio, the M 4.7 earthquake of February 2011 in central Arkansas, the M 4.4 earthquake of September 2011 near Snyder, Texas, the M 4.8 earthquake of October 2011 near Fashing, Texas, the M 5.7 earthquake of November 2011 in central Oklahoma, and the M 4.9 earthquake of May 2012 in east Texas are all suspected to have been induced by oil and gas recovery activities [*Kim,* 2013; *Horton,* 2012; *Kerenan et al.,* 2014].

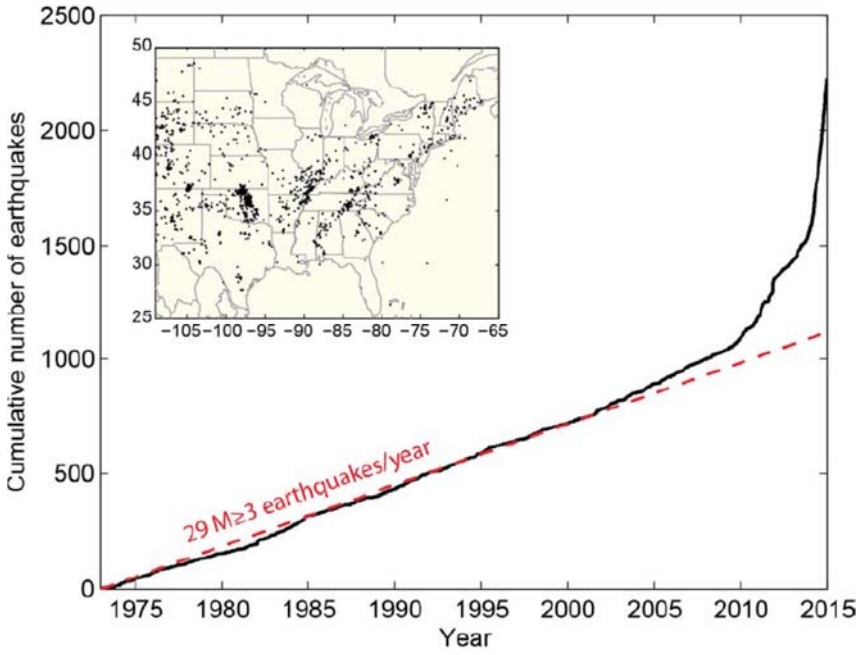

Figure 2.13: Cumulative number of earthquakes with M ≥ 3 in the central and eastern United States from 1967 to 2014 [*Folger and Tiemann,* 2015]. The dashed line corresponds to the long-term rate of 29 earthquakes per year. (Insert) Distribution of epicenters in the central and eastern region.

In the United States, injection wells used for oil and gas wastewater disposal and enhanced recovery are classified as class II wells [www.epa.gov]. According to the Environmental Protection Agency (EPA), class II fluids are primarily brines that are brought to the surface while producing oil and gas. Approximately over 2 billion gallons of brine are injected in the US per day, mostly in Texas, California, Oklahoma and Kansas. The EPA Underground Injection Control (UIC) program under the Safe Drinking Water Act (SDWA) regulates the subsurface injection of fluids to protect subsurface drinking water aquifers [*Folger and Tiemann,* 2015]. Class II wells fall into three categories, namely: disposal wells, enhanced recovery wells, and hydrocarbon storage wells. The EPA reports [*Ellsworth*, 2013] that there are about 180,000 class II wells in operation

in the United States. *Ellsworth* [2013] noted that of the more than 30, 000 class II wastewater disposal wells, only a small fraction appears to be associated with damaging earthquakes.

The mechanics of how earthquakes are induced by human activities are fairly well understood [e.g., *Germanovich et al.,* 2010; *Garagash and Germanovich,* 2012]. Modification of fault-driving stresses, fault shear strength and/or fault pore pressure can all lead to fault slip, which in turn results in the sudden and explosive release of elastic strain energy in the fault [*Germanovich et al.,* 2010; *Garagash and Germanovich,* 2012]. *Ellsworth* [2013] also notes that some factors that enhance the probability of a particular stress or pore-pressure perturbation inducing earthquakes include the magnitude of the perturbation, its spatial extent, ambient stress condition close to the failure condition, and the presence of faults well oriented for failure in the tectonic stress field. In addition, the fault permeability is a major factor controlling pore pressure diffusion. This may be a main factor that controls the timing of the seismic events. Induced seismic events sometimes occur shortly after fluid injection or hydraulic fracturing while other seismic events may occur long after the inducing event has ceased [*Ellsworth,* 2013].

2.4.1. Possible Injection-Induced earthquakes

Recently, several researchers have investigated the possibility of a correlation between increased seismicity in various regions of north America and the injection of fluids into the subsurface. The following are examples of recent seismic events that may have been induced by fluid injection:

1. *Rubinstein et al.* [2014] investigated the seismicity in the Raton Basin of northern New Mexico and southern Colorado and found that the deep injection of wastewater from the coal-bed methane field was responsible for inducing the majority of the seismicity since 2001. They observed clear correlation between the timing and location of increased seismicity and of industrial activity. They state that the August 2011 M 5.3 event is the second largest earthquake to date for which there is clear evidence that the earthquake sequence was induced by fluid injection.
2. *Horton* [2012] studied the earthquake swarm in central Arkansas and noted that the study area experienced an increase in the number of M 2.5 or greater earthquakes since 2009, when the first of eight deep-well injection disposal wells became operational.

3. *Frohlich* [2012] reports that the increased seismicity near Dallas-Fort Worth and Cleburne, Texas identified a possible linkage between high injection rates of oilfield-related wastewater and earthquakes of M 1.5 or greater and found that all 24 of the most reliably located earthquake epicenters occurred within about 1.5 miles of one or more injection wells [*Folger and Tiemann,* 2015]. It was concluded in the study that injection might trigger earthquakes only if the injected fluid reached critically oriented faults in the vicinity.
4. *Kim* [2013] concluded that the recent earthquakes in Youngstown, Ohio were induced by the fluid injection at a deep injection well due to increased pore pressure along some pre-existing faults located near the wellbore. This author found that the expanding high fluid pressure front increased the pore pressure along its path and progressively triggered the earthquakes. This author's study reported that the Youngstown area was, until then, aseismic before experiencing over 100 small earthquakes between January 2011 and February 2012. Figure **2.14** shows the correlation between seismicity and injected volume and pressure.

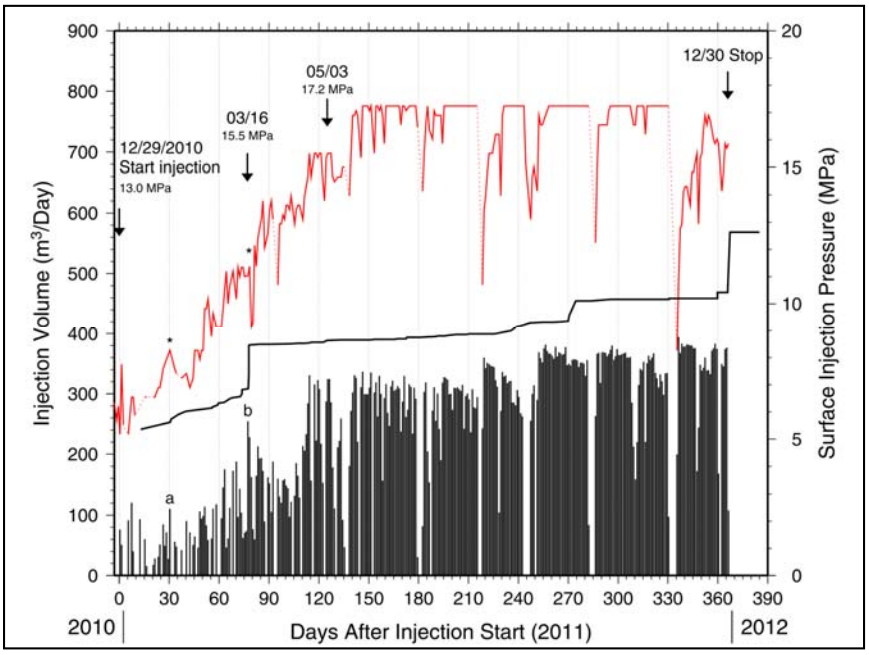

Figure 2.14: Graph of surface injection pressure and volume each day after the start of injection at Northstar 1 well during its operation from 29 December 2010 to 30 December 2011 [*Kim,* 2013]. Cumulative seismic moments of earthquakes are plotted as continuous solid line. Pressure is plotted in red. Daily total injection volume is plotted with solid bars. Instances of sharp increase of daily injection volume are indicated by a and b, which correspond to occurrence of earthquakes.

5. *The OKGS and the USGS* [2014] jointly report that the rate of earthquakes in central Oklahoma increased by fifty percent between October 2013 and May 2014. *Folger and Tiemann* [2015] report that since 2009, 20 earthquakes of M 4.0 to M 4.8 have struck central Oklahoma and that the largest earthquake in Oklahoma history - M 5.6 - occurred on November 5, 2011, near Prague*. The USGS statistical analysis suggested that the increased rate of seismicity could be due to deep-well wastewater injection.
6. According to the Kansas Geological Survey, several earthquakes were recorded in south-central Kansas in 2013 and 2014 near some wastewater injection wells. *Folger and Tiemann* [2015] state that although a definitive link to wastewater injection was not established, increased seismicity in Kansas near areas of wastewater injection led the Kansas governor to convene a task force on induced seismicity.
7. *Yeck et al.* [2014] investigated the temporal variations in maximum magnitudes of induced earthquakes at the Paradox Valley Unit (PVU) using two methods. First, they considered the relationship between the total cumulative injected volume and the history of observed largest earthquakes at the PVU. Second, they explored the relationship between maximum magnitude and the geometry of individual seismic clusters. Their results suggest that the PVU has the potential to induce events up to roughly M 5 in the region directly surrounding the well.

*After this work was completed, a larger earthquake of magnitude M 5.8 occurred on September 3, 2016 with the epicenter near Pawnee, Oklahoma. The epicenter depth was 5.6 km [www.earthquake.usgs.gov].

2.4.2. Hydraulic fracturing-induced earthquakes

It has been reported that the largest hydraulic fracturing induced earthquakes have been lower than the seismic damage threshold for modern building codes [*Holland,* 2013; *BC Oil and Gas commission,* 2012]. Their magnitudes tend to be generally small probably because the injections are short-term and add smaller volumes of fluid into the subsurface compared to disposal wells. Therefore, hydraulic fracturing induced earthquakes are generally thought to present less risk than disposal wells [*Folger and Tiemann,* 2015]. The following are examples of earthquakes that were possibly induced by hydraulic fracturing:

1. The British Columbia Oil and Gas Commission [www.bcogc.ca/node/8046/download] investigated some nearly 40 seismic events between April 2009 and December 2011 in the Horn River Basin, northeast British Columbia. They concluded that the seismic events ranging in size from M 2.2 to M 3.8 were linked to fluid injection during hydraulic fracturing activities near pre-existing faults.
2. *Green et al.* [2012] reports that hydraulic fracturing injections in Blackpool, England led to a series of small earthquakes smaller than M 2.3 between March 2011 and May 2011.
3. *Holland* [2013] reports that the investigation of a sequence of felt events with maximum M 2.9 in south-central Oklahoma revealed a clear temporal correlation between hydraulic fracturing operations in a nearby well and the earthquake occurrences. The study concluded that the lack of similar seismic activity before the hydraulic fracturing and after the hydraulic fracturing stopped, among other factors, suggests a link to the fracturing activities.
4. Recently, *Skournal et al.* [2014] reported that 77 earthquakes identified in Poland township, Mahoning County, Ohio, were closely related spatially and temporally to active hydraulic fracturing operations. They used an optimized multistation cross-correlation template-matching routine to arrive at this finding.
5. *Friberg et al.* [2014] also reported that a series of small earthquakes in Harrison County, Ohio, indicated that hydraulic fracturing operations affected a previously unmapped fault in the Precambrian crystalline rocks below the sedimentary rocks that were being hydraulically fractured.

2.5. CONCLUSIONS

In this chapter, a literature review of earthquake nucleation studies is presented. Three examples of laboratory studies of fault growth using triaxial equipment are discussed. A key question that needs to be answered concerns the adequacy of small scale laboratory experiments to simulate the earthquake nucleation process. In Chapter 3, we will estimate the size of the slip patch that is required to properly simulate earthquake nucleation. There is another limitation with laboratory investigations of faulting processes. Many field studies show that large, pre-existing weaknesses like bedding planes, joints, and dikes, rather than small flaws, control the location and geometry of some natural faults. Such large discontinuities are commonly absent and under-represented in laboratory shear failure tests. In order to narrow the gap between laboratory results and the reality of earthquake nucleation, we describe an experimental approach that aims to induce new faults or reactivate existing faults in-situ, at scales of 10 -100 m in Chapter 3.

Previous field experiments in the study of earthquake nucleation were also conveyed. Investigations in the deep gold mines of South Africa, fluid injection studies in the oil fields of Rangely, Colorado, investigations in the deep borehole at KTB, Germany and at the SAFOD were reported. Finally, waste-fluid-injection induced seismicity as well as hydraulic fracturing induced seismicity were presented. One disadvantage of these methods of earthquake nucleation study, is that there is no control of the size or the location of fault slip in these methods. In the method that we propose in Chapter 3, we seek to be able to control both the size and the location of the earthquake.

The main points of this chapter can be summarized by:

1. A discrepancy exists between the slip weakening distances inferred from laboratory faulting experiments and those evidenced from seismological studies. Laboratory experiments typically use slip weakening distances ranging from 10^{-5} – 10^{-3} m while recent seismological investigations have produced values in the range of 10^{-1} – 10^{0} m. In Chapter 3, we show that a scale of at least a few m is required to adequately simulate the earthquake nucleation process.

2. In the laboratory, artificial ways have to be used to stabilize the fault growth under triaxial compression conditions. However, fault growth under artificially slowed conditions may not be completely representative of the dynamic loading conditions in the seismogenic zone.
3. Laboratory models need to be validated using field experiments at appropriate scales.
4. To understand the earthquake preparation process or the rock mass behavior during the earthquake process, investigations should be conducted closer to the hypocenter. Therefore, scientists have drilled deep holes to seismogenic zones to measure and observe seismic activity. In some cases, investigators have even attempted to trigger fault nucleation through pore pressure manipulation. However, the costs are prohibitive and the holes are not always close enough for monitoring seismic processes accurately. Another disadvantage of using deep boreholes to study earthquake nucleation is the lack of opportunity to fix possible malfunctioning of monitoring-instruments.
5. Deep underground mines with existing faults have also been used as a stage for monitoring mining-induced seismicity. When underground drifts are excavated in the highly stressed rock mass of these deep mines, there is a re-distribution of stresses in the local stress field. A seismogenic zone forms ahead of the advancing stope face during the mining process. A major disadvantage of this is that there is no control of the timing or the magnitudes of the seismic events. In Chapter 3, we propose an experimental approach that aims to induce new faults or reactivate existing faults in a controlled way.
6. The Rangely, Colorado experiment between 1969 and 1973 demonstrated that earthquake control may be possible. It was found that earthquake triggering occurred during fluid injection while stabilization of seismic zones took place during fluid extraction of the experiment cycle. Further, it was found that seismicity began when the volume of fluid injected was equal to the amount that had previously been extracted. Also, seismic activity occurred when a critical pore pressure of the injected fluid was attained. Another important finding from the Rangely experiment was the short time scale within which seismicity was arrested through fluid withdrawal. It was reported that cessation of seismic activity occurred within one day of the initiation of fluid extraction from the experiment

in 1973. These findings are important in the earthquake nucleation experiment that we have designed for deep mines (Chapter 3).

7. *Raleigh et al.* [1976] proposed a scheme of how the strength of a major fault can be reduced so as to prevent a major earthquake. The scheme uses a systematic approach of fluid extraction and injection at certain locations and times.
8. Some parameters that are important for selecting a fault for a fault-reactivation experiment are (1) the size and orientation of the fault, (2) the complete state of stress in the fault zone, (3) the size of the pore pressure perturbation, and (4) the permeability of the fault gouge and parent rock. These parameters are also critical for the earthquake nucleation experiment that we have designed for the Homestake mine in the Black Hills of South Dakota (Chapter 3).
9. There appears to be a correlation between the recent sharp rise in seismicity in some states, and the rise in deep-well injections, to a large extent and hydraulic fracturing, to a smaller extent. One conclusion of this review is that seismicity occurs mainly during fluid injection and maybe ceasing during fluid extraction.
10. Similar instrumentation to those used for monitoring the earthquake preparation processes at SAFOD, KTB, and in the deep gold mines of South Africa can be used in the proposed earthquake nucleation experiment at the Homestake mine. These include geophones, accelerometers, acoustic emission sensors, tiltmeters, strainmeters, seismometers, and electromagnetic sensors, which can be placed in advantageous positions for data collection.

3. EARTHQUAKE NUCLEATION EXPERIMENT IN A DEEP MINE

3.1. INTRODUCTION

In this work, we designed field experiments for the Homestake mine that are probably the first field-scale experiments where fault initiation is designed to be actively controlled. We designed the experiments to quantify rupture mechanisms in both intact ("fresh") and faulted rock, including the sizes of the smallest frictional slip event, mechanisms of slip triggering and slip nucleation, mechanisms of strength-gain and fault-healing promoted by reactive fluids and other agents, and the role of fault weakening in the transition between quasi-static and dynamic fault rupture. The ultimate goal of such experiments is to improve our understanding of processes of earthquake triggering.

Most earthquakes are thought to be the result of unstable slip on existing faults. Activation of the Homestake fault in response to the controlled fluid injection and thermally changing background stresses is likely to be localized on a crack-like patch. Slow patch propagation, moderated by the injection rate and the rate of change of the background stresses, may become unstable, leading to the nucleation of a small earthquake (dynamic) rupture. This controlled instability is intimately related to the dependence of the fault strength on the slip process and has been analyzed for the Homestake fault conditions. Scale analyses indicate that this transition occurs for the nucleation patch size $\approx$1 m. This represents a fundamental limitation for laboratory experiments, where the induced dynamic patch could be tractable, and necessitates larger scale field tests $\approx$10-100 m.

Advancing the understanding of faulting and fracturing processes is important to many fields of earth science and engineering including seismology, resource recovery and environmental remediation, economic and structural geology, and disposal of radioactive wastes and carbon dioxide in the deep subsurface. Experiments involving fluid-rock reactions in the deep subsurface have implications ranging from the evolution of rock properties to geochemical cycles.

Contemporary interpretation of rock faulting is still strongly influenced by the work of *Coulomb* [1773] and *Anderson* [1905], but central issues of fault evolution still remain unsolved. Topics of localization, nucleation, and propagation of single faults and the development of fault systems have been of central interest to many research groups during the last twenty years. One model for the nucleation and propagation of faults in brittle rocks [*Reches and Lockner*, 1994] stems from the triaxial laboratory experiments on Westerly granite of *Lockner et al.* [1991]. This model, based on the interaction among tensile microcracks that develop in a self-organized pattern, predicts that faults propagate in plane, at an angle of 20 to 30 degrees relative to the axis of maximum compression. The model provides a physical explanation for 'internal friction', the empirical parameter in the Coulomb failure criterion, and is consistent with many field and laboratory observations, but it has not yet been directly verified beyond standard laboratory scales.

One approach to overcoming the size limitations in the laboratory integrates field mapping into studies of faulting processes. Many field studies show that large pre-existing weaknesses (e.g., bedding planes, joints, and dikes), rather than small flaws, commonly control the location and geometry of natural faults [e.g., *Behre,* 1937; *Segall and Pollard*, 1983: *Martel and Pollard,* 1988, *Christiansen and Pollard*, 1997; *d'Alessio and Martel*, 2005]. Such weaknesses commonly are absent in the rocks used in laboratory shear failure tests, but tests on highly anisotropic rocks show that the planes of weakness exert a strong control on the location and orientation of shear failures [*Donath*, 1961]. Recent field studies and some laboratory tests thus suggest that large pre-existing weaknesses strongly influence the nucleation, growth, and geometry of natural faults.

3.2. HOMESTAKE FAULT

Highly deformed Proterozoic rocks host the former Homestake mine. These rocks are primarily phyllite and schist that were metamorphosed from green schist to amphibolites facies [*Caddey et al*. 1991]. The general structure consists of the Lead anticlinorium and synclinorium, and the Poorman anticlinorium to the west. The longest wavelength of these folds is of the order of kilometers, although rock units within these folds are themselves highly folded at scales ranging

from cm to 100s of meters [*Caddey et al*., 1991]. Regional foliation is roughly parallel to the axial planes of the folds, with a strike approximately N20W and a steep dip to the NE [*Rahn and Roggenthen*, 2002]. Ductile shear zones are also oriented roughly parallel to the regional foliation [*Caddey et al*. 1991]. Despite the complex folds in the vicinity of the Homestake mine, the orientation of the foliation is remarkably uniform across the region.

During our field work in the Homestake mine, we found a large fault exposed on multiple mine levels. The fault is subparallel to the local foliation in the Poorman formation and extends at least 1.5 km along strike and dip, with a center ≈1.5 km deep. It strikes ≈340°, dips ≈60° NE, and is characterized by a ≈0.4-m-thick gouge (**Figure 3.1a**) that contains crushed host rock and black material that appears to be graphite. We have not found clear evidence for the sense of fault slip, but secondary features suggest that it is a normal fault. The size and distinct structure of this fault make it a promising target for in-situ experimentation on fault strength, hydrological properties, and slip nucleation processes. Developing an earthquake nucleation experiment on the example of the Homestake fault is important for designing such experiments in general deep mine conditions.

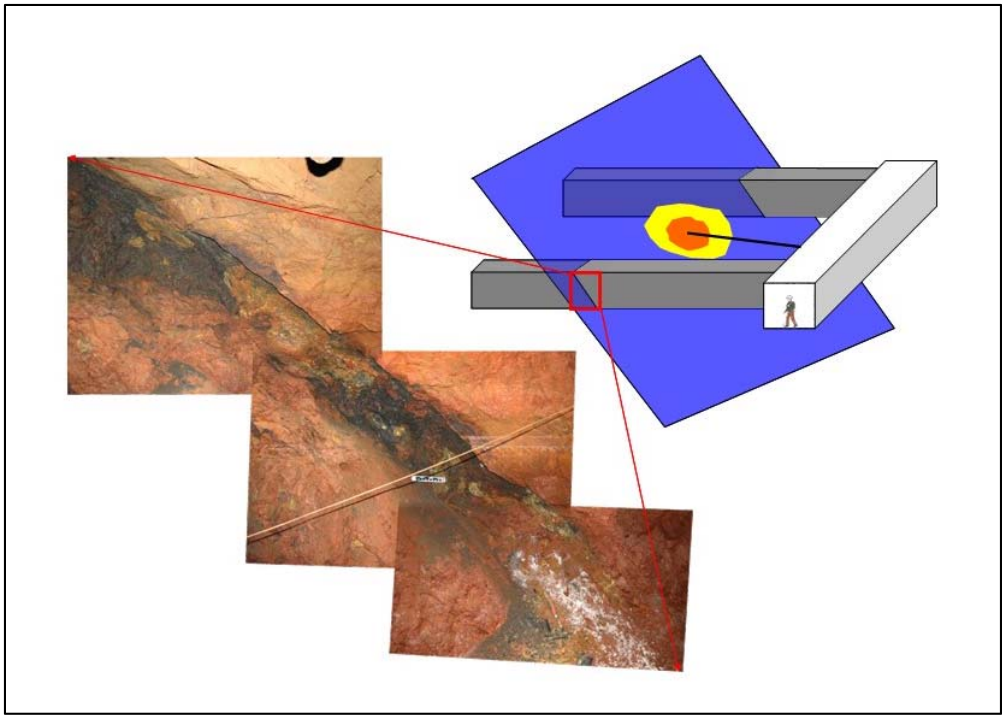

(a)

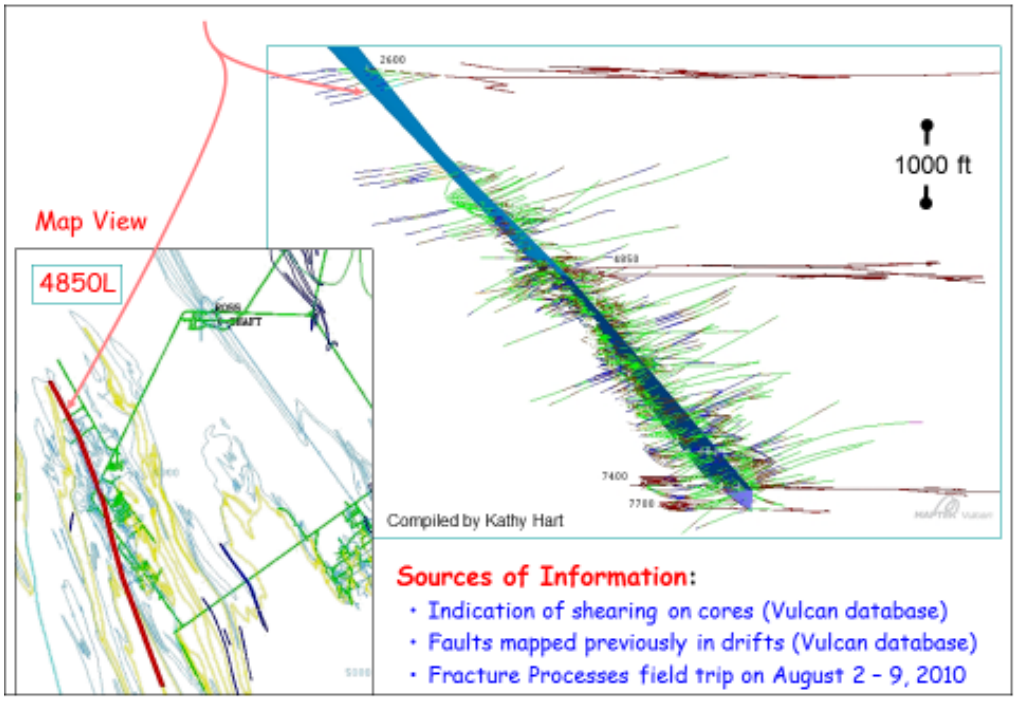

(b)

Figure 3.1: (a) Homestake fault gouge and schematics of fluid injection to nucleate dynamic slip. Shown drift configuration corresponds to the 4850-ft level in the Homestake mine (b). Well-developed fault which can be accessed at several levels. Cross section projection of 4850 mine level of Homestake mine shows large fault that can be accessed at several drifts.

3.3. NUCLEATION OF DYNAMIC RUPTURE ON A PRESSURIZED FAULT

Most earthquakes are thought to be the result of unstable slip on existing faults. Locally elevated pore pressure is a viable mechanism for reduction of fault strength and earthquake triggering. In nature, possible sources of elevated pressure near faults that are associated with induced or triggered seismicity include (1) deep fluid injection into the crust [e.g., *Healy et al*., 1968]; (2) fault-valve systems when a fault of low permeability transects a super hydrostatic pressure gradient [*Sibson*, 1992]; (3) metamorphic dehydration in thrust and normal fault systems. In engineering applications (waste disposal, petroleum production, water reservoir management), faults have been reactivated due to manipulations with subsurface fluids [e.g., *Raleigh et al.,* 1976; *Nicholson and Wesson,* 1992; *McGarr,* 1991 and 2014].

Although the mechanics of fault reactivation due to pore pressure perturbation is generally well understood, considerable uncertainty persists regarding (1) the conditions under which the reactivation of fault slip leads to the nucleation of dynamic (earthquake) rupture; (2) the extent that a dynamic rupture can propagate before it is arrested, and (3) what distinguishes micro-seismic events from earthquakes.

These questions can be addressed by analyzing nucleation and arrest of dynamic slip on a pressurized part of the Homestake fault (**Figure 3.1a**). We expect that slip on the Homestake fault could be activated in response to controlled fluid injection near the fault (**Figure 3.1a**). This activation is likely to be localized on a growing crack-like patch (or series of patches) that is either weaker than the rest of the fault or that sustains a locally elevated shear stress (**Figure 3.2a**). Such an experiment would exploit the evolving, locally-peaked pore pressure profile associated with along-the-fault diffusion from a fluid source. As a result, frictional strength of the fault, given by the product of the local normal effective stress and slip-weakening friction coefficient, reduces below the background shear stress within the pressurized region, which expands with time. The resulting nucleation and growth of a shear patch (crack) would initially be moderated by the pressure diffusion and, therefore, quasi-static. In the framework of the Homestake fault, the longitudinal and transverse permeabilities of the fault may be different [e.g., *Wibberley and Shimamoto*, 2003], and slip is likely to propagate both in the direction of fault dip and strike

(**Figure 3.1a**). Yet, the slip-weakening nature of friction suggests that quasi-static patch growth may eventually become unstable, leading to the nucleation of dynamic (earthquake) rupture [*Campillo and Ionescu*, 1997; *Uenishi and Rice*, 2003].

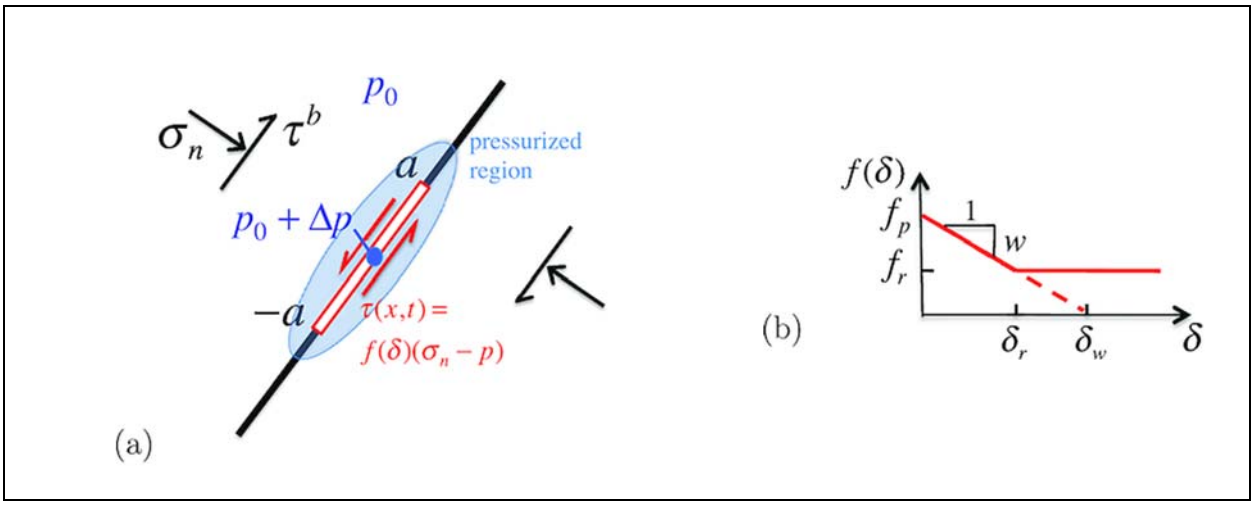

Figure 3.2: (a) A growing slip patch (shear crack) due to fluid injection into a uniformly loaded fault. (b) Friction coefficient $f(\delta)$ (with (horizontal solid line) or without (inclined dashed line) residual cut-off) as a function of slip magnitude in the linear friction-weakening law with slope w.

The main question in designing a fluid-injection, deep mine faulting experiment is the assessment of the rock mass dimensions for conducting such an experiment since only a finite mine region can be adequately instrumented. The main parameter in this assessment is the size of the slipping regions (patch) at the moment when the quasi-static patch development becomes dynamic and does not require, anymore, any change in the pore pressure. *Uenishi and Rice* [2003] analyzed nucleation processes under the assumptions of linear slip-weakening (e.g., **Figure 3.2b**) of the fault and a locally elevated shear stress. They estimated the nucleation length, that is, the extent to which the slipping patch has to grow before the onset of dynamic rupture.

The nucleation model developed by *Uenishi and Rice* [2003] considers slip nucleation in conditions with elevated shear traction on a fault when effective stresses are not altered. Recently, *Garagash et al.*[2009], *Germanovich et al.* [2010], and *Garagash and Germanovich* [2012] have developed a theoretical model of dynamic slip nucleation driven by local, non-homogeneous fluid pressure changes Δp (**Figure 3.3**). A similar approach has been independently used by *Viesca and Rice* [2012] to analyze nucleation of a dynamic submarine landslide. In this work, we use the model of *Garagash and Germanovich* [2012] to evaluate the potential slip patch

size at the onset of dynamic propagation. Such an event is, in essence, an earthquake nucleation, and it is important to know the patch size in order to design the fault nucleation experiment and for instrumentation of the test site.

3.3.1. Fault Slip Due to Pore Pressure Loading

We first review the work of *Garagash and Germanovich* [2012] and consider a mode II shear crack of length 2*a* in the uniform background stress field characterized by the normal σ_n and τ^b shear components (**Figure 3.2a**). Shear stress τ on the fault plane is related to fault slip δ by the equation of quasi-static elastic equilibrium [e.g., *Bilby and Eshelby,* 1968]

$$\tau(x,t) - \tau^b = \frac{\mu^*}{4\pi} \int_{-a(t)}^{a(t)} \frac{\partial \delta(s,t)}{\partial s} \frac{ds}{x - s} \tag{3.1}$$

where $\mu^* = 2\mu/(1-\nu)$ is the plane-strain modulus, ν is the poisson's ratio and μ is the shear modulus. Slip rate $V = \frac{\partial \delta}{\partial t}$ vanishes at the crack tips, so that [e.g., *Rice,* 1968]

$$\int_{-a(t)}^{a(t)} \frac{\tau(x,t) - \tau^b}{\sqrt{a(t)^2 - x^2}}\, dx = 0 \tag{3.2}$$

where the shear traction distribution $\tau(x,t) = \tau(-x,t)$ along the crack is symmetric. In this case, the stresses at the tip are bounded and continuous. Inside the slipping region $-a \le x \le a$, the shear stress is equal to the fault shear strength,

$$\tau = f(\delta)\bar{\sigma} \tag{3.3}$$

where $\sigma = \sigma_n - p$, is the effective stress normal to the fault. The friction coefficient

$$f(\delta) = f_p - w\delta \qquad (0 \le \delta \le f_p/w) \tag{3.4}$$

decreases linearly with slip δ (**Figure 3.2b**) from its peak value f_p [e.g., *Ida,* 1972]. The implicit assumption associated with using the unlimited slip-weakening relation (3.4) is that during the nucleation process, the quasi-static slip is small enough, such that the corresponding reduced strength remains above the residual fault strength. That this assumption is satisfied is evaluated a posteriori.

Elastic equilibrium (3.1) and constitutive laws (3.3)-(3.4) can be used to describe qausi-static development of a slipping patch in response to a change of the background loading τ^b [*Uenishi and Rice,* 2003; *Dascalu et al.,* 2000] and/or change of the fault strength associated with the corresponding increase of pore pressure [*Garagash and Germanovich,* 2012; *Viesca and Rice,* 2010]. The latter is the focus of the field experiment design in this dissertation.

Consider the no-slip initial conditions when the background shear stress τ^b is smaller than the ambient peak strength $\tau_p = f_p(\sigma_n - p_0)$, where p_0 is the ambient pore pressure on the fault plane. A pore pressure perturbation Δp at a given location x = 0 along the fault at $t \geq 0$ reduces the shear strength, which is sufficient to activate the slip if Δp is sufficiently large, so that

$$\tau^b \geq \tau_p - f_p \Delta p \tag{3.5}$$

The spreading of the region with reduced fault strength by the pore pressure diffusion results in enlarging the slip zone.

To illustrate this type of slip process [*Garagash and Germanovich,* 2012] consider an evolving pore pressure perturbation along the fault (**Figure 3.2a**) in the form of

$$p(x,t) - p_0 = \Delta p(t)\Pi(\xi), \quad \xi = x/\sqrt{\alpha t} \tag{3.6}$$

where α is the hydraulic diffusivity and $\Pi(\xi)$ is a function describing instantaneous spatial profiles of the pressure perturbation such that $\Pi(0) = 1$. Such a situation can be envisioned if a fluid is injected into a fault plane through a borehole drilled into the fault plane (orthogonal cross-section of which is shown in **Figure 3.2a**) to trigger an earthquake in more controllable conditions than it would happen otherwise [*Garagash et al.,* 2009; *Germanovich et al.,* 2010]. Examples of the injection scenarios, for which the pressure along the fault is described by (3.6), include fluid injection into the fault zone characterized by negligible transverse permeability [e.g., *Carslaw and Jaeger,* 1959], under a constant overpressure Δp,

$$\Delta p(t) = const, \quad \Pi(\xi) = Erfc\,|\xi| \tag{3.7}$$

or, at a constant flow rate *q* [*L/T*],

$$\Delta p(t) = \frac{2}{\sqrt{\pi}}\frac{\eta q}{k}\sqrt{\alpha t}, \quad \Pi(\xi) = \exp\left(\frac{-\xi^2}{4}\right) - \frac{\sqrt{\pi}}{2}\,|\xi|\,Erfc\frac{|\xi|}{2} \tag{3.8}$$

where η is the fluid viscosity and k is the longitudinal permeability (i.e., along the fault) of the fault zone. Both in (3.7) and (3.8), $\Pi(0) = 1$, so that $\Delta p(t) = p(0,t) - p_0$ represents the pressure change in the injection point, $x = 0$.

By nondimensionalizing the set of equations (3.1), (3.2), (3.3), (3.4) and (3.6), *Garagash and Germanovich* [2012] show that the normalized slip, δ/δ_w, and the normalized half-length of the slipping patch (zone), a/a_w, can be expressed in terms of the normalized coordinate, x/a, normalized time, at/a_w^2, and two dimensionless loading parameters, namely, fault understress, $\frac{\tau_p - \tau^b}{\tau_p}$, and fluid overpressure, $\Delta p/\overline{\sigma_0}$, $\overline{\sigma}_0 = \sigma_n - p_0$. Hereafter,

$$a_w = \frac{\mu}{\tau_p}\delta_w\,, \quad \delta_w = \frac{f_p}{w} \tag{3.9}$$

are the characteristic patch length and slip weakening scale, respectively. To solve the nondimensionalized set of equations, *Garagash and Germanovich* [2012] used the expansion of slip into a series of Chebyshev polynomials. Development of slip due to the fluid injection with a constant value of overpressure (equations (3.6) and (3.7)), can be seen in **Figure 3.3** for $\Delta p/\bar{\sigma}_0 = 0.5$. **Figure 3.3a** shows evolution of the normalized crack half-length with the advancement of the pore pressure diffusion "front" (characterized by its normalized position $\sqrt{\alpha t}/a_w$) for various values of the normalized background stress τ^b/τ_p. Both time to instability (or nucleation time), t_c, and the critical length of the crack (or the length of the nucleation patch), $a_c = a(t_c)$, correspond to the points with the vertical slope in **Figure 3.3a**. Values of the nucleation time and length increase with decreased background loading. The dotted parts of the curves correspond to the crack growth under physically meaningless reversal of the pore pressure diffusion (time decrease). Therefore, after the slip zone reaches a critical size, quasi-static equations cannot describe its further development, which corresponds to the initiation of dynamic slip (earthquake nucleation).

For smaller values of the background stress ($\tau^b/\tau_p \leq 0.6$), dotted curves in **Figure 3.3a** are terminated when the fault frictional strength (equations (3.3)-(3.4)) is reduced to zero (dashed line in **Figure 3.2b**) at the center of the crack when $\delta_{x=0} \to \delta_w$. *Garagash and Germanovich* [2012] note that, clearly, the frictional model with unconstrained slip-weakening

(3.4) ought to be amended at the slip values $\geq \delta_w$, for example, by introducing a non-zero residual friction. The effect of the residual friction on the dynamic slip nucleation is beyond the scope of this work, however.

Development of the slip distribution with the normalized position of the diffusion front is shown in **Figures 3.3b** for the background stress of $\tau^b/\tau_p = 0.75$ and overpressure $\Delta p/\bar{\sigma}_0 = 0.5$. The bold line corresponds to the instability of the quasi-static crack growth and nucleation of the dynamic slip.

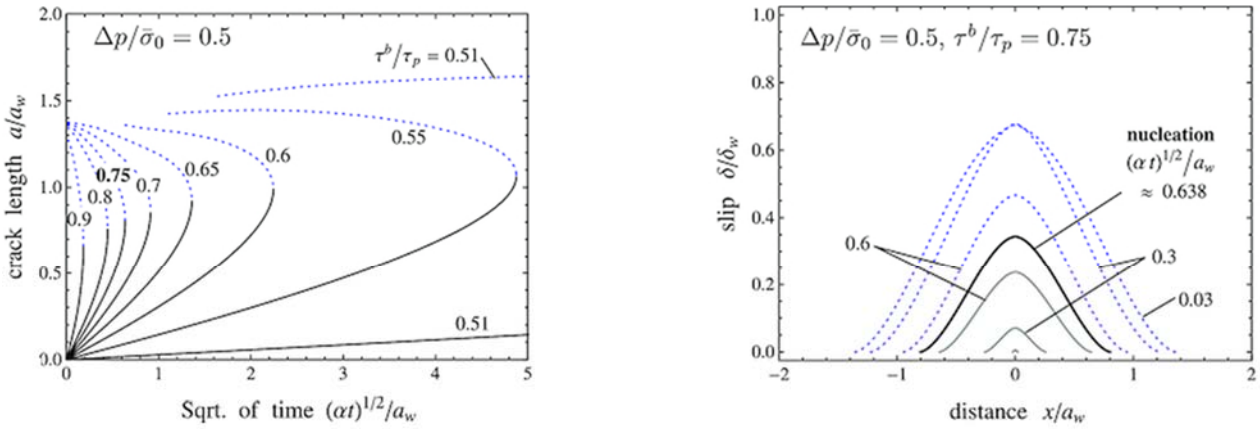

Figure 3.3: (a) Development of the crack half-length for the overpressure at the crack center $\Delta p/\bar{\sigma}o$ = 0.5 and various values of the background stress τ^b/τ_p. The rightmost points of each curve (i.e., with vertical slope) correspond to the instability of quasi-static crack growth. Beyond these points, continued quasi-static growth would require either reduction of the background stress or, conceivably, injection shut-in. Dotted parts of the curves correspond to the crack growth under physically meaningless reversal of the pore pressure diffusion (time reversal) at the fixed level of background stress. (b) Development of slip distribution for $\Delta p/\bar{\sigma}o$ = 0.5 and τ^b/τ_p = 0.75. The heavy line corresponds to the instability of the quasi-static slip growth under sustained injection of fluid at the crack center. Dotted lines correspond to a physically unrealistic solution depicted part (a) (also by dotted lines) [*Garagash and Germanovich*, 2012].

3.3.2. Limiting cases

Garagash and Germanovich [2012] identified two limiting cases when, at the nucleation time, the slip zone is much larger or much smaller than the pressure diffusion scale in the fault zone. A "large" slip zone (**Figure 3.4a**), $a_c \gg \sqrt{\alpha t_c}$, is expected in critically loaded faults, which are stressed almost to their strength level ($\tau_p - \tau^b \ll f_p \Delta p$). A "small" slip zone (**Figure 3.4b**), $a_c \ll$

$\sqrt{\alpha t_c}$, would appear in faults that are pressurized merely enough to activate the fault slip ($\tau_p - \tau^b \simeq f_p \Delta p$) and only at the slip zone center, where the pressure is the largest. In these limiting cases, the solution at the instability can be established for a general pressurization scenario, not constrained to a specific form of the pressurization function $\Pi(\xi)$ in (3.7). *Garagash and Germanovich* [2012] called these two end-members "critically-loaded fault" and "marginally-pressurized fault," respectively.

Homestake fault is a mature, stable fault, with no observed seismicity prior, during, or after the mining operations in the Homestake gold mine. Hence, if a fluid is injected into this fault at an, appreciably, low rate, the extreme case of a marginally-pressurized fault will be realized. In this case, a localized pore pressure increment Δp is just enough to activate the fault slip near x = 0. The subsequent quasi-static growth of the slipping patch will be much slower than the diffusive growth of the pressurized zone. As a result, at the instability, the crack will be well within the pressurized region ($a_c \gg \sqrt{\alpha t_c}$), and, therefore, will be almost uniformly pressurized, so that $p(x, t_c) \simeq p_0 + \Delta p$ for $|x| \leq a_c$ (**Figure 3.4a**).

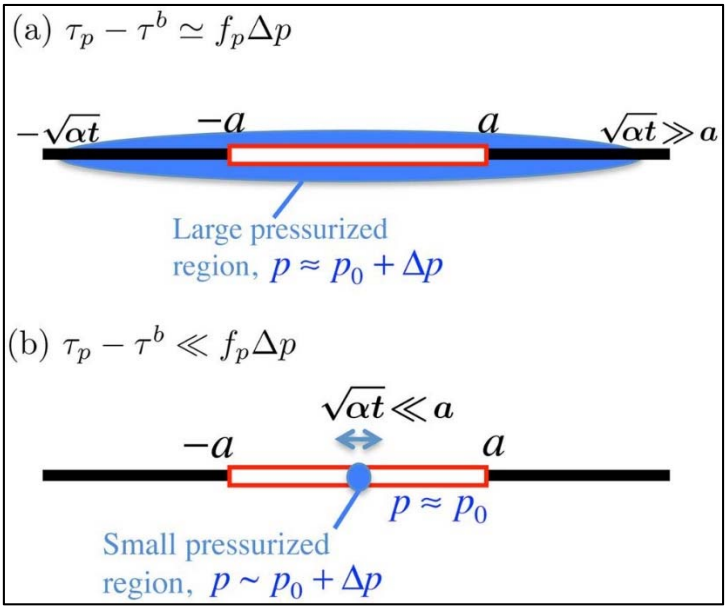

Figure 3.4: Two limiting responses of a fault to pressurization [*Garagash and Germanovich*, 2012]. (a) Marginally pressurized fault ($f_p \simeq (\tau_p - \tau^b)/\Delta p$), and (b) Critically loaded fault ($\tau^b \simeq \tau_p$).

When the normal effective stress distribution along the crack is uniform, ($\bar{\sigma}(x) = \bar{\sigma} = \text{const}$), the nucleation half-length is given by [*Uenishi and Rice*, 2003]

$$\frac{a_c}{a_w} \simeq 0.579 \frac{\bar{\sigma}_0}{\bar{\sigma}} \quad (\bar{\sigma} = \text{const}) \tag{3.10}$$

Consequently, an asymptotic expression for the nucleation length for a marginally-pressurized fault follows from (3.10) in the form of

$$\frac{a_c}{a_w} \simeq 0.579 \frac{\tau_p}{\tau^b} \tag{3.11}$$

where the limit value $(\tau_p - \tau^b)/f_p$ of overpressure Δp has been used to evaluate $\bar{\sigma} \approx \bar{\sigma}_0 + \Delta p$ in (3.10).

For injection at a constant injection rate, $q = \text{const}$, expression (3.8) for the overpressure evolution in the marginally-pressurized fault can be written as

$$\frac{\Delta p(t)}{(\Delta p)_w} = \frac{\sqrt{\alpha t}}{a_w}, \quad (\Delta p)_w = \frac{2}{\sqrt{\pi}} \frac{\eta}{k} q a_w \quad (q = const) \tag{3.12}$$

where $(\Delta p)_w$ is a characteristic pressure drop over distance a_w from the crack center. Then, assuming that the instability follows shortly after the slip activation and setting $\Delta p(t_c)$ in (3.12) to the value of $\left(\tau_p - \tau^b\right)/f_p$, results in the expression for the time of nucleation

$$\frac{\sqrt{\alpha t_c}}{a_w} \simeq \frac{\tau_p - \tau^b}{f_p (\Delta p)_w} \tag{3.13}$$

This assumption is valid for slow injection rates

$$q \ll \frac{\left(\tau_p - \tau^b\right)\sqrt{\pi} k}{2\eta a_w} \tag{3.14}$$

when the characteristic pressure drop, $(\Delta p)_w$, is small compared to $\Delta p(t_c) \simeq \left(\tau_p - \tau^b\right)/f_p$.

It is possible that condition (3.14) may be too restrictive and, in fact, is not needed. It is worth stressing that because $f_p \Delta p \simeq \tau_p - \tau^b$, the normalized slip at nucleation is small ($\delta/\delta_w \ll 1$) while the normalized nucleation time is large ($\sqrt{\alpha t_c}/a_w \gg 1$). That the slip is small ($\delta \ll \delta_w$) is consistent with the fact that the cut-off part of the slip weakening friction law was neglected (solid horizontal line in **Figure 3.2b**). Hence, for marginally pressurized faults with a small slip zone, ($a_c \ll \sqrt{\alpha t}$), the residual friction is likely not achieved by the moment of dynamic slip nucleation.

A critically-stressed fault, which is stressed almost to its static strength level, requires only a small stress or strength perturbation to reach the instability, hence, $\tau_p \simeq \tau^b$. In the context of this work, a small strength perturbation is achieved by finite pore pressure increase Δp at the center of the crack over small injection times, such that at the instability, the size of the pressurized region is small compared to the size of the quasi-statically slipped crack, $\sqrt{\alpha t_c} \ll a_c$ (**Figure 3.4b**). As a result, the pressure is largely unperturbed (uniform) along the crack with the exception of the small pressurized "island" at the center. The corresponding asymptotic solution

$$\frac{a_c}{a_w} \simeq 0.579 \tag{3.15}$$

for the critical length of the quasi-static crack follows from (3.10) and $\bar{\sigma} \approx \bar{\sigma}_0$. The corresponding asymptotic solutions for the nucleation time [*Garagash and Germanovich*, 2012]

$$\frac{\sqrt{\alpha t_c}}{a_w} \simeq 0.687 \sqrt{\frac{\tau_p - \tau^b}{f_p (\Delta p)_w}} \qquad (q = const) \tag{3.16}$$

where $(\Delta p)_w$ is defined in (3.12). Because in general, $\tau_p > \tau^b$, comparing (3.11) and (3.15) shows, that the dynamic patch nucleation size is the smallest for critically-stressed faults.

3.3.3. General case

In the general case, *Garagash and Germanovich* [2012] solved the system of equations (3.1) – (3.8) numerically. **Figure 3.5** illustrates the critical crack half-length and the nucleation time in terms of the two loading parameters, the fault understress $(\tau_p - \tau^b)/\tau_p$ and the fluid overpressure $\Delta p/\bar{\sigma}_0$. For a given value of the overpressure, the solution exists in the range of background loading conditions, $0 < \left((\tau_p - \tau^b)/\tau_p\right) \leq \Delta p/\bar{\sigma}_0$, where the lower and upper bounds of the understress $\tau_p - \tau^b$ correspond to the asymptotics of the critically loaded and marginally pressurized faults, respectively. These asymptotic cases are characterized by the vanishing slip and the extreme values of the nucleation time, which is consistent with the numerical solution of *Garagash and Germanovich* [2012].

The maximum overpressure value that *Garagash and Germanovich* [2012] used, $\Delta p/\bar{\sigma}_0$ = 1, corresponds to the complete loss of frictional strength at the injection point and possible onset of the along-the-fault hydraulic fracture. They note that because $\bar{\sigma}_0$ is, generally, not the least effective normal stress, it is also possible that hydraulic fracturing may be initiated and propagated off the fault plane for Δp less than $\bar{\sigma}_0$. It can be seen in **Figure 3.5** that the *Uenishi and Rice* [2003] value (3.15) of the normalized nucleation length is recovered for small nucleation times (i.e., when the pore pressure perturbation is localized near the crack center), which is synonymous to a critically loaded fault [*Garagash and Germanovich*, 2012].

The prominent feature of **Figure 3.5a** is the weak dependence of the nucleation length on the fluid pressure. In other words, the nucleation length is largely controlled by the proximity of the fault loading to the static strength, quantified by the understress parameter $(\tau_p - \tau^b)/\tau_p$. The minimum nucleation length for a given background loading is given by the asymptote of the marginally pressurized fault,

$$\min(a_c/a_w) \simeq 0.579\ (\tau_p/\tau^b) \tag{3.17}$$

corresponding to the minimum value of pressure required to activate the slip. The maximum nucleation length is constrained by the value of the overpressure that would cause an incipient fault opening (hydraulic fracture) and the local loss of shear strength. It can be approximated (with $< 1\%$ error) by a two term expression

$$\max(a_c/a_w) \simeq 0.682\ \left(\tau_p/\tau^b\right) - 0.103\left(\tau^b/\tau_p\right) \tag{3.18}$$

Garagash and Germanovich [2012] concluded that change of the pressure boundary condition at the fluid source from a constant overpressure (equation (3.7)) to a constant fluid flux condition (equation (3.8)) leaves the nucleation length, including its minimum (3.17) and maximum (3.18) values, and critical slip predictions, practically unchanged. This follows from comparing **Figures 3.5a** and **3.5b** for the nucleation length.

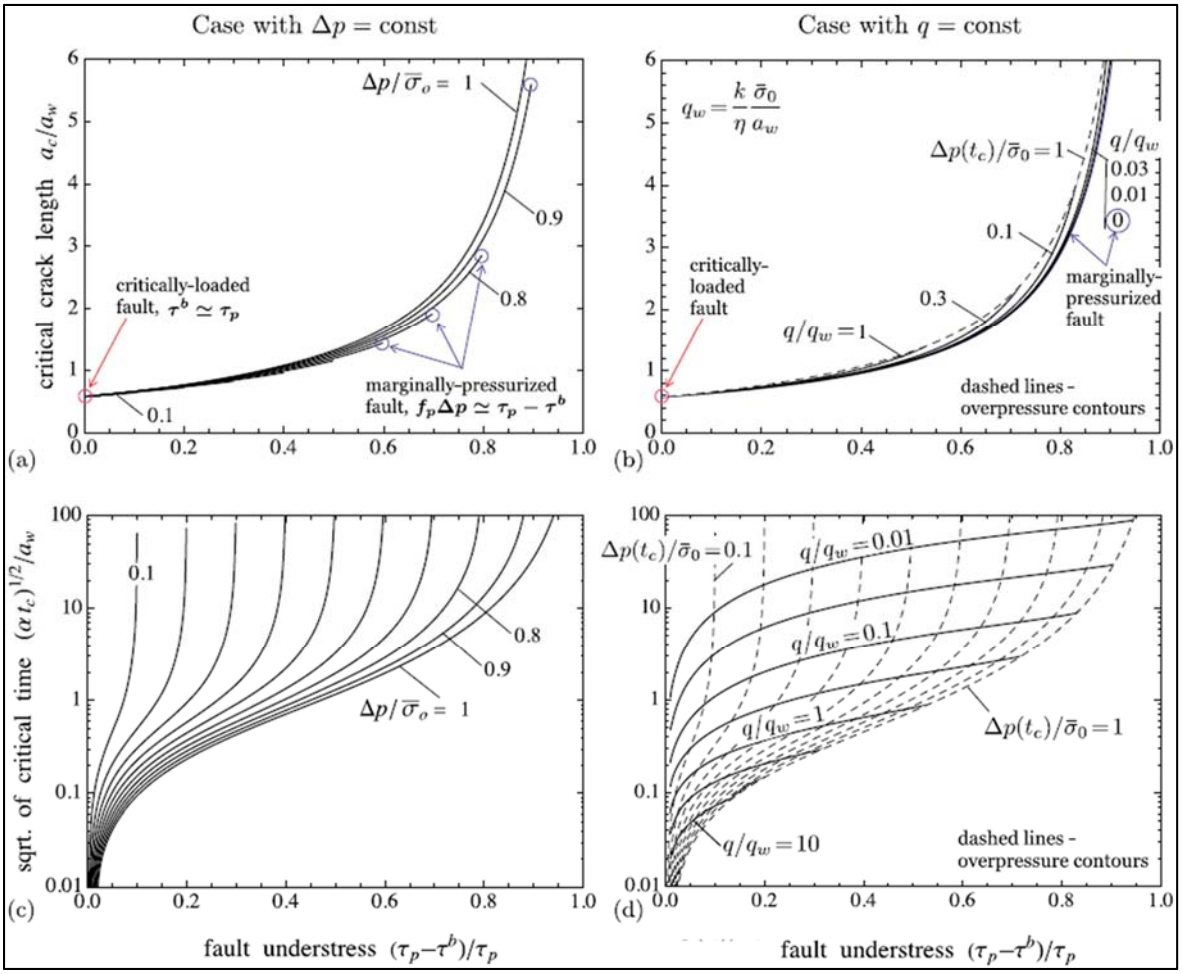

Figure 3.5: (a-b) Normalized crack half-length and (c-d) square root of time at the instability as functions of the fault understress $(\tau_p - \tau^b)/\tau_p$ for various constant values of the prescribed fluid overpressure $\Delta p/\bar{\sigma}_0$ (left) and injection rate q/q_w (right), where $q_w = (k/\eta)(\bar{\sigma}_0/a_w)$ is a characteristic flow rate. In the case of constant injection rate, the contour lines of the overpressure at nucleation, $\Delta p(t_c)/\bar{\sigma}_0 = (2/\sqrt{\pi})(q/q_w)(\sqrt{\alpha t_c}/a_w)$, are shown by dashed lines (right). The nucleation crack length ((a) and (b)) for two injection scenarios ((3.7) and (3.8)) are very close [*Garagash and Germanovich*, 2012].

3.4. NUCLEATION PATCH SIZE FOR THE HOMESTAKE FAULT CONDITIONS

Results of *Viesca* and *Rice* [2010] are consistent with the results of *Garagash* and *Germanovich* [2012], reviewed above. The proximity of the fault loading to the static strength is the main parameter controlling the length of dynamic nucleation. This proximity can be described by parameter τ_p/τ^b, which is equivalent to the fault understress parameter $\left(\tau_p - \tau^b\right)/\tau_p$ introduced by *Garagash* and *Germanovich* [2012]. This parameter defines the upper (3.17) and lower (3.18) estimates of the dynamic patch nucleation. We further use expressions (3.17) and (3.18) to evaluate the nucleation size in the Homestake mine conditions.

Uenishi and Rice [2003] suggest that a laboratory derived rate- and state-dependent friction law for an established slip surface [e.g., *Ruina*, 1983] can be approximated, over a range of slip distances, by a linear slip dependence (3.4) with the slip-weakening rate, w, ranging from 0.15 mm^{-1} to 3 mm^{-1}, which is consistent with the values of slip-weakening rate $W = w\bar{\sigma}_0$ of the frictional strength inferred by *Rice* [2006] and *Wong* [1986] from the post-failure stage of triaxial experiments on initially intact granite specimens [*Rummel et al*., 1978]. We, therefore, choose the characteristic value of $w = 1$ mm^{-1} and, based on the Byerlee law [*Byerlee*, 1978; *Burov*, 2010], $f_p = 0.85$.

The host rock shear modulus, characteristic for Homestake mine conditions, is $\mu \simeq 40$ GPa [*Pariseau*, 1985; *Pariseau et al.*, 1987]. *Tesarick et al*. [2002] report the in-situ stress magnitudes in the Homestake mine that are consistent with the in-situ stress measurements reported by *Pariscau et al.* [1984]. In-situ stress measurements have been conducted at the Homestake mine at depths ranging from 6000 to 9000 feet, by the method of stress relief overcoring on hollow inclusion cells and borehole deformation gauges [*Johnson et al.,* 1993; *Callahan*, 2010]. The depth, *z*, of interest for the nucleation experiment varies from 3000 ft (914 m) to 8000 ft (2438 m) because this range of depths is accessible from the mine levels 4100L, 4850L, and 7400L (**Figure 3.6**). *Tesarick et al*. [2002] suggest that at these depths,

$$\sigma_V = 0.02828z, \quad \sigma_H = 14.33 + 0.01199z, \quad \sigma_h = 0.834 + 0.01244z \tag{3.19}$$

where $\sigma_h < \sigma_H < \sigma_V$ and z should be in meters to obtain the in-situ stresses in megapascals. Neither of these works, however, reports the directions of the in-situ stresses, although their magnitudes generally agree with the measurements conducted by *Johnson et al*. [1993] in one location at the depth of 3650 ft. *Callahan* [2010] reports the results of most recent stress measurements at three locations at the depth of 1617 m (4850L mine level). This author concludes that the vertical lithostatic stress, σ_V, can be reliably evaluated from (3.19). Horizontal stresses are more uncertain, however. For example, Callhan [2010] suggests that the minimum horizontal $\sigma_h \approx 0.8\sigma_V$ while in (3.19), $\sigma_h \approx 0.46\sigma_V$. Given this uncertainty, we further assume that

$$\sigma_V = \rho_r g z, \quad \sigma_H = 0.75\sigma_V, \quad \sigma_h = 0.5\sigma_V, \tag{3.20}$$

where $\rho_r = 2800$ kg/m^3 [*Callhan*, 2010]. To evaluate a possible range of the nucleation patch size, we test two end-member scenarios when either σ_H or σ_h is oriented along the fault strike. The shear and normal stresses on the fault is then expressed by

$$\tau^b = (\sigma_V - \sigma_H)\sin\theta\cos\theta, \quad \bar{\sigma}_0 = \sigma_V \sin^2\theta + \sigma_H \cos^2\theta - \rho_w g z \tag{3.21}$$

or

$$\tau^b = (\sigma_V - \sigma_h)\sin\theta\cos\theta, \quad \bar{\sigma}_0 = \sigma_V \sin^2\theta + \sigma_h \cos^2\theta - \rho_w g z \tag{3.22}$$

respectively, where $\theta \approx 60°$ is the fault dip, $\rho_w \approx 1000\ \mathrm{kg/m^3}$ is the pore fluid (water) density. Hydrogeology of the Homestake mine environment is complex [*Murdoch et al.*, 2012], but for our purpose (first-order estimate) the pore pressure in the fault zone can be considered hydrostatic, which is reflected in the last terms in (3.21) and (3.22).

The peak fault strength is defined by

$$\tau_p = f_p \bar{\sigma}_0 \tag{3.23}$$

while combining (3.17) and (3.18), we have

$$\min(a_c) \le a_c \le \max(a_c) \tag{3.24}$$

where

$$\begin{cases} \min(2a_c) = 1.158\ a_w \dfrac{\tau_p}{\tau^b} \\ \max(2a_c) = 1.364\ a_w \dfrac{\tau_p}{\tau^b} - 0.206\ a_w \dfrac{\tau^b}{\tau_p} \end{cases} \tag{3.25}$$

and a_w is given by (3.9).

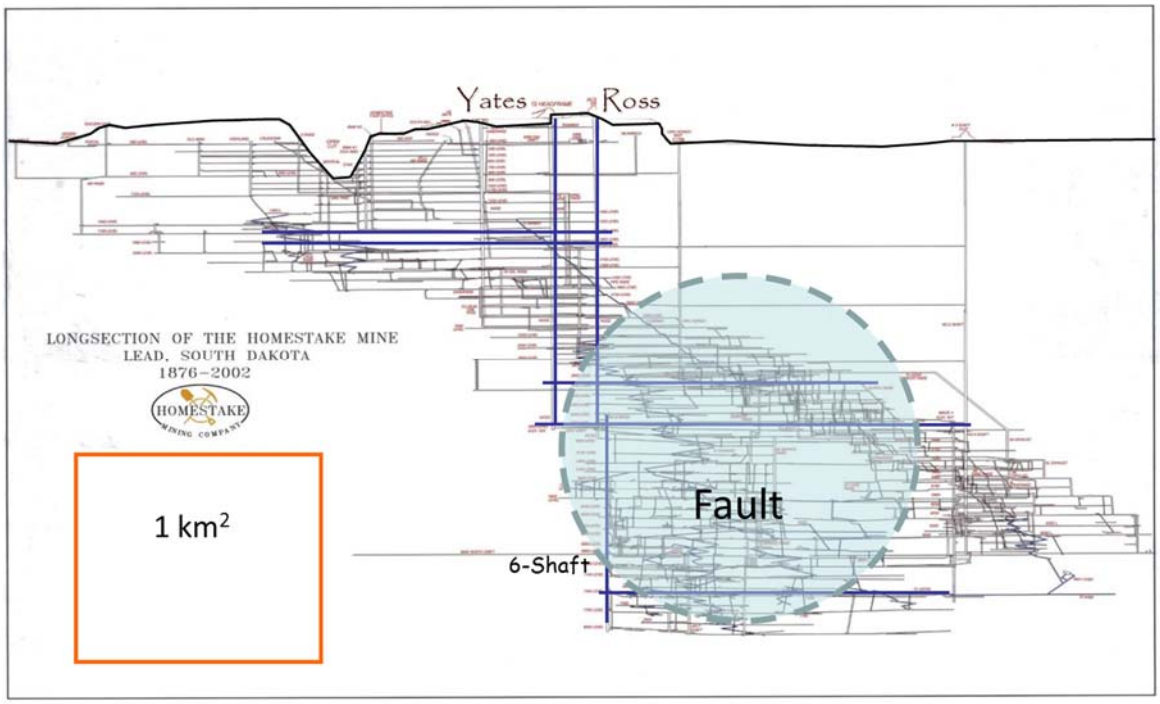

Figure 3.6: Projection of locations of the mine workings and Homestake fault onto the East-North-East mine cross-section. The fault can be accessed from several mine levels.

Bounds (3.24) together with equations (3.21) – (3.23) estimate the minimum and the maximum extents of the dynamically slipping patch as a function of depth. They are plotted in **Figure 3.7**. As can be seen, the difference between the upper and lower bounds is not large, that is, 17.5 percent and 16 percent for the cases of σ_H and σ_h oriented along the fault strike, respectively. The nucleation size decreases with depth and equals ≈3 m for the larger horizontal stress (equation (3.22)) and the largest depth (8000 ft.). It is ≈17 m for the smaller horizontal stress (equation (3.23)) and the smallest depth (3000 ft.). Half an order of magnitude variation centered about these values is plausible according to the estimated range for *w*.

Therefore, our (scale) analyses for the Homestake fault conditions indicate that the onset of dynamic slip occurs for a patch size on the order of 1 m to 10 m. Creating a dynamic patch of this size will require an experimental configuration of at least 10 m to 100 m. This appears feasible under field conditions in the Homestake mine (**Figure 3.1b**), but it demonstrates why the characterization of a dynamic slip patch is beyond the reach of laboratory experiments. This result is significant also because the Homestake fault conditions of 1 to 3 km depth are representative of many mines around the world.

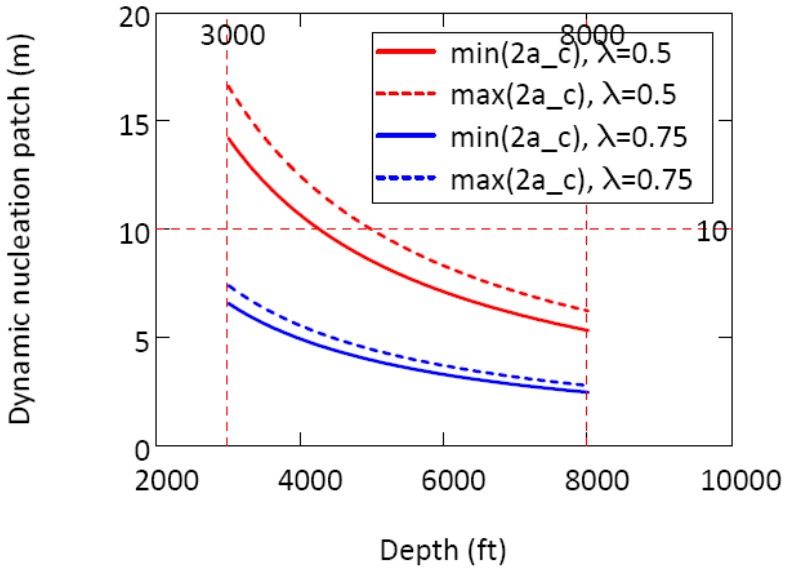

Figure 3.7: Minimum (solid lines) and maximum (dashed lines) of the slipping patch (meters) at the onset (nucleation) of dynamic slip as a function of depth (feet). The greatest depth for the Homestake mine conditions is limited to about 7400 feet. Note that the depth is expressed in feet as it is customary at the Homestake mine.

3.5. FAULTING IN INTACT ROCK

3.5.1. Thermal method of rock faulting

Two conventional views address fault nucleation in intact rock. One holds that faults nucleate at a small flaw with a process zone, and they grow when a specified stress state is exceeded at fault tips [e.g., *Reches and Lockner*, 1994; *Dyskin and Germanovich*, 1995]. This view is similar to the Barenblatt-Dugdale concept [e.g., *Broek*, 1982] for tensile fractures and resembles the shear band model of *Palmer and Rice* [1973]. The other view is based on a distributed damage model that assumes faults nucleate when critical mechanical conditions cause damage localization in a narrow zone [e.g., *Germanovich et al.*, 1994]. Size limitations have complicated efforts to distinguish between these two alternatives in the laboratory. Larger experiments have a much better potential to determine which mechanism prevails, or perhaps to identify a new mechanism for fault nucleation at field scale.

The key to possible experiments is a simple strategy based on thermal techniques that have been used to control fractures [e.g., *Wu et al*., 2007] and can be employed for creating faults in crystalline rock. Changes in temperature alter the stress state in rocks. Therefore, thermal techniques could be used to locally alter in-situ stresses enough to cause controlled faulting. The general process involves heating to increase compressive stresses, or cooling to reduce them.

To see how this technique could create a fault, consider a simple Mohr failure diagram (**Figure 3.8**). In the ambient stress state, given by the black semicircle in **Figure 3.8**, σ_{min}, the least compressive stress, is horizontal, and σ_{max}, the greatest compressive stress, is vertical. For shear failure to occur, the stresses must be manipulated for the stress circle to touch the failure envelope (red line). This can occur, for example, if (i) σ_{max} is increased and σ_{min} is fixed (green dotted circle), or (ii) σ_{min} is decreased and σ_{max} is fixed (blue dashed circle). As **Figure 3.8** suggests, a smaller stress increment is required to cause shear failure when reducing σ_{min} than when increasing σ_{max}.

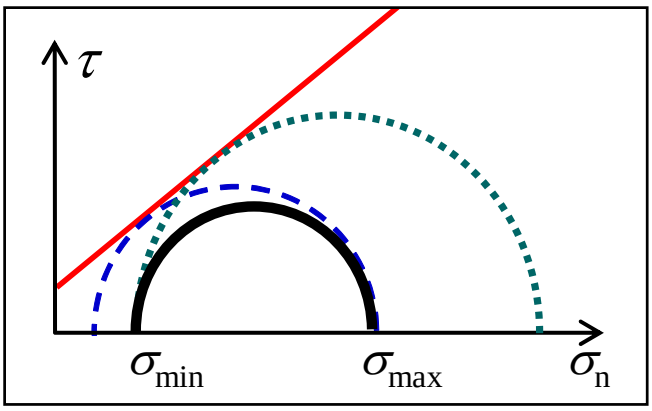

Figure 3.8: Mohr-Coulomb diagram of the loading history. Dashed blue line corresponds to the cooling process described in the text. Compression is positive, τ and σ_n are the shear and normal stresses, respectively.

This principle could be applied at the homestake mine (DUSEL) by using cooling to decrease σ_{min} or by heating to increase σ_{max}. For example, cooling along two vertical planes (**Figure 3.9**), or *thermal panels*, would reduce the horizontal compression between the planes, while the vertical compression remained practically unchanged (**Figure 3.10**). Thermal panels could be created as arrays of parallel boreholes containing heat exchangers. Reducing the horizontal compression sufficiently will cause the stress state to reach failure conditions between the vertical planes (blue circle in **Figure 3.9**). Faulting is expected to occur between the vertical planes as a result.

3.5.2. Estimation of dimensionless nucleation time and stress

As a representative example, consider two thermal panels (inclusions) separated by *w*, with each containing *N* boreholes spaced by distance *b* (**Figure 3.9**). Let each borehole be cooled by a constant temperature ΔT. The time of heat diffusion between the boreholes in each array represents the time required for establishing the thermal panels based on these borehole arrays and scales as

$$t \simeq \frac{b^2}{D}. \tag{3.26}$$

At that time, the horizontal stress change between the thermal panels scales as

$$\Delta\sigma_3 \simeq \frac{2\alpha\Delta T E\sqrt{Dt}}{L}. \tag{3.27}$$

where we assumed that the panels can be visualized as thin, closely spaced thermal inclusions. Specifically, we assumed that $L = (N-1)b \gg w$. In equations (3.26) and (3.27), D is the thermal diffusivity, E and α are the Young's modulus and the coefficient of linear thermal expansion, respectively, for the host rock, and L is the height of the borehole array. For N = 10 boreholes in each array, b = 1 m, w = 4 m, ΔT = -100 ˚C, and parameters characteristic for the Homestake mine ($E = 10^{11}$ Pa, $\alpha = 10^{-5}$ °C^{-1}, $D = 10^{-6}$ m^2/s), equations (3.26) and (3.27) result in $t \approx 11$ days and $\Delta\sigma_3 \approx$ -22 MPa. Per Mohr-Coulomb condition with $\emptyset = 40°$, σ_1 = 25 MPa, and σ_3 = 23 MPa (for characteristic depth and rock density of 1 km and 2800 kg/m^3, respectively), the stress change required to cause failure is approximately -17 MPa. Therefore, faulting in the intact rock will take place somewhat earlier than 11 days. This scaling is consistent with the results of numerical analysis shown in **Figure 3.10**.

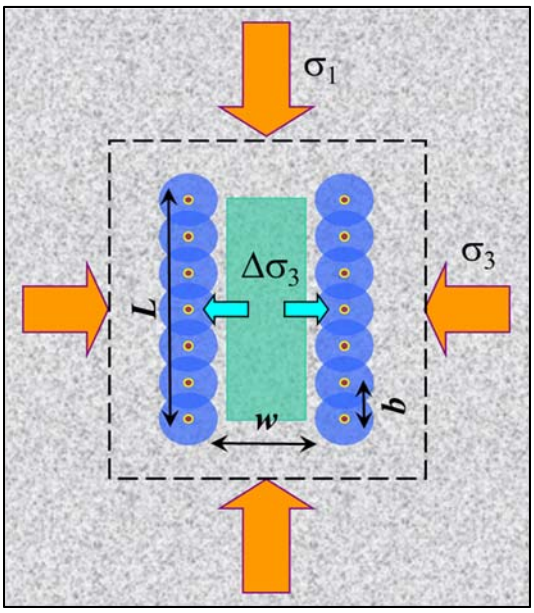

Figure 3.9: Perturbation of the ambient stress state by cooling along two vertical planes containing boreholes, with the planes separated by a distance w, and the height of the borehole array is L, and vertical separation between boreholes b.

3.6. FIELD EXPERIMENT DESIGN

A robust implementation approach for creating new faults would be to circulate chilled fluid through arrays of boreholes drilled along vertical planes; boreholes could be either horizontal or vertical (**Figure 3.11**). This will reduce the horizontal compression normal to the planes of the

boreholes while the vertical stress remains nearly unchanged. The cooled boreholes and change in stress state are represented by the blue lines in **Figure 3.9**.

Borehole arrays shown in **Figure 3.11** would manipulate stresses at scales from less than one meter to approximately ten meters (**Figure 3.11**). The boreholes in each array would be drilled either horizontally or vertically from common rooms (**Figure 3.11**). Instrumentation for monitoring the faulting process would be deployed in additional holes flanking the borehole arrays. Our scaling and numerical analyses (**Figure 3.10**) of these designs show that the thermal technique can create differential stresses sufficient to induce faulting within a period of approximately 11 days.

(a)

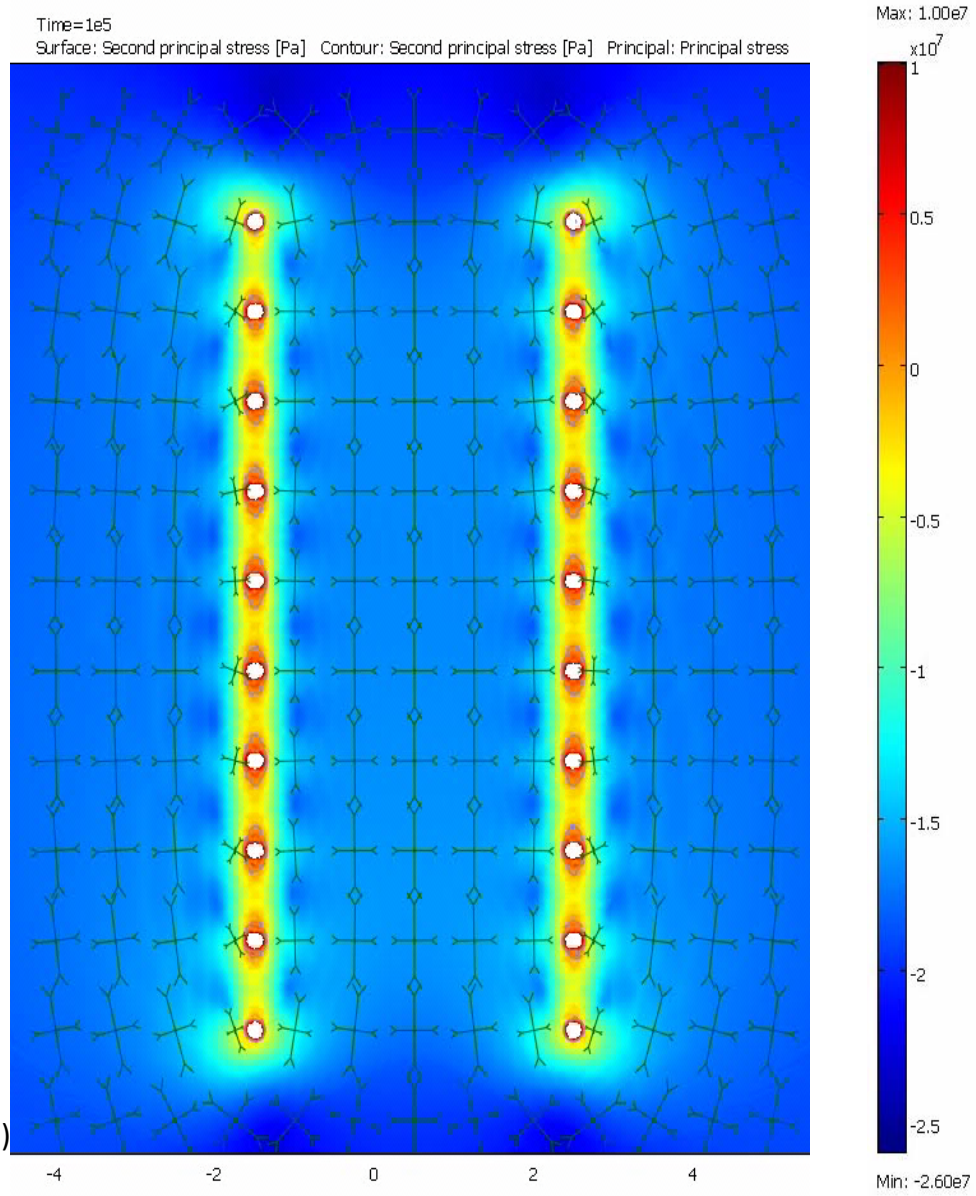
Time=1e5
Surface: Second principal stress [Pa] Contour: Second principal stress [Pa] Principal: Principal stress
Max: 1.00e7
x10^7
1
0.5
0
-0.5
-1
-1.5
-2
-2.5
Min: -2.60e7
-4
-2
0
2
4

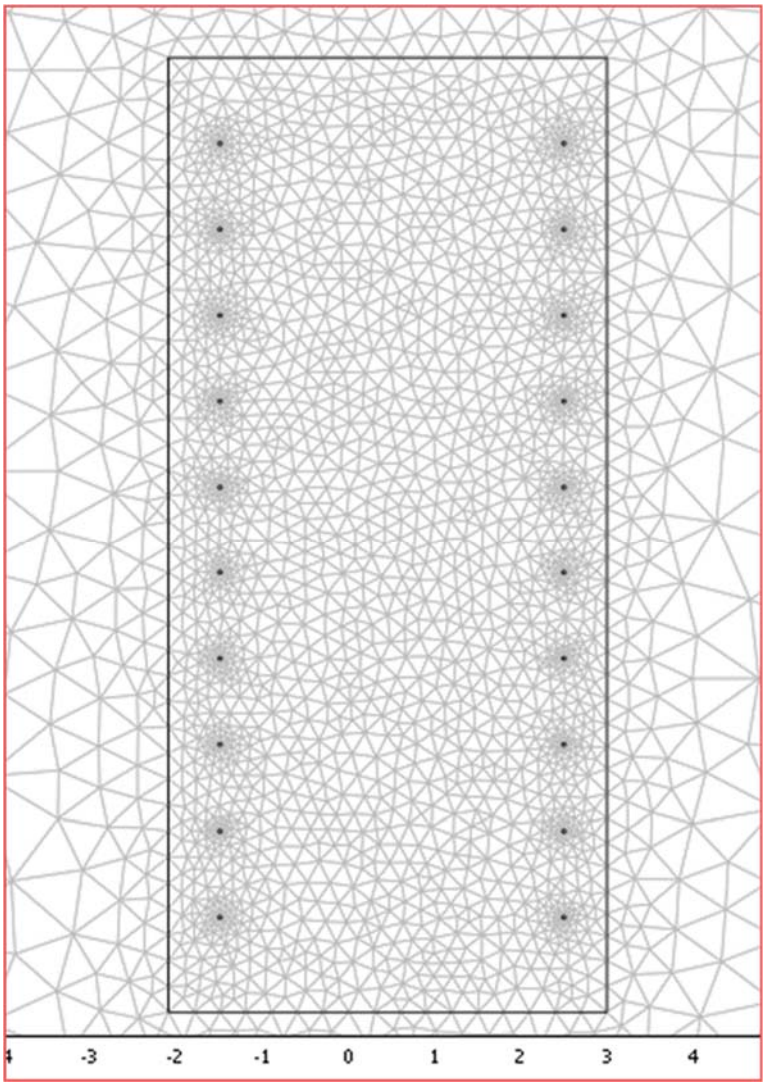

(b)

Figure 3.10: (a) Temperature and stresses at time $t = 10^5$ sec (≈ 1 day) in a 100 m by 100 m block with 25 MPa (vertical) and 23 MPa (horizontal) stresses on the block boundaries (not shown). The central region of the block (shown) contains two arrays of 10 boreholes (10 cm diameter each) spaced by 1 m. At the initial moment, the surface temperature of each borehole is reduced by 100°C and then maintained constant. Colors show temperature change from –100°C (blue) to –50°C (yellow) to the original temperature (red). Bars show principal stresses. While remote stresses are almost the same, the horizontal stress between the cooled regions is considerably reduced (the vertical stress has not changed significantly). The state of stress in the region between the borehole arrays is approximately uniform. (b) One of the configuration and FEM meshes used for the numerical simulations. Only the central region of the numerical model is shown.

The thermal technique can be used to study how new faults form in intact rock, but it can also be applied (in addition to the fluid injection described in Section 3) to induce slip on existing faults. In this case, [*Byerlee,* 1978] fault slip would be moderated by a combination of controlled fluid injection and thermally changing background stresses. The slip patch is expected to span one to several meters before it becomes unstable and propagates dynamically along a fault surface. To accommodate the scale required to nucleate an unstable patch (10 m to 100 m), the experiment could be implemented using two thermal panels at different mine levels along the existing Homestake fault (**Figure 3.6**).

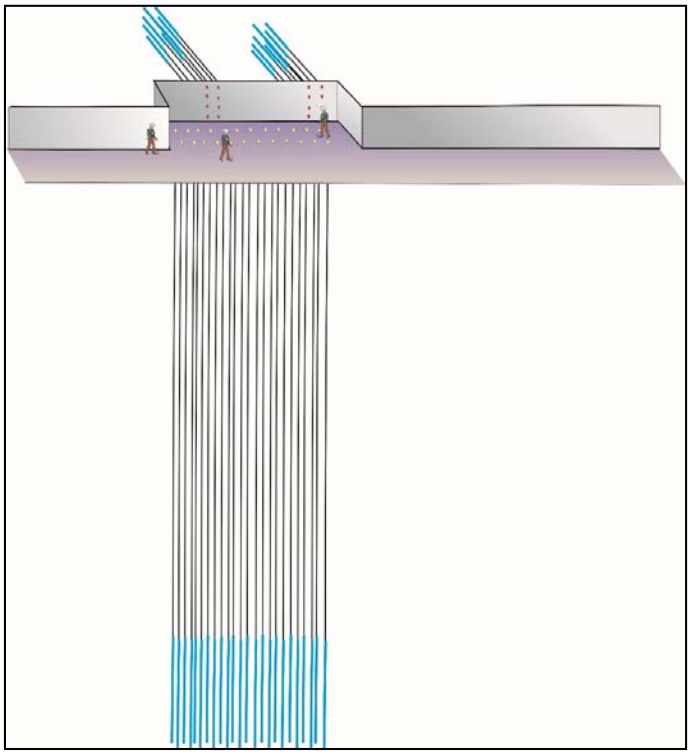

Figure 3.11: Horizontal or vertical arrays of boreholes used to control stresses by cooling (blue). Faults of different scales are expected to be created in accordance with Figures 2 and 3.

Ongoing dewatering operations at Homestake are expected to affect stresses and displacements in the vicinity of the Homestake fault. This poroelastic effect can be used to better characterize the fault [*Murdoch et al*., 2012]. The nucleation, propagation, and arrest of dynamic fault slip will be governed by fluid overpressure source, diffusion, and the magnitude of the

background loading in relation to the peak and residual strength in the fault zone at the ambient pore pressure level. More information on in-situ stresses and fault gouge than currently available is required to characterize the fault. Yet, our modeling (**Figure 3.7**) suggests that a suitable place for such an experiment is where the Homestake fault intersects the 4850-ft mine level (**Figure 3.6**) and at greater depths.

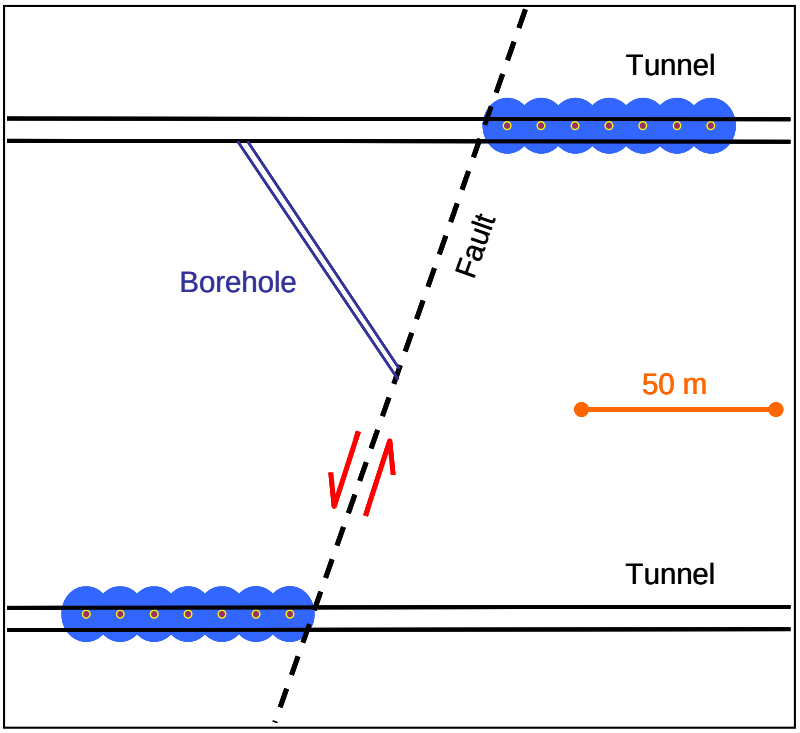

Figure 3.12: Slip nucleation experiment on the pre-existing (Homestake) fault. Borehole is used to change pressure in the fault vicinity and to specify the place of fault nucleation. Horizontal or vertical arrays of boreholes used to control stresses by cooling (blue).

3.7. DISCUSSION

Many aspects of faulting processes remain poorly understood, in large part because of a scarcity of controlled field experiments at appropriate scales. In this work, we suggest that the in-situ stresses in the Homestake mine are sufficient to drive faulting, and the mine workings present an opportunity to conduct such experiments. Specifically, faults could be activated in-situ at scales ≈ 10 – 100 m using thermal techniques and fluid injection to modify in situ stresses and the fault strength to the point where the rock fails.

During our recent field work in the former Homestake gold mine in the northern Black Hills, South Dakota, we found a large fault present on multiple mine levels. The fault is subparallel to the local foliation in the Poorman formation, a Proterozoic metamorphic rock deformed into regional-scale folds with axes plunging ≈ 40° to the SSE. The fault extends at least 1.5 km along strike and dip, with a center at least ≈1.5 km deep. It strikes ≈340°, dips ≈ 60° NE, and includes ≈ 0.4 m of distinct gouge.

Most earthquakes are thought to be the result of unstable slip on existing faults. It is possible that slip on the Homestake fault could be initiated in response to the controlled fluid injection near the fault plane. This activation is likely to be localized on a crack-like patch. Slow patch propagation, moderated by the injection rate, may become unstable, leading to the nucleation of a small earthquake (dynamic) rupture. This controlled instability is intimately related to the slip-weakening dependence of the fault strength on the slip process and has been analyzed for the Homestake fault conditions. Scale analyses indicate that this transition occurs for a patch size on the order of ≈ 1 m. Creating a dynamic patch of this size will require an experimental configuration of 10 m to 100 m. This shows why studying the evolution of a dynamic slip patch is likely to be beyond the reach of laboratory experiments. This also underscores the need for a controlled field experiment in mine conditions where 10 m to 100 m scales are feasible.

3.8. CONCLUSIONS

Typically, earthquake nucleation is studied in the laboratory at the cm-to-dm scale, and results are then extrapolated or up-scaled by orders of magnitude to simulate field conditions. In this chapter, we have described an experimental approach that aims to activate faults in-situ at scales of ~10 – 100 m using fluid injection and thermal techniques to modify in-situ stresses and the fault strength to the point where the rock fails. Deep mines present an opportunity to conduct such experiments as they have sufficient in-situ stresses to drive faulting. The main conclusions of this chapter are summarized by:

1. The main question in designing a fluid-injection, deep mine faulting experiment is the assessment of the rock mass dimensions for conducting such an experiment since only a finite mine region can be adequately instrumented. The main parameter in this assessment is the size of the slipping regions (patch) at the moment when the quasi-static patch development becomes dynamic and does not require anymore, any change in the pore pressure.
2. We use the model of *Garagash and Germanovich* [2012] to evaluate the potential slip patch size at the onset of dynamic propagation. Such an event is in essence an earthquake nucleation and it is important to know the patch size in order to design the fault nucleation experiment and for instrumentation of the test site. The nucleation size decreases with depth and equals ≈3 m for the larger horizontal stress (equation (3.22)) and the largest depth (8000 ft.). It is ≈17 m for the smaller horizontal stress (equation (3.23)) and the smallest depth (3000 ft.). Therefore, our (scale) analyses for the Homestake fault conditions indicate that the onset of dynamic slip occurs for a patch size on the order of 1 m to 10 m. Creating a dynamic patch of this size will require an experimental configuration of at least 10 m to 100 m. This appears feasible under field conditions in the Homestake mine, but it demonstrates why the characterization of a dynamic slip patch is beyond the reach of laboratory experiments. This result is significant, also because the Homestake fault conditions of 1 to 3 km depth are representative of many mines around the world.

3. The nucleation length is largely controlled by the proximity of the fault loading to the static strength, quantified by the understress parameter $\left(\tau_p - \tau^b\right)/\tau_p$. In other words, the nucleation length is weakly dependent on the fluid pressure but strongly dependent on the proximity of the fault loading to the static strength.
4. In this work, we calculate both the minimum and maximum nucleation length required for instability. The minimum nucleation length for a given background loading is given by the asymptote of the marginally pressurized fault while the maximum nucleation length is constrained by the value of the overpressure that would cause an incipient fault opening (hydraulic fracture) and the local loss of shear strength (equation (3.24) and (3.25)).
5. Because $\bar{\sigma}_0$ is, generally, not the least effective normal stress, it is also possible that hydraulic fracturing may be initiated and propagated off the fault plane for Δp less than $\bar{\sigma}_0$.
6. Our field design of an earthquake nucleation experiment in a mine consists of two methods. In the first method we propose pore pressure perturbation of a fault by fluid injection on the fault to reactivate it. In the second method, a robust implementation approach for creating new faults would be to circulate chilled fluid through arrays of boreholes drilled along vertical planes; boreholes could be either horizontal or vertical. This will reduce the horizontal compression normal to the planes of the boreholes while the vertical stress remains unchanged. Our scaling and numerical analyses of these designs show that the thermal technique can create differential stresses sufficient to induce faulting within a period of approximately 11 days.
7. The thermal technique can be used to study how faults form. The two methods (thermal and fluid injection techniques) can also be used in tandem to reactivate an existing fault.

4. FLUID-DRIVEN FRACTURING OF PARTICULATE MATERIALS IN TRIAXIAL EXPERIMENTS AND LOW STRESS REGIMES

4.1. INTRODUCTION

Hydraulic fracturing in unconsolidated particulate media has been studied extensively at Georgia Tech [*Chang et al.,* 2003; *Chang,* 2004; *Hurt et al.,* 2005; *Germanovich and Hurt,* 2007; *Huang et al.,* 2011; *Zhang and Huang,* 2011; *Callahan*, 2011; *Huang et al.,* 2012; *Zhang,* 2012; *Germanovich et al.,* 2012; *Hurt and Germanovich,* 2012; *Hurt,* 2012; *Zhang et al.,* 2013]. Studies on this topic have also been conducted by other researchers [e.g., *Jaworski et al.,* 1981; *Chudnovsky et al.,* 1988; *Chudnovsky et al.,* 2015; *Panah and Yanagisawa,* 1989; *Murdoch,* 1993; *Khodaverdian et al.,* 2010b; *Khodaverdian and Mcelfresh,* 2000; *Soga et al.,* 2004; *de Pater and Dong,* 2007; 2009; *Golovani et al.,* 2010; *Golovani et al.,* 2011; Jasarevic *et al.,* 2010; *Dong and De Pater*, 2008; *Dong*, 2010]. To our knowledge, synthetic sands were used as unconsolidated particulate media in most of these studies. This chapter presents hydraulic fracturing experiments that were performed in a natural sand that was obtained from a petroleum reservoir. We call this sand the Bromide formation sand owing to its source being in the Bromide geological formation. In this work, we utilize and advance experimental techniques to characterize the process of hydraulic fracturing in cohesionless particulate materials. The experimental results from the Bromide formation sand are compared and contrasted with those obtained with synthetic materials under similar conditions. Results from over 40 experiments conducted on the Bromide formation sand and synthetic sands under low stress (up to 160 psi) regimes are presented and discussed. The goal of this study was to improve our understanding of hydraulic fracturing in cohesionless particulate media by using natural sands obtained from a production well. Specifically, we seek to answer the following questions:

1. Does the hydraulic fracturing behavior in natural sands resemble that in synthetic sands in terms of fracture geometries, fluid leakoff, and pressure signatures?
2. Are the hydraulic fracture initiation and propagation mechanisms in natural sands similar to those in synthetic sands?

3. Which synthetic material most closely resembles the natural sands in terms of mechanical properties and deformation mechanisms?
4. What is the flow rate dependency of the peak pressure in natural sands, if any?

The structure and organization of this chapter is as follows. In Section 4.2, the experimental setup and procedure is outlined. The geology of the Bromide formation, from which the natural sand was obtained, is described briefly as well as mechanical properties of other materials used in our experiments. Experiments conducted in the Bromide formation sand are presented in Section 4.3 while those performed in synthetic sands are described in Section 4.4. Then comparisons between experimental results for natural sands and synthetic particulate media are made in Section 4.5. Finally, discussions and conclusions about these results are presented in Section 4.6.

4.2. Triaxial SET UP AND EXPERIMENTAL PROCEDURE

The laboratory set up consisted of a triaxial cell, a pressure control panel, a computerized data acquisition system, a pneumatic loading frame, and a fracturing fluid delivery system, which included a pump, a displacement piston and an injection source. The cohesionless particulate materials used in our experiments included the Bromide formation sand, silica sand USM100 [www.ussilica.com], quartz sand F110, silica flour Sil-CO-Sil 106, and their mixtures [*Hurt,* 2012]. The general experimental protocol included cleaning, drying, mixing, compaction, saturation, loading and injection. A brief description of the laboratory setup, the materials and the experimental procedure follows below.

4.2.1. Laboratory Setup

Triaxial cell

The triaxial cell used in our experiments is similar to the typical triaxial cells used in geotechnical engineering experiments, but larger in size. A schematic and a picture of this cell are presented in **Figure 4.1**. A comprehensive description of the triaxial pressure cell is given in *Hurt* [2012]. The cell contains a cylindrical specimen with a diameter of 12 in and a height of 22 in. This sample is

placed inside a large membrane that is flexible and impermeable. Two rigid capstone plates are placed at the top and bottom of the sample. An injection source is inserted from the bottom and has a 2-inch perforation zone approximately 11 in above the bottom plate. In this work, the injection source is a simulation of the borehole in petroleum applications. Therefore, the names injection source and borehole are used interchangeably. Even though the name "borehole" may carry the connotation that a hole was bored into the sample, it should be understood that for purposes of this work the name borehole points to the injection source, which was installed in place and not drilled into the sample. The end of the injection source is plugged with a bolt and is located at approximately 12.5 in above the bottom plate. A description of the design of this injection source is also presented in *Hurt* [2012]. The sample and the membrane are located inside a hydrostatic cell as shown in **Figure 4.1**. The maximum hydrostatic confining load applied to the sample was 80 psi. Vertical loading on the sample was applied from the top using a pneumatic cylinder fixed to a loading frame. The maximum vertical load was 160 psi. In all our experiments, a vertical stress to horizontal confining stress ratio of 2:1 was maintained. Results of previous studies have shown that this ratio does not significantly affect the fracture geometry (unless the ratio is close to 1) [*Hurt,* 2012].

The triaxial cell allows for saturation of the sample as well as application of vacuum. It also has gauges allowing for the measurement of pore pressure changes and volumetric strain fluctuations. The triaxial cell is connected to a pressure panel through which pressure and vacuum supply are regulated.

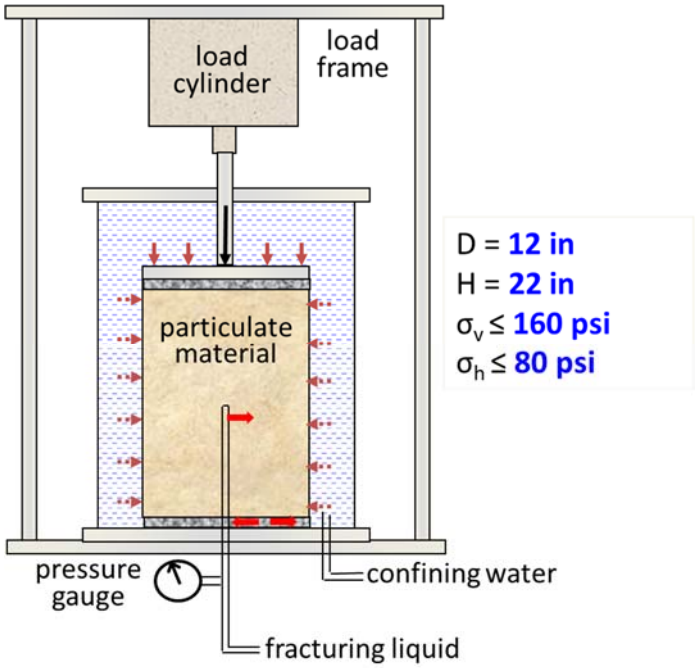

(a)

(b)

Figure 4.1: (a) Schematic and (b) picture of triaxial cell and loading frame [*Hurt,* 2012].

Fluid injection system

The fracturing fluid injection system comprised of the injection source (borehole simulation), high pressure tubing, a displacement chamber and an injection pump. The borehole (injection source) was connected to the cylinder of a positive displacement chamber filled with fracturing fluid. The displacement chamber was in turn connected to a larger triplex plunger pump. The flow rate can be set on the pump to values ranging from 50 ml/min to 15,000 ml/min. The fluid flow rate was controlled by the displacement of a piston, translated inside the chamber by hydraulic oil. The borehole fluid pressure was recorded continuously during the test using the pressure transducer connected to a computer. A pressure vs time graph was plotted and observed on the computer screen in real time during each test. A data log of experiments and conditions under which they were conducted is presented in Appendix A while a log of experimental results and sample experiments with plots and pictures are presented in appendix B.

Data acquisition system and pressure control panel

The data acquisition system consisted of a pressure transducer connected to the fluid injection line. This transducer is connected to the borehole at a point located 2 feet below the injection zone. The transducer is in turn connected to a computer through a USB-1024LS 24-Bit Digital Input/Output (I/O) module [www.coleparmer.com]. A custom-designed Matlab software was used with this module to collect pressure data and also to plot the data on a live computer screen in real time (Appendix C). A pressure transducer was also attached to a FLUKE89 device [www.fluke.com] as a backup data collection device.

An S-500 master control triaxial panel [www.durhamgeo.com] was used to manually regulate the working pressure, volume change and fluid flow on the triaxial cell. Gauges on the panel were used to monitor air pressure and vacuum.

4.2.2. Materials and mechanical properties

We advance previously developed hydraulic fracturing experimental techniques by using a natural cohesionless sand obtained from an oil well. As stated in Section 4.1, we call this sand the Bromide formation sand owing to its source being in the Bromide geologic formation. The purpose of this phase of the research was to asses and verify that laboratory hydraulic fracturing in natural particulate media from a petroleum reservoir is possible and whether or not using natural sand is more advantageous than the use of artificially processed sands. We also conducted experiments in synthetic cohesionless particulate materials such as silica sand USM100, Quartz sand F110, silica flour SIl-CO-SIl 106 and their mixtures and compared results from these materials with results from the Bromide formation sand. The main synthetic materials tested were an 80/20 percent mixture of USM100 and silica flour, and an 80/20 percent mixture of F110 and silica flour. The following are general descriptions and mechanical properties of the materials used in our experiments.

Bromide formation sand

The Bromide formation sand, used in our experiments, was obtained from well number 3 located in the Southwest Clothier field, section 29 in Cleveland county, Oklahoma. It was sampled at a

subsurface depth of approximately 7700 feet in the Bromide formation, a member of the middle Ordovician Simpson Group. The Bromide formation crops out in the Arbuckle and Wichita mountains and in the Criner Hills of Oklahoma [*Loeblich,* 1942; *Pope,* 2004]. It is exposed at the surface in Carter, Johnston, Murray and Pontotoc counties of Oklahoma [*Amsden*, 1983; *Webby et al.,* 2004; *Pope,* 2004]. The formation has been a source of oil and gas in Oklahoma and is known for its rich fossils and echinoderm skeletons (marine animal skeletons). Geologically, the value of echinoderms is in their ossified skeletons, which are major contributors to many limestone formations. To characterize the Bromide formation sand we used lithological reports from water supply wells, petroleum exploration wells, laboratory sieve analyses, microscope images and published literature.

As stated before, the Bromide formation sand was obtained from the Bromide formation in Oklahoma, which is the youngest member of the Simpson group of the Ordovician age (see **Figure 4.2**). The Bromide formation overlies the Tulip Creek formation and underlies the Viola Springs formation. It is approximately 295 feet thick and can be subdivided into a lower member, 125 feet thick, and an upper member, 170 feet thick [*Flores and Keighin,* 1989; *Puckette et al.,* 2009]. According to *Flores and Keighin* [1989], this formation mainly consists of interbedded sandstone, siltstone, mudstone, and limestone with the lower part of the formation containing thick sandstone units and the formation as a whole consisting of 35 percent sandstone. The Simpson Group as a whole contains about 60 percent sandstone and conglomeratic sandstone [*Flores and Keighin,* 1989]. *Puckette et al.* [2009] call the sandstone in the Bromide formation "Bromide formation sandstone" and we will adopt this nomenclature in this work.

Bromide formation sandstones and other sandstones in the Simpson group are classified as quartz arenites as they are composed of more than 95 percent detrital quartz grains [*Puckette et al.,* 2009]. The higher compaction of grain-to-grain contacts of quartz sandstones at great depths leads to a higher degree of cementation as silica cement is generated. The porosity of the Bromide formation at the source of the Bromide formation sand used in our experiments was 15 percent and the core-measured permeability was approximately 200 mD [*Puckette et al.,* 2009]. The permeability of the Bromide formation sand under our experimental conditions was measured to be approximately 3.6 darcy.

The Bromide formation sandstone was crumbly and easily disaggregated into loose sand. It was also disaggregated by the drill bit and high pressure fluids during drilling. The Bromide formation sand was yellowish brown. *Wright* [1965] suggests that this color signifies the presence of sandstones containing quartz cement and that it is free of clay.

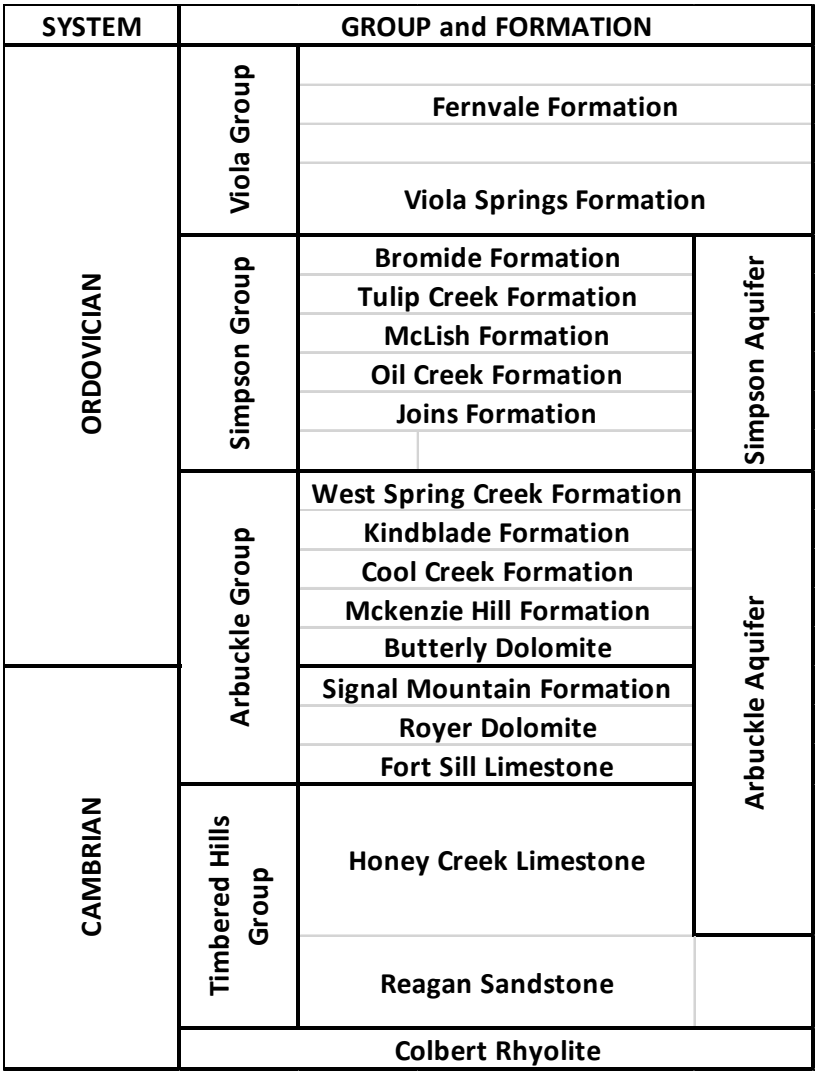

Figure 4.2: Stratigraphy of the Ordovician and Cambrian rocks that outcrop in the Arbuckle mountains [*Johnson,* 1989].

We have performed a number of laboratory analyses on the Bromide formation sand to characterize this material. These included angularity analysis using a camera microscope, sphericity and roundness (Krumbein shape factor) [*Krumbein and Sloth,* 1963], grain size

distribution (GSD) examination by sieve analysis in accordance with ASTM D 422-63, maximum and minimum void ratio calculations in accordance with ASTM D 4253 and D 4254, respectively, and mechanical properties testing. The particles were found to be well rounded (**Figure 4.6**) with a roundness factor of 0.9 [*Krumbein and Sloth,* 1963]. The particle roundness of the Bromide formation sand grains suggests that they may have been transported by water and air during their geological history [*Santamarina,* 2001]. The shape of the particles may be an important factor in affecting the engineering response of granular soils [*Holubec and D'Appolonia*, 1973; *Krumbein and Sloth,* 1963]. This sand is bulky, fine-to-medium grained and poorly graded. Poorly graded (uniform graded) granular materials consist of particles of similar sizes. The mean particle diameter of the Bromide formation sand is approximately 0.34 mm (340 μm) while its maximum and minimum void ratios are 1.00 and 0.62, respectively. Under our test conditions, the maximum particle density was 1.68 g/cm^3 at confining stresses of 80 psi. This corresponds to the sample porosity of 37 percent. **Figure 4.4** and **Table 4.1** present these properties for the Bromide formation sand and for other materials used in our experiments.

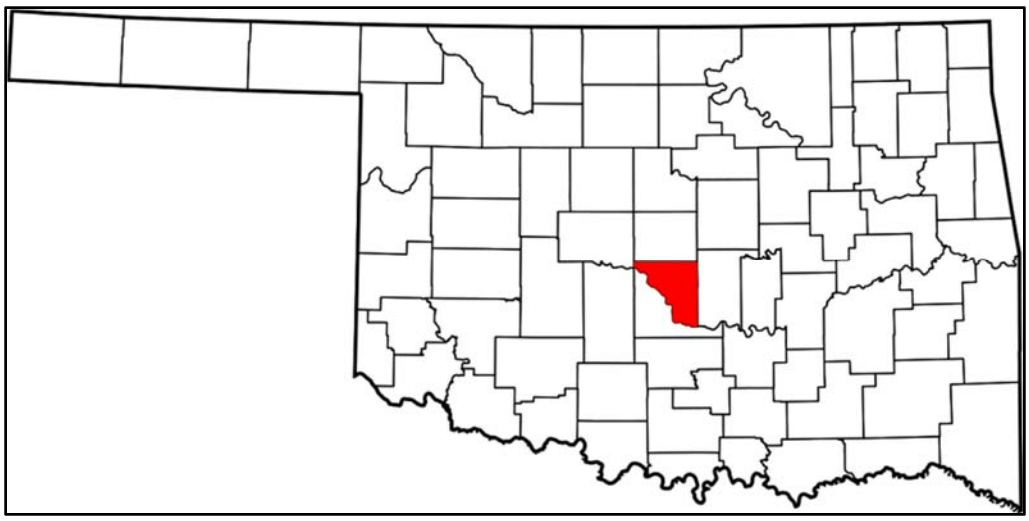

Figure 4.3: Red shaded area on map shows well location from which the Bromide formation sand was obtained in the Southwest Clothier field, section 29 in Cleveland County, Oklahoma [http://maps.normanok.gov/OilWell.html].

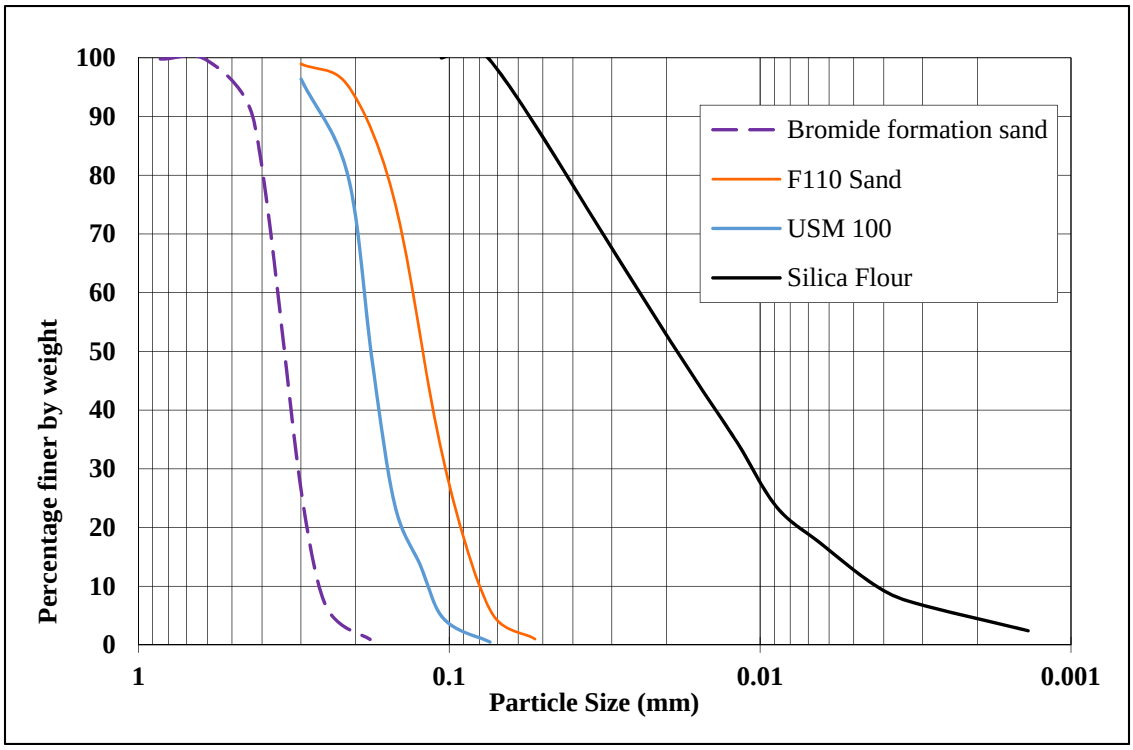

Figure 4.4: Grain size distributions for Bromide formation sand, F110 Sand, USM100 sand, silica flour, and silica/F110 mixture.

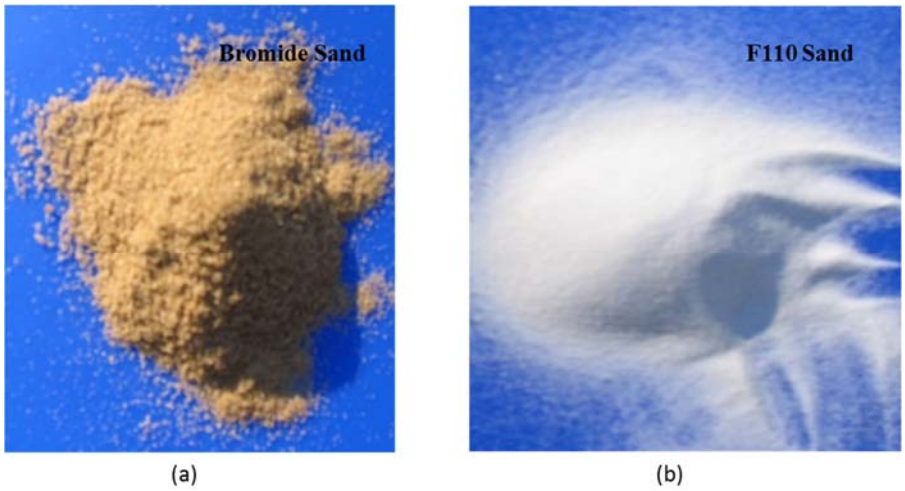

Figure 4.5: (a) Natural Bromide formation sand and (b) synthetic F110 Ottawa sand.

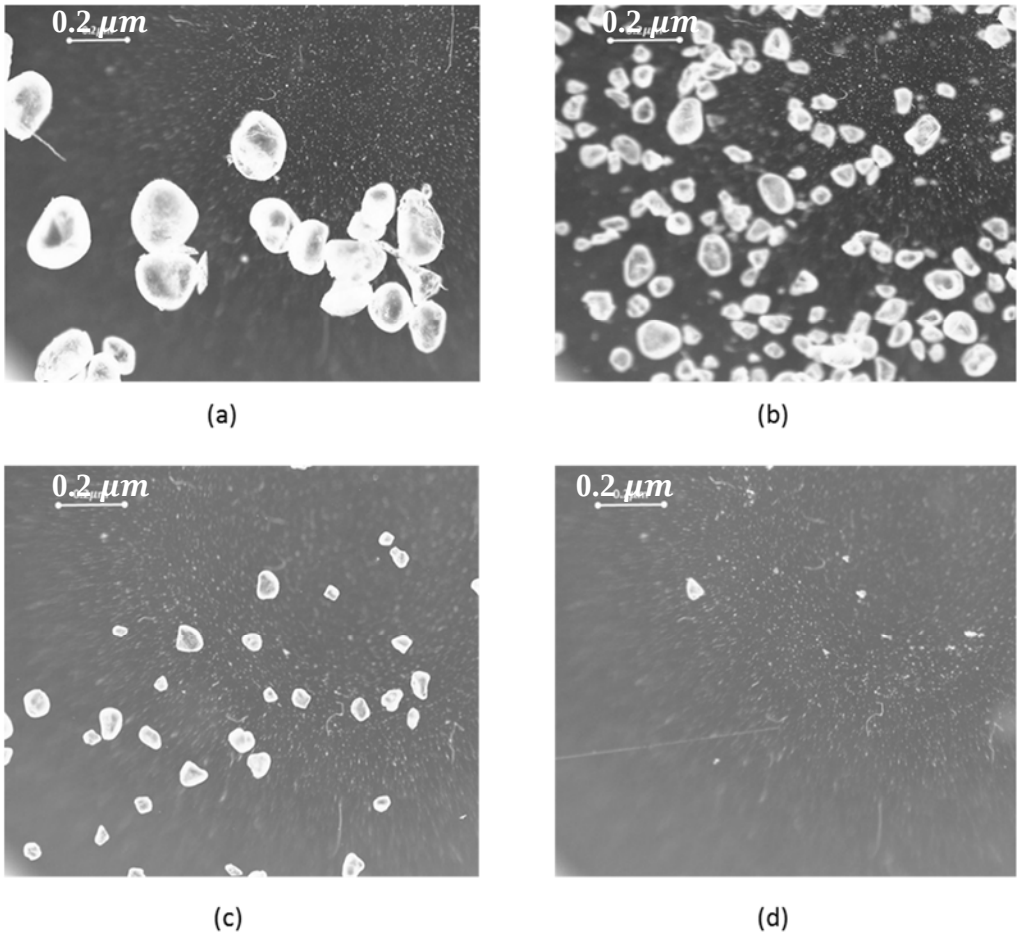

Figure 4.6: Camera microscope pictures at 4 x 0.10 lens magnification. (a) Bromide formation sand showing well rounded shape, (b) F110 Ottawa fine sand, (c) USM100 fine sand showing sub-rounded to sub-angular particle shape, and (d) silica flour particles showing angular shape.

Table 4.1: Mechanical properties of particulate materials used in triaxial experiments. Properties were measured based on the ASTM D 4253 and ASTM D 4254 standards and under the experimental conditions discussed in the main text.

	ρ min ASTM	ρ max ASTM	ρ max EXPT	η max ASTM	η min ASTM	η min EXPT	e max	e min	e min
	g/cm^3	g/cm^3	g/cm^3				ASTM	ASTM	EXPT
Bromide Formation Sand	1.33	1.63	1.68	0.50	0.38	0.37	1.00	0.62	0.58
Sand USM100	1.56	1.78	1.88	0.41	0.33	0.29	0.69	0.49	0.41
Sand F110	1.45	1.65	1.71	0.45	0.38	0.35	0.83	0.60	0.55
Silica Flour (Silt)	1.04	1.71	1.87	0.61	0.39	0.29	1.56	0.64	0.42
20/80 Silica Flour/USM100 mix	1.59	1.93	1.99	0.40	0.27	0.25	0.67	0.37	0.33
20/80 Silica Flour F110 mix	1.48	1.79	1.90	0.44	0.32	0.28	0.79	0.48	0.39

Table 4.2: Mechanical properties of particulate materials used in triaxial experiments. Permeability measurements were conducted using the constant head method (ASTM D 2434).

	D_{10}	D_{30}	D_{60}	D_{50}	C_U	C_c	k @ 80 psi
	µm	µm	µm	µm	D_{60}/D_{10}	$(D_{30})^2/(D_{10}D_{60})$	Darcy
Bromide formation sand	270	310	360	340	1.33	0.99	3.6
Fine sand USM100	130	160	190	180	1.46	1.04	1.8
Fine sand F110	80	100	140	130	1.75	0.89	1.3
Silica flour (Silt)	4.2	11	25	19	5.95	1.15	0.02
20/80 Silica flour/USM100 mix	130	160	190	180	1.46	1.04	0.2

Silica sand USM100

USM100 is a white monocrystalline whole grain alpha-quartz mineral sand. It is part of the Ottawa fracturing sand products from the U.S. Silica company [www.ussilica.com]. It exhibits exceptional strength, durability, integrity, and purity. USM100 does not degrade or dissolve during handling and pumping associated with normal hydraulic fracturing operations [*U.S. Silica Company,* 2014; www.ussilica.com]. The USM100 material is a sub-rounded to sub-angular, poorly graded sand with a mean particle size of 175 μm. It has a specific gravity of $\approx$2.65 and a permeability of $\approx$1.8 Darcy at maximum density and 80 psi confining stress. **Table 4.2** highlights some of the USM100 properties. A grain-size distribution for USM100 was determined following ASTM D 422 and is shown in **Figure 4.4**.

Table 4.3: Summary of the USM100 sand properties [www.ussilica.com].

Krumbein Shape Factors[1]			
Roundness			0.7 - 0.8
Sphericity			0.7 - 0.8
Bulk Density (g/cm^3)			1.48 - 1.60
Bulk Density (lb/ft^3)			92 - 100
Particle Density (g/cm^3)			2.64 - 2.65
Particle Size Distribution	mm	U.S. Sieve No.	Weight Retained (%)
	0.300	50	3.6
	0.212	70	16.5
	0.177	80	31.8
	0.150	100	24.3
	0.124	120	10.4
	0.104	140	9.2
	0.074	200	3.9
	<0.074	Pan	0.5
		total	**100**
Mean Particle Diameter (mm)			0.175
Median Particle Diameter (mm)			0.168
Crush Resistance Classification (K-value)[2]			11 K

[1] *Krumbein and Slot* [1963].
[2] www.fracsandtesting.com.

Maximum and minimum void ratios were established in accordance with ASTM D 4253 and ASTM D 4254, respectively. The minimum void ratio was determined using a shaking table as per these ASTM standards. The maximum and minimum void ratios for the USM100 sand used in our tests were 0.69 and 0.49, respectively. The minimum void ratio under our experimental conditions of maximum density and confining stresses of 80 psi was 0.41. This corresponds to the sample porosity of $\emptyset = 29$ percent.

Quartz sand F110

The Ottawa F110 sand used in our tests was a fine, poorly graded quartz sand with an average particle size ranging from 110 to 130 µm. It was sourced from the U.S. Silica company, Mill Creek plant mine, in Oklahoma. The sand and its mechanical properties are described in detail in *Hurt* [2012]. The grain size distribution of this sand is presented in **Figure 4.4**. The maximum and minimum void ratios of the sand under ASTM D 4253 and ASTM D 4254, conditions were 0.83 and 0.60, respectively. Fracture tests were conducted at maximum density with F110 void ratios of 0.55 under confining stresses of 80 psi. This corresponds to the sample porosity $\emptyset = 35$ percent. The sample permeability under these conditions was approximately 1.3 Darcy [*Hurt,* 2012].

Silica flour SIl-CO-SIl 106

The silica flour used in our tests was SIL-CO-SIL 106 and was obtained from the ITC Minerals and Chemicals Company [www.ussilica.com]. SIL-CO-SIL 106 is a high purity, inert, white ground silica. This silica flour is well graded and has a good representation of particle sizes over a wide range. It offers low moisture, natural hardness, chemical resistance, high brightness, and low oil absorption. It has an angular shape and a mean particle size of 19 µm. This material is also described comprehensively in *Hurt* [2012]. It has a specific gravity of approximately 2.65. The average permeability of the silica flour at a confining stress of 80 psi was about 20 millidarcy. Due to the low permeability, it was difficult to saturate silica flour samples and therefore all experiments in this material were performed under dry conditions. *Chang* [2004] and *Hurt* [2012] show, however, that the experimental results for dry and saturated materials are similar. **Table 4.4** gives a summary of a few more properties of the SIL-CO-SIL 106. Only a few tests were conducted in dry silica flour. The fracture morphologies that were formed in dry silica flour were very different from those obtained in the Bromide formation sand and other materials. The fractures in silica flour were thin with much less leakoff and had multiple wings. These have been described as petal wing fractures by *Chang* [2004], *Wu* [2006], and *Wu et al.* [2007].

Table 4.4: Properties of silica flour SIL-CO-SIL 106 [www.ussilica.com].

Property	Unit	Value
Particle Size, retained of 325 mesh	%	22.3
Hardness	Mohs	7
PH	1	7
Reflectance	%	89.4
Yellowness Index	1	3.63
Specific Gravity	1	2.65
Silicon Dioxide	%	99.7
Particle Size, retained on 140 mesh	%	1

Flour-Sand Mixtures

Hurt [2012] examined a number of different mixtures of fine sand and silica flour as possible candidates for fracturing tests. It was found that the fraction of silica flour in the mixture had a profound effect on the permeability of the mixture and the deformation mechanisms of the sample. This was attributed to the effect of sample permeability, which depends on this fraction [*Hurt,* 2012]. It was also concluded that mixtures with a fraction of silica flour of 15% or less, exhibited fines migration during the sample saturation stage of the experiment. *Hurt* [2012] selected the mixture with 20% silica flour because of the above stated reason and also because this mixture better resembles particle distributions in real petroleum formations.

In this work we also selected two fine sand and silica flour mixtures with 20% composition by weight of silica flour. These were 20% silica flour plus 80% fine sand F110 (20/80 Silica Flour/F110) and 20% silica flour plus 80% fine sand USM100 (20/80 Silica Flour/USM100). The earlier experiments were conducted using F110 while the later tests were performed in USM100 as the manufacturer discontinued the supply of F110 and replaced it with USM100. These mixtures were also selected because they were faster to saturate and because at 20% fractions of silica flour, the mixture still exhibited cohesionless behavior. Silica flour can complicate the assumption of cohesionless samples in our study, when it exceeds 50% composition [*Mitchell and Soga,* 2005].

As shown in **Table 4.1**, the maximum and minimum void ratios of the 20/80 Silica Flour/USM100 mixture were 0.67 and 0.37, respectively, while the minimum void ratio at experimental maximum density standards was 0.33. This corresponds to the sample porosity φ = 25%. The maximum and minimum void ratios of the 20/80 Silica Flour/F110 mixture were 0.79 and 0.48, respectively, while the minimum void ratio at experimental maximum density conditions was 0.39. This corresponds to the sample porosity $\varphi = 28\%$. At the experimental conditions of maximum density and confining stresses of 80 psi, the permeability of these mixtures was approximately 200 millidarcy.

Fracturing fluid

A guar-based fracturing fluid was the major fluid used in our experiments and simulated industrial fluids (**Figure 4.7**) [*Ayoub, personal communications*, 2010]. The fluid was made fresh in the lab for each test, using a proprietary formula provided by Schlumberger (SLB). It can be described as a guar cross-linked gel with a resin component that allows for solidification of the leakoff region [*Hurt*, 2012]. This fluid was ideal for our experiments because it could solidify in a water saturated environment, was immiscible in water, and had a high viscosity to minimize leakoff. In our experiments, the fracturing fluid was injected into a porous, permeable medium at high pressures and flow rates. A filter cake formed on the wall between the fracture and the particulate medium after the filtrate invasion into the porous medium. We call the filtrate invasion zone, the leakoff. As a polymer fluid, there may be two distinct types of leakoff processes resulting in the formation of an internal or external filter cake. The pressure gradient between the injection fluid and the pore fluid is a major factor in the formation of the internal filter cake. The external filter cake forms when the solvent in the polymer separates from the invading fluid and leaks off into the porous medium. Polymer chains then build up on the fracture walls and act as an additional porous matrix [*Hurt,* 2012].

A coloring agent was mixed with the fracturing fluid so as to isolate the fracture aperture and the leakoff zone from the uninvaded zone during fracture excavation (mine back). Colors of blue and red were used, with blue being the most dominantly used.

Rheology of fracturing fluid

A Bohlin C-VOR-150 rheometer [www.malvern.com] was used to measure the rheological properties of guar cross-linked fluid. **Figure 4.8** shows some results of the rheological tests for the guar cross-linked gel. The viscosity of this fluid decreases with increasing shear rate, better known as a property called power law, shear thinning. This phenomenon was expected due to the cross-linked nature of the fluid. The data are very nicely fit with a power law relation over the higher shear rates range with n = 0.17 and a K value of 75 Pa × $\sec^{n}$ (where n is the power law exponent or fluid flow behavior index, K is the the consistency index, indicative of pumpability of the fluid). *Hurt* [2012] also confirmed the power law, shear thinning nature of the guar cross-linked fracturing fluid. The fracturing fluid stability over time was also examined. **Figure 4.8** shows a drop in the viscosity after 4 hours of aging time, as the resin begins to harden.

Polymer based constitutive fluid flow models are used to characterize the rheological behavior of the fracturing fluid in our tests (**Table 4.4** where τ is the shear stress, τ_0 is the yield stress, μ is the Newtonian viscosity, and $\dot{\gamma}$ is the shear rate). The Herschel-Bulkley law [e.g., *Herschel and Bulkley,* 1926] represents a generalization of models used to characterize the rheology of petroleum fluids [*Montgomery, 2013*]. The power law model is a special case of the Herschel-Bulkley law when the yield stress τ_0 is equal to zero. This is the most common fluid model used for current fracturing fluids, which defines the effective fluid viscosity as

Table 4.5: Constitutive models used in characterization of fracturing fluid rheology.

Model	Constitutive equation	Examples
Herschel-Bulkley	$\tau = \tau_0 + K\dot{\gamma}^n$	Bingham fluids
Power Law	$\tau = K\dot{\gamma}^n$	Guar cross-linkers
Newtonian	$\tau = \mu\dot{\gamma}$	Water, oil, glycerin

$$\mu_{eff} = K\dot{\gamma}^{n-1} \tag{4.1}$$

For this model the shear stress/shear rate data give a linear relationship on log-log scales. The value of $n = 1$ implies a Newtonian fluid, $n > 1$ is called a shear stiffening fluid, and $n < 1$ is

a shear softening fluid. Parameter *n* is generally less than 1 for fracturing fluids [*Montgomery,* 2013]. In the Herschel-Bulkley law, $n = 1$ implies a Bingham plastic model. A Bingham plastic fluid differs from a Newtonian fluid in that a non-zero plastic yield stress value must be overcome to initiate fluid flow. Model (4.1) is used in **Figure 4.8** to characterize rheology of the guar based fluid used as a fracturing fluid in our experiments.

Figure 4.7: Guar cross-linked gel used as fracturing fluid. Fluid remains as a cohesive unit as it is being poured out into a glass beaker.

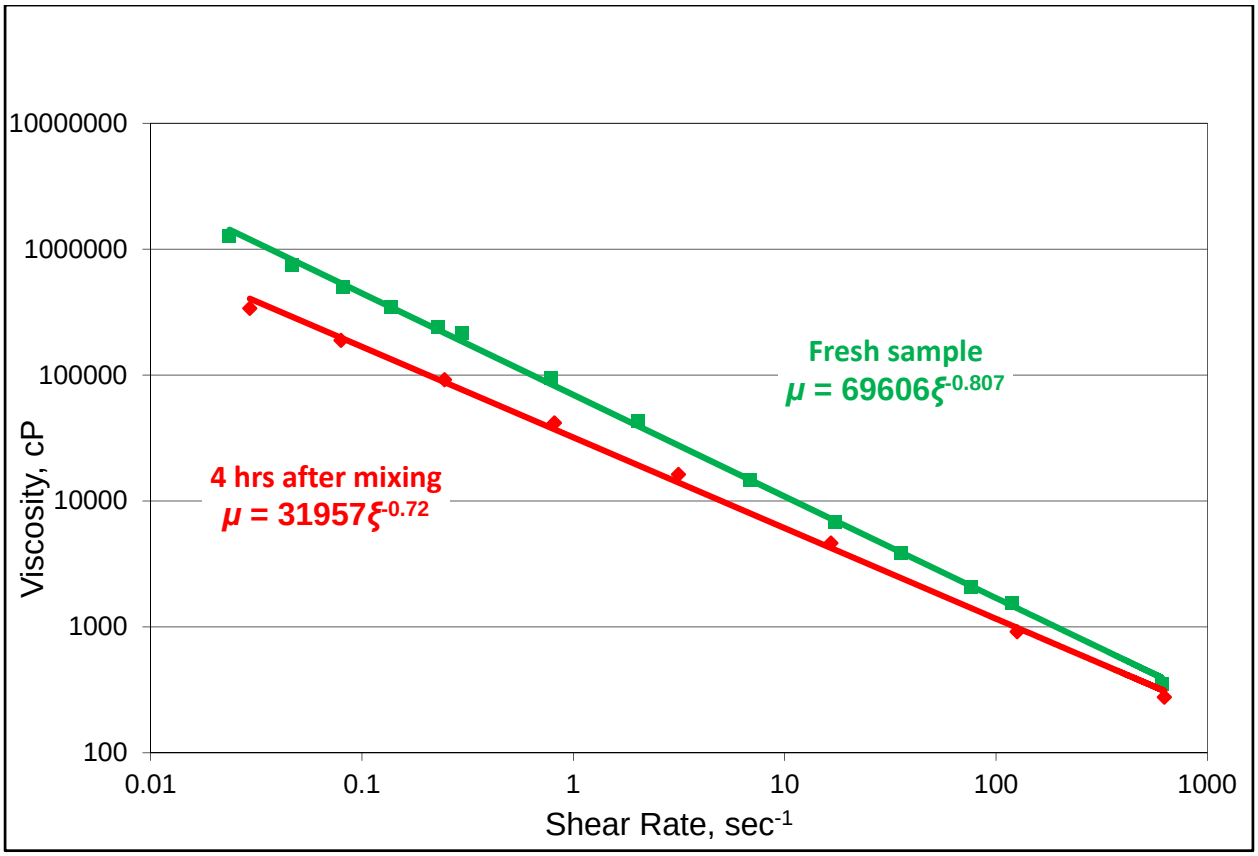

Figure 4.8: Power law dependence of viscosity vs shear rate for guar fluid. The viscosity of the guar fluid decreases with shear rate showing that it is a shear thinning fluid. Results from 2 tests conducted over 4 hours to investigate the effect of aging on fracturing fluid behavior. With 4 hours of aging time, the viscosity falls as the fluid flow index, n, increases from 0.19 to 0.28 and the consistency index, K, decreases from 70 Pa × sec^n to 32 Pa × sec^n.

4.2.3. Experimental Procedure

The following general procedure was followed for all our tests in this work. First the sample material was prepared by cleaning, drying, and mixing (as described below). Then the block sample was prepared by compaction and saturation. Finally, the test loads were applied to the block sample and the fracturing fluid was injected while the injection pressure was observed in real time. The fracturing fluid was allowed to set under load over a period of 24 hours before fracture excavation could begin. A schematic summarizing this procedure is given in **Figure 4.9**. The details of these processes are also described below. The employed experimental procedure is similar to *Chang* [2004], *Germanovich et al.* [2012], and *Hurt* [2012].

Cleaning, drying, and mixing

The Bromide formation sand contained oil residues when it arrived from the oil rig. A significant amount of time and effort was, therefore, dedicated to the cleaning of this material before using in our tests. After trying several techniques to clean this soil, we finally arrived at a method that was both simple and economical. The soil was first washed with boiling water for 3 to 4 hours. A water volume of twice that of sand was used in this process to ensure that the sand was fully submerged. A large wooden spoon was used to stir the water-soil mixture so as to allow the water to contact as much of the oil as possible in the pore volumes. The hot water was then rinsed out of the mixture leaving a wet soil. The wet soil was then placed in a large pan and placed in an oven. The soil was heated at a temperature of 165 degrees Celsius for approximately 4 hours. It was observed that the water in the form of steam was first driven out of the soil before the oil. Water has a lower boiling point than oil. As the soil continued heating, the oil was smoked out of the mixture. This process was repeated for 2 to 3 cycles until no presence of oil in the sand was evident to the naked eye and under x20 magnification for randomly selected samples.

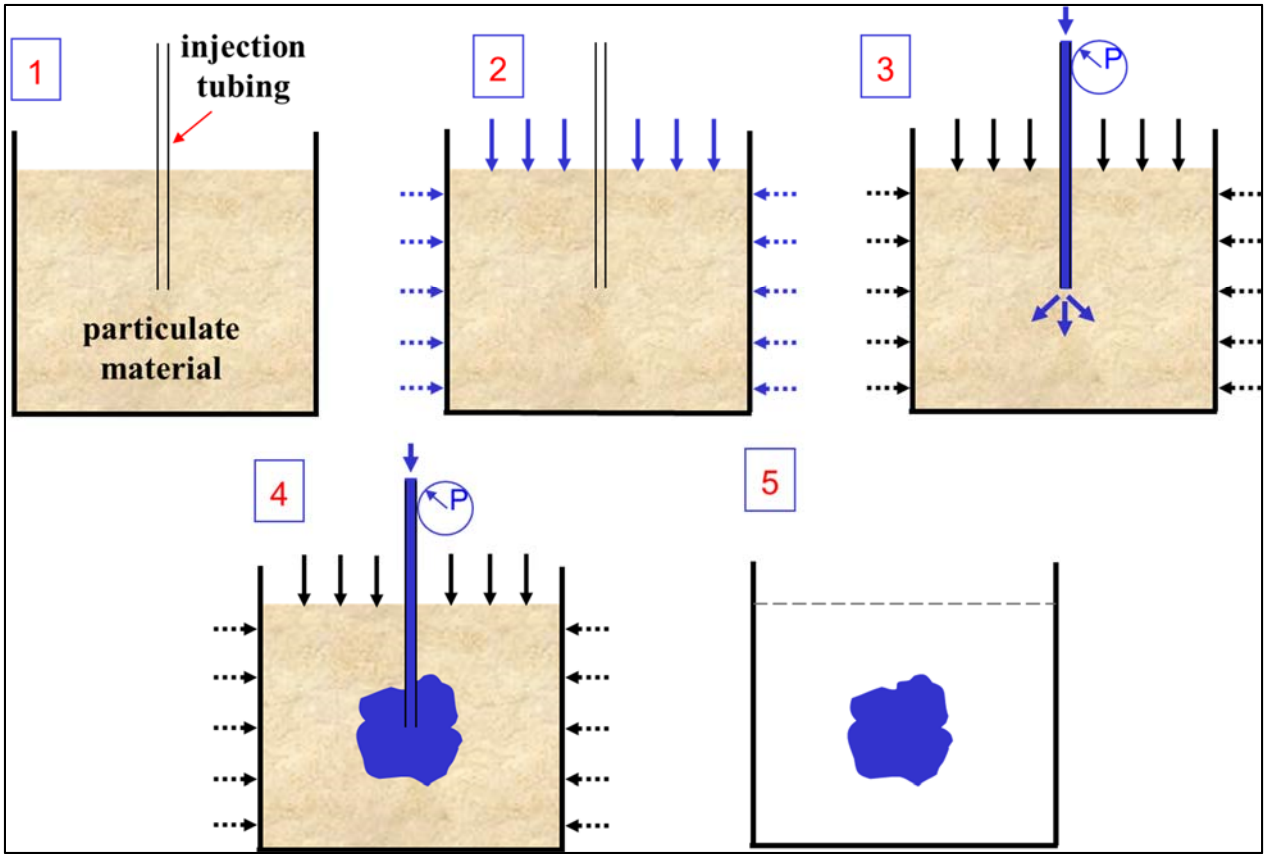

Figure 4.9: Schematic showing general experimental procedure [*Germanovich et al*., 2012; *Hurt*, 2012].

Special care was taken for retaining all particles in the sample during cleaning, but, unavoidably, some particles may have been washed out. The final particle distribution is shown in **Figure 4.4**. It is possible that the original sand had a somewhat large fraction of particles smaller than 100 μm. The percentage of fines, play a significant role in the hydraulic fracturing behavior. Therefore, it is important to maintain the particle gradation of the natural sands as much as possible.

Block sample compaction

An injection source, simulating a borehole, was first installed in the center of the triaxial cell. A perforation zone was located at approximately 11 in above the bottom platen. A complete description of the injection source is presented in *Hurt* [2012]. Also, a 50 x 50 mesh was placed around the perforation zone (**Figure 4.10**). The mesh served two purposes. First, it helped prevent fines migration into the borehole during compaction and saturation. Second, it helped

to hold the fracture in place after fracture formation and solidification at the stage of its excavation. The sample block is prepared inside a gum rubber tube membrane that is attached to the base and top plates by means of rubber O-rings to seal it in place. A rigid plastic mold is placed and tightened around the membrane as the sample is being compacted. A disk filter is placed at the bottom and top of the block sample.

The sample was compacted in the triaxial cell in 4.5 inch compacted layers. Six lifts of approximately 24 lbs. were compacted using the rodding technique with a 1-inch diameter rod. This compaction technique is described in *Chang* [2004], *Hurt* [2012], and *Hurt and Germanovich* [2012]. A technique called "under-compaction" developed by *Ladd* [1978] and modified by *Chan* [1985] was also used to select the amount of rodding to apply to each layer. This technique takes into account the possibility that with the addition and compaction of subsequent lifts, the preceding lifts become denser. To account for this non-uniformity in compaction, *Ladd* [1978] proposed that each additional lift be placed at a higher density. Chan [1985] proposed that each lift be placed at a relative density one percentage point higher than the preceding lift. Following these recommendations, we rodded the bottom lift 200 times, followed by 210 times, 220 times, 230 times, 240 times, and 250 times for the top lift. This ensured that there was nearly uniform compaction throughout the height of the sample. Once the compaction procedure was completed, the top layer was leveled off and then caped with a porous filter disc.

Our samples were typically compacted to a density of approximately 0.061 lb/in^3 (2.0 g/cm^3). This density was consistent with that in true-triaxial tests conducted in high stress regimes described in Chapter 5. After the top layer was leveled off and caped with a filter, the top platen was then installed above the filter and the cylindrical gum rubber membrane wrapped around the top plate. Several rubber O-rings were then inserted to fix the membrane in place. Once the top plate was in place, the top hoses were then connected to the platen. Vacuum was then applied to the block sample from the top. Then the rigid mold was removed and the transparent cell chamber wall was placed around the sample, and the tension rods were tightened in place. The cell was then filled with tap water while a pressure release valve was left open at the top. Once the cell chamber was full of water, a 5 psi hydrostatic pressure was applied on the sample, so that the vacuum on the sample could be removed. The block sample was now

ready for saturation. The experimental set up at different stages of sample preparation is shown in **Figure 4.11**.

Figure 4.10: Image showing injection source design used in this work. Bottom injection source shows perforation holes drilled at 90-degree phasing. Top injection source shows wire mesh attached to source by soldering.

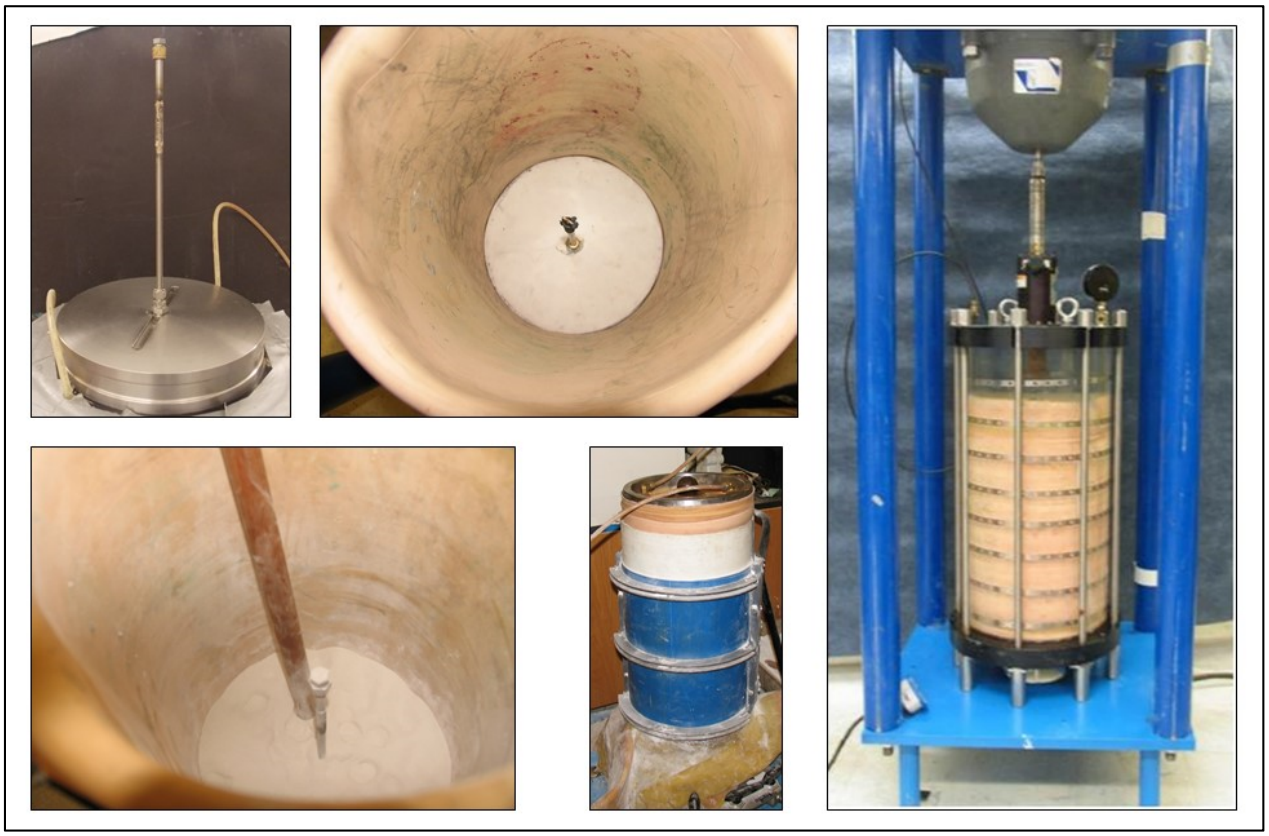

Figure 4.11: Images showing different stages of sample preparation described in the main text.

Block Sample Saturation

The objective of the sample saturation was to fill the voids in the specimen with water without considerably pre-stressing the sample. After the sample was compacted and the triaxial cell chamber assembled, the saturation phase started. A small confining stress of 5 - 10 psi was applied on the specimen during saturation to stabilize the specimen. Backpressure was also applied to the sample during its saturation. "Back pressure" is a pressure applied to the specimen pore-water to cause air in the pore space to compress and to pass into solution in the pore-water thereby increasing the percent saturation of the specimen [ASTM D 4767-11]. Applying backpressure to the specimen pore water improves saturation as most of the air is driven into solution. Removing as much air as possible prior to the application of backpressure reduces the amount of air that needs to be driven into solution. The use of de-aired water for saturation makes the process easier and faster. Flushing the sample with carbon dioxide (CO_2) prior to saturation also greatly improves the saturation process as the heavier and more water-soluble CO_2 displaces air and dissolves into water more readily than air. Using a modified version of the ASTM D 4767 standard, the following steps were followed for the block sample saturation process:

1. The triaxial cell was setup with all the inflow and outflow tubing connected.
2. A small hydrostatic stress ranging from 5 to 10 psi was applied on the sample.
3. Vacuum was applied on the sample for 15 minutes through the top outflow tubing.
4. Vacuum was stopped while the block sample was flushed with CO_2 through the borehole injection tube for 15 minutes. Pressure in the injection tube was maintained at the range of 5 to 10 psi.
5. The sample was then flushed with vacuum again as described in step 3.
6. Step 4 was repeated.
7. Finally, step 3 was repeated with the sample being placed under vacuum for 4 hours.
8. De-aired water was then allowed to percolate into the block sample through the bottom flow tube at a water head of 7 feet.

The volume of water injected into the sample was monitored and when three pore volumes of water, estimated based on the sample porosity, passed through the sample, saturation was assumed to be completed. The Skempton pore pressure coefficient *B* [*Detournay and Cheng,* 1993] was calculated and used to monitor the level of saturation. This can be done based on ASTM D 4767-95 standard, which uses the Skempton coefficient as a measure of soil sample saturation. ASTM D 4767-95 suggests to consider the saturation complete if $B \geq 0.95$ and, according to this standard, the value of saturation is given by the value of *B* expressed in percentage. In general, for soil samples,

$$C \ll C_f \text{ and } C \ll C_s \tag{4. 2}$$

where *C* is the drained compressibility of soil, and C_f and C_s are the compressibilities of fluid and solid constituents, respectively. In this case, $B \approx 1$ [e.g., *Detournay and Cheng,* 1993; *Wang,* 2000] for a fully-saturated material. In our case, to determine B, we increased both vertical and confining stresses by $\Delta\sigma$ and measured the pore pressure response, Δu . By definition [ASTM D 4767-95],

$$B = \frac{\Delta u}{\Delta \sigma} \tag{4. 3}$$

During measurements of B, all outflow and inflow valves were closed. Then, the confining stress acting on the specimen was increased by a value of $\Delta\sigma_3$. The water level in the triaxial cell was then allowed to stabilize for 2 minutes. The valve to the pore pressure gauge was then opened and the increase in pore pressure, Δu, was read. This was repeated three times.

To simulate submarine sediment characteristics, most common for petroleum formations, our experiments targeted normally – consolidated particulate materials. Therefore, it was important to keep the effective stress acting on the specimen, below the effective stress values at which the tests were to be conducted. Because the saturation was taking place at $\sigma_1 = 20$ psi, $\sigma_3 = 10$ psi, we chose $\Delta\sigma < 5$ psi.

The total porosity, P_t, of the sample can also be used to calculate the degree of saturation (equation 4.4).

$$B = \frac{V_w}{VP_t} \tag{4. 4}$$

Where V_w and V are the volume of water in the sample and the total sample volume, respectively.

On average, the saturation process for our samples took approximately 11 hours per sample, and we were able to attain saturation levels better than 95 percent in most of our tests. As stated above, saturation of silica flour samples was difficult due to time constraints and we therefore performed tests for silica flour under dry conditions. The saturation fluid in all of our tests was water. *Hurt* [2012] saturated some of his samples with oil to simulate field conditions and found that there was no significant difference in fracture behavior in oil saturated versus water saturated samples. We have not run experiments with oil saturated samples due to the limited available sample size and the necessity to clean the sample after each experiment with oil.

Block sample loading and fluid injection

When the sample saturation process was completed, preparations for the fracturing fluid injection began. The external loads on the sample were applied using the pressure control panel. In all of our experiments, a vertical stress to the horizontal confining stress ratio of 2 to 1 was maintained. In the majority of our tests at Georgia Tech the vertical stress was 160 psi and the horizontal confining stress was 80 psi. After, reaching the final loading stresses, the sample was allowed to stabilize for approximately one hour. During this time, a cross-linked, guar-based, sand-lock fluid was prepared in accordance with a proprietary recipe provided to us by a Schlumberger laboratory. The rheology of this fluid is described in detail in Section 4.2.2 of this work and by *Hurt* [2012]. The fracturing fluid was mixed with a coloring agent to aid with the subsequent excavation process. After the fracturing fluid preparation and after the sample had stabilized under load, the fluid was placed in the displacement piston. The piston was then connected to the injection tube and the pump. The pressure transducer was also connected to

the injection tube. The distance between the pressure transducer in the injection tube and the injection point was approximately 2 feet. *Hurt* [2012] measured the pressure drop (due to viscous losses) between the transducer and the injection source and found it to be negligible. The top flow tubes to the sample were left open during the experiment to allow for drained loading conditions.

The pump system used for our tests allowed for injection flow rates ranging from 50 ml/min to 15,000 ml/min. After setting the flow rate on the pump system, the pressure monitoring system on the PC was turned on followed by the FLUKE-back-up-pressure monitoring system [www.fluke.com]. The pump was then turned on to initiate the fluid-injection process. We were able to monitor the injection pressure in real time as well as the sample pore pressure. Volumetric deformation of the sample could also be calculated from the displaced pore water volume. The pump was stopped after about one minute of injection while the transducer was allowed to record data for approximately five minutes. After the test run, the fracture was allowed to solidify under load for approximately 24 hours. Excavation was then conducted in a manner to preserve the fracture geometry and morphology. The term fracture morphology is used in this work in the sense of both the fracture shape and the leakoff surface.

4.3. EXPERIMENTS WITH BROMIDE FORMATION SAND

In this section, we present the results of a series of experiments we conducted in the Bromide formation sand. The goal of this part of our work was to develop and compare hydraulic fracturing experiments in natural cohesionless particulate materials with those in synthetic materials such as quartz sand F110 and USM100. In this section, we begin by detailing the various fracture geometries and morphologies observed. Then, we present and discuss some deformation features that were observed in the fracturing of this natural sand. Further, we describe the pressure curves and pressure signatures that are characteristic of the Bromide formation sand. Next, we discuss the effect of the injection flow rate and the material permeability on the fracture geometry and the peak pressure. Finally, we demonstrate the consistency and reproducibility of hydraulic fracturing behavior in the Bromide formation sand.

4.3.1. Fracture geometry and deformation features

Currently, the absolute majority of hydraulic fracture models assume simple, planar, fractures that are symmetrical relative to the wellbore. Some notable exceptions are based on speculations on possible fracture geometry [*Wu,* 2006; *Germanovich et al.,* 1997a, 1997b]. In our experiments in the Bromide formation sand, we found that the fractures are more complex with multiple wings that are rarely symmetrical relative to the wellbore. The images in **Figures 4.12** and **4.13** illustrate the typical hydraulic fracture geometries and morphologies obtained in our experiments in the Bromide formation sand. The fractures in the Bromide formation sand showed features evidencing cavity expansion, branching, asymmetrical wings, as well as fluid leakoff. The orientation of the fractures was primarily vertical and perpendicular to the direction of the minimum horizontal confining stress. This is consistent with a fracture opening in a direction subparallel to the minimum principal stress direction and propagating in a direction along the intermediate principal stress direction. The geometries were generally quasi-planar with a dominant main fracture with two main wings, plus offshoots and several branches or multiple segments within each wing. In our experiments, the fluid driven fractures mostly exhibited a quasi-penny-shaped geometry, although this probably was a limitation of our experimental setup and the sample size.

It appears that the fracture offshoots formed mostly close to the injection source, but that these offshoots also form along the length of the main fracture further away from the borehole. The offshoots were generally orientated at acute angles to the fracture tip propagation direction. It appears the offshoots near the injection source were oriented at larger angles relative to the main fracture compared to those in the far-field. This may have been related to the injection flow rate as discussed later in this section.

There are several possible causes of fracture branching and segmentation in our tests. These include (1) sample heterogeneity, (2) stress-field heterogeneity, and (3) generic instability of the fracture process zone.

Evidence of cavity expansion around the borehole was clearly seen in several of our experiments. Tests with the lowest injection flow rates showed the best evidence of cavity

expansion. **Figure 4.14** shows evidence of cavity expansion. The emanation of multiple offshoots from the injection source area suggests that cavity expansion persisted even after initiation of the main fracture.

In most of our tests, it was found that the wings of the fractures were asymmetrical relative to the position of the borehole. In experiments both in natural sand and in synthetic sand, we observed several instances in which one wing of the fracture was much longer than the other wing measured in the horizontal direction. On average, the asymmetry ratio (length of the short fracture wing divided by the length of the long fracture wing) ranged from approximately 0.43 to 0.88 in the Bromide formation sand tests. Some asymmetry ratios are presented in Table 4.4 for some selected tests. Although the significance of asymmetrical fractures has not been fully recognized in design applications, *Tiab et al.* [2010] reports that it may be a more realistic outcome of hydraulic fracturing. Currently, most hydraulic fracture models assume that fractures are initiated and propagated identically and symmetrically about the wellbore. *Warpinski et al.,* [1998a] demonstrated the asymmetrical nature of hydraulic fractures by using micro-seismic monitoring techniques. Other workers have also reported asymmetric fractures from field studies [e.g., *Kochnev et al*., 2007; *Fischer et al*., 2008]. Our findings of asymmetrical fractures is significant as the asymmetry is directly observed in a natural particulate material.

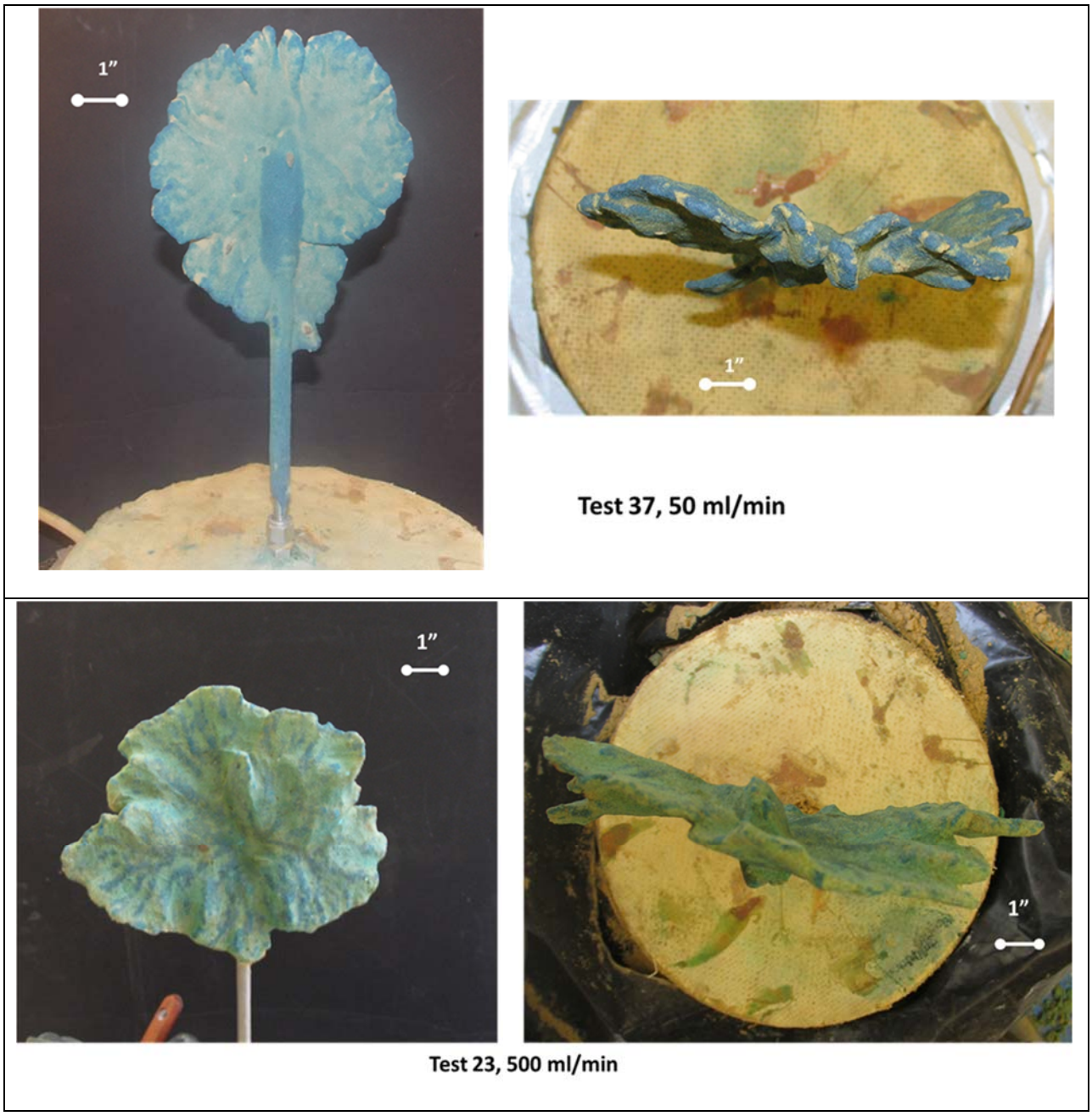

Figure 4.12: Fractures observed in tests 23 and 37 with Bromide formation sand under different flow rates of 50 ml/min and 500 ml/min, respectively. Fractures from these two tests are presented showing the front and top views.

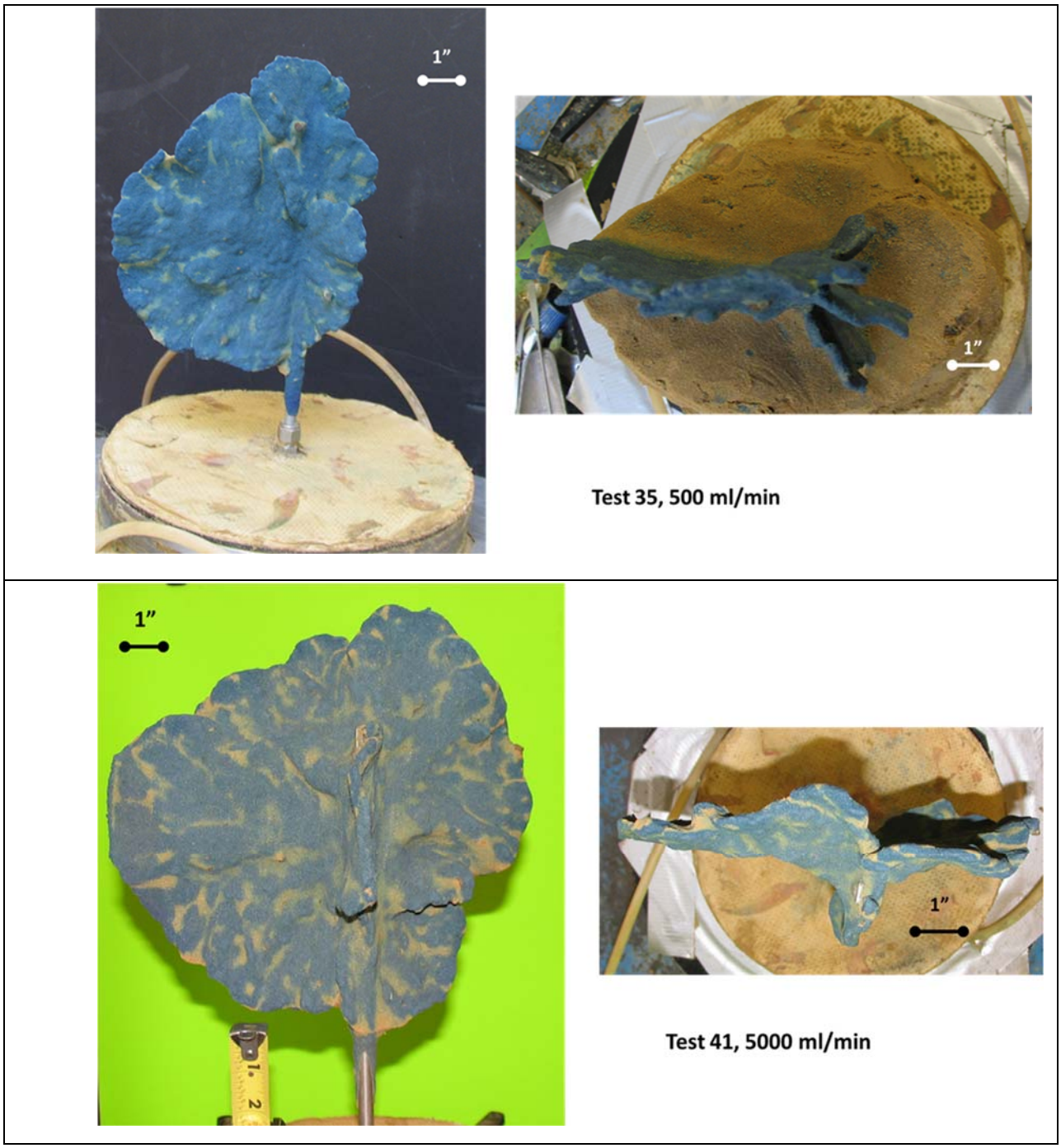

Figure 4.13: Fractures observed in tests 35 and 41 with Bromide formation sand under different flow rates of 500 ml/min and 5000 ml/min, respectively. Fractures from these two tests are presented showing the front and top views. Offshoots near the injection source and throughout length of fracture. An offshoot wing at ≈ 90 degrees to the main fracture propagation direction was observed for tests at higher injection flow rates.

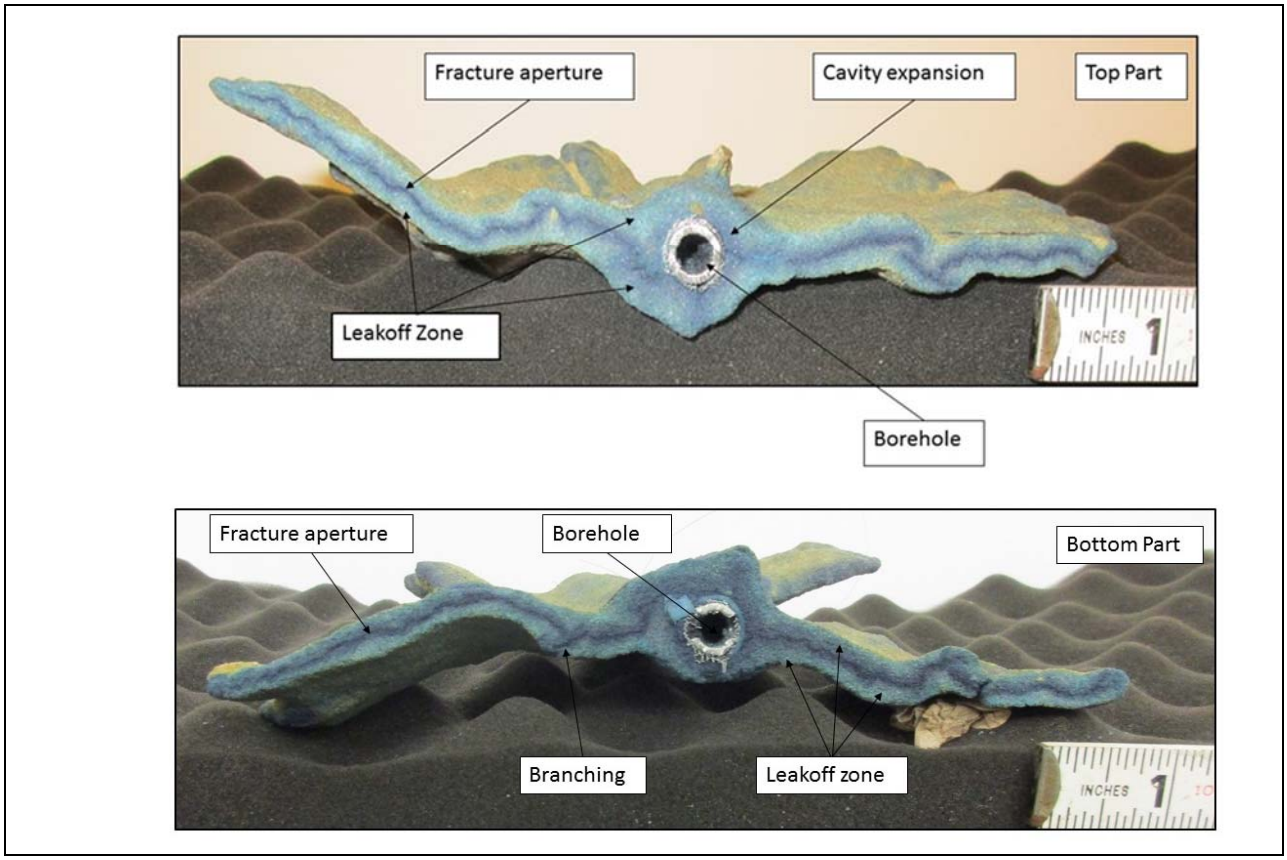

Figure 4.14: Cross section images from test 37 illustrating evidence of branching and cavity expansion near injection source. Fracture wings appear to be less asymmetrical at lower injection flow rates than at higher flow rates. Fracture placed on felt cushion in order to hold it in a horizontal direction.

Table 4.6: Asymmetry ratios for three selected tests in the Bromide formation sand.

Test number	**37**	**23**	**41**
Asymmetry Ratio	0.88	0.80	0.75
Injection flow rate (ml/min)	50	500	5000

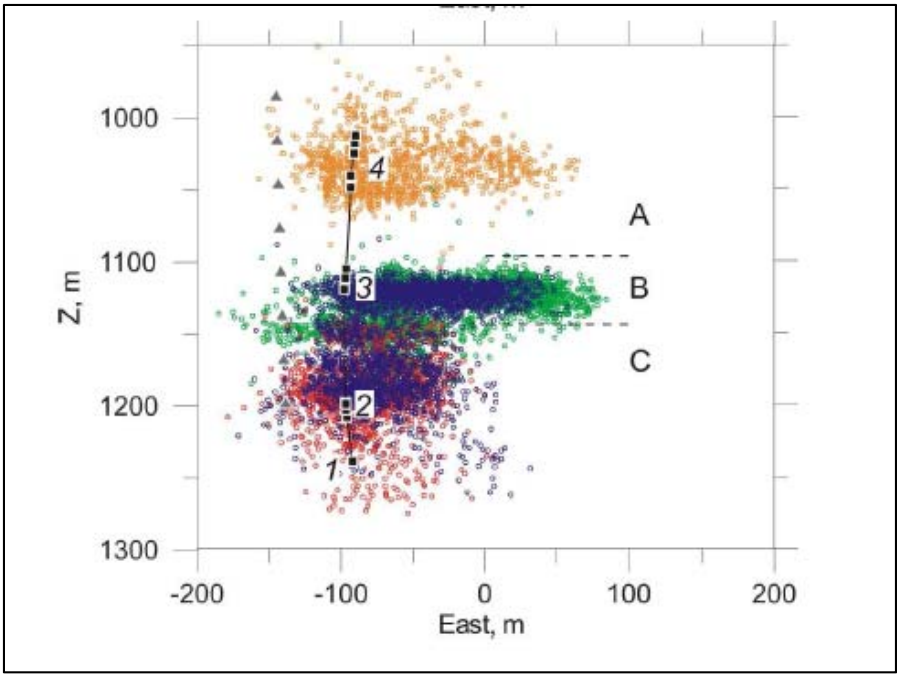

Figure 4.15: Microseismicity monitoring of hydraulic fracturing in the Canyon Sands formation in western Texas [*Fischer et al.,* 2009]. Different colors indicate events at different injection stages (1, 2, 3, and 4) stimulated from injection points indicated by black rectangles. Fracture asymmetry can clearly be seen in formation layers A and B.

4.3.2. Injection pressure signature

Hydraulic fracture initiation pressure is an important parameter, for example, in hydraulic fracturing stimulation of petroleum wells or frack and pack treatments for sand control. Pressure signature prediction is also of interest in situations where fracturing is undesirable, such as drilling or tunneling. The typical injection pressure for tests performed in the Bromide formation sand is shown in **Figure 4.16**. The steep linear rise in the injection pressure, followed by a sharp drop after the peak value, is consistent with hydraulic fracture initiation. After the sharp drop, the pressure curve flattens out until there is a gradual drop in pressure after the pump is stopped. The initial steep rise of the pressure curve probably represents the cavity expansion stage, while the peak pressure is related to the point of fracture initiation or breakdown. The next part of the pressure curve represents the fracture propagation pressure (see **Figure 4.16**) while the magnitude of the pressure drop from the propagation pressure to the final flattening of the pressure curve, after the pump is stopped, represents the fracture closure pressure. As shown in **Table 4.5,** the peak pressures and propagation pressures in our experiments were consistently greater than both the horizontal confining stresses and the vertical loads. On average, the initiation pressure was larger than the confining stress by a factor of 3.1. This finding is consistent with what other workers have found in fracture studies in man-made particulate media [e.g., *Hurt,* 2012; *DePater and Dong,* 2007]. In **Figure 4.17**, four curves from four tests conducted under the same conditions in the Bromide formation sand are shown for comparison. These plots suggest that the test results are relatively consistent and repeatable.

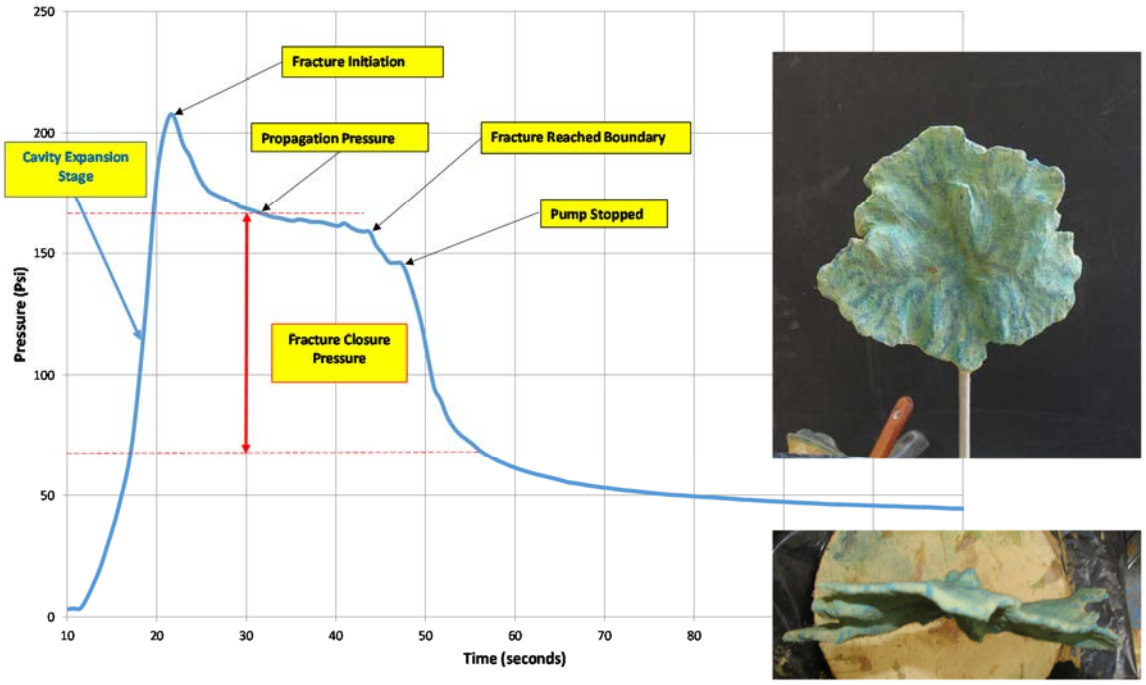

Figure 4.16: Injection pressure for hydraulic fracturing in Bromide formation sand (test 23).

Table 4.7: Summary of the peak injection pressures for 6 typical tests in Bromide formation sand.

Test Number	**23**	**30**	**32**	**35**	**36**	**41**	**Average**
Peak pressure (psi)	209	278	215	258	322	210	249
Peak pressure/σ_c	2.6	3.5	2.7	3.2	4.0	2.6	3.1
Propagation pressure (psi)	175	224	200	197	N/A	230	199
Pressure drop after peak (psi)	26	38	20	44	N/A	N/A	32
Closure Pressure (psi)	92	83	85	85	N/A	90	86

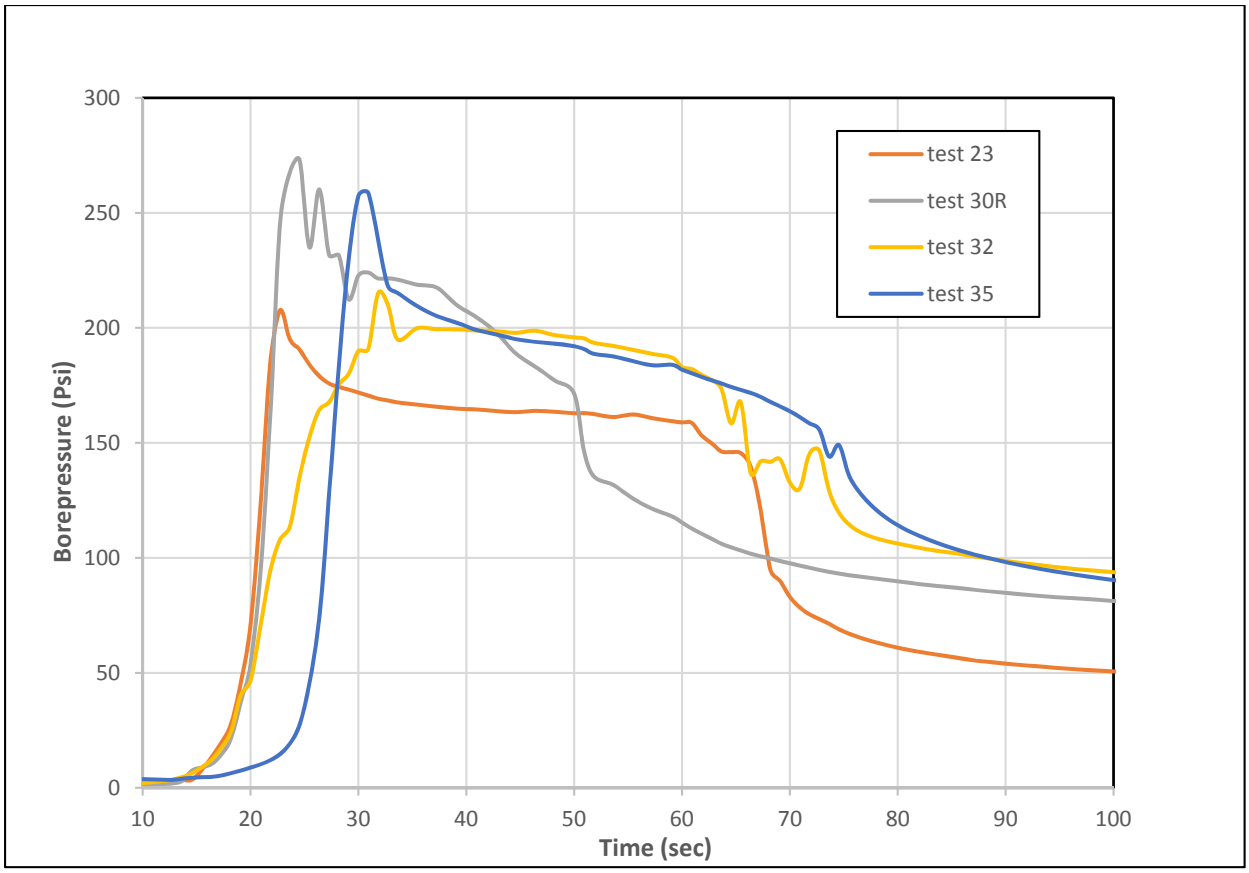

Figure 4.17: Injection pressure curves from four tests conducted under the same conditions in the Bromide formation sand.

4.3.3. Effect of injection flow rate on initiation pressure and fracture-geometry

Another important result of this study is the flow rate dependency of pressure behavior during the fracturing experiments with Bromide formation sand. Several tests were performed in the Bromide formation sand in which all other parameters were held constant while varying the flow rates and observing the resulting pressure behavior. The effect of the flow rate on the peak pressure over three orders of magnitude was examined. **Figure 4.18** demonstrates the typical results using three of these tests. Our experiments show that there is a significant increase in peak pressure with increase in the injection flow rate. This conclusion is consistent with results from laboratory hydraulic fracturing tests in salt conducted by other researchers showing flow rate dependency of pressure behavior as shown in the **Figure 4.19** [*Doe and Boyce,* 1989]. However, it should be noted that the mechanical properties of salt differ significantly from those of materials used in our experiments. In *Hurt* [2012] page 140, it was reported that fluid flow

rates showed no quantifiable effects on injection pressures. However, *Hurt* [2012] performed most of his experiments using high viscosity silicon as the fracturing fluid while our experiments were conducted using industrial guar fluids.

We also observed that there was a pattern in the geometry of the hydraulic fracture with the change in fluid flow rates. This pattern can be summarized as follows. At low flow rates (50 ml/min in our experiments), the fractures are strongly orientated in one plane with pairs of wings extending on opposite sides of the borehole. These wings on opposite sides of the borehole also appear to be more symmetrical in size at low flow rates. As the flow rate increases by an order of magnitude (to 500 ml/min), offshoot wings begin to form near the borehole and throughout the length of the fracture wings. Also, the offshoot wings are inclined at an acute angle to the main fracture. These offshoot wings are also much shorter in length than the main fracture wings. For high flow rates (about 5000 ml/min), these offshoot wings are almost perpendicular to the direction of the main fracture. In our experiments, minimum and maximum horizontal stresses are the same. The offshoot wing angle may be controlled by their difference in other conditions, which requires further testing (see also Chapter 5). The offshoot wing initiation may be affected by local stress changes caused by the previously initiated wings.

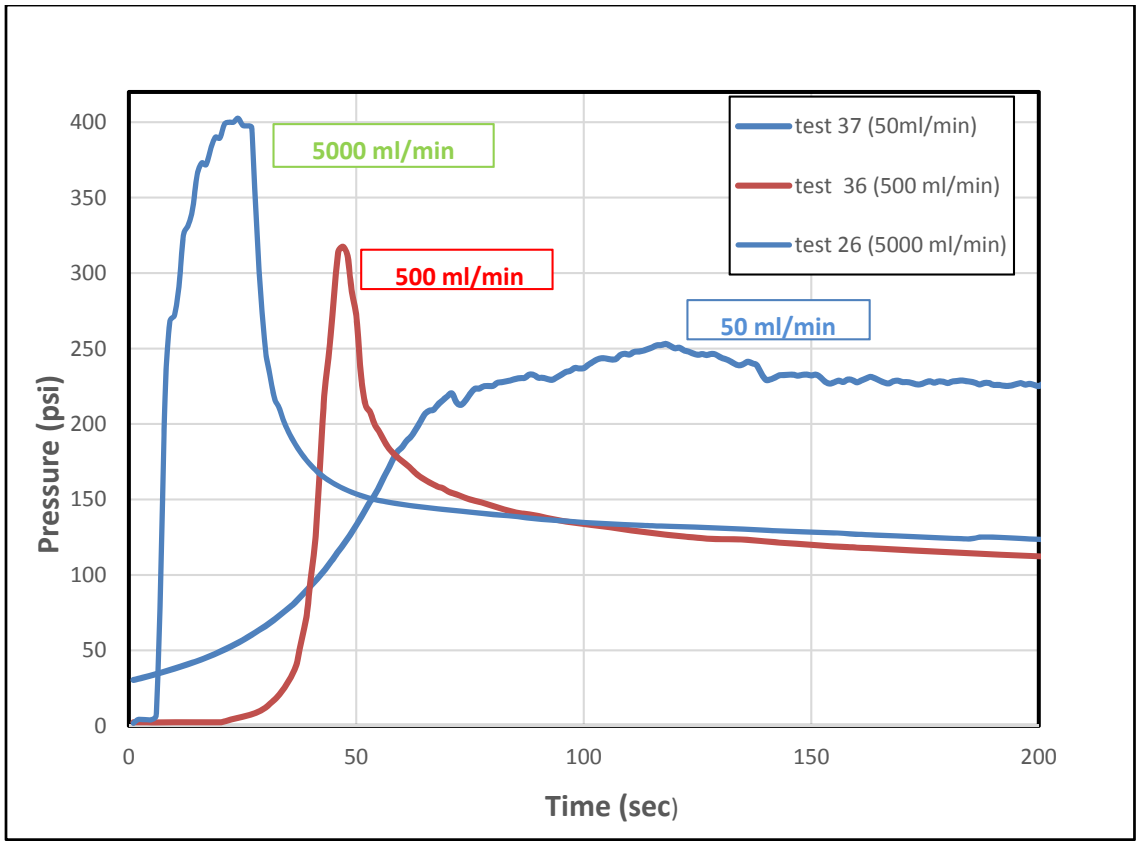

Figure 4.18: Pressure-time curves in Bromide formation sand showing flow rate dependency of pressure behavior in tests 26, 36, and 37.

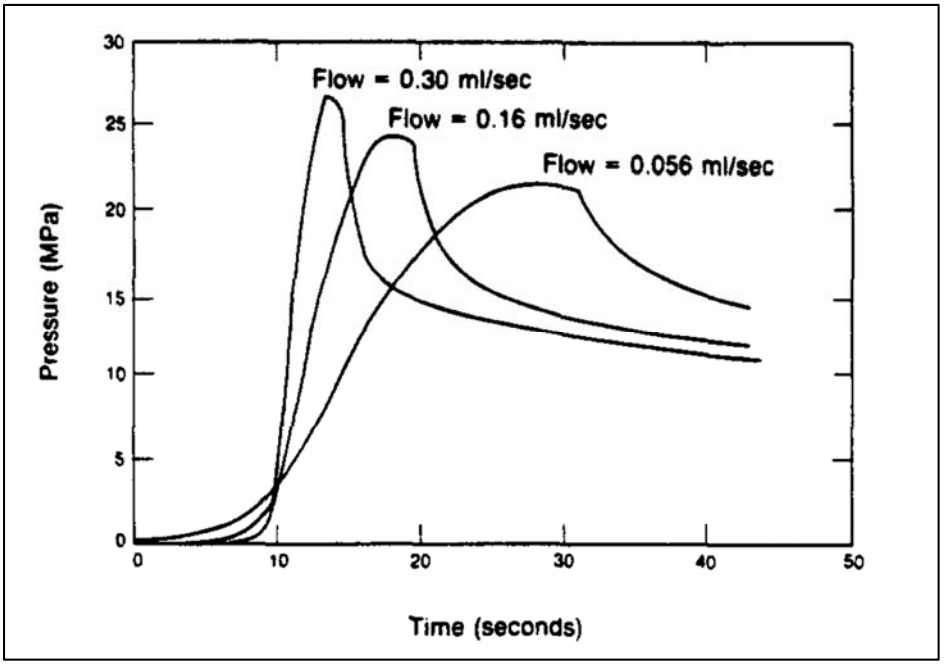

Figure 4.19: Pressure-time records for a lab hydraulic fracturing test in salt showing flow rate effect on pressure behavior [*Doe and Boyce,* 1989].

4.3.4. Experimental consistency and repeatability

A minimum of three experiments were conducted under the same conditions. For each experiment that is presented in this section, there are at least two other experiments that were conducted under the same conditions to support the finding. For example, in **Figure 4.17**, four plots from four experiments (23, 30, 32, and 35) are presented and demonstrate consistency and reproducibility. Based on this approach, our test results demonstrate that our findings on the hydraulic fracturing pressure signatures, on the fracture geometry and morphology, on the effect of injection flow rate on peak pressure and fracture geometry, and on the fracture asymmetric wings are consistent and reproducible.

4.4. EXPERIMENTS IN SYNTHETIC MATERIALS

4.4.1. Silica Flour

Experiments were performed in silica flour SIL-CO-SIL 106 in order to calibrate the experimental techniques in this work with those of previous researchers. Silica flour was difficult to saturate as this process took excessive amounts of time in our laboratory setup. Therefore, all our experiments in silica flour were performed under dry sample conditions. Tests in silica flour were performed under horizontal confining stresses ranging from 10 psi to 80 psi. The fluid injection flow rate was 500 ml/min for most of the tests and the guar industrial fracturing fluid described in Section 4.2.2 was used as the injection fluid. **Figures 4.20, 4.21, 4.22 and 4.23** show the typical results of our tests in silica flour. The fractures in the silica flour samples where thin, demonstrating that the fluid leakoff was low owing to the low permeability of the sample. The fractures were also typically petal-like and, in some cases, had multiple wings. This was consistent with observations made by *Chang* [2004], *Germanovich and Hurt* [2012], and *Hurt* [2012]. Fractures were vertical and perpendicular to the minimum horizontal stress. On each wing, multiple segments were evident.

The ratio of the peak pressure to the horizontal confining stress ranged from approximately 4 to 12. This ratio was much higher than that in the Bromide formation sands, the Ottawa sand F110 and the Ottawa sand USM100. This difference may be attributed to the

differences in permeability, particle sizes, low confining stress conditions, and particle shapes (or combinations of all these). We also conducted experiments to investigate the sensitivity of the peak pressure to the confining stresses. All parameters were held constant, except the confining stresses, which were varied from 10 psi to 80 psi. The ratio of the applied vertical stress to horizontal confining stress was held constant at 2 to 1. Our results are shown in **Figure 4.22**. We conclude that the peak pressure increases with increasing confining stress.

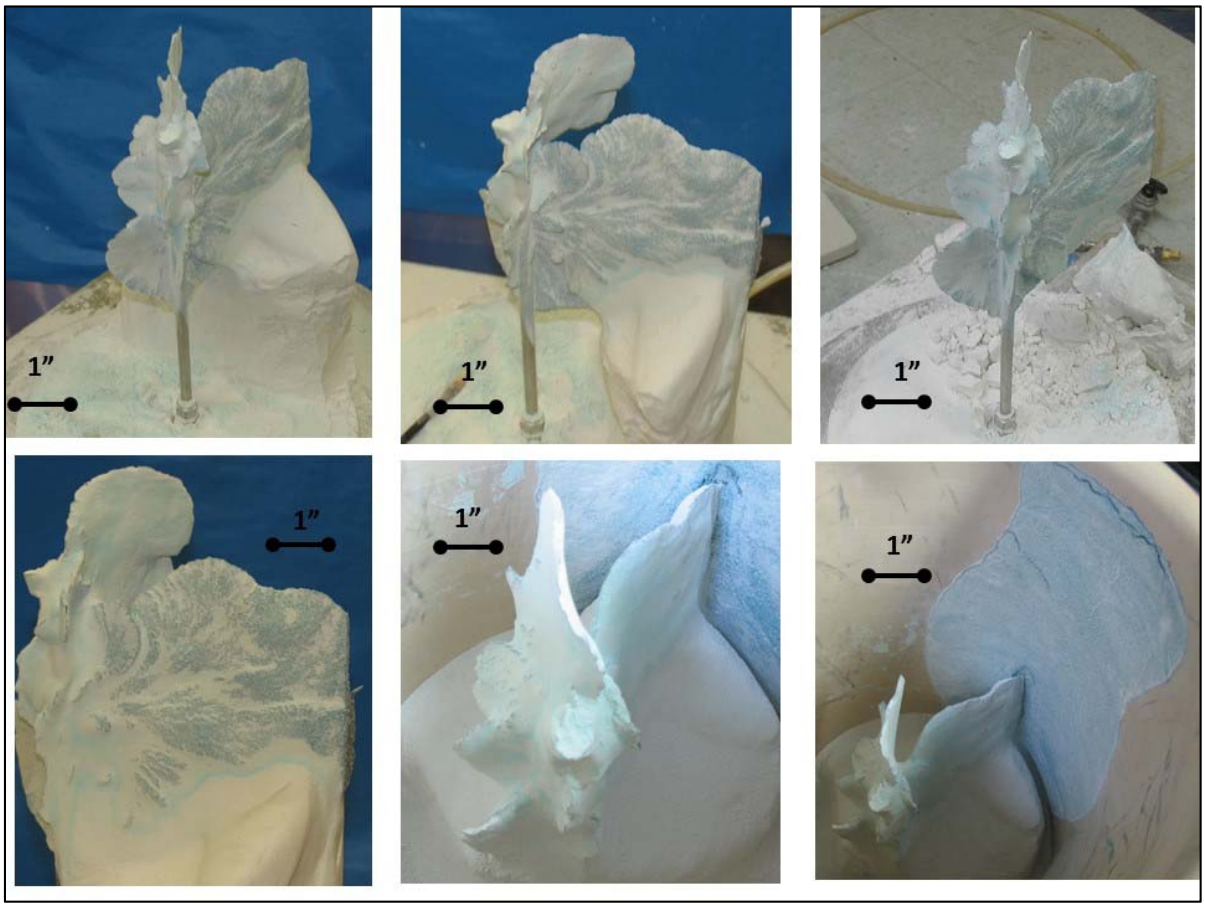

Figure 4.20: Images from test 1, showing thin, multi-winged petal-like fractures in Silica flour material.

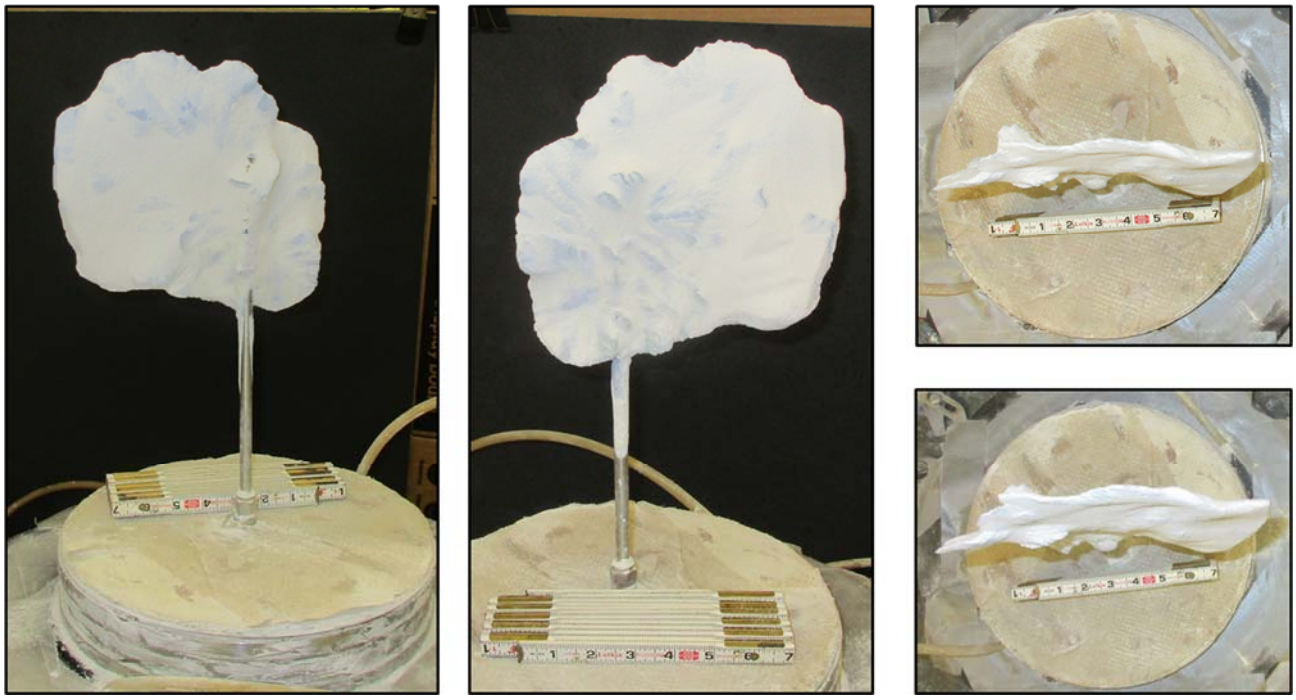

Figure 4.21: Images showing fracture geometry of test 46, conducted in dry Silica flour sample.

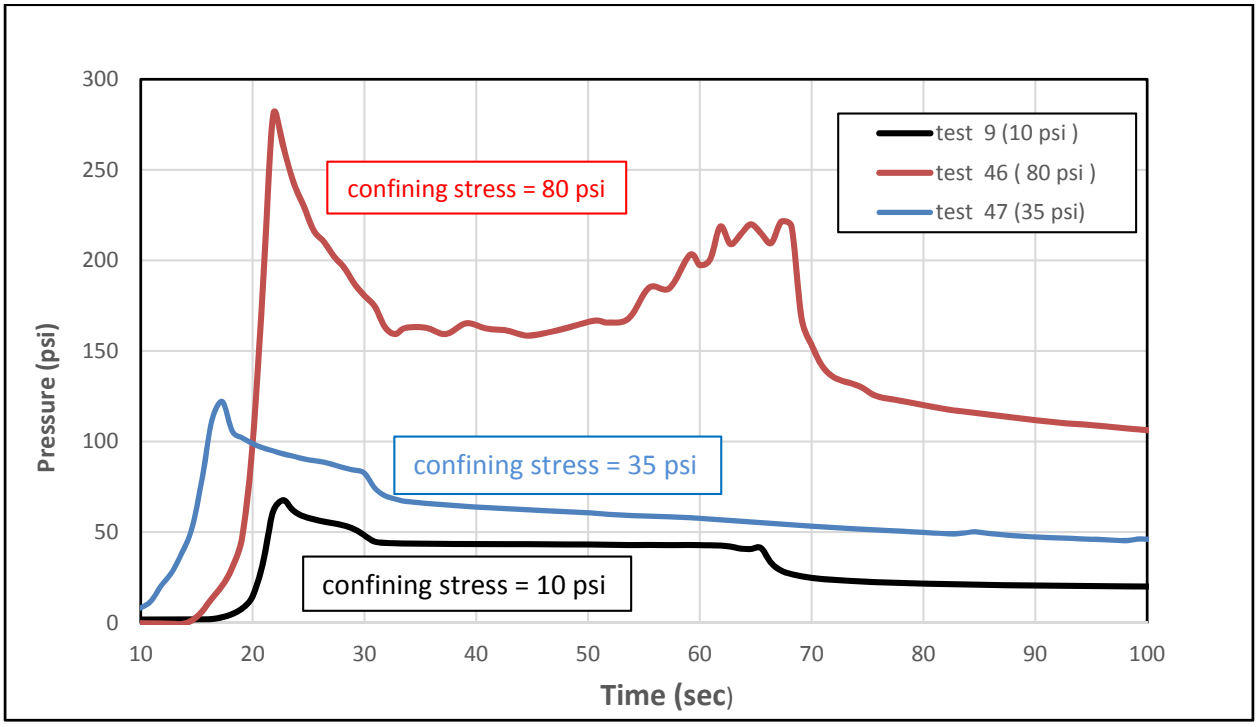

Figure 4.22: Plots showing sensitivity of peak pressure to confining stress in Silica flour tests. There is a clear increase in pressure with increasing confining stress.

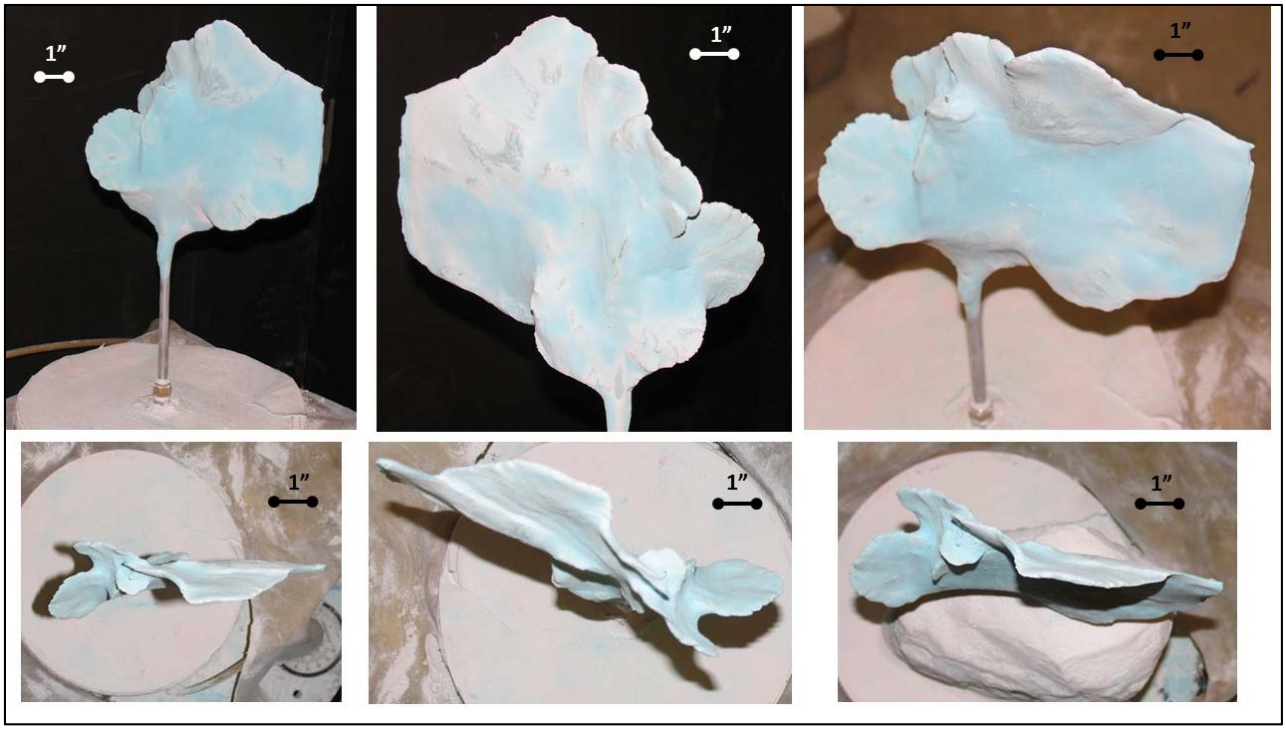

Figure 4.23: Test 9 images, showing typical fracture morphology in silica flour samples.

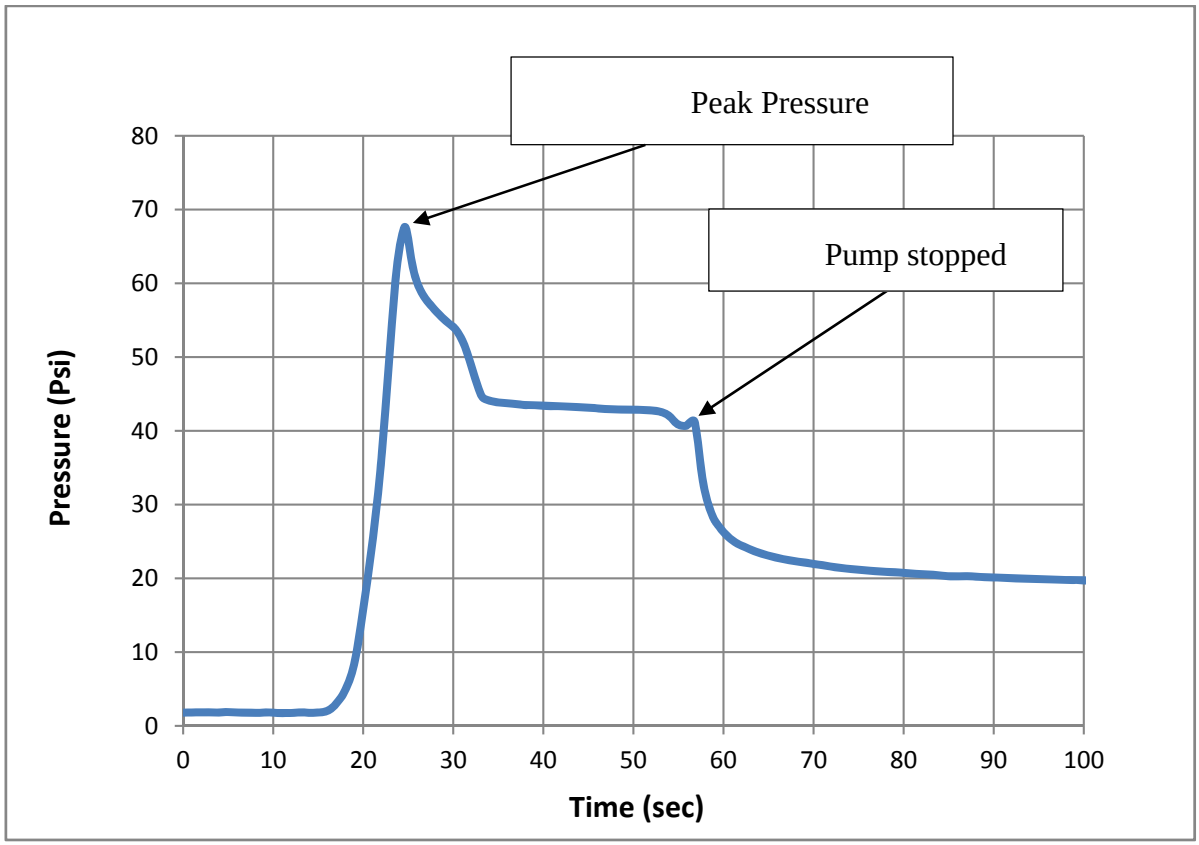

Figure 4.24: Injection pressure for silica flour fracturing.

4.4.2. Ottawa fine sand (F110 and USM100)

Over ten tests were conducted in Ottawa fine sands F110 and USM100. Three of these tests are presented in this section. The main objective of these tests was to compare and contrast the fracture behavior between these synthetic sands and the fracture behavior in natural sands obtained from an oil production well. **Table 4.6** presents the general conditions under which experiments in Ottawa fine sands F110 and USM100 were conducted. Samples were prepared by rodding and saturation as described in Section 4.2.3. All tests were conducted using a cross-linked guar gel as the fracturing fluid (Section 4.2.2).

The geometries of the resulting fracture were generally planer (compared to the fractures in silica flour) with multiple offshoots. The fractures were also nearly vertical and propagated subparallel to the direction of the maximum horizontal stress (equal to the minimum confining horizontal stress in our case). The fractures mostly exhibited a penny-shaped, fluid driven, radial model. Evidence of plastic deformation features, such as cavity expansion and shear bands (see Chapter 5), was observed. These features were better preserved in tests conducted at lower injection flow rates. The fracture aperture and the leakoff thickness were larger in experiments conducted in pure Ottawa fine sand than in other sample materials used in this experimental series. The leakoff in the pure Ottawa fine sand experiments correlates with the permeability of these samples. Therefore, these tests confirmed that the amount of leakoff into a formation increases with an increase in the permeability of the formation. **Figure 4.25**, shows images of features in typical experiments conducted in F110 and USM100. **Figure 4.27**, shows the leakoff zone of typical fractures in Ottawa fine sand being thick.

Table 4.8: Test conditions for experimental series for Ottawa fine sand samples.

Number of experiments	10
Saturation of material	95 %
Injection source	Cylindrical
Pore pressure conditions	Drained
Fracturing fluid	Cross-linked guar gel (Power-law fluid)
Injection flow rates	50 ml/min, 500 ml/min, 1000 ml/min
Fluid injection volumes	300 ml, 350 ml, 400 ml
Mean particle size	180 µm
Permeability	1.8 D
Loads	160 psi, 80 psi

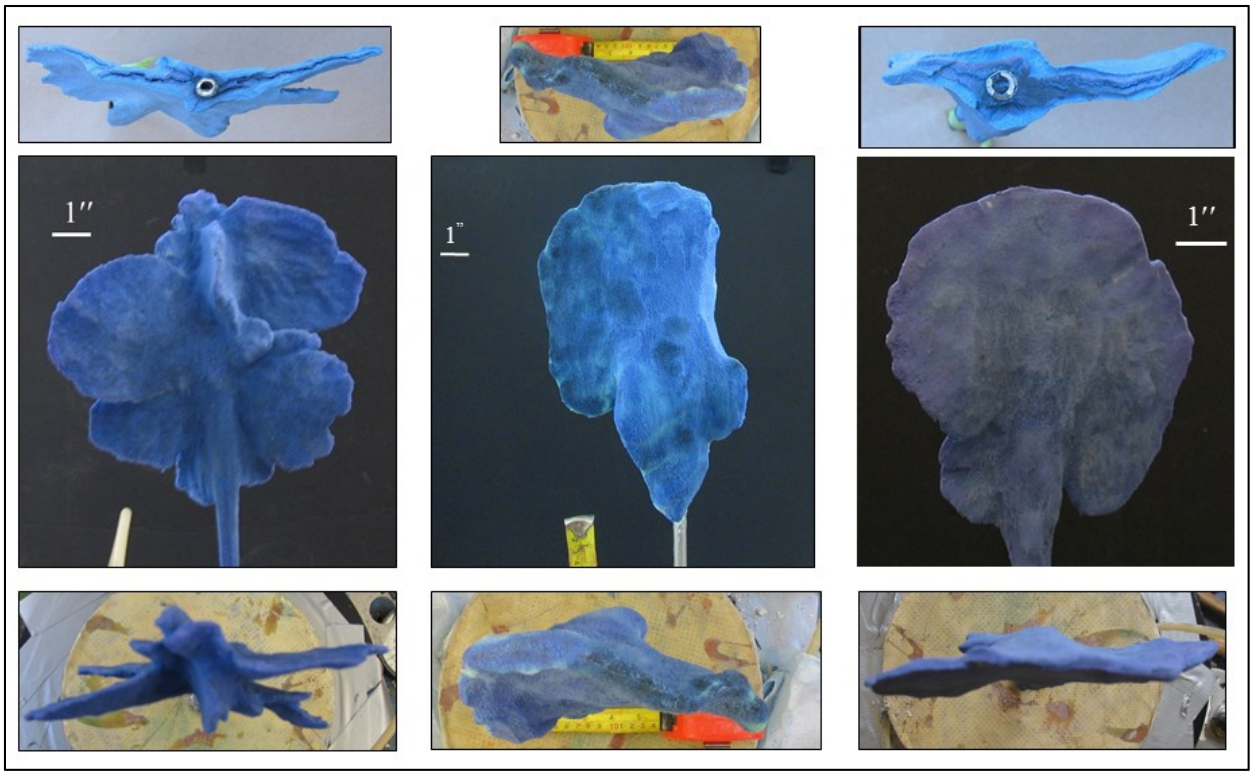

Figure 4.25: Fractures observed in tests 29, 44, and 33 with Ottawa fine sand. Fractures from three tests are presented showing a sectioned view, the front view and the top view.

The results of test number 44 are presented in **Figure 4.27**. In this test, the peak pressure was approximately 320 psi. This represented a peak pressure to confining stress ratio of approximately 4 to 1, which was typical for tests in Ottawa fine sand F110 and USM100. It was observed that the drop from peak pressure after initiation to propagation pressure was not sharp, but gradual. From this observation, it appears that the propagation of the fracture front was steady and not explosive. This may be a signature of the interplay between the fracture front and the grain to grain interaction ahead of the fracture front. Another possible explanation for this behavior could be the interaction between the fracture front and the leakoff behavior in the highly permeable regions ahead of the fracture front. **Figure 4.29** shows three plots from three experiments in Ottawa fine sands to illustrate the consistency in pressure signatures in these materials.

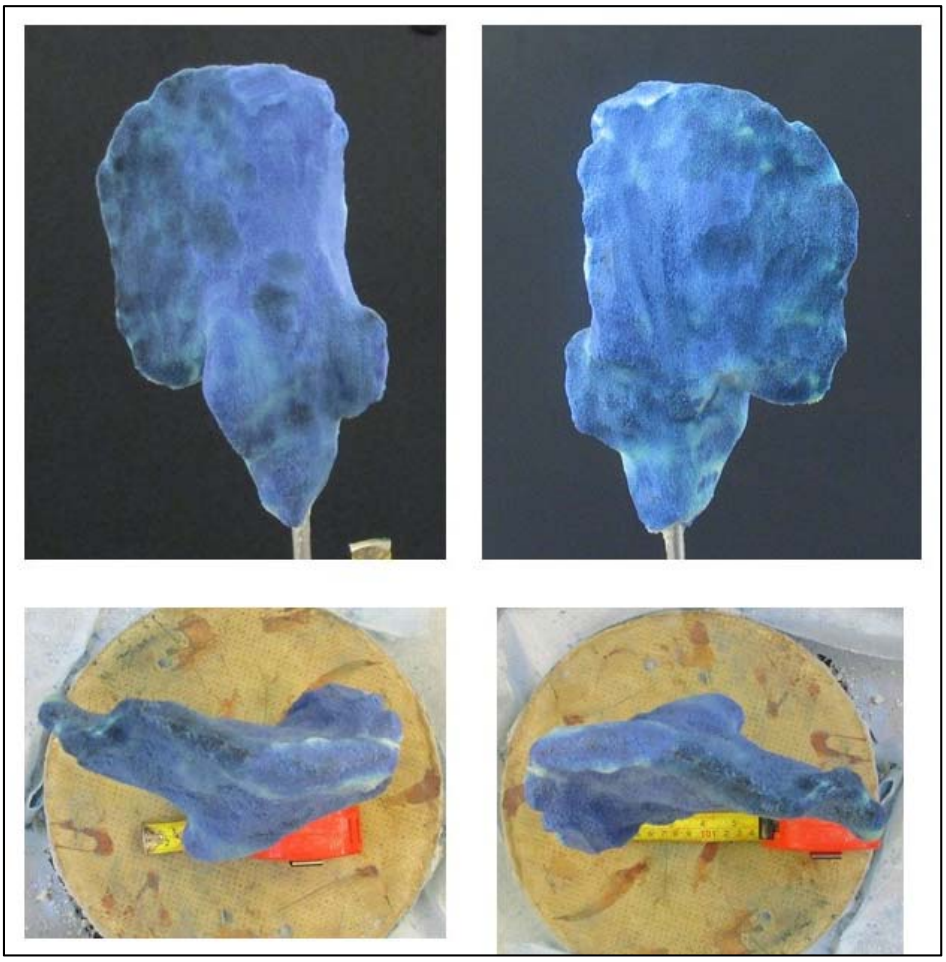

Figure 4.26: Images from test 44 conducted in USM100, showing front view on top left, rear view on top right and top views for each showing a thick leakoff geometry.

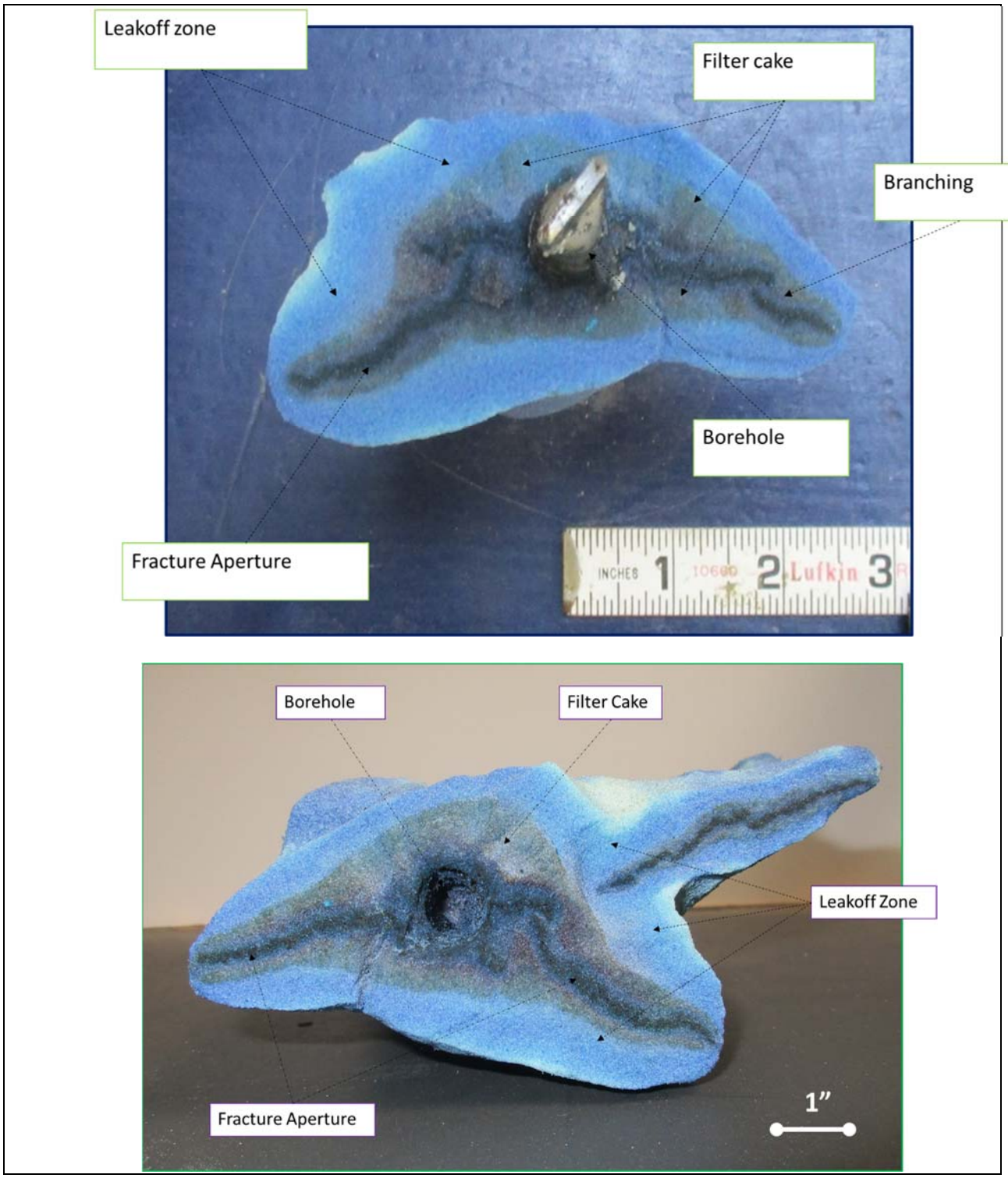

Figure 4.27: Cross sectioned images from test 44 conducted in USM100 fine sand. Different zones of fracture morphology clearly shown.

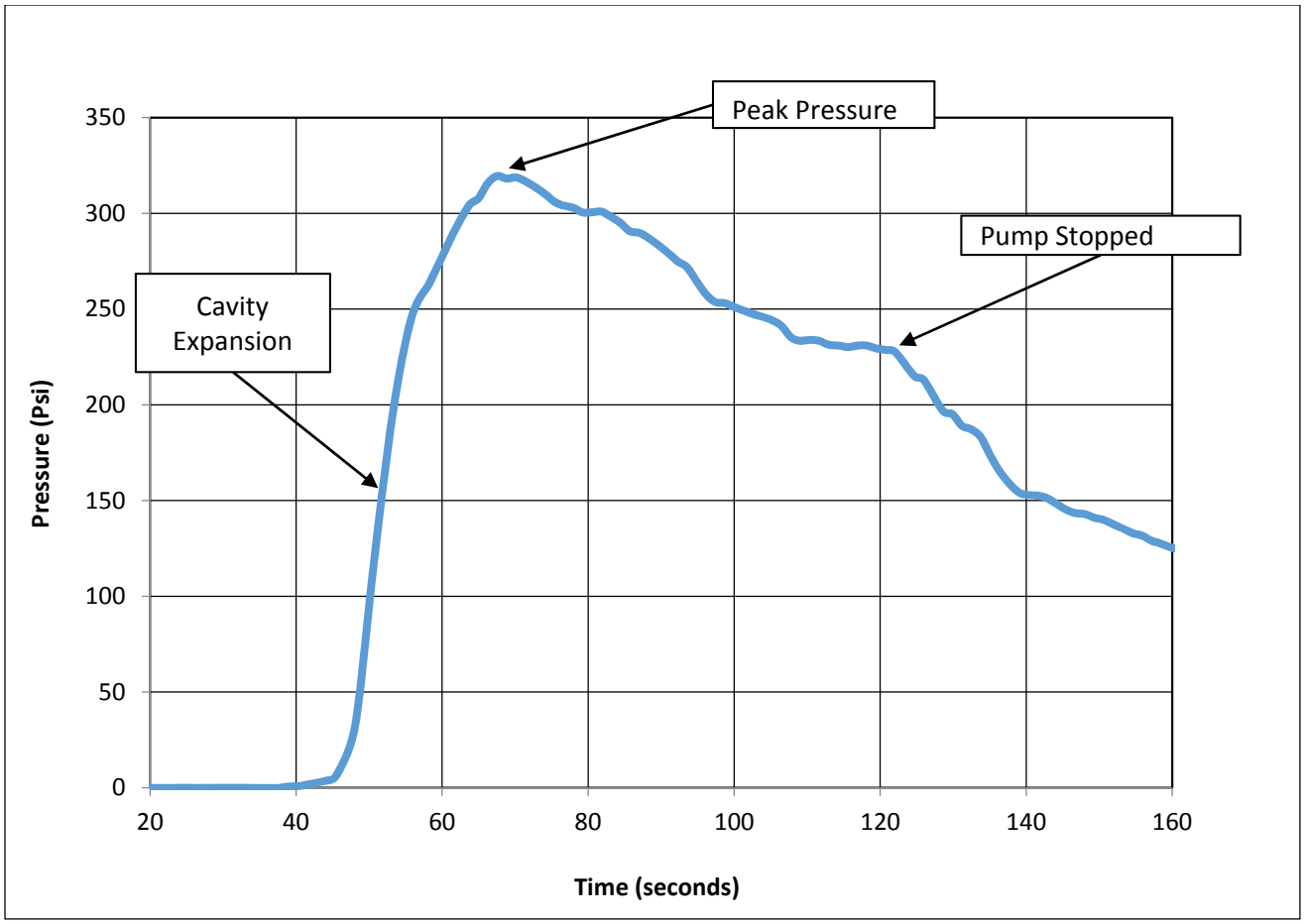

Figure 4.28: Injection pressure signature for test 44 in Ottawa fine sand.

Table 4.9: Summary of the peak injection pressures for 6 typical tests in Ottawa fine sands F110 and USM100. All tests were conducted at confining stresses of 80 psi and vertical stresses of 160 psi.

Test Number	**24**	**27**	**28**	**29**	**33**	**44**	**Average**
Peak pressure (psi)	247	210	325	318	308	320	288
Peak pressure/σ_c	3.1	2.6	4.1	4.0	3.9	4.0	3.6
Propagation pressure (psi)	231	122	300	200	250.0	235	223
Pressure drop after peak (psi)	16	88	25	118	58	85	65
Closure pressure (psi)	110	40	175	40	150	105	103

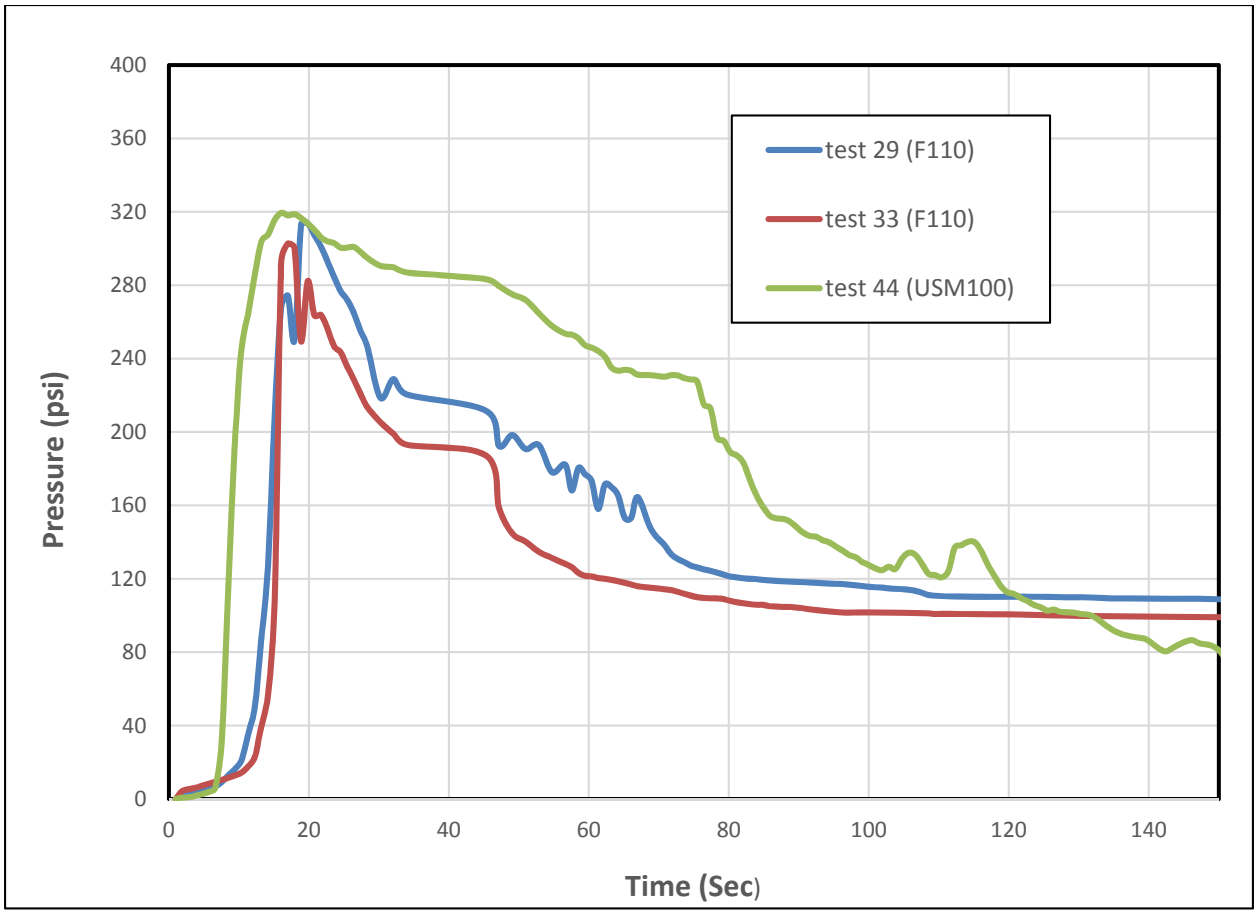

Figure 4.29: Injection pressures from three tests conducted under the same conditions in Ottawa fine sands F110 and USM100.

4.4.3. Mixtures

Experiments were also performed in sample mixtures comprising of 20 % silica flour and 80 % USM100 or F110 sand. The results from these tests were then compared between themselves and to those from natural sands from the Bromide formation (Section 4.22). Table 4.8 shows the number of experiments and the test conditions under which this series of experiments was performed.

Figure 4.30 shows images from representative experiments conducted in a mixture sample. In test 15, a red coloring agent was used in the fracturing fluid while for test 45, a blue coloring agent was used. As can be seen in **Figure 4.30**, the fracturing fluid reached the boundary during both tests. The peak pressure or initiation pressure was approximately 440 psi in test 15,

while it was 320 psi in test 45. The fractures were vertical, planar and had multiple segments. The wings of the main fracture were asymmetrical relative to the borehole.

Table 4.10: Test conditions for experimental series for mixture samples.

Number of experiments	5
Saturation of material	95 %
Injection source	Cylindrical
Pore pressure conditions	Drained
Fracturing fluid	Cross-linked guar gel (Power-law fluid)
Injection flow rates	50 ml/min, 500 ml/min, 1000 ml/min
Fluid injection volumes	300 ml, 350 ml, 400 ml
Mean particle size	80 µm
Permeability	200 mD
Loads	160 psi, 80 psi

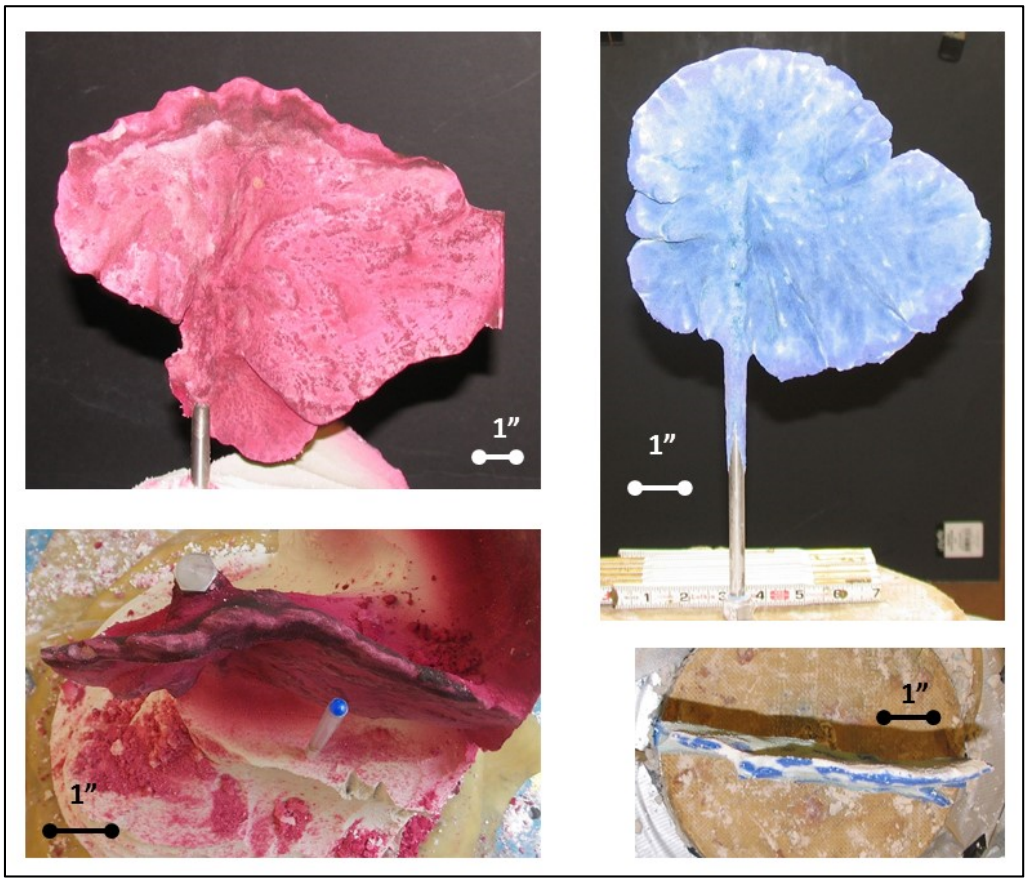

Figure 4.30: Typical fracture morphology for tests in 20% silica flour and 80% USM100 mixture materials. Front and top views from tests 15 and 45 are presented.

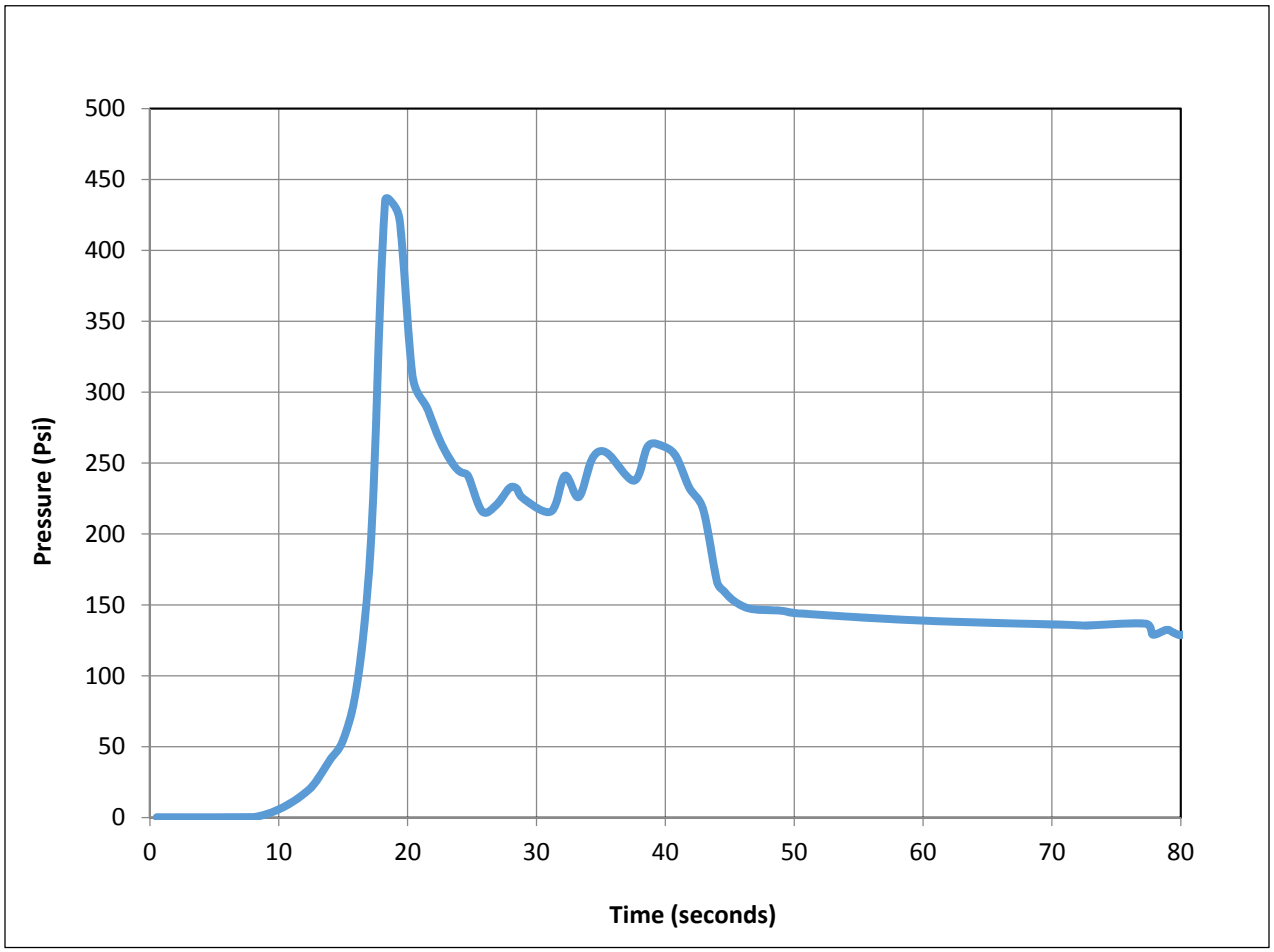

Figure 4.31: Injection pressure in test 15.

In **Figure 4.31**, there is a pressure rise of 52 psi/sec during the cavity expansion stage of the fracturing process. Fracture initiation occurs at a peak pressure of 435 Psi. This is followed by a sharp injection pressure drop before the fracture begins to propagate at a pressure of approximately 240 psi. The injection pump is stopped at the 40 s mark. After this the fracture closes and there is a pressure drop of approximately 100 psi. This is called the closure pressure. Both the fracture geometry and the injection pressure signatures are consistent with a fracture that opens in a direction parallel to the minimum principal stress and propagates in a direction parallel to the intermediate principal stress (minimum principal stress and intermediate principal stress are equal for our case). **Table 4.11** presents a summary of injection pressures for four tests conducted in 20% silica flour/80% Ottawa F110 or USM100 fine sand.

Table 4.11: Summary of injection pressures for 4 typical tests in the sand and silica flour mixtures (20% of silica flour and 80% of Ottawa F110 or USM100 fine sand). All tests were conducted at confining stresses of 80 psi and vertical stresses of 160 psi.

Test Number	15	39	40	45	Average
Peak pressure (psi)	435	195	236	302	292
Peak pressure/σ_c	5.4	2.4	3.0	3.8	4
Propagation pressure (psi)	225	180	226	175	202
Pressure drop after peak (psi)	210	15	10	127	91
Closure pressure (psi)	100	45	84	84	78

4.5. DISCUSSION

We compared the fracture geometries, pressure signatures, and fracture initiation pressure dependency on injection flow rates of experiments in the natural Bromide formation sands to those conducted in the synthetic particulate materials. Comparisons exclude tests in silica flour as these tests were conducted mostly for preparation and calibration of experimental techniques. Our overall finding was that hydraulic fracture behavior in the Bromide formation sand, in terms of the above stated properties, is comparable to that in the synthetic sands used in this work. The comparisons are discussed in detail below.

In both the synthetic sands and the natural sands, the fractures were vertical, quasi-planar and perpendicular to the minimum principal confining stresses. Results from tests in both materials evidenced fracture geometries with asymmetrical wings relative to the location of the injection source. Also, in both synthetic and natural materials, the fractures geometries were complex with multi-segmented fracture wings with branching offshoots near the injection source and in the far-field. **Figures 4.12**, **4.13**, and **4.25** illustrate these observations. However, the thickness of the leakoff zone was a function of the permeability of the material and therefore varied within our spectrum of materials. Due to the laboratory limitations in the measurement of the fracture aperture, it was not possible to make a determination as to whether fracture aperture follows the same trends as the leakoff zones relative to the material permeability.

Figure 4.32 illustrates some key findings of pressure signature comparisons. The fracture pressure behavior appears to be generally the same in both types of materials. In hydraulic fracturing experiments in both natural sands and in synthetic sands, there is a sharp linear rise in injection pressure at the beginning of fluid injection, then there is a drop in pressure after fracture initiation followed by a flattening down of the pressure curve as the fracture propagates away from the borehole and finally another drop in pressure when pumping is stopped (due to fracture closure). However, we also found that the injection pressures in Ottawa F110 and USM100 sands (including peak pressures) were slightly higher than those in the natural sands. We attribute this slight difference in pressure magnitudes to the differences in grain particle shape between natural sands and man-made sands. Bromide formation sand particles are generally well rounded while F110 and USM100 grain particles are sub-rounded to sub-angular (see **Figure 4.6**). *Holtz and Gibbs* [1956] observed that angular quarry materials have much higher shear strength than sub-rounded river materials. According to *Holubec* and *D'Appolonia* [1973] angularity of the particles increases the maximum void ratio, strength, and deformability of cohesionless soils. This suggests that the use of synthetic sands to simulate reservoir formation sands in laboratory experimental modelling may be improved by engineering their grain particle shape to match that of the natural reservoir material under investigation. Table 4.9 illustrates the differences in the mechanical properties of the materials used for tests in our research.

Table 4.12: Comparison of mechanical properties and peak pressures from various materials used in triaxial experiments.

	P_{peak} (*psi*)	*k* (*darcy*)	$\frac{P}{\sigma_c}$	Mean particle size (μm)	Particle shape
Silica flour	120	0.02	1.5	19	Angular
Bromide formation sand	250	3.6	3.1	300	Well rounded to sub-rounded
20% Silica	320	0.2	4	80	Sub-angular to sub-rounded
USM100	320	1.8	4	180	Sub-rounded to sub-angular

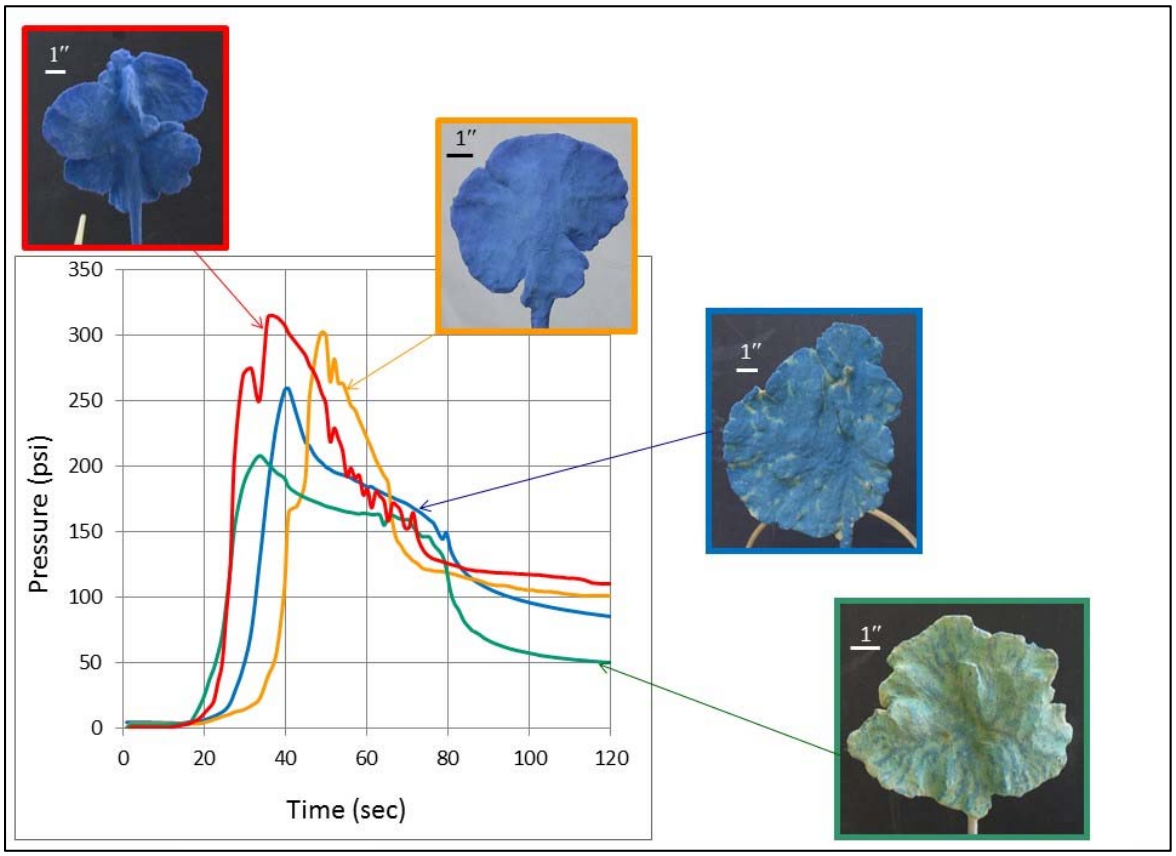

Figure 4.32: Comparison of pressure signatures and fracture geometries between Bromide formation sands (blue and green plots) and synthetic sands (red and yellow plots). All tests (29, 33, 35, and 23 from left to right) were performed at an injection flow rate of 500 ml/min, $\sigma_V = 160$ psi, and $\sigma_h = 80$ psi.

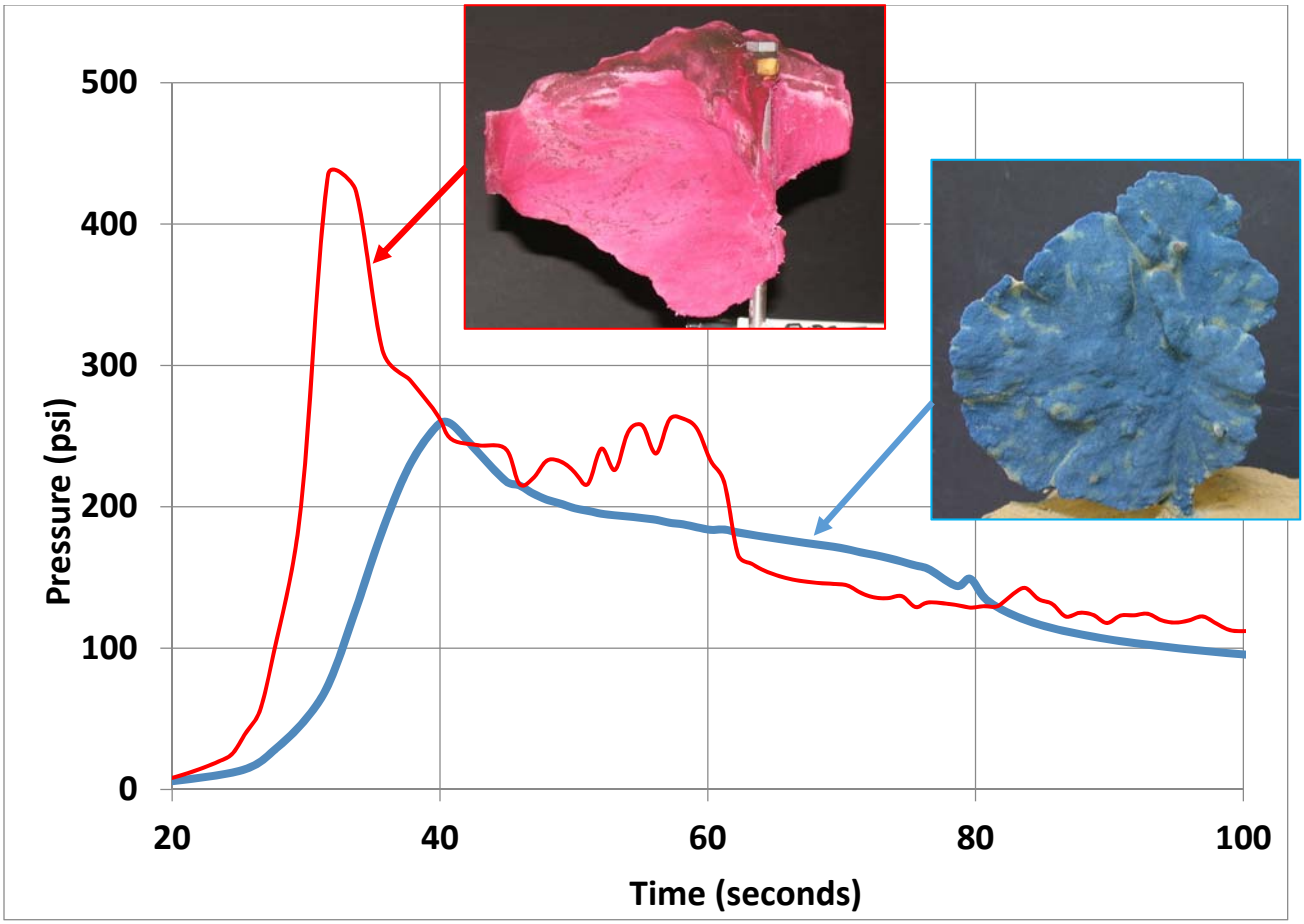

Figure 4.33: Comparison of pressure signatures and fracture geometries between Bromide formation sand (blue plot) and synthetic mixture sand (red plot). Blue coloring agent was used in Bromide formation sand test and red coloring agent was used for the synthetic mixture sand test. Leakoff thicknesses for fractures in the Bromide formation sand were approximately equal to those for silica/Ottawa fine sand mixtures. This is consistent with the permeability differences between these synthetic sands and the Bromide formation sand. Both tests (15 and 35 from left to right) were performed at an injection flow rate of 500 ml/min, $\sigma_V = 160$ psi, and $\sigma_h = 80$ psi.

We also found that the injection pressure behavior during the fracturing experiments in both Bromide formation sand and synthetic sand showed sensitivity to the fluid injection flow rate. Several tests were performed in which all other parameters were held constant while varying the flow rates and observing the pressure response. Injection flow rates were varied over three orders of magnitude in these tests. **Figure 4.18** demonstrates the typical results in the Bromide formation sand and **Figure 4.33** shows the typical results from the synthetic sand. Our experiments show that in both the natural sand and the synthetic sand there is a significant increase in the fracture initiation pressure (peak pressure) with increase in the injection flow rates.

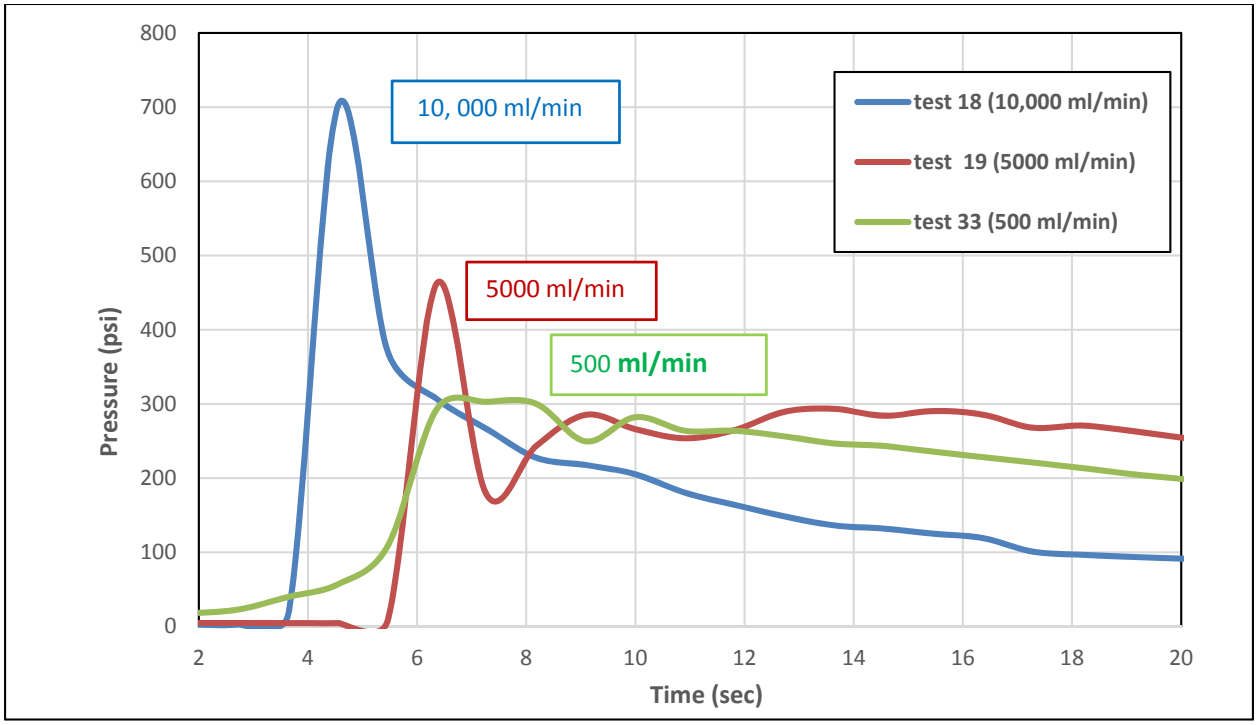

Figure 4.34: Pressure-time curves in synthetic sands showing flow rate dependency of pressure behavior in tests 18, 19, and 33.

Finally, we applied *Germanovich and Hurt* [2012], *Hurt and Germanovich's* [2012], and *Hurt's* [2012] dimensionless model of fracture initiation to our results in order to characterize hydraulic fracturing in synthetic sands and the Bromide formation sand. For fracture initiation,

which occurs at or near the peak injection pressure, P_{peak}, they considered 11 parameters with 3 basic dimensions, that is,

$$P_{peak} = f(K, n, E, \nu, k, c, \tan\emptyset, Q, \sigma_1, \sigma_3), \tag{4.2}$$

where ν and k are the Poisson ratio and the permeability, respectively. The cohesion and the friction angle of the material are represented by c and $\emptyset$, respectively. The injection rate is represented by Q while the confining stresses are represented by σ_1 and σ_3. Thus, 8 dimensionless groups would be required. To reduce the number of parameters, *Germanovich and Hurt* [2012], *Hurt and Germanovich* [2012], and *Hurt* [2012] grouped and collected only independent parameters resulting in five parameters, with three basic units. Namely,

$$P_{peak} = f(Q, K, k, \sigma_0). \tag{4.3}$$

They then applied the Π −theorem [e.g., *Barenblatt*, 2003] to obtain the relationship

$$\frac{P_{peak}}{K}\left(\frac{k^{3/2}}{Q}\right)^n = f\left[\frac{\sigma_0}{K}\left(\frac{k^{3/2}}{Q}\right)^n\right] \tag{4.4}$$

between dimensionless peak injection pressure and confining stress.

We plotted over 30 data points and obtained a reasonable fit with a simple power law curve fitting (**Figure 4.35**). Although values of dimensionless groups plotted in **Figure 4.35** vary over three orders of magnitude, there is a correlation between results from synthetic sands and the Bromide formation sand. This simple dimensionless relationship between confining stress and the peak of the injection pressure is significant because it can be used to determine the governing relationships of hydraulic fracturing in cohesionless particulate media. A similar plot showing our data points from tests in triaxial (low stress regimes) and in true-triaxial (high stress regimes) conditions, together with *Germanovich and Hurt* [2012] and *Hurt's* [2012] data points, and those from the literature is presented in Chapter 5.

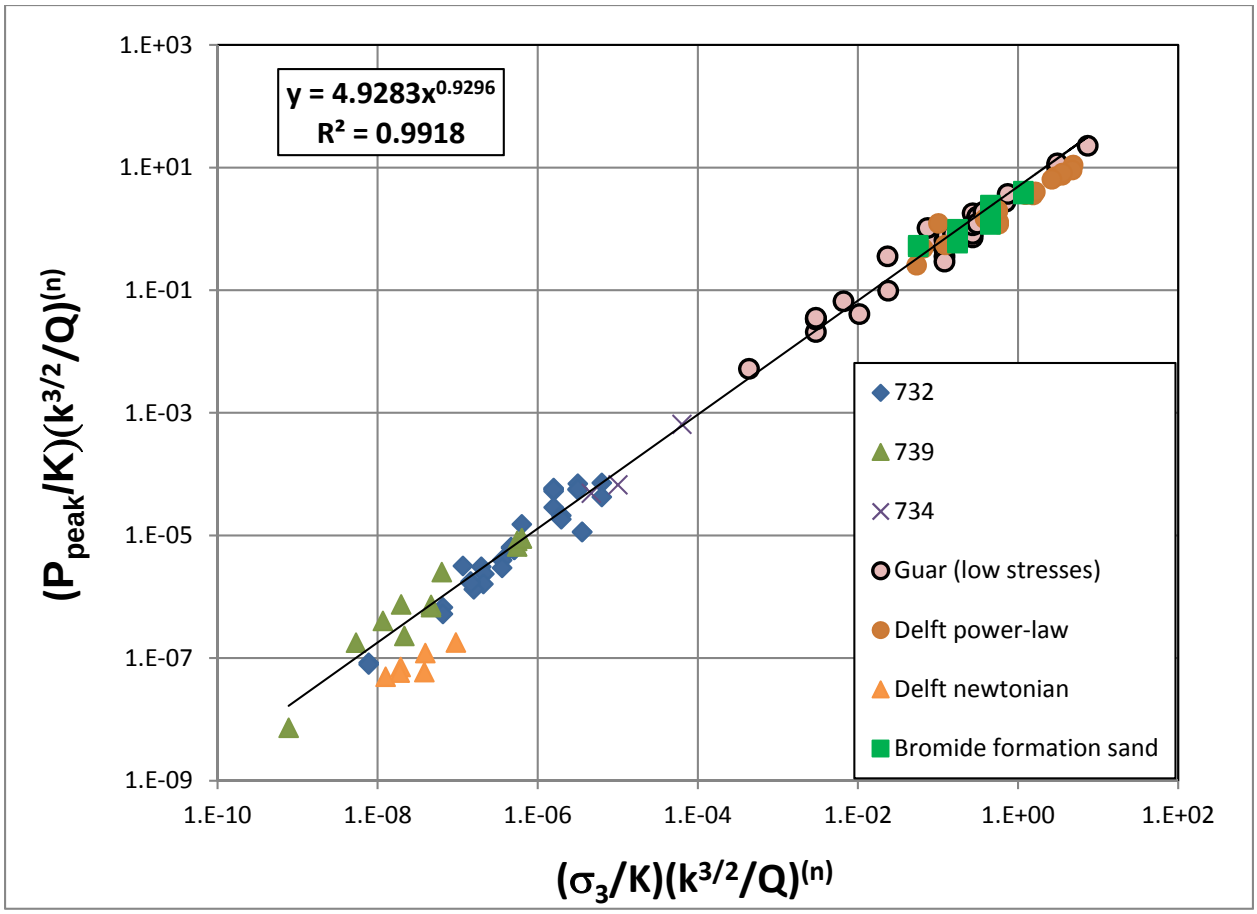

Figure 4.35: Dependence of dimensionless peak injection pressure on dimensionless confining stress. Plot based on more than 30 results from both Bromide formation sand and synthetic sand, showing a power law curve fitting. Data from *Germanovich and Hurt* [2012] and *Hurt* [2012] and the Delft group [*Bohloli and De Pater,* 2006; *De Pater and Dong,* 2007; 2009; *Dong,* 2010; *Dong and De Pater,* 2008] are also plotted.

4.6. CONCLUSIONS

In this chapter, we present hydraulic fracturing experiments that were conducted in a natural sand obtained from an oil production well. Hydraulic fracturing experiments performed in man-made cohesionless particulate materials are also presented and compared and contrasted with those performed in the natural sand. Also, we analyzed the flow rate dependency of the peak pressure in natural sands. The natural sand was obtained from a depth of approximately 7700 feet, that is, from the Bromide formation, a member of the middle Ordovician Simpson group in Cleveland county, Oklahoma. We call this natural sand the Bromide formation sand. The main conclusions of this chapter can be summarized as follows.

1. Leakoff behavior in both natural sands and man-made sands is sensitive to the permeability of the material being fractured. As expected, the thickness of the leakoff zone increases as the permeability increases.
2. Similar deformation features, such as cavity expansion features, fracture multi-segmentation, asymmetrical fracture wings, and fracture offshoots both near the borehole and in far field, were observed in man-made sands and natural sands. These features are also a manifestation of hydraulic fracture complexity in cohesionless, particulate materials.
3. Hydraulic fracturing in the Bromide formation sand showed a flow rate dependency of the pressure behavior. Our results show that there is a significant increase in peak pressure (initiation pressure) with increase in the fluid injection flow rate. This result is consistent with experiments in synthetic samples.
4. The dimensional analysis of our results from both synthetic sands and the natural Bromide formation sand shows a power law dependence of the dimensionless peak injection pressure versus the dimensionless confining stress.
5. Hydraulic fracture behavior in the natural Bromide formation sand is similar to that in man-made cohesionless particulate materials in terms of fracture pressure signatures, fracture morphologies, and geometries. Therefore, it appears that experiments with synthetic sands are sufficiently representative.

6. Fluid rheology tests confirmed that the guar based fracturing fluid used in our tests is a shear thinning fluid whose viscosity reduces with the increasing shear rate. When this fluid ages with time, the viscosity falls as the resin component begins to harden.

5. FLUID-DRIVEN FRACTURING OF PARTICULATE MATERIALS IN TRUE-TRIAXIAL EXPERIMENTS AND HIGH STRESS REGIMES

5.1. INTRODUCTION

To date, hydraulic fracturing in cohesionless particulate media has been studied only in low stress regimes (up to 200 psi) and has not been adequately carried out under true-triaxial tests in high stress regimes (up to 1600 psi) that are more realistic in the in-situ conditions. It should be noted that the terms “high stress” and “low stress” regimes are used in this work strictly for comparison between tests conducted in triaxial conditions and those conducted in true-triaxial conditions. The investigation detailed in this chapter centers on hydraulic fracturing experiments in particulate materials conducted in a true-triaxial loading frame under high stress regimes (up to 1600 psi). Four tests were performed in a research experimental series under true-triaxial conditions. The goals and objectives of this test series were:

1. To advance and improve experimental techniques to study fluid-assisted fracturing in cohesionless, sediment-like particulate materials.
2. To verify and characterize the presence of plastic yielding features such as shear banding and cavity expansion.
3. To investigate the plausibility of using the acoustic emission monitoring technique to gain additional insights into the fracturing process, fracture geometry mapping and also to give a reference for interpreting microseismic data recorded in the field.
4. To access the plausibility of using the ultrasonic transmission monitoring technique to capture hydraulic fracturing dynamics such as fracture initiation and propagation.
5. To study scale (size) and stress effects, if any, on hydraulic fracturing morphology and pressure signatures in particulate media.

The following is an overview of the preparations, challenges, and pertinent findings of our hydraulic fracturing experiments in an unconsolidated sand block sample. In Section 5.2 the industrial laboratory setup, where the tests were performed, is described while the different steps of the test procedure that we took are detailed in Section 5.3. The results of our tests are

covered in Section 5.4 and comparisons are made across the various tests in Section 5.5. Finally, the results are discussed in detail in Section 5.6 before the presentation of the conclusions in Section 5.7.

For clarity and to avoid ambiguity, the following notations and definitions are adopted for this chapter and the rest of this work:

1. The maximum principal stress, σ_1, is vertical and applied on the top and bottom faces of the true-triaxial block sample.
2. The intermediate principal stress, σ_2, is applied in the horizontal direction on the north and south faces of the true-triaxial block sample.
3. The minimum principal stress, σ_3, is applied in the horizontal direction on the east and west faces of the true-triaxial block sample.
4. Occasionally we use notation σ_V, σ_H, and σ_h instead of σ_1, σ_2, and σ_3, respectively.
5. Quantities ΔV_2 and ΔV_3 are the flat-jacks volume changes in the corresponding principal stress directions. Quantity ΔV_1 is the axial actuator volume change corresponding to σ_1. These quantities are proportional to the mean displacements of sample sides perpendicular to σ_1, σ_2, and σ_3 directions, respectively.
6. The terms wellbore and borehole may be used interchangeably to denote the injection source. These terms should not be construed to infer that a hole was drilled into the sample. The injection source was built in place in our tests and the terms borehole and wellbore are only used to mimic field terminology.
7. In this chapter and in chapter 6 we discuss true-triaxial tests 1, 2, 3, and 4. We omit the qualifier “true-triaxial” and use it only if we want to distinguish these tests from the triaxial tests 1 through 49 discussed in previous chapters.

Table 5.1 summarizes the general design test conditions under which these tests were conducted. Test 1 was a pilot test conducted by *Hurt* [2012] to evaluate feasibility, adverse events and to improve upon the study design prior to the performance of our full-scale tests 2, 3, and 4.

Table 5.1: Summary of true-triaxial test conditions.

Test numbers	1, 2, 3, and 4.
Sample Size	11 in by 11 in by 15 in. (also 28.5" by 28.5" by 35.5").
Rock Type	Tests 2, 3, and 4 used USM100 sand (80%) and Sil-Co-Sil106 silica flour (20%) mixture compacted to 2.0 $\mathrm{g/cm^3}$. Test 1 used F110 sand (80%) and silica flour (20%) mixture compacted to 1.9 $\mathrm{g/cm^3}$.
Fracturing Fluid	Guar based sandlock, power-law fluid with n = 0.41 and K = 11 $\mathrm{Pa} \times \mathrm{sec}^n$
AE and UT Sensors	12 sensors for AE and UT monitoring were distributed on two opposite faces of the block in test 4.
Loading Conditions	$\sigma_1 = 1600$ psi, $\sigma_2 = 1200$ psi, $\sigma_3 = 800$ psi
Flow rate	500 ml/min
Fracture Initiation	Test 1,2, and 3 used stainless steel perforated injection tube 0.375-inch OD (outside diameter) and 0.277-inch ID (inside diameter). Test 4 used aluminum alloy 6061 perforated flow tube with 0.5 in OD and 0.26 in ID.

5.2. TRUE-TRIAXIAL LABORATORY SET UP

All the tests discussed in this chapter were conducted at an industrial geomechanics laboratory in Salt Lake City, Utah. The laboratory has a large poly-axial loading frame and a small poly-axial loading frame, which can generate true triaxial stress states in block samples. Both these loading frames are controlled and monitored from a central computer system. Tests 1, 3, and 4 were conducted in the small loading frame, while test 2 was conducted in the large loading frame. The general setup of the conducted experiments is summarized by the schematic presented in **Figure 5.1a.**

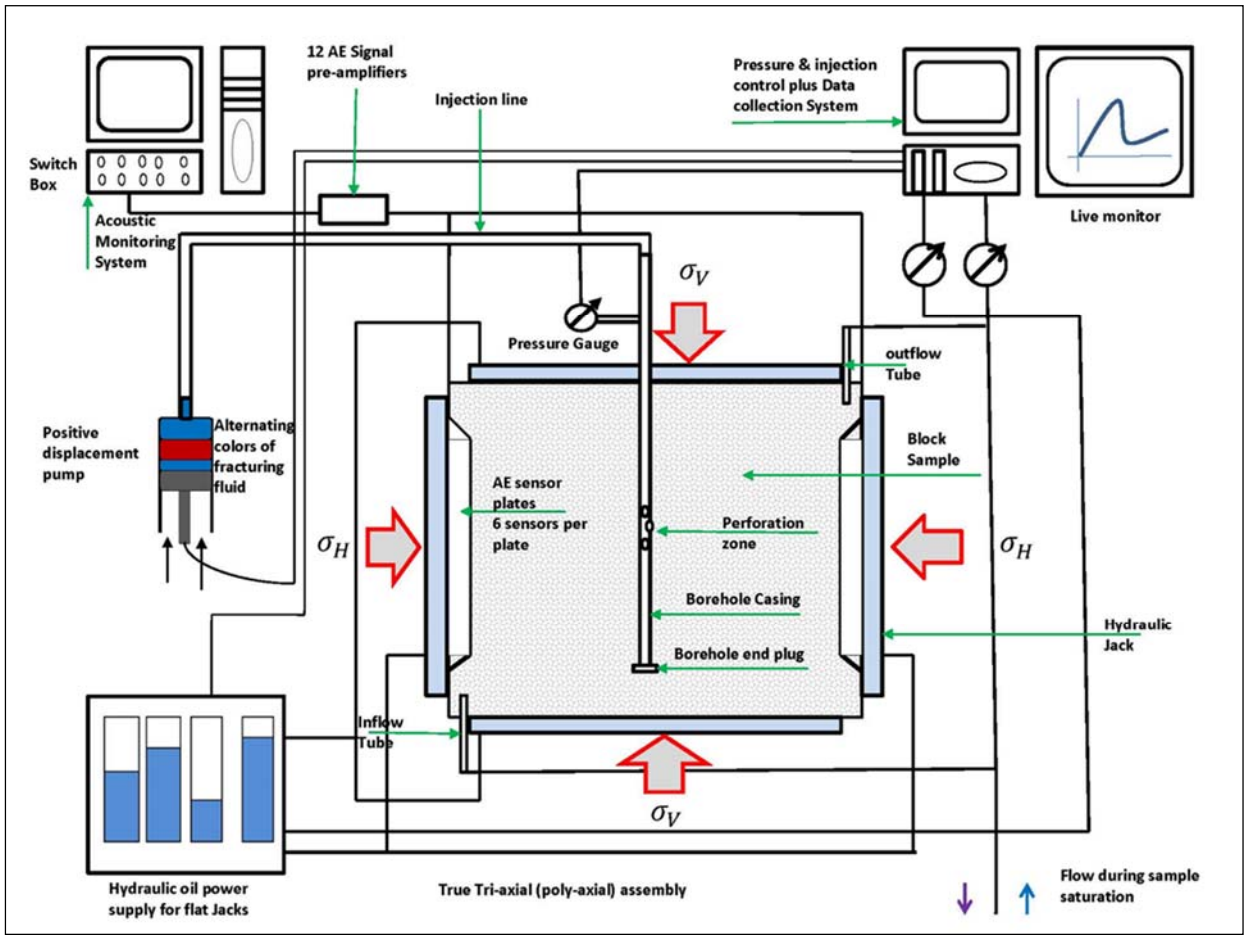

Figure 5.1a: Schematic of overall apparatus setup for experiments. Schematic not drawn to scale.

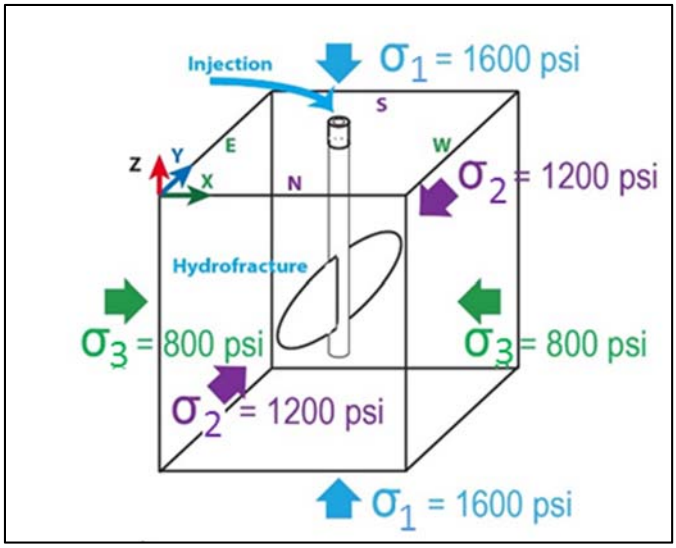

Figure 5.1b: Block sample configuration with the N, S, E, W directions and the applied stress conditions.

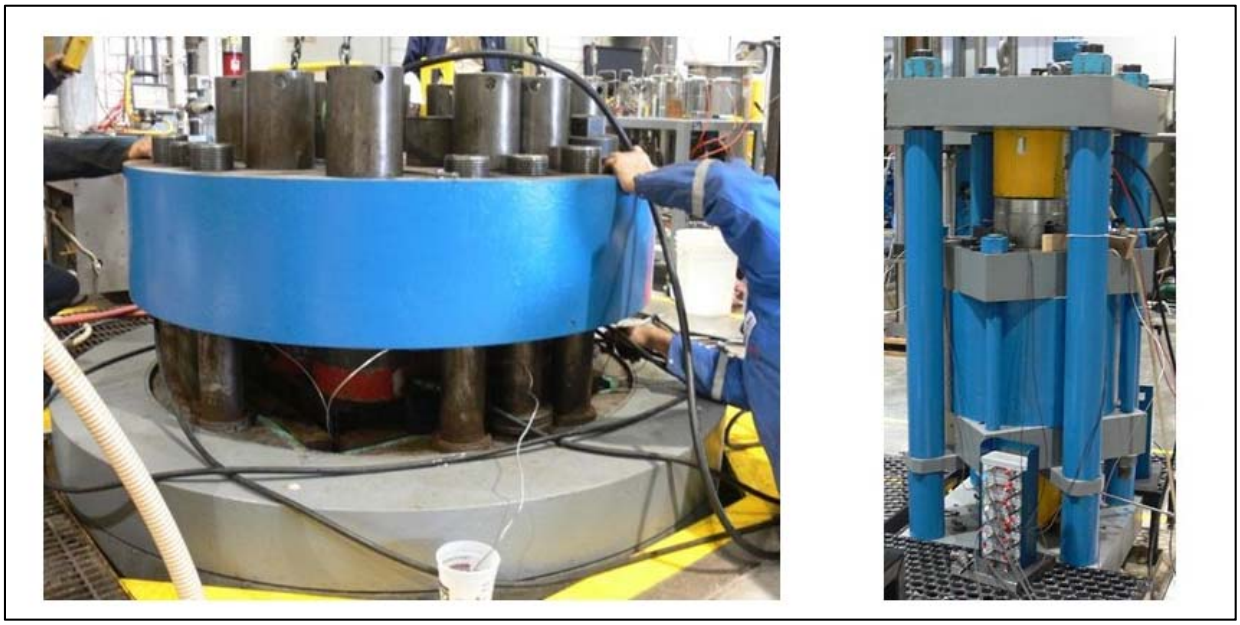

Figure 5.2: (a) Large and (b) small polyaxial loading frames at Terratek.

5.2.1. True-triaxial test frame

Pictures of the two loading frames are shown in **Figure 5.2**. The true-triaxial frame simulates *in-situ* stresses by applying independent stresses in three orthogonal directions on a block sample. The specimen is placed in the loading frame and true-triaxial compressive stresses are applied by means of four flat-jacks for the horizontal directions and hydraulic rams in the vertical direction.

The flat-jacks are steel bladders that are pressurized with fluid to expand and transmit loads to the face of the sample. These pressure plates must be slightly smaller than the sample faces in order to avoid direct mechanical contact between adjacent plates. The stress frames both allow for the stresses to be applied independently in three principal stress directions: σ_1 direction, the σ_2 direction, and σ_3 direction as shown in **Figure 5.1b**. The loading applied was such that equal pressure was applied on opposite sides of the block sample and the three axial loads, σ_1, $\sigma_2, \text{and } \sigma_3$ were controlled independently. Before the experiment is run, the confining stresses are ramped up at such rates that all three principal stresses reach the design stress at the same time. Once the design stresses are reached, the loads are held at these levels until the experiment is complete and the fracture sample is ready for excavation.

5.2.2. Pore can and block sample geometry

The block sample was a cuboid built inside a metal pore-can by compacting particulate materials around a pre-installed cylindrical metal casing (injection source). This pore-can was made of thin sheets of stainless steel. The dimensions of the pore can for tests 1, 3, and 4 were $11 \text{ in} \times 11 \text{ in} \times 15 \text{ in} (279 \times 279 \times 381 \text{ mm}^3)$ and the dimensions of the pore-can for test 2 were $28.5 \text{ in} \times 28.5 \, in \times 35.5 \text{ in} (72 \times 72 \times 90 \text{ cm}^3)$. A 1-inch-thick urethane seal was preinstalled at the bottom of the can before preparation of the sample. The urethane was made in liquid form and allowed to set for a period of 24 hours. After sample installation in the can, another 1-inch-thick urethane seal was prepared and installed at the top of the can. This layer was also allowed to set for approximately 24 hours. The purpose of the urethane was to seal the sample against fluid loss during saturation.

Flow tubes were embedded in the block sample to aid with saturation (**Figure 5.1a**). In test 1, a flow tube in the bottom northwest corner of the block and the borehole injection source were used as inflow and outflow during the saturation process. In test 2, a flow tube in the top, towards the north boundary of the block and the borehole injection source were used as inflow and outflow during the saturation process. Both in test 3 and test 4, a flow tube in the bottom northwest corner of the sample, a flow tube in the top southeast corner of the sample, and the borehole injection source were interchangeably configured as inflow and outflow during the

saturation process. The flow tubes are shown in **Figure 5.1a** and described in detail later in Section 5.3. All flow tubes had a mesh around their perforations and were embedded about 4 in into the sample.

5.2.3. Fracture fluid injection system

The fluid injection line runs from the displacement chamber through approximately 15 feet of high-pressure hydraulic hose to the metal injection source. The displacement chamber contains a displacement piston that is controlled by a positive displacement pump. Fluid injection flow rates and injection fluid volume can be set to a desired value using this assembly. Smooth hydraulic tubing is used to minimize viscous losses. The injection source is placed in the center of the block sample as described above and has a 1.5 in perforation zone in the volumetric center of the sample. A pressure transducer to measure injection pressure is connected to the injection source about 6 in outside the pore can. The fluid pressure is recorded continuously during the test. The entire system is automated, with the pump and displacement chamber assembly being controlled from a central computer and the pressure transducer being connected to the central computer, for injection pressure data acquisition (**Figure 5.1a**).

The cylindrical metal casing in the center was a simulation of the borehole and had a 1.5-inch long perforation zone in the center of the sample. In tests 1, 2, and 3, stainless steel tubing with an internal diameter (ID) of 0.277 in and an outside diameter (OD) of 0.375 in was used as an injection source. In test 4 an aluminum alloy 6061 [www.mcmaster-carr.com] injection source was used in order to facilitate post-test fracture examination in a CT scan machine. Stainless steel interferes with the X-rays during CT scanning and often ruins the quality of the CT images. The ID of the aluminum injection source was approximately 0.26 in and the OD was 0.5 in. The ID was kept consistent in all 4 experiments to allow for good comparison across the 4 experiments.

The perforation zone design was the same for all 4 experiments and resembled that of the injection sources for the experiments conducted at the Georgia Tech lab. It consisted of 4 pairs of holes with a spacing of 0.5 in and a 90 degree phasing between alternate pairs of holes. The perforation design is described in detail in Chapter 4 of this work and in *Hurt* [2012].

The injection source end was plugged by welding. The injection sources and end plugs were pressure tested at the Georgia Tech lab to ensure they would withstand the operating pressures of the experiments. In tests 1 and 2, the plugged end of the injection source was seated at the bottom of the can and glued to a 2 inch by 2-inch metal plate. In tests 3 and 4 the plugged end was located 3 in above the bottom of the can and was not glued to a 2-inch by 2-inch plate.

5.2.4. Data acquisition system

Both experimental input-variable manipulation and data collection were conducted through a central computer system (**Figure 5.1a**). Using this central computer, the principal stresses were applied through the flat-jacks and hydraulic rams to the faces of the block sample. As stated above, the fracturing fluid injection rate was also controlled through this computer. Output data was also collected through this system. The pressure transducer for the injection source was connected to the computer so that the injection pressure data could be collected continuously during the test. Also, the pore pressure transducer linked the central computer to the pore volume at the inlet and outlet tubes at the bottom and top of the can. This allowed for the pore pressure to be recorded throughout the sample saturation process and the test run. Fluid volumetric changes in the flat-jacks (ΔV_2, ΔV_3) and the axial actuator (ΔV_1), respectively, were also independently recorded throughout the experiment through this data collection system. Additionally, the injected fracturing fluid volume was recorded relative to time. The data acquisition system also included a live monitor screen through which the current pressure and fluid volume conditions could be observed. Therefore, we were able to monitor the loading pressure conditions, the pore pressure conditions, the injection pressure conditions, the fracturing fluid flow conditions, and the flat-jack volume response conditions in real time before and during the test run.

5.2.5. Acoustic monitoring system

An important feature of our experimental setup in test 4 was the active acoustic monitoring system, which enabled the collection of data about the evolution of the hydraulic fracture, from initiation to fracture arrest. This system contributed to the acquisition of outstanding

observations during tests performed in unconsolidated particulate block samples. The acoustic monitoring system consisted of 12 acoustic SE-150_M sensors made by DECI (Dunegan Engineering Consultants Inc. [www.deci.com]), 2 Aluminum plates for holding the sensors in place inside the block sample, 12 AEP3 signal pre-amplifiers, and an AMSY-6 data acquisition system manufactured by Vallen systems inc. [www.vallen.de] with a maximum of 20 MHz sampling rate and 16-bit amplitude resolution. A sampling rate of 5 MHz was used in test 4. The objectives of the monitoring system were to record reliable signals and acoustic emission (AE) data that could be used to reproduce the AE spatial and temporal evolution, to determine the moment of fracture initiation, and to map the fracture geometry. Accurate AE data acquisition requires that the signal level is well above the noise floor. Signal attenuation in granular media is more problematic than in rock samples. Therefore, oversampling and averaging were key in obtaining good data. The general principle of the monitoring equipment is included in **Figure 5.1a**.

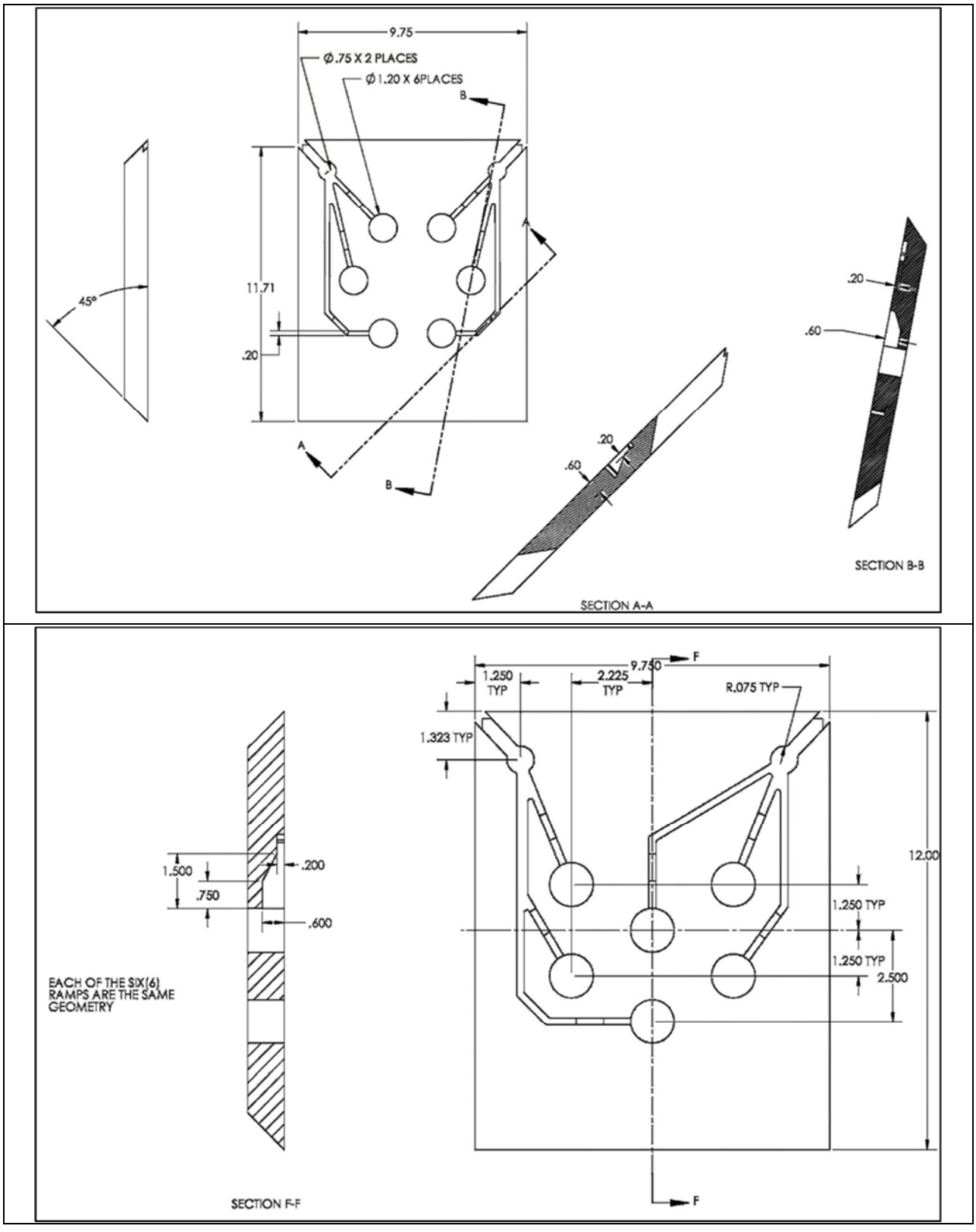

Figure 5.3: Schematic of design for two plates to hold a total of 12 sensors.

A total of 12 acoustic SE-150_M sensors were embedded in two aluminum plates in direct contact with the east and west faces (perpendicular to the σ_3 stress) of the block sample (**Figure 5.1b**). We designed these two aluminum plates to hold the sensors in place in the block sample. The plates were machined at the Georgia Tech research institute (GTRI) machines services department [http://www.gtri.Georgia Tech.edu/machine-services]. The dimensions of the plates were $12\ in\ \times 9.75\ in\ \times 1\ in$. They were beveled at the edges at 45 degrees to minimize mechanical interactions between the loading plate and the sensor plates at the top and bottom of the block. A water jet table was utilized for fabrication of the plates. The water jet cutter is a tool capable of cutting a wide variety of materials using a high pressure jet of water, or a mixture of water and an abrasive substance. A schematic of the plate designs is shown in **Figure 5.3**. Cables to the sensors were installed in grooves machined into the plates to prevent obstruction during the compaction of the block sample. The sensor plates were positioned on the east and west faces (**Figure 5.1b**) of the block sample, parallel to the intermediate principal stress direction, to optimize the amount and quality of data obtained (as it was anticipated that the fracture propagation would be oriented perpendicular to the minimum horizontal principal stress). **Figures 5.4 – 5.6** show pictures of the plates with the sensors installed.

Sensors were selected that could function under saturated water conditions. Each sensor could be configured alternatively as sender, receiver, or passive. Monitoring consisted in sending short acoustic pulses into the block sample and listening to the acoustic events generated from the interactions of the input pulse with the internal features of the block sample. The block sample and fracture response to the acoustic energy depended on their own characteristics [*Michlmayr et al.,* 2012]. The pulses emitted by the sensors could either be compressional or shear waves. Ultrasonic Transmission (UT) measurements provided time-dependent P-wave velocity during loading of the block and during fracturing. The biggest challenge to the application of the AE method in granular block samples is strong signal attenuation [*Michlmayr et al.,* 2012]. To overcome this limitation, it was important that the block sample was densely compacted, fully saturated and the signals were amplified by 49 dB using Vallen AEP3 preamplifiers with high pass filtering of 50 kHz and low pass filtering of 1000 kHz [*Stanchits* et al., 2014a, b].

The sensors were connected to a switchbox (acquisition board), which consisted of switch

channels. Through the switchbox, each sensor can be switched between two of the three possible states namely idle, sender, or receiver. Visualization, data processing and analysis of the signal is done using a conventional PC. Fully digitized waveforms of AE and UT signals were recorded by an AMSY-6 data acquisition system made by Vallen Systems Inc. The software used for advanced analysis and evaluation of the AE hypocenter coordinates was developed by *Stanchits* [2014]. This software allows for time-dependant anisotropic and heterogeneous P-wave velocity inversion based on periodically measured wave velocities, typically at 1 to 5 s intervals, during the test.

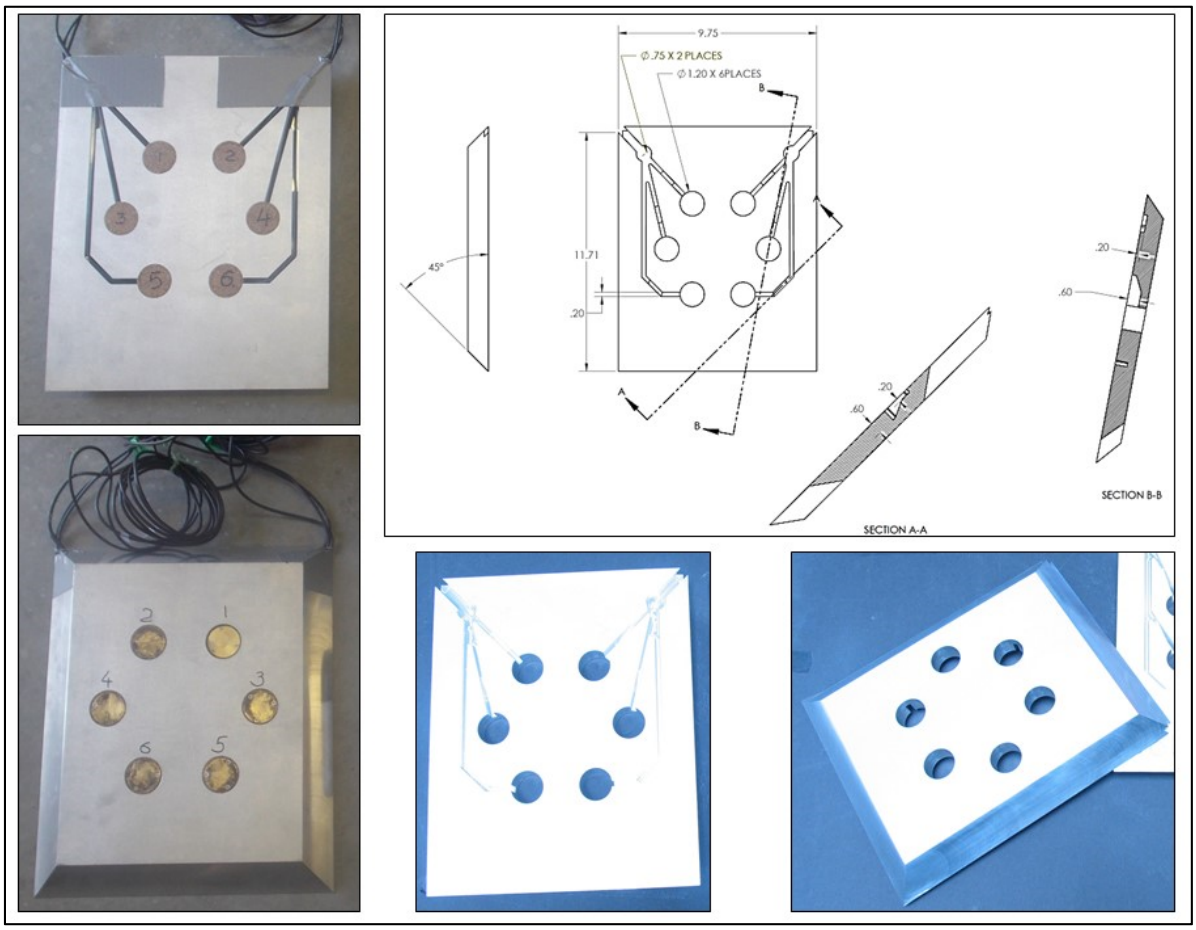

Figure 5.4: One of two plates used to hold sensors 1 through 6 during sample preparation and test run.

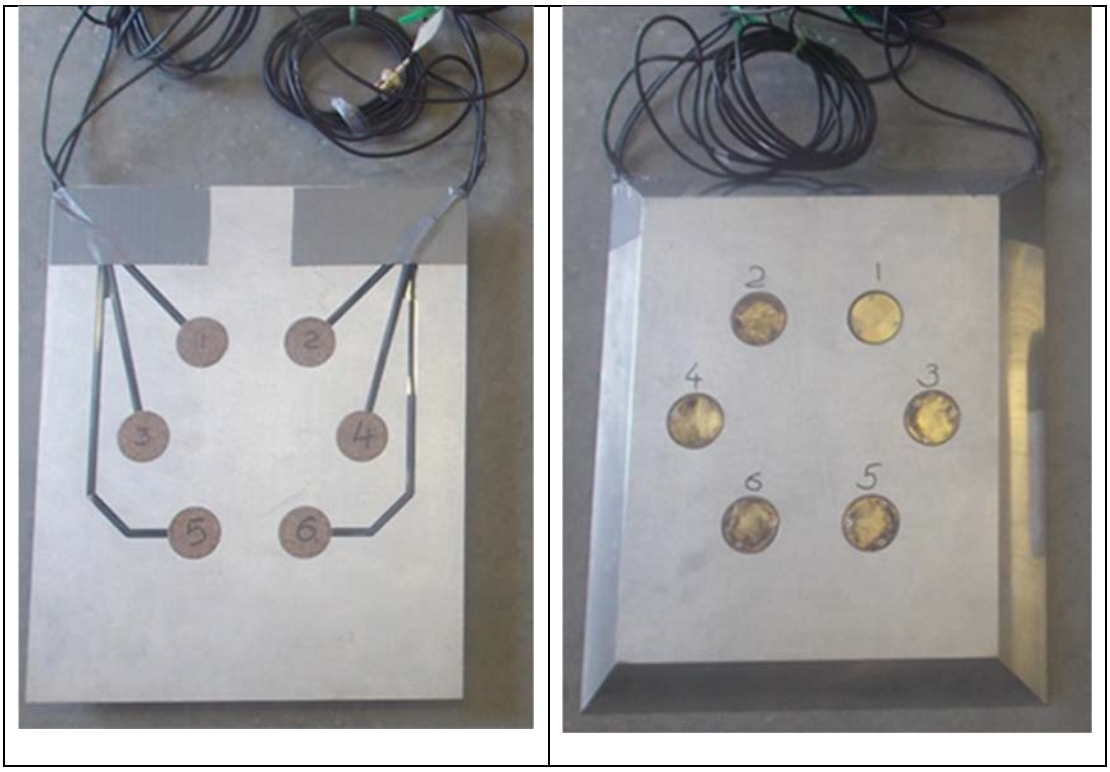

Figure 5.5: Pictures of two views of first late with sensors 1 through 6 installed and ready for deployment in block sample.

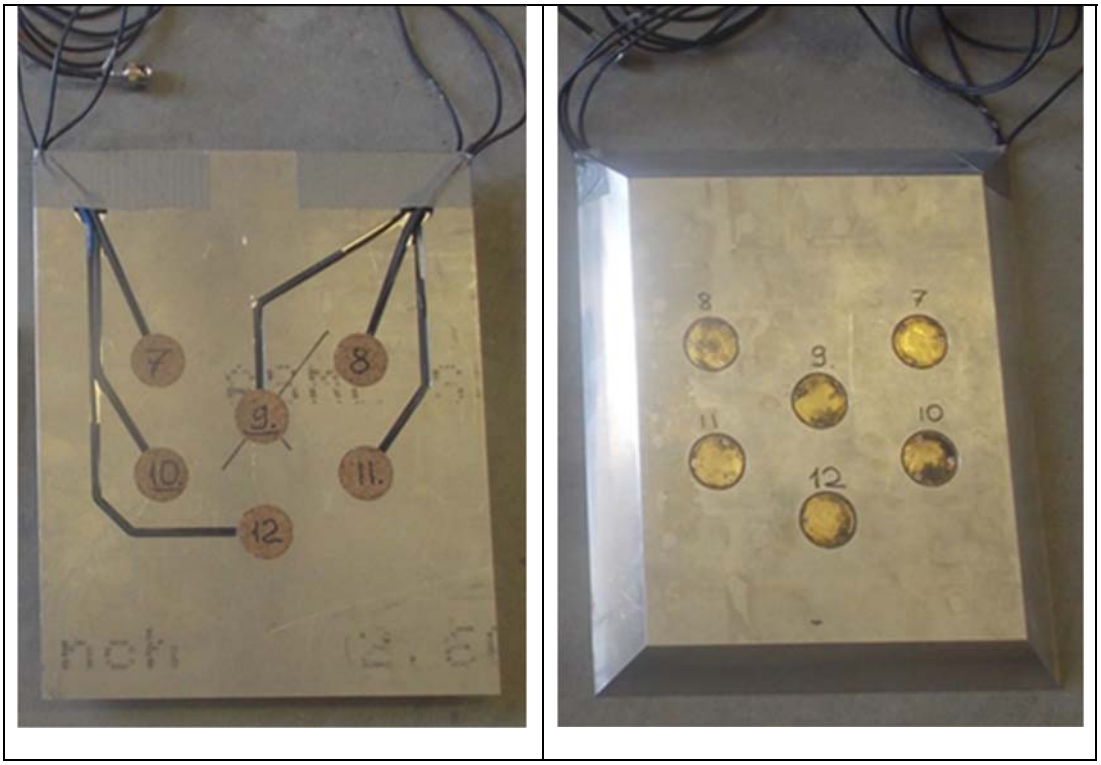

Figure 5.6: Pictures of two views of second plate with sensors 7 through 12 installed and ready for deployment in block sample.

5.3. TEST PROCEDURE

The test procedure was generally the same for tests 1, 2, 3, and 4 with a few minor variations. Tests 1, 3, and 4 were conducted in small block samples ($11\text{ in} \times 11\text{ in} \times 15\text{ in}$ ($279 \times 279 \times 381\text{ mm}^3$)) while test 2 was performed in a large block sample ($28.5\text{ in} \times 28.5\text{ in} \times 35.5\text{ in}$ ($72 \times 72 \times 90\text{ cm}^3$)) to investigate size effects on the hydraulic fracturing behavior. The following is a description of the step by step test procedures for the small block samples and the large block sample.

5.3.1. Small block sample (tests 1, 3, and 4)

Block sample preparation

All block samples were prepared on-site using mixtures of silica sand USM100 or F110 (F110 in test 1 and USM100 in tests 3 and 4) and silica flour SIL-CO-SIL 106. These materials and their mechanical properties are described in detail in Chapter 4 of this work. The materials were first oven dried until all moisture was driven out. Dry samples of 80% silica sand USM100 or F110 and 20% silica flour SIL-CO-SIL 106 were weighed and thoroughly mixed by means of a roller drum mixer (**Figure 5.7**). For each test, the volume of the sample mix prepared was at least 1.5 the volume of the pore can. The sample was mixed in the drum roller for 2 to 3 hours until no segregation of the two materials could visually be observed in the sample mix.

The sample was then compacted in the pore can in 3 inch loose layers. The pore-can served to mold the cohesionless particulate block sample and to hold the saturation in place. A robust acoustic monitoring system was used to monitor the process of hydraulic fracturing in unconsolidated particulate cohesionless materials. Eight sensors were used in test 1 and twelve sensors were utilized in test 4. Sensors were held in place using two aluminum plates in test 4, while the sensors in test 1 were held in place on the wall faces by means of epoxy glue. The design of the sensor plates and the locations of the sensors were presented in the previous section. The locations of the sensors for test 1 are described in *Hurt* [2012]. In test 4, during the sample compaction, the acoustic sensor plates were held in place on the west and east walls by means

of G-clamps (**Figure 5.9**). A perforated cylindrical metal injection source was installed in the center of the can with temporary bracing to hold it in place during compaction. The end of the injection source was located 3 in above the bottom to prevent interaction with the bottom loading plate during the loading phase of the experiment. For the small block sample in tests 1, 3 and 4, five layers of approximately 27 lbs each were compacted using the rodding technique with a 1-inch diameter rodding rod. The compaction method was the same as that in test 1 and is described in detail in *Chang* [2004], *Hurt* [2012], and *Hurt and Germanovich* [2012]. To prevent the can from bulging outwards during sample compaction, the middle of the can was clamped on the outside with a clamp adapter. A level was used to measure the vertical alignment of the injection source throughout the compaction process. The block samples were compacted to a density of approximately 2.0 g/cm^3, which was consistent with sample densities in low stress regime triaxial experiments (Chapter 4). Once the sample compaction was completed, the top layer was leveled off and caped with liquid urethane. The saturation configuration in test 1 consisted of a flow tube in the bottom northwest corner of the block and the borehole injection source as inflow and outflow during the saturation process. Both in test 3 and test 4 a flow tube in the bottom northwest corner of the sample, a flow tube in the top southeast corner of the sample, and the borehole injection source were interchangeably configured as inflow and outflow during the saturation process. **Figure 5.11** is a schematic drawing showing these flow tube configurations. Where applicable, the top flow tube was inserted through the liquid urethane into the top southeast corner of the block. The urethane was then allowed to set for approximately 24 hours. The pictures in the **Figures 5.7 – 5.10** show various stages of the sample preparation process.

Figure 5.7: Mixing of materials in roller drum mixer. Materials were mixed until no clear segregation was visible.

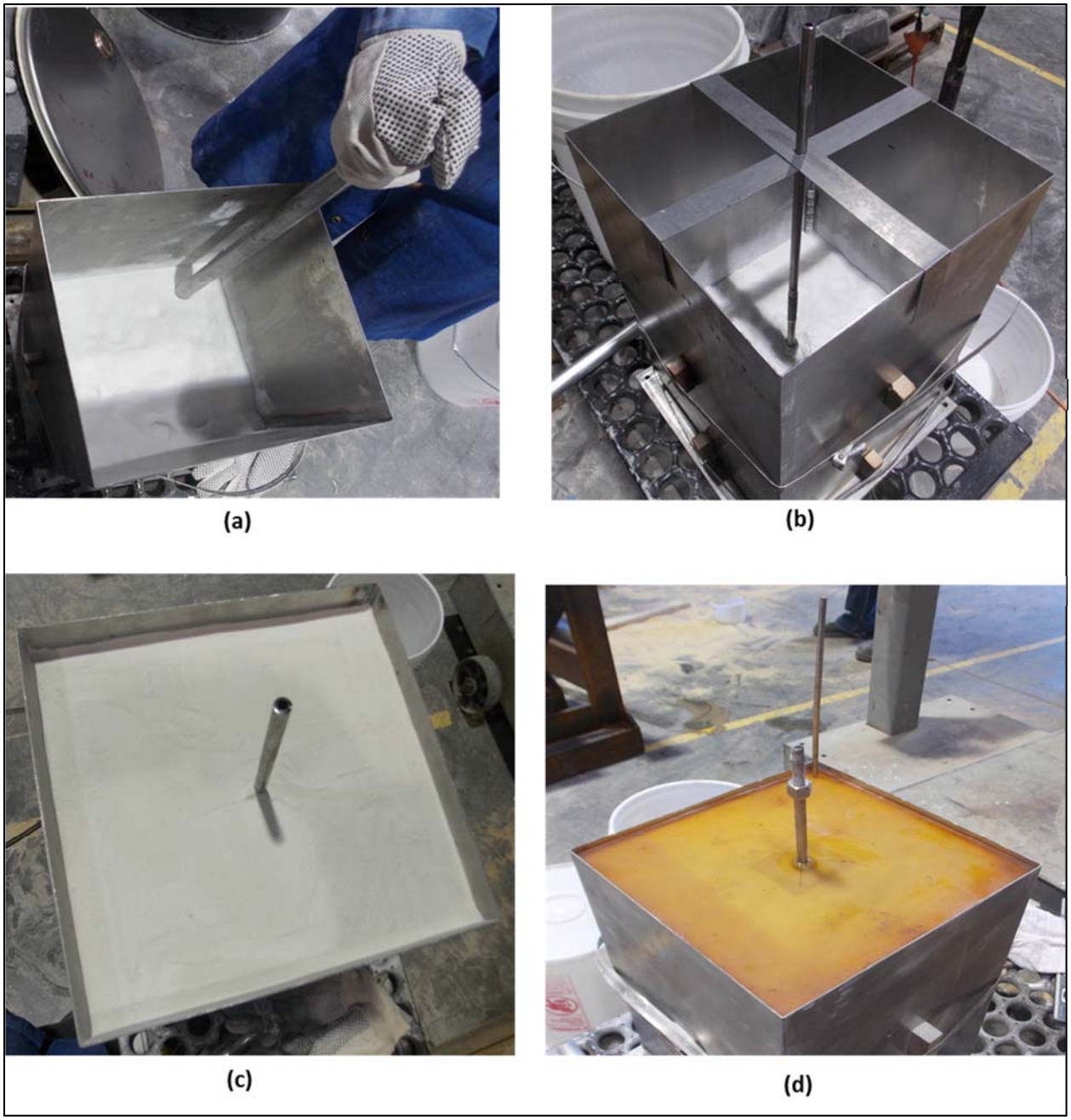

Figure 5.8: Several typical stages of the small block sample preparation process (with no sensor plates).

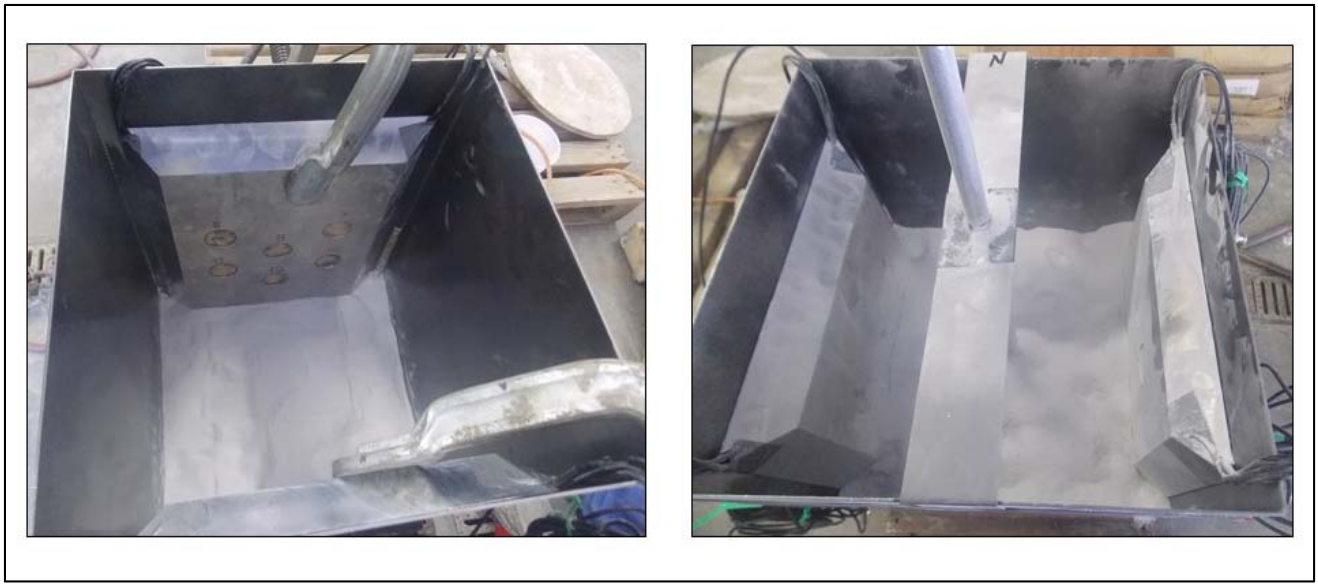

Figure 5.9: Block sample preparation. Sensor plates held with a G-clamp during compaction.

After the sample preparation procedure described above was completed, the top plate was installed. The pore can was then placed in the loading frame. The flat-jacks were placed on each of the four lateral sides of the can and connected to the hydraulic actuator system, which in turn is connected to the central control computer. A highly incompressible oil fluid was used in the actuator so that pressure can be transmitted to the attached flat-jack practically instantaneously when applied. The lateral loads were applied on the sample by applying hydraulic pressure on the flat-jacks. The top and bottom stresses were applied by hydraulic rams directly to the end platens of the sample. The loading was applied so that equal pressure was applied on opposite sides of the sample and the three principal stresses, $\sigma_1, \sigma_2, \text{and } \sigma_3$, were controlled independently. In tests 3 and 4, loads were applied by the motion of both the top and bottom loading plates, whereas samples 1 and 2 received loads by displacing only the top plate with the bottom plate being rigid.

In test 4, the cables from the embedded acoustic emission sensors where at this time connected to the pre-amplifiers, which, in turn, where connected to the switch box and the AE data acquisition computer system. **Figure 5.10** shows the above described stages of the experiments.

Figure 5.10: Sample placement in loading frame.

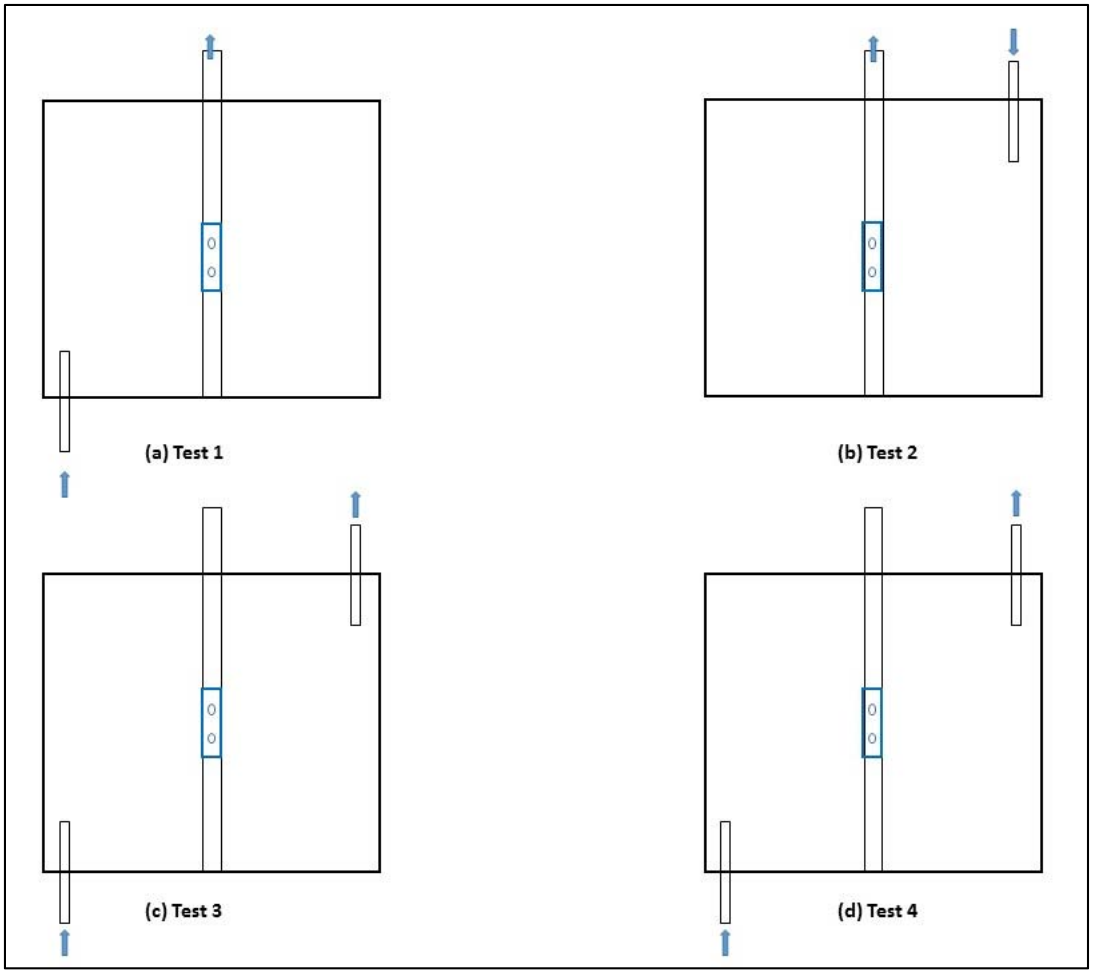

Figure 5.11: Flow tube configurations during saturation of tests 1, 2, 3, and 4. The design flow direction of water is shown by the arrows.

The next phase of the experiment was the saturation of the block sample. The objective of the saturation process is to fill the voids in the specimen with water without undesirable pre-stressing of the specimen both externally and internally through the injection source. Saturation of the specimen was conducted with the sample under confining loads in order to avoid swelling of the sample. Saturation is usually accomplished by applying backpressure to the specimen pore water to drive air into solution (see also Section 4.23, page 93). Removing as much air as possible prior to applying backpressure reduces the amount of air that will have to be placed into solution. The use of de-aired (deionized) water for saturation makes the process easier and faster. The use of CO_2 also greatly improves the saturation process as the heavier and more water-soluble CO_2 displaces air and dissolves into water more easily than air. Using a modified version of the ASTM

D 4767 standard [*Wang*, 2000], the following general steps were followed for the block sample saturation process:

1. The plumbing was connected to the inflow and outflow tubes in the specimen.
2. The pore-can was loaded to saturation loading conditions of $\sigma_1 = 200$ psi, $\sigma_2 = 150$ psi, and $\sigma_3 = 100$ psi.
3. After loading the sample, vacuum was applied through the injection source for 15 minutes while the bottom inlet and top outlet flow tubes were kept closed. Vacuum was then stopped.
4. The sample was then flushed with CO_2 from the bottom inlet flow tube at a pressure of 50 psi for approximately 15 minutes. The top flow tube and the injection source were kept open.
5. The sample was then flushed with vacuum again as described in step 3.
6. Step 4 was then repeated.
7. Finally, step 3 was repeated with sample being placed under vacuum overnight.

During these steps, the block sample was loaded to confining stresses of $\sigma_1 = 200$ psi, $\sigma_2 = 150$ psi, and $\sigma_3 = 100$ psi in readiness for saturation. These loads were proportional to the final working loads that would be applied during the test. During test 4, a signal test was performed at this moment, on all 12 AE sensors to verify that they were all responding. All sensors were found to be responding but there was no transmission of signals from sensors on one plate to those on the other because the sample was not yet saturated.

Saturation was then started by injecting water from the bottom northwestern corner flow tube as shown in the **Figure 5.11**. In test 1, the injection source was opened and used as the outlet for the water saturation. In tests 3 and 4, the injection source was closed and a top southeastern flow tube was used as the water outlet. A low flow rate was used on the inflow to facilitate a homogeneous saturation progression. Backpressure was also applied to optimize the saturation process. A degree of saturation of approximately 95 % was achieved in test 3. This was calculated based on the porosity of the sample and the total volume of water that was flushed

into the block sample as described in Section 4.2. Due to the challenges that were encountered during test 4, only a degree of saturation of approximately 80% was attained. These challenges and the general saturation procedure followed in test 4 are now described below.

Saturation for sample 4 was started by injecting water from the bottom flow tube at a backpressure of 50 psi while vacuum was applied at the top flow tube and the injection source was closed as shown in **Figure 5.12a**. The backpressure was applied by means of an external pump. From the inflow volume reader, it was observed that there was no water flowing into the sample at this backpressure and external loading conditions. The loading stresses were then increased to $\sigma_1 = 300$ psi, $\sigma_2 = 225$ psi, and $\sigma_3 = 150$ psi, while the backpressure was increased to 100 psi. There was still little to no flow into the sample. An attempt was also made to inject water from both the bottom and the top flow tubes while the injection source was under vacuum as shown in **Figure 5.12b**. No flow was recorded. The loading stresses were increased again to σ_1 = 800 psi, σ_2 = 600 psi, and σ_3 = 400 psi and the water flow cycle reversed (**Figure 5.12c**). Water was now injected from the injection source at a backpressure of 183 psi while vacuum was applied to both the bottom and top flow tubes. An average water inflow into the sample of 50 ml/min was observed within a few minutes. Within two hours this water inflow rate had increased up to 64 ml/min and water was observed flowing out through the transparent vacuum pipe attached to the outlet. Vacuum was now removed and the outlet valves were kept open. Saturation was continued for 4 hours under these conditions while the outflow rate was monitored and measured by means of a graduated measuring cylinder and a stop watch. After 2.5 pore volumes (pore volume equals the porosity times the sample volume) of water had been allowed through the sample, an average outflow rate of 48 ml/min was recorded.

Before we could complete the saturation process, we needed to verify that there was uniform flow throughout the sample by comparing several flow cycles. First the bottom flow tube valve was closed while the top flow tube valve was kept open (**Figure 5.12d**). A steady water flow rate of approximately 50 ml/min was observed through the outlet. After one hour, the top flow tube valve was closed and the bottom tube valve was opened (**Figure 5.12g**). Little to no flow was observed through the bottom flow tube. It later came to be discovered during the excavation

phase of the experiment that the bottom flow tube was clogged with some small black beads that were obstructing free water flow. Water flow was reversed, so that water was injected through the top tube while the injection source was the outflow and the bottom tube valve was closed (**Figure 5.12e**). A steady inflow rate of approximately 60 ml/min and an outflow rate of 50 ml/min were observed at a backpressure of approximately 120 psi. The injection source was then closed and the bottom flow tube was opened (**Figure 5.12f**). An inflow rate of 96 ml/min and an outflow rate of approximately 82 ml/min were observed at a backpressure of 120 psi. The backpressure was then reduced to 75 psi to slow down the flow and allow the saturation to stabilize. The inflow rate reduced to 48 ml/min and the outflow rate to 42 ml/min. The saturation was held at these conditions for approximately 4 hours. Finally, the flow cycle was reversed once again with water being injected from the bottom tube and outflow at the top tube while the injection source was closed (**Figure 5.12h**). After a few minutes, a steady flow was observed with an inflow rate of 46 ml/min and an outflow rate of approximately 43 ml/min. Approximately 5760 ml of water is estimated to have been injected in the sample. At a porosity of 28 percent, this represents a saturation of approximately 80 percent.

It should also be noted that there were some challenges in applying constant backpressure as the pump that was used could not hold a constant backpressure. We therefore changed the external pump to the CAT pump [www.pumps-and-parts.com], which worked better and supplied the constant backpressure that was needed. There is a possibility that the high backpressure of 183 psi applied through the injection source may have disturbed the sample, especially at the region around the perforation zone. Some of the difficulties with saturation were encountered because the bottom flow tube was clogged. During the excavation phase of the experiment, we observed the bottom flow tube to be clogged with small black beads. It would have been advantageous to have checked flow in this tube before placement and compaction of any sample materials. Finally, we also observed minute amounts of particles in the outflow water at the end of the saturation phase. It is possible that the high backpressures that were used in the saturation process pre-stressed the sample and may have also caused small levels of particle migration.

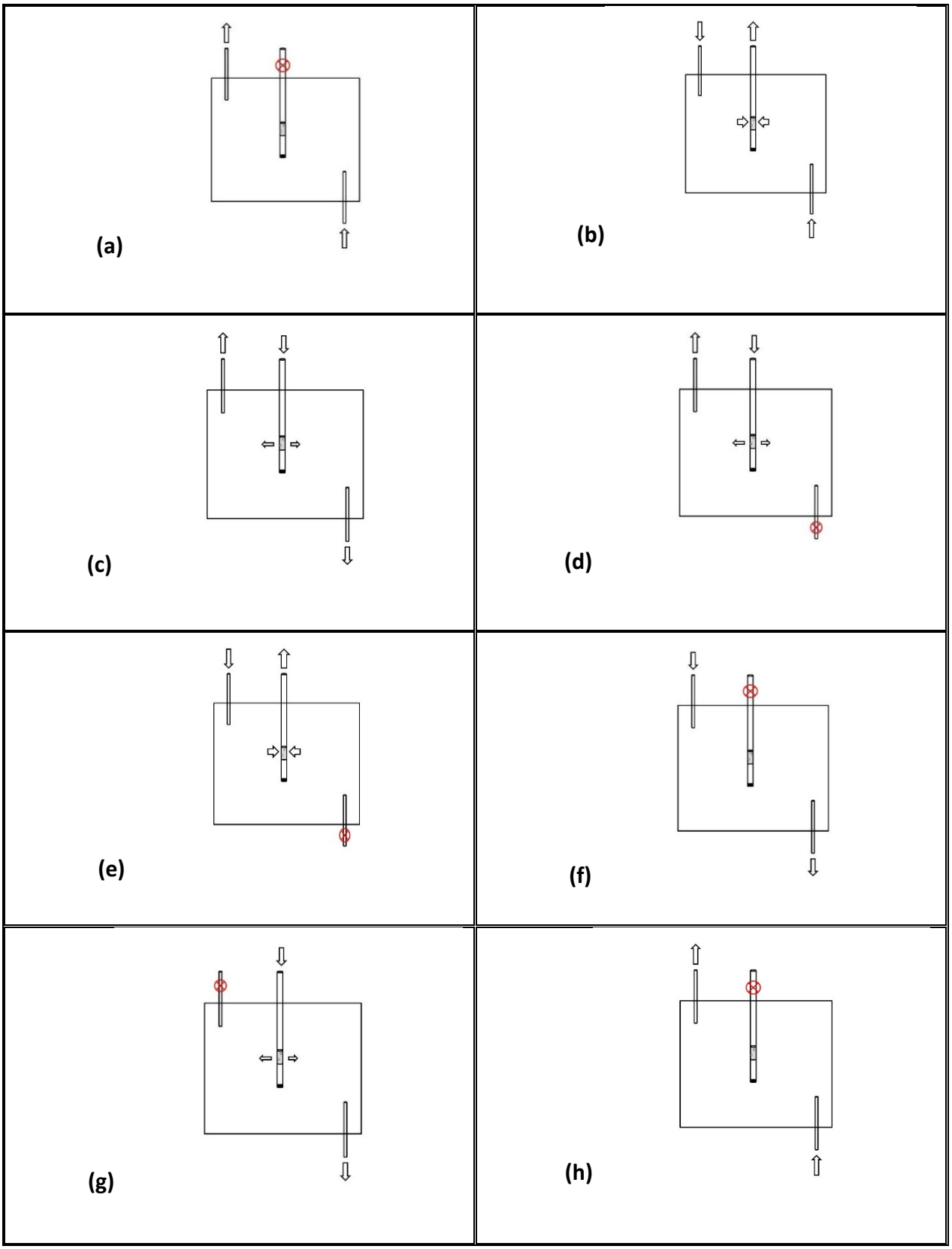

Figure 5.12: Schematics of water flow directions during the saturation phase. Schematic not drawn to scale.

After the saturation phase, the next phase was injection of the fracturing fluid and running the test. First, 1000 ml of a guar based sand-lock fluid was prepared using a proprietary formula provided by Schlumberger. In *Hurt* [2012] and in Chapter 4 of this work, the rheology of this cross-linked gel is described in detail. No coloring agent was used in test 1. In test 3 a blue coloring agent was used while two coloring agents, red and blue, were used in test 4 in order to study the sequence of fracture propagation. The main purpose of coloring agents was to distinguish the fracture from the sample material during the excavation process. After the preparation of the fracturing fluid, the 1000 ml volume of fluid was placed in the injection chamber. In test 4 the fluid was distributed so that 250 ml blue fluid was at the front (at the top in the chamber), with 500 ml of the red fluid in the middle and 250 ml of blue fluid at the rear. After the placement of the fracturing fluid in the chamber, the external loads were applied at three independent rates so that they all reached the design final loads at the same time. As stated above, the external loads for these four tests were σ_1 = 1600 psi, σ_2 = 1200 psi, and σ_3 = 800 psi.

After reaching the final stress state, the block was allowed to stabilize for a few minutes. The top and bottom flow tubes were left open to allow for drained pore pressure conditions during the test. In test 1 and 4, the acoustic sensors were tested at this time to ensure that all sensors were able to send and receive signals. After checking the sensors, the system was ready for the injection cycle.

The fluid injection was initiated at a lower rate of 15 ml/min to displace dead volume of the plumbing. After displacement of the dead volume, the injection of fracturing guar fluid was immediately started at the design flow rate of 500 ml/min. The AE data was being collected continuously from the saturation phase to the end of the test. The AE data collection timing was also synchronized with the fluid injection timing for post fracture data analysis. In tests 1 and 3, injection was performed until a total of approximately 500 ml of fluid was injected into the sample while approximately 450 ml of fluid were injected during test 4. During the injection process, the injection pressure curve was monitored in real time. The results are reported in Section 5.4. After the injection phase was completed, the fractured sample was kept under the

final stress conditions overnight, to allow the cross-linked guar fluid to cure while being in contact with the sample.

Acoustic monitoring

Acoustic monitoring was successfully employed to monitor the process of hydraulic fracturing in test 1 and 4. Based on the pilot study in test 1, the application of both ultrasonic transmissions and acoustic emissions was improved in test 4 to obtain information about the evolution of the fracture geometry with time. In this test, the sensors were concentrated in the injection source locale in order to increase monitoring of the spatial resolution during the early stages of fracture growth. The sensors were positioned in the plates parallel to the preferred fracture plane, to optimize the collection of useful data. The implementation and results of this technique are discussed in detail in Chapter 6.

Fracture Excavation

After the fracture had been allowed to dry and solidify overnight, inside the sample, the excavation process began. The can was taken out of the loading frame and placed on a flat table top. Upon inspection of the outside of the can in test 4, it was observed that the blue fracturing fluid had leaked out on the bottom part of the west wall. The top loading plate and the top urethane plate were removed, thereby exposing the top of the block sample for excavation. Care was taken to not break the solidified fracture during excavation. The blue and red dyes on the fracturing fluid helped with the identification of the fracture contours and limits. Layers of the particulate material were carefully removed to expose the colored leak-off zone of the fracture. The morphology of the colored zone was traced and closely followed in separating the fracture and leak-off from the surrounding sample material. In test 1 the fracture reached the bottom boundary. The fracture also reached the bottom boundary in test 4, before it traveled on the bottom boundary to the west wall boundary and upwards on the west wall and then stopped. In test 4, it was observed that the fracture tip was blue in color while the red fluid was on the sides of the solidified fracture. The fracture plane was generally slanting from the center at the top and towards the west wall at the bottom in test 4. During excavation, it was increasingly harder to

remove layers of the surrounding sample material closer to the leak-off perimeter of the fracture in all three tests. It appears there was more consolidation of the material closer to the fracture than further away from the fracture. We have also observed this phenomenon in our low stress regime tests at Georgia Tech. The Figure below shows pictures of several stages of the excavation process in tests 3 and 4. At the end of excavation in test 4, we were able to remove the bottom flow tube and clearly observed that it was severely clogged.

Figure 5.13: Images showing early stages of excavation for test 3.

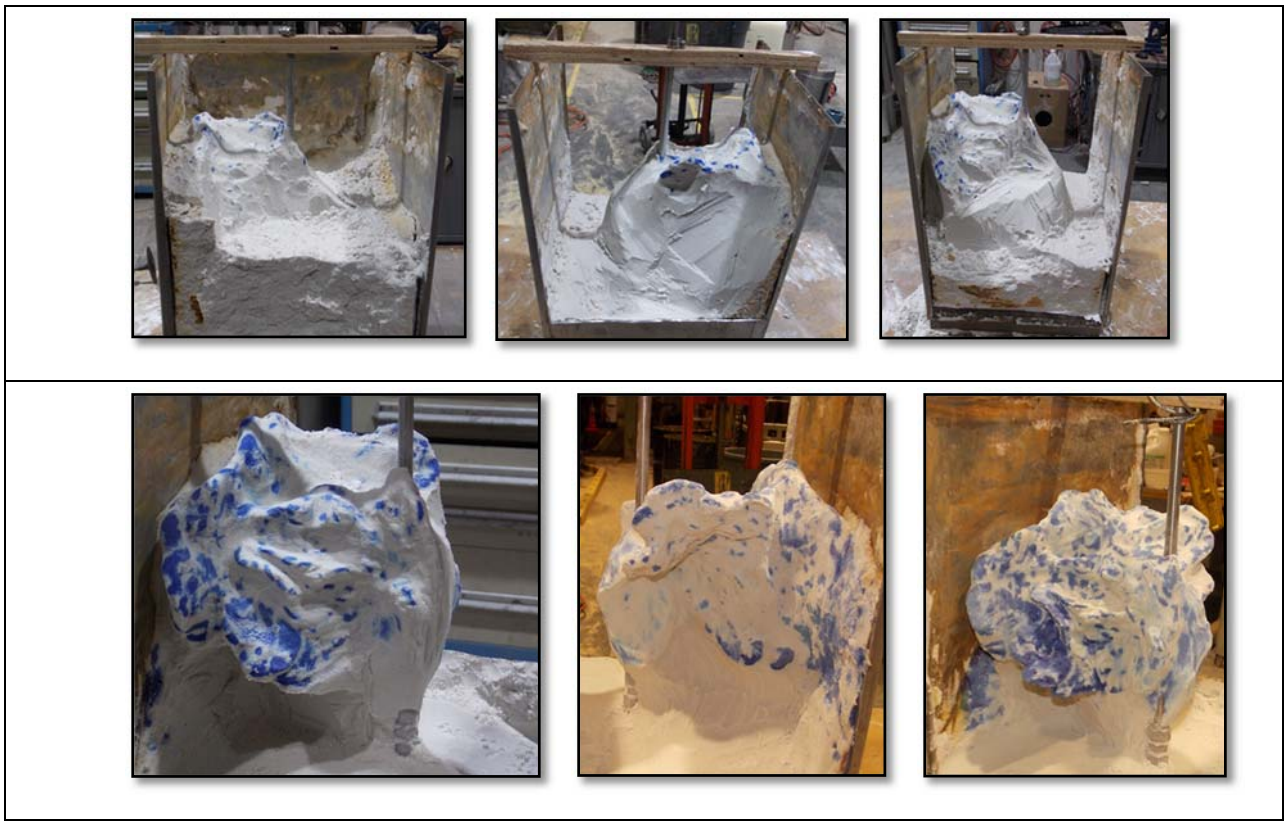

Figure 5.14: Images showing mid to late stages of excavation for test 3.

The permeability of the sample materials was measured for low stress triaxial tests, but block sample permeabilities for high stress true-triaxial tests were not measured due to time constraints. As increasing stress closes and compresses the pore space, permeability at high confining stresses will decrease [*Wang et al.,* 2016]. However, our experiments were conducted in such a way that the block sample material was not allowed to consolidate over significantly long periods of time but fractured immediately after applying the high confining stresses. Also, based on our volumetric measurements of fluctuations in pore water volume from the saturation phase to the point of the test run, the permeability of the sample was still within the measured range.

Figure 5.15: Several image views of final fracture for test 3.

Figure 5.16: Pictures of several of the early stages of the excavation process from test 4.

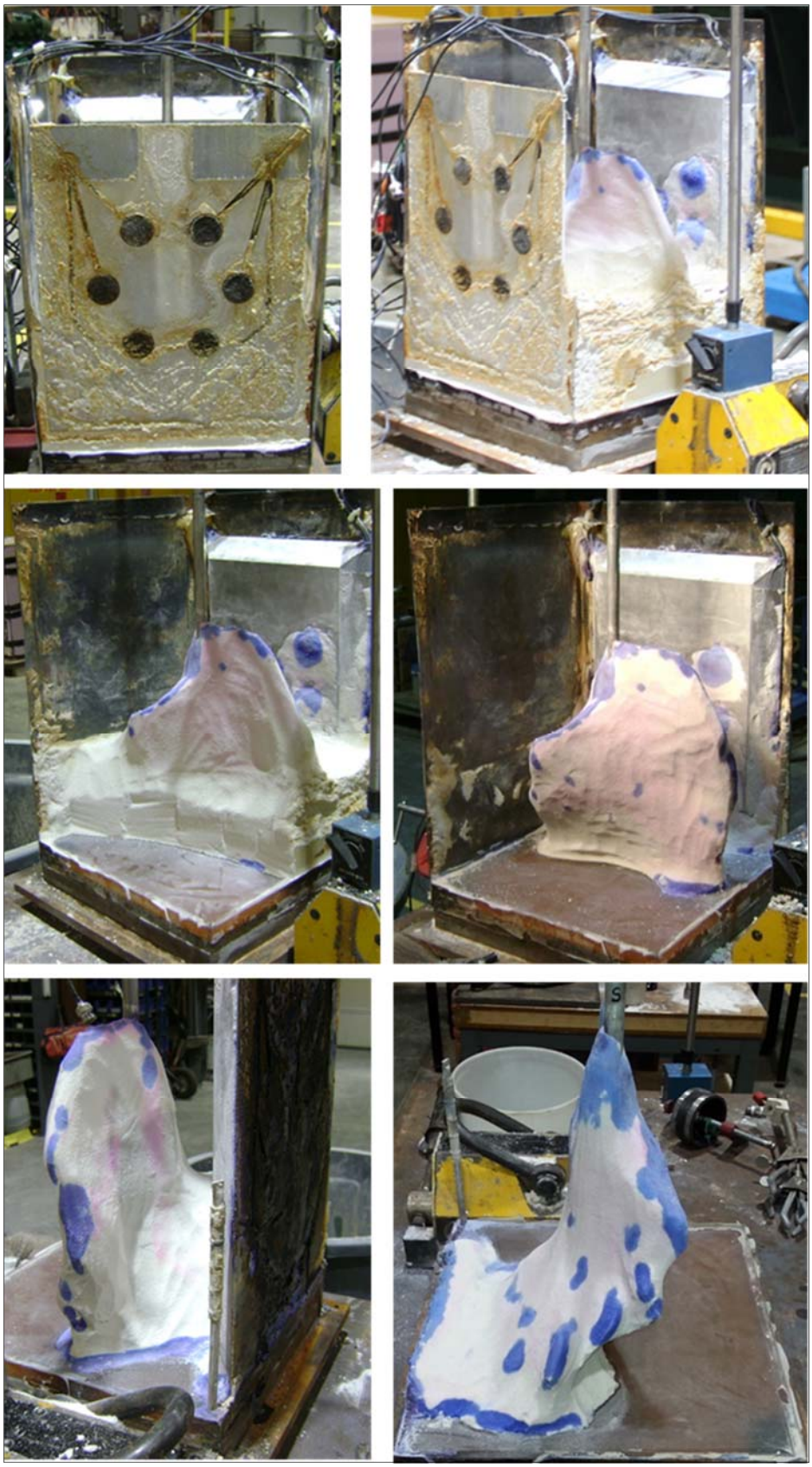

Figure 5.17: Several pictures of the mid to late stages of the excavation process from test 4.

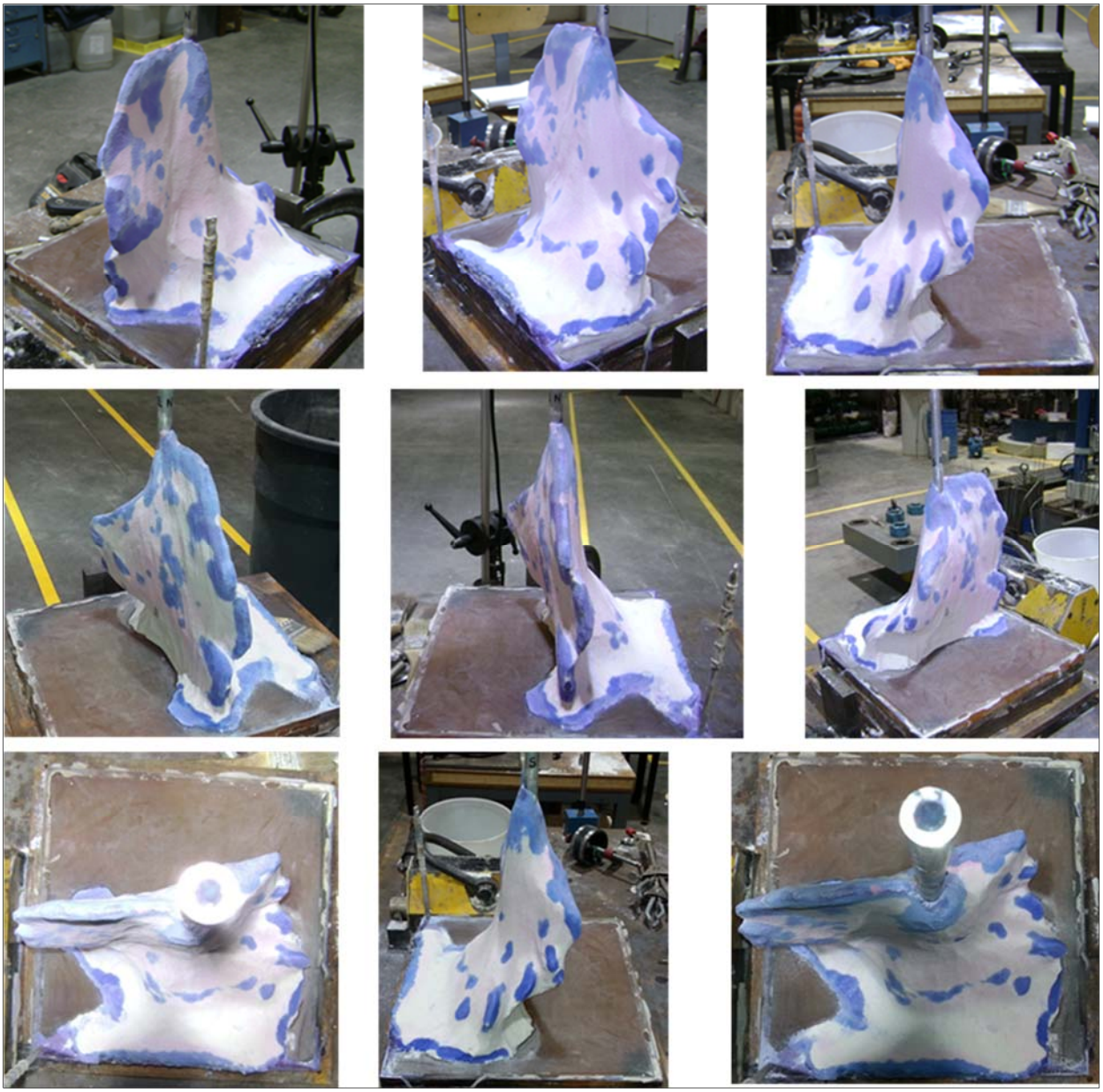

Figure 5.18: Pictures of several views of the final fracture after excavation was completed in test 4.

CT Imaging

Computed Tomography (CT) imaging was conducted on the solidified fracture in all four tests. This technology uses computer processed x-rays to make cross section images (virtual slices) of specified areas of the scanned object. This allows the user to observe what is inside the object without having to cut it open. The CT scan was set to take cross section images at 1 mm intervals. The data points thus obtained were used for a 3D reconstruction of the fracture (see Appendix B). In tests 1 and 3, the stainless steel injection source was carefully detached from the fracture before the fracture could be placed in the CT imaging machine. On the other hand, in test 4 the aluminum alloy 6061 injection source was not detached from the fracture during placement in the CT scan machine. Therefore, the fracture CT scan in test 4 underwent the least amount of disturbance. The fracture was scanned in a perpendicular direction to the axis of the injection source as shown in **Figures 5.19** and **5.20**.

Figure 5.19: Fracture from test 3 placed in CT-machine with scans taken perpendicular to injection source axis.

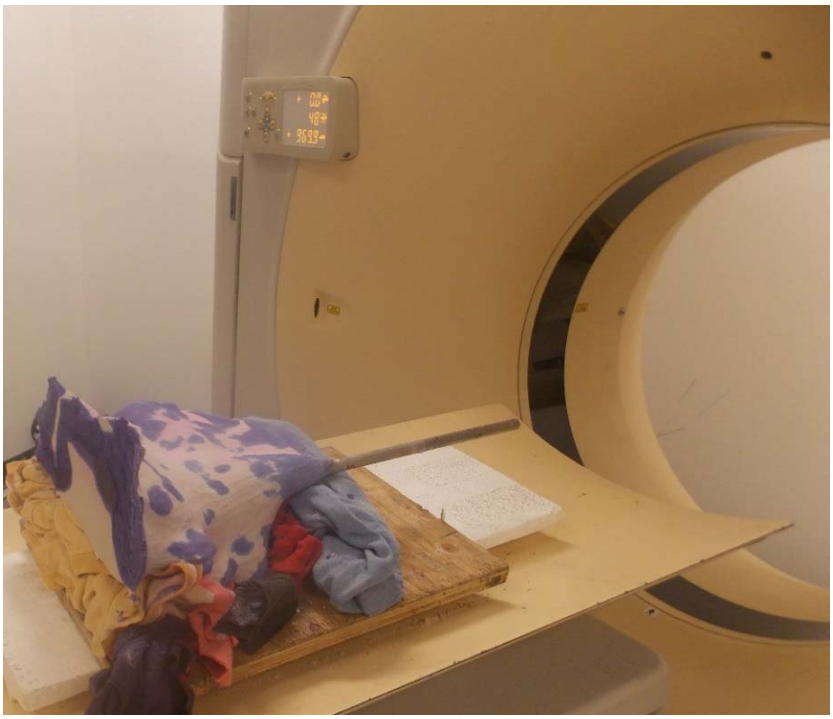

Figure 5.20: Fracture placement in CT-scan machine for test 4. Scans taken perpendicular to injection source axis at one scan per 1 mm.

5.3.1. Large block sample (Test 2)

Block Sample Preparation

The main purpose of the large block sample test was to study the effect of size on the behavior of hydraulic fracturing in particulate cohesionless materials. In this section, we describe the experimental processes and procedures that were followed in test 2. The block sample for this test was prepared on site from a mixture of 80% silica sand USM100 and 20% silica flour SIL_CO_SIL 106. Oven dried samples of these materials were weighed and mixed in a roller drum mixer.

When a satisfactory mixture consistency had been achieved, the sample was compacted in the large pore-can in 3 inch loose layers. The pore-can dimensions were 28.5 in × 28.5 in × 35.5 in. In comparison to the small block pore-can, the large pore-can was approximately 16 times larger in terms of volume. The large compacted block sample was also larger than the small block sample by 16 times in terms of sample mass. The two sizes of samples allowed us to compare and contrast the boundary effects on the fracturing processes in the four tests. We used the same compaction method that was used for the small block samples and compacted the large block to a density of 0.069 lb/in^3 (1.9 g/cm^3). Twelve layers of approximately 165 lbs each were compacted. Stress films were attached to all the lateral faces of the large pore-can both on the inside and on the outside. This was in order to check for the homogeneity of the confining stresses on the block sample. The uniform color of the stress film after the test, illustrates that the stress loadings on the faces of the block sample was homogenous (**Figure 5.25**).

After the sample compaction was completed, the top layer was leveled off and caped with urethane. The urethane was allowed to set and solidify overnight before the top plate could be placed. The pore-can was then placed in the loading frame. Flat-jacks were placed on each of the four lateral sides of the pore-can and connected to the hydraulic actuator system, which, in turn, was connected to the central control computer. A highly incompressible oil fluid was used in the actuator so that pressure could be transmitted to the attached flat-jacks instantaneously when applied. The lateral loads were applied on the sample by applying hydraulic pressure on the flat-jacks. The top and bottom stresses were applied by hydraulic rams directly to the end platens of

the sample. The loading was applied so that equal pressure was applied on opposite sides of the sample and the three principal stresses, $\sigma_1, \sigma_2, \text{and } \sigma_3$ were controlled independently. As mentioned above, in tests 3 and 4, loads were applied from both the top and bottom, whereas samples 1 and 2 received loads only from the top with the bottom plate being rigid. **Figures 5.21** through **5.23** show the various stages of the sample preparation process.

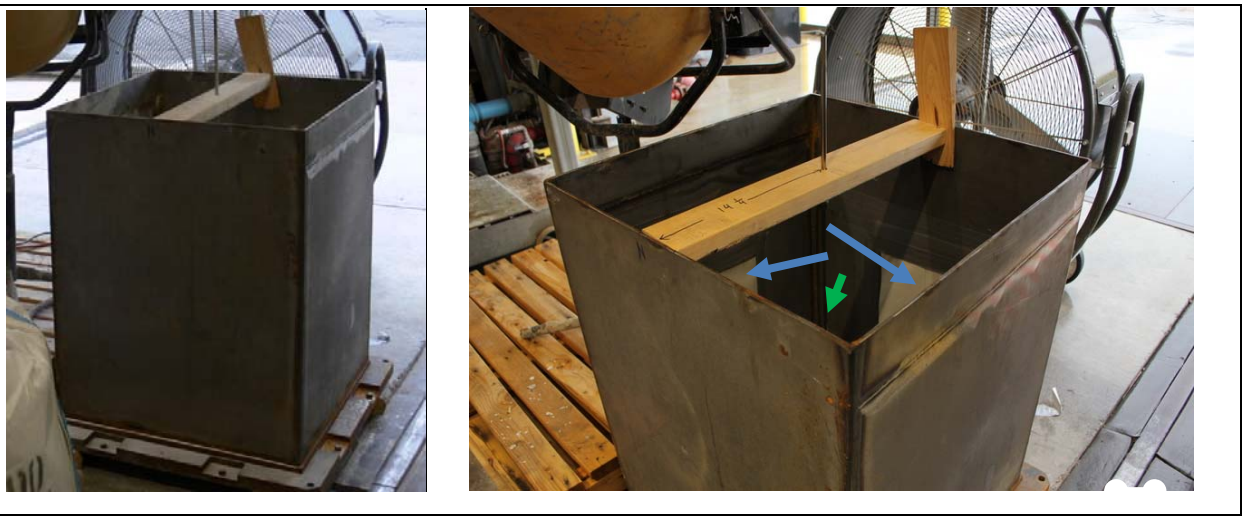

Figure 5.21: Large pore-can (28.5 in × 28.5 in × 35.5 in) with injection source and stress film installed (marked by the green and blue arrows, respectively).

Figure 5.22: First stage of sample preparation. Stress film (marked by blue arrows) attached to lateral faces of pore-can and also on top of the urethane.

Figure 5.23: Placement of the large pore-can (28.5 in × 28.5 in × 35.5 in) into the loading frame.

The next phase of the sample preparation process was the saturation of the block sample. Confining loads applied to the sample were σ_1 = 600 psi, σ_2 = 300 psi, and σ_3 = 300 psi. Vacuum was applied through the injection source for approximately 2 hours. A vacuum reading of 25 psi was obtained. Then, the sample was flushed with CO_2 from the top inflow tube at a pressure of 50 psi for approximately 2 hours. After that, the sample was flushed with vacuum overnight.

After these steps, saturation was started by injecting water from the top inflow tube while the injection source was under vacuum. The block sample was held under these conditions for 24 hours while monitoring the total amount of water that was injected. After 24 hours, vacuum

was removed from the injection source and the amount of water outflow was measured. When better than 95 % saturation was achieved, the saturation process was stopped.

After the saturation phase, the block sample was loaded to the test loads of σ_1 = 1600 psi, σ_2 = 1200 psi, and σ_3 = 800 psi. The sample was allowed to stabilize under these loads for a few minutes. The top flow tube was left open to accommodate drained loading conditions. Fracturing fluid injection was initiated at a lower rate of 15 ml/min to displace dead volume in the plumbing. After displacement of the dead volume, the injection of the fracturing guar fluid was immediately started at the design flow rate of 500 ml/min, and 500 ml of fracturing fluid was injected into the sample. Similar to the small block test, the injection pressure curve was monitored in real time. The results are reported in Section 5.4. After the injection phase was completed, the fractured sample was kept under the final stress conditions overnight to allow the guar-based fracturing fluid to cure while being in contact with the sample.

Fracture excavation

After the fracture had been allowed to dry and solidify overnight, inside the sample, the excavation process began. The pore-can was taken out of the loading frame and placed on a flat surface. The top loading plate and the top urethane plate were removed, thereby exposing the top of the block sample for excavation. Care was taken to not break the solidified fracture during excavation. The blue and red dyes on the fracturing fluid helped with the identification of the fracture contours and limits. Layers of the particulate material were carefully removed to expose the colored leak-off zone of the fracture. The morphology of the colored zone was traced and closely followed in separating the fracture and leak-off from the surrounding sample material. Figure 5.24 shows pictures of several stages of the excavation process in test 2.

Figure 5.24: Stages of fracture mineback in test 2.

Figure 5.25: Fracture excavation and the uniform red color on the stress film (indicated by arrow) showing that applied stresses on the loaded faces were homogenous.

Figure 5.26: Fracture excavated in test 2.

CT Imaging

CT imaging was also conducted on the solidified fracture from test 2. In this test, the stainless steel injection source was carefully detached from the fracture before the fracture could be placed in the CT imaging machine. Stainless steel is known to cause interference with the x-rays and compromising the quality of the CT images. The fracture was scanned in a perpendicular direction to the axis of the injection source as described in Section 5.3.1. The results of the CT scanning are presented and discussed in detail in Section 5.4.

5.4. EXPERIMENTAL RESULTS

In this section and in Chapter 6, the results of our experimental series (tests 2, 3, and 4) are presented. This section focuses on characterization of the fracture morphologies, pressure signatures, evidence of plastic deformation mechanisms, and the characterization of the main factors that affect hydraulic fracturing in cohesionless, sediment-like particulate materials. Chapter 6 focuses on results of acoustic monitoring in our experiments. In this section, the test results for the small block sample and the large block sample are grouped and presented separately. Test 1 was conducted as a preliminary experiment in order to study feasibility and to improve the experimental design for our subsequent full scale tests. The results of this pilot study are reported in detail by *Hurt* [2012]. For each test discussed below, we first present a characterization of the fracture morphologies. Then the pressure signatures and flat-jack volumetric responses are discussed, followed by a presentation of evidence of plastic deformation mechanisms.

5.4.1. Small block results (Test 3)

Fracture geometry and orientation

The resulting fracture was predominantly vertical and showed complexity. The main wing propagated in the direction perpendicular to σ_3 and branched into two parts as it approached the boundary on the north wall (**Figure 5.1b**) of the block sample. One of these wings reached the boundary. The branching of the main fracture wing may have been caused by fracture tip

interactions with the boundaries. The fracture was thick with several “bubbly” spheroidal features on its surface. The main fracture was also asymmetrical about the injection source. The average fracture height was approximately 4.5 in and the fracture length was approximately 7.5 in for the longest wing. The front thickness was approximately 0.25 in (aperture plus leakoff). **Figures 5.27**, **5.28**, and **5.29** show the main features of the fracture from test 3.

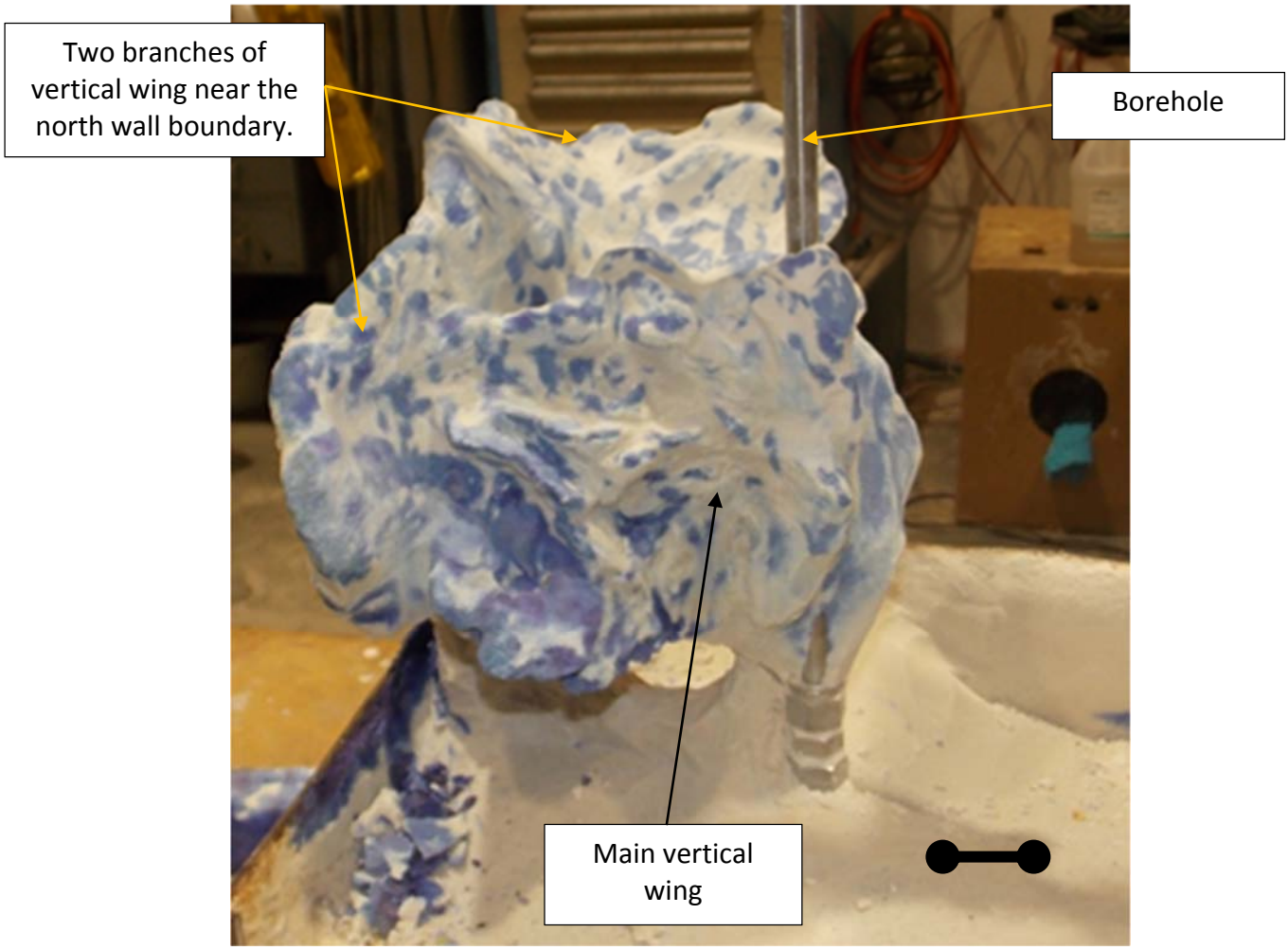

Figure 5.27: Excavated fracture for test 3 showing main vertical. Branching of the main wing may have been due to boundary effects.

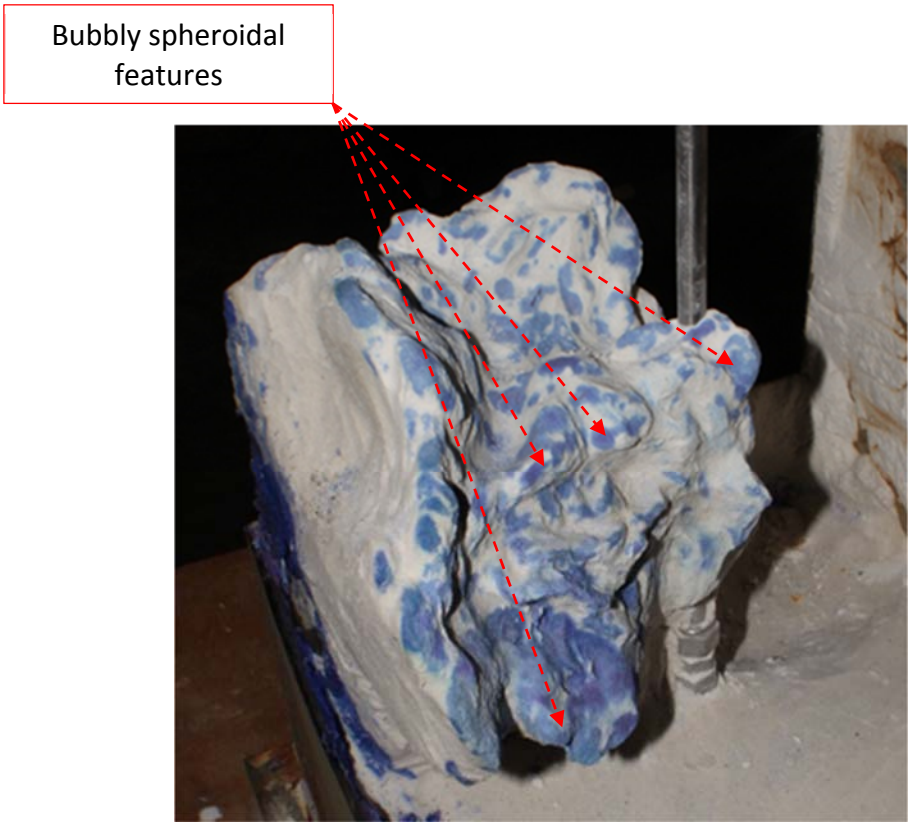

Figure 5.28: Fracture from test 3, showing bubbly spheroidal features.

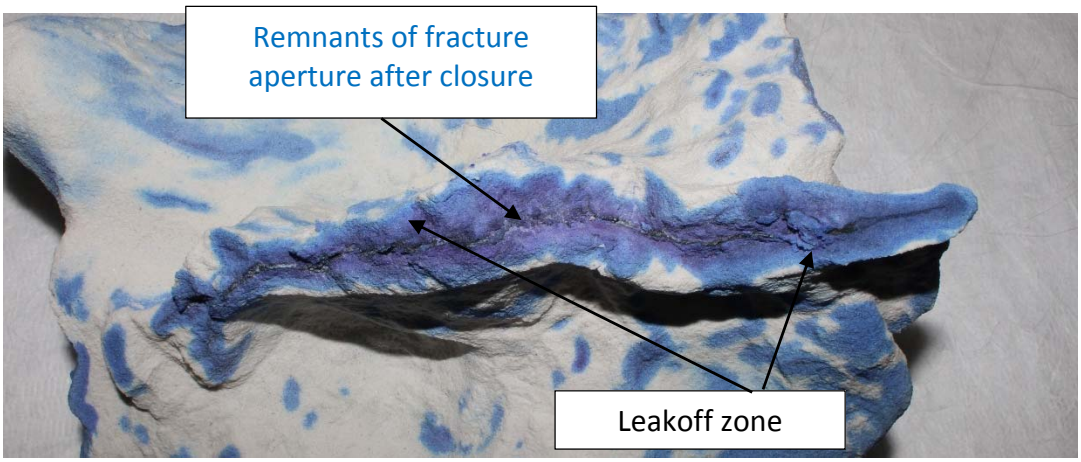

Figure 5.29: Sectioned fracture from test 3 exposing the fracture aperture remnants and leakoff zone.

Injection pressure signature

The injection pressure results for test 3 are shown in **Figure 5.30**. The pressure curve was generally smooth during fluid injection. There is a linear rise in the injection pressure before peak pressure is reached. We interpret this part of the curve as the cavity expansion phase. A "kink" in the pressure curve appears at approximately 4775 psi. This "kink" in the pressure curve may have been due to a local instability such as shear bands emanating from the expanding cavity or

the initiation of a small fracture. Both these instabilities may have resulted from the dilation of the sample material. After the "kink" but before the peak pressure, the injection pressure curve begins to flatten prior to the sharp drop in pressure that occurs at the peak pressure. This flattening in the curve may be a consequence of the beginning of a softening mechanism such as fluidization. Fluidization occurs when particles lose their inter particle forces due to increases in pore pressure [e.g., *Wu,* 2006]. The mechanism of fluidization is equivalent to liquefaction in soil mechanics terms, where the effective stress becomes zero when the total stress is equal to the pore pressure.

A peak pressure of 7800 psi was recorded before a sharp drop in the injection pressure. The rise in pressure followed by a sharp drop is consistent with hydraulic fracture behavior. The ratio of the peak pressure to minimum principal stress was 9.8 and was nearly identical to that in test 2. After the peak, the pressure dropped below σ_1 but remained greater than σ_2 (and σ_3). There was a small pressure rise during the propagation phase. This small increase in pressure during fracture propagation may have been due to the fracture interacting with the boundaries. These pressure behavior observations are consistent with the fracture propagating in a direction perpendicular to the minimum principal stress direction and the fracture opening in a direction parallel to the minimum principal stress direction. After the injection pump is stopped, there is a gradual decay in the curve during fracture shut-in before the curve becomes flat at a constant value of approximately 1300 psi.

As stated in Section 5.3, dead volume was displaced out of the plumbing by injecting at low rates in the beginning of the experiments (**Figure 5.30**, **5.39**, **5.48**). In all our true-triaxial tests there was a delay in the pressure response during the transition from the low injection rate of 15 – 30 ml/min to the design injection rate of 500 ml/min. This was due to the presence of water in the plumbing left over from the saturation phase. Therefore, water was being displaced from the injection source into the formation during this transition. Due to the low viscosity of water, the pressure generated by the water diffusion into the formation was minimal relative to the pressure generated by the injection of the fracturing fluid.

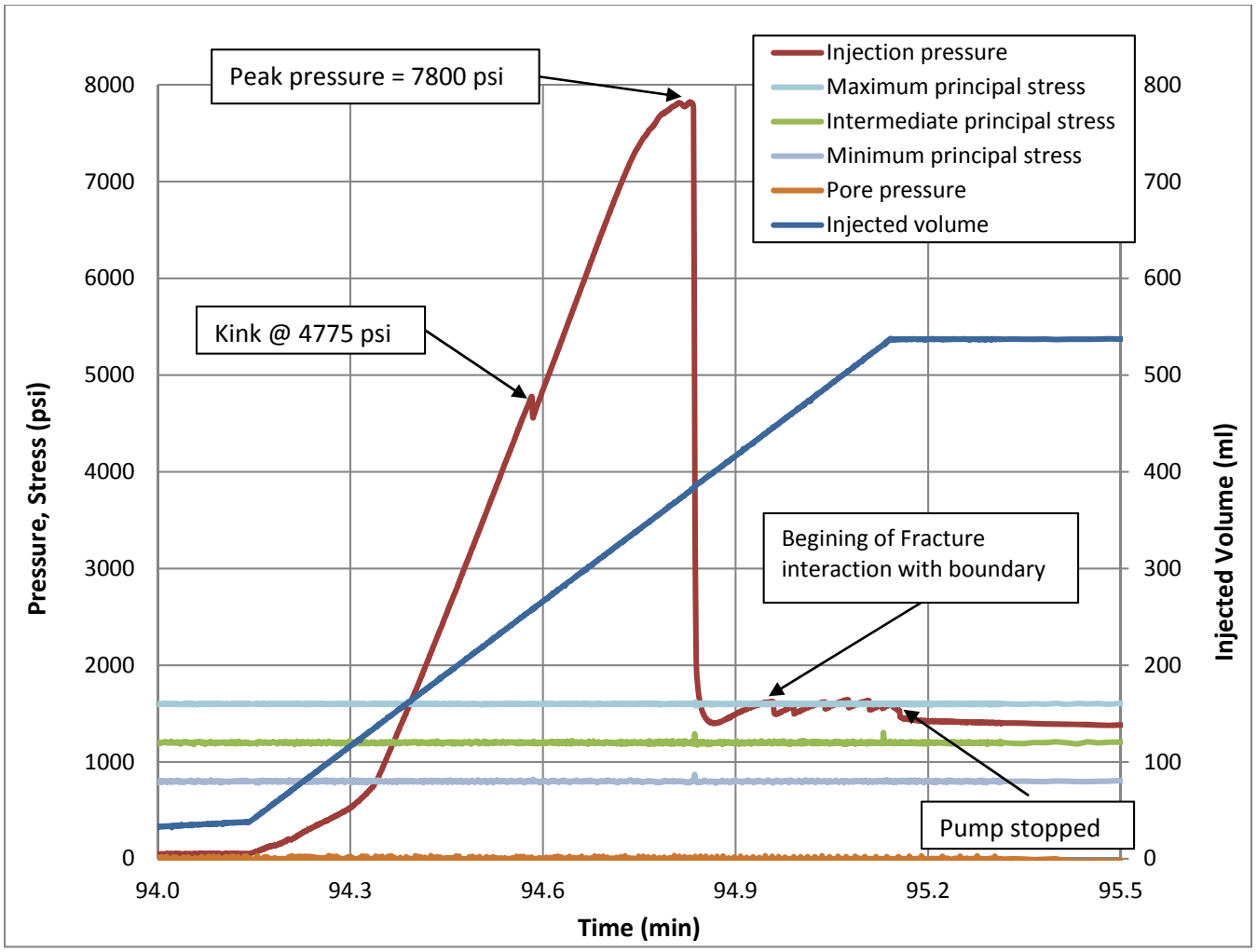

Figure 5.30: Pressure-time dependence for test 3.

Flat-jack volume response

Figure 5.31 shows plots of the flat-jacks volumetric responses with the injection pressure curve. Before the peak pressure, there is a small decrease in ΔV_3 coinciding with the kink in the pressure curve. This response may be attribute to the dilation of the sample due to shear bands emanating from the expanding cavity zone near the injection source or due to the formation of a small fracture. Between the kink and the peak pressure, ΔV_3 begins a gradual drop. This response may have been to the dilation of the sample due to cavity expansion. It may also have resulted from the possible fluidization mechanism at this stage. At the point of the peak pressure, there are sharp drops in ΔV_3 and ΔV_2. This may have been due to the fracture opening in a direction parallel to σ_3. Therefore, the drop in the flat-jack volume in the intermediate principal stress direction

may have been due to the fracture propagating perpendicular to σ_3. After this, ΔV_2 continues to drop. This may have been caused by interaction between the fracture and the boundaries. After the injection stop, there was a small increase in ΔV_3. This response may have been an indication of contraction during fracture closure.

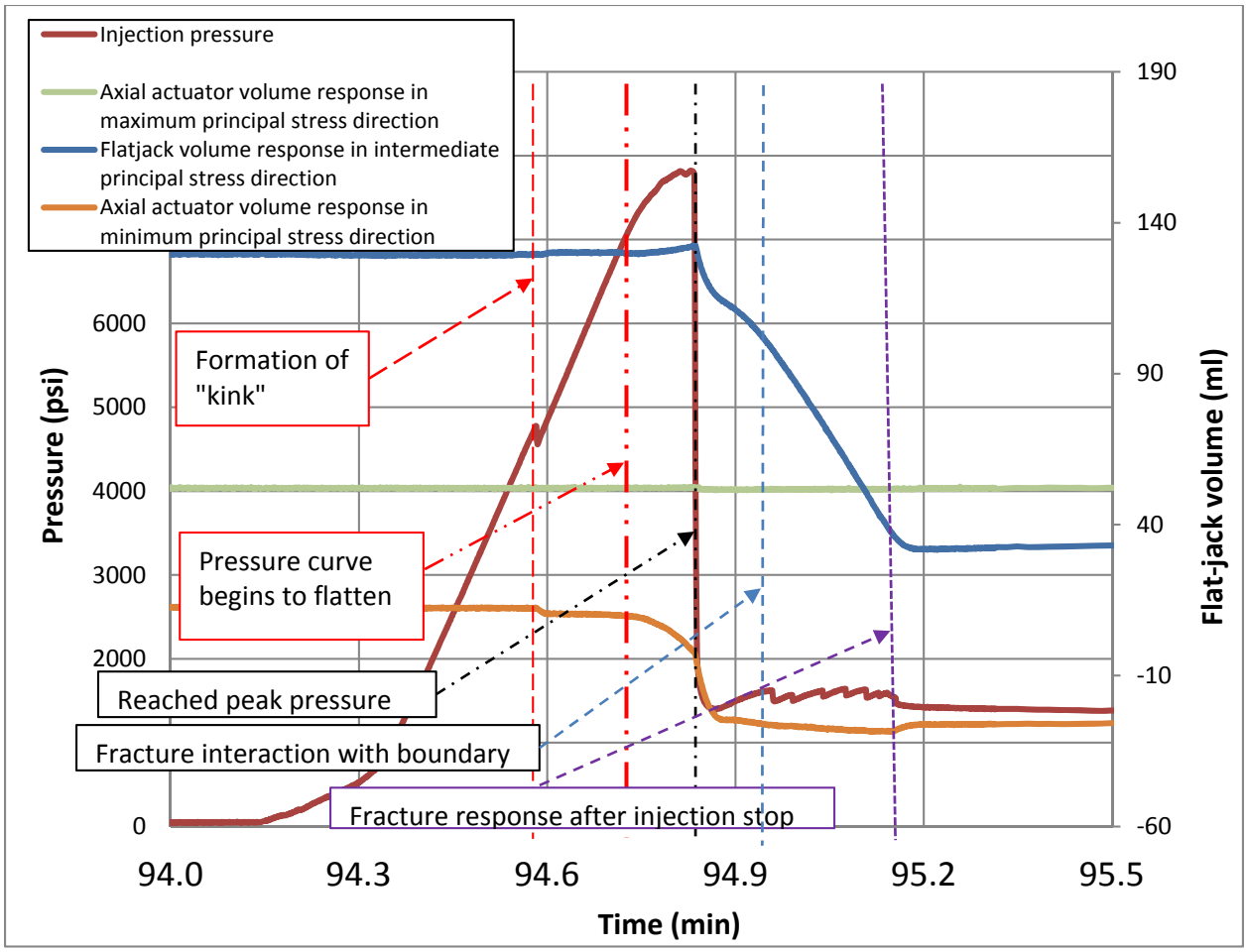

Figure 5.31: Volumetric flat-jack response compared to injection pressure curve.

Evidence of shear bands and other plastic deformation features in test 3

Small scale details of the fracture profile were obtained from CT images of selected cross-sections of the fracture plane. Results of CT scans from test 3 are presented in **Figures 5.32** through **5.35**. An important feature of this work was the observation of shear bands in hydraulic fracturing of cohesionless particulate media in true-triaxial loading. Shear bands are defined as narrow zones of large shear strain gradients, developing during severe deformation of post-peak softening

materials [e.g., *Mitchel and Soga,* 2005]. In our CT scan images, we observed thin gray striations emanating from fracture aperture remains. We interpret these to be shear bands. Figures 5.32 through 5.35 and similar figures in test 4 below (Section 4.4) show important features such as strain localization, manifesting shear bands, evidence of cavity expansion near the injection source, and fracture initiation features. CT sectioning was performed both perpendicular and parallel to the injection source. These observations allow us to conclude that failure mechanisms during the hydraulic fracturing of cohesionless materials are inelastic.

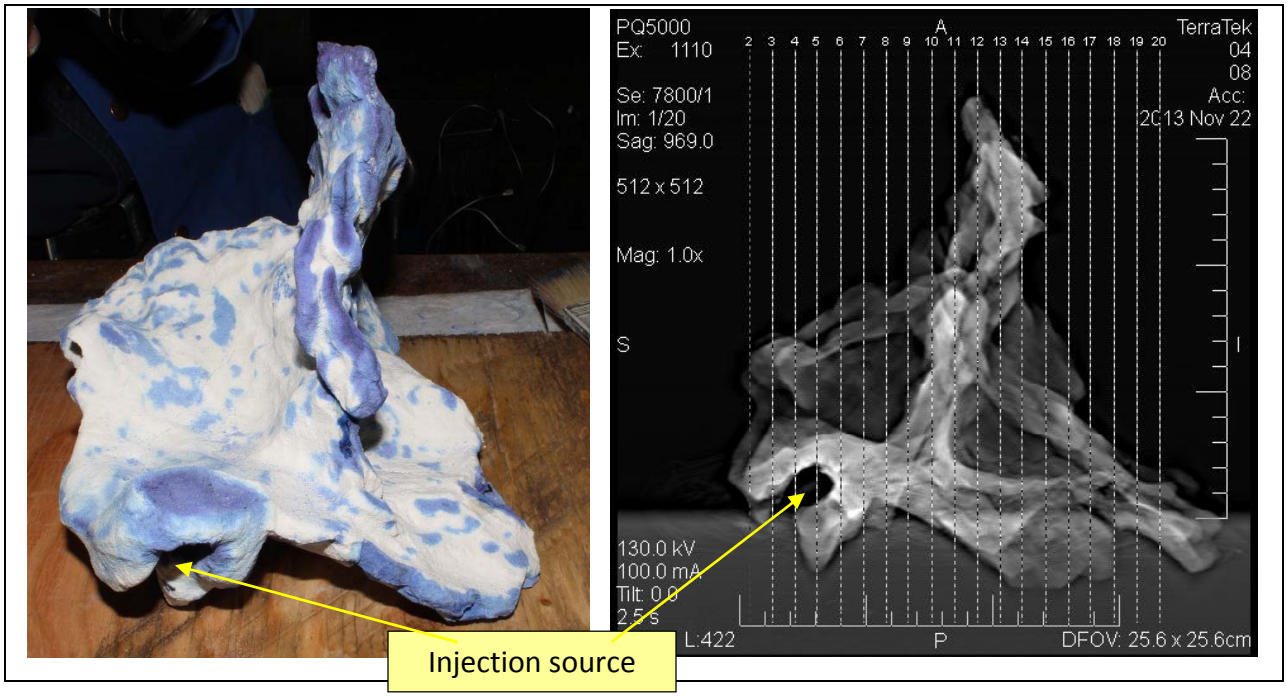

Figure 5.32: Matching CT sectioning parallel to injection source with fracture and 20 CT scan cross sections at 1 mm spacing.

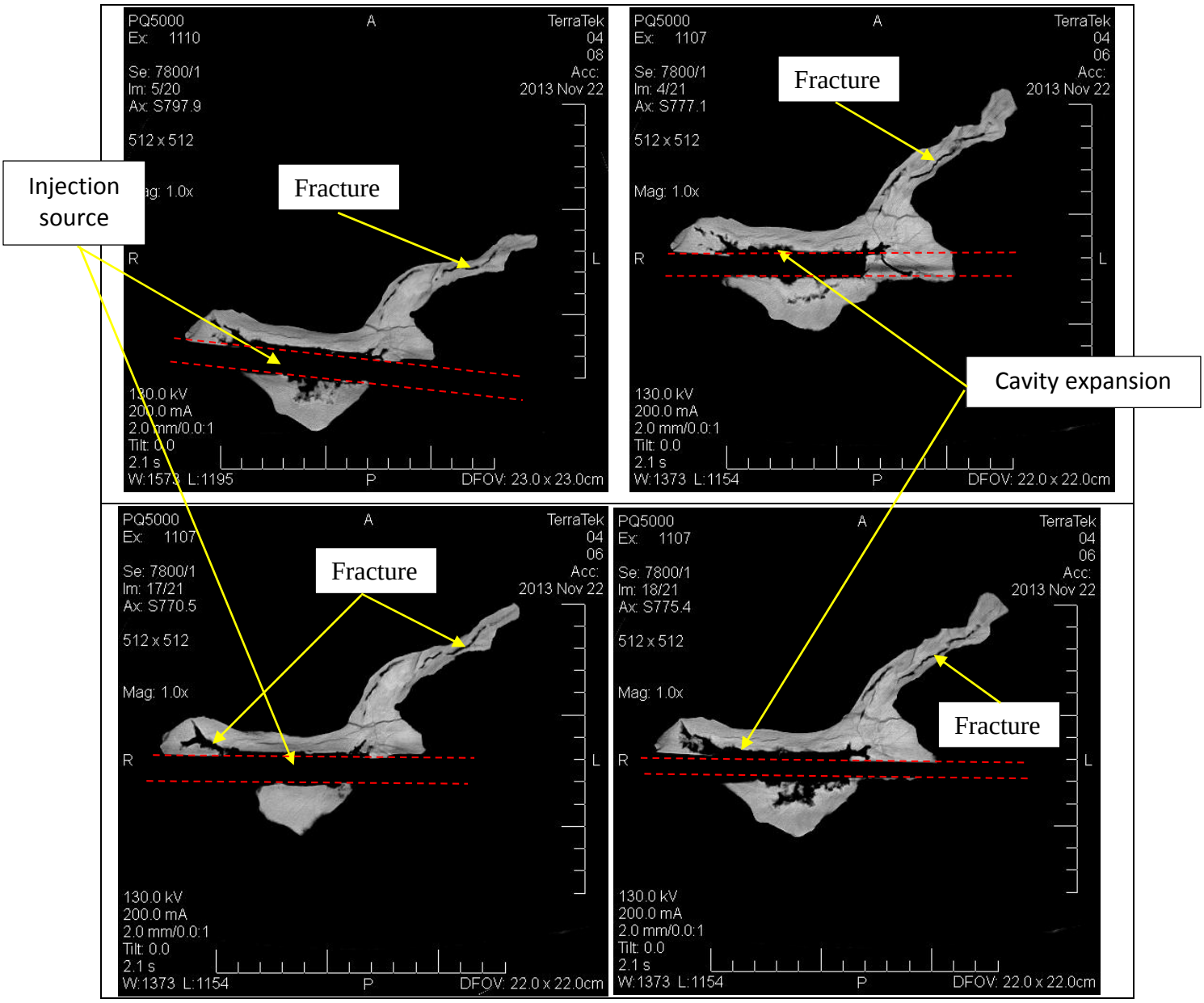

Figure 5.33: CT scan sections 4, 5, 17, and 18 showing cavity expansion. Section numbers are shown in Figure 5.32. The red dashed straight lines inside the dark areas indicate the boundaries of the injection source. The white areas represent the leakoff zone of the fracture. The dark zones between the boundaries of the injection source and white leakoff zones are areas where cavity expansion occurred.

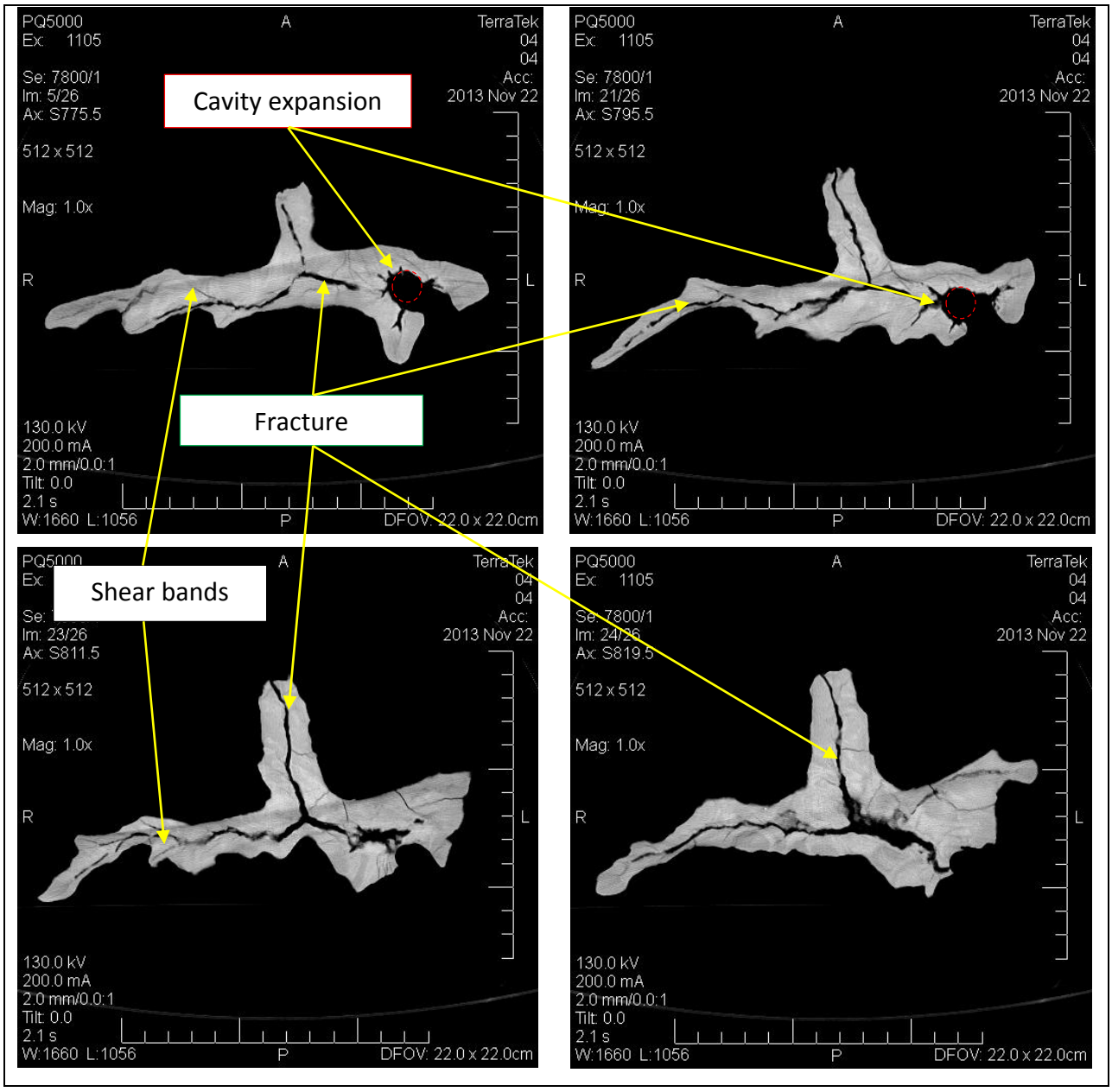

Figure 5.34: CT sections 5, 21, 23 and 24 showing shear bands and branching. The extents of the injection source are shown by the red dashed circles in the top images. The white features show the leakoff zone outside the remnant fracture aperture shown by the main black lines with off shoot gray lines. We interpret the thinner gray striations branching from the black remnant fractures as shear bands. Notice the shear bands branching at acute angles relative to the main fracture and in the direction of the fracture. The black circular zones between the leakoff zone and the extents of the injection source evidence cavity expansion.

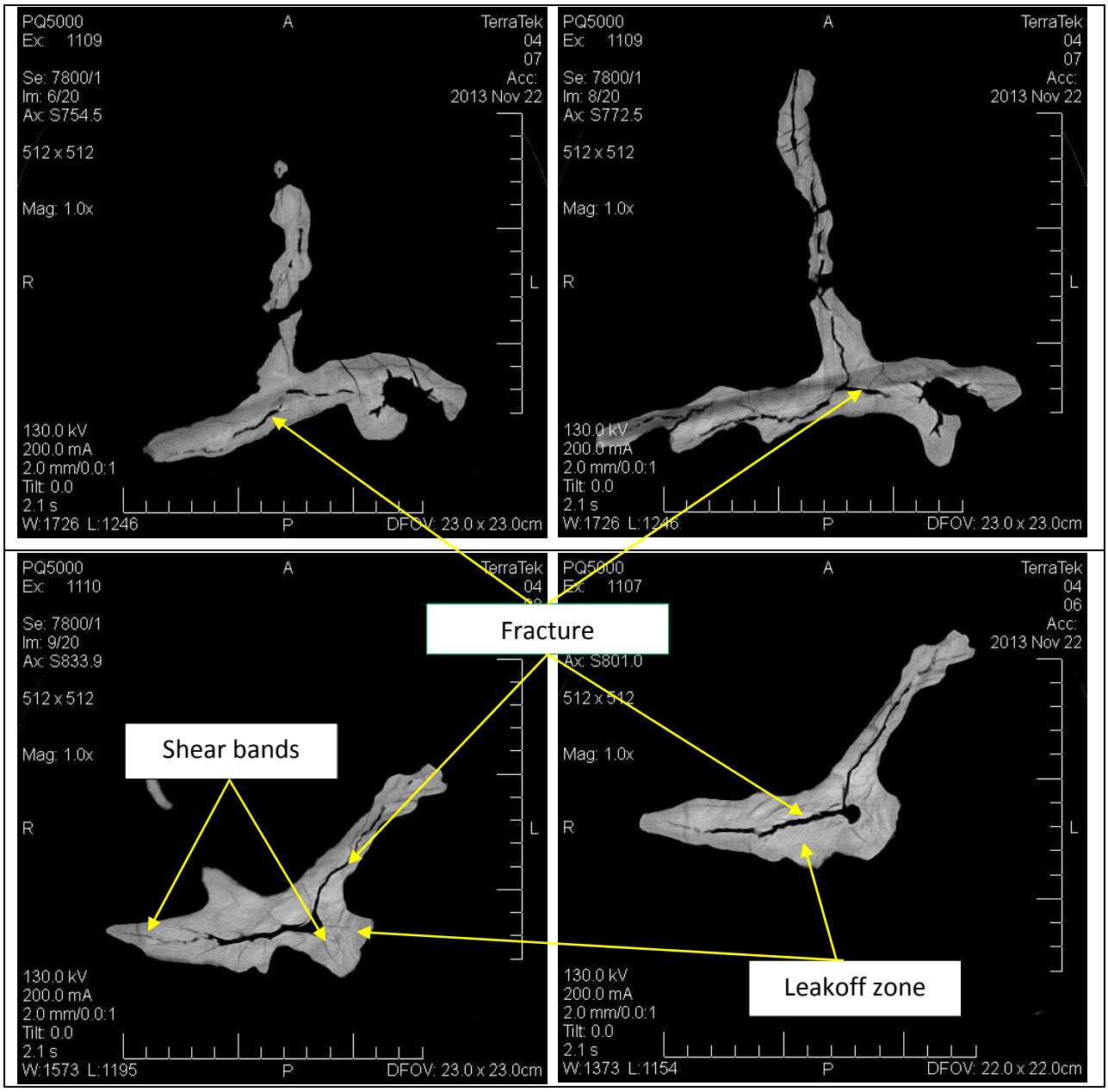

Figure 5.35: CT images from test 3 showing shear bands. The white features show the leakoff zone outside the fracture aperture remnants shown here by the prominent black lines emanating from the wellbore. The thinner gray striations emanating from the fracture aperture remnants at acute angles relative to the fractures are the shear bands. Shear bands are observed both along the length of the fracture and the outside the expanding cavity.

5.4.2. Small block results (Test 4)

Fracture geometry and orientation

The fracture had two wings with multiple segments. The fracture geometry was predominantly vertical and showed complexity. Fracture wings were asymmetrical about the wellbore with the larger wing propagating in the north direction, perpendicular to σ_3, while the smaller wing propagated in the south to south-eastern direction from the injection source (**Figure 5.36, 5.37, 5.38**). It appears that the north wing initiated and propagated first before the south wing. After the initiation of the north wing, the initiation of the south wing may have been sensitive to the new local stress field and not necessarily the remote boundary confining stresses. This is supported by the fact that the south wing propagated in the southeast direction and not perpendicular to the remote minimum principal stress. The main evidence, however, supporting the conclusion that the north wing initiated first is the acoustic emission data reported in Chapter 6. Both wings appeared to be multi-segmented with the north wing having 3 segments and the south wing having 4 segments. The fracture leakoff is thicker in the zone closest to the perforation zone and thinner (and planer) further away from the injection source. It appears the fracture was more brittle, further away from the injection zone. This may be a consequence of the block sample being well saturated in the area closest to the perforation zone and having partial saturation in the areas away from the injection source. The fracture reaches the boundary at the bottom plate. A few details of the geometry of the fracture are presented in **Figures 5.36** to **5.38**.

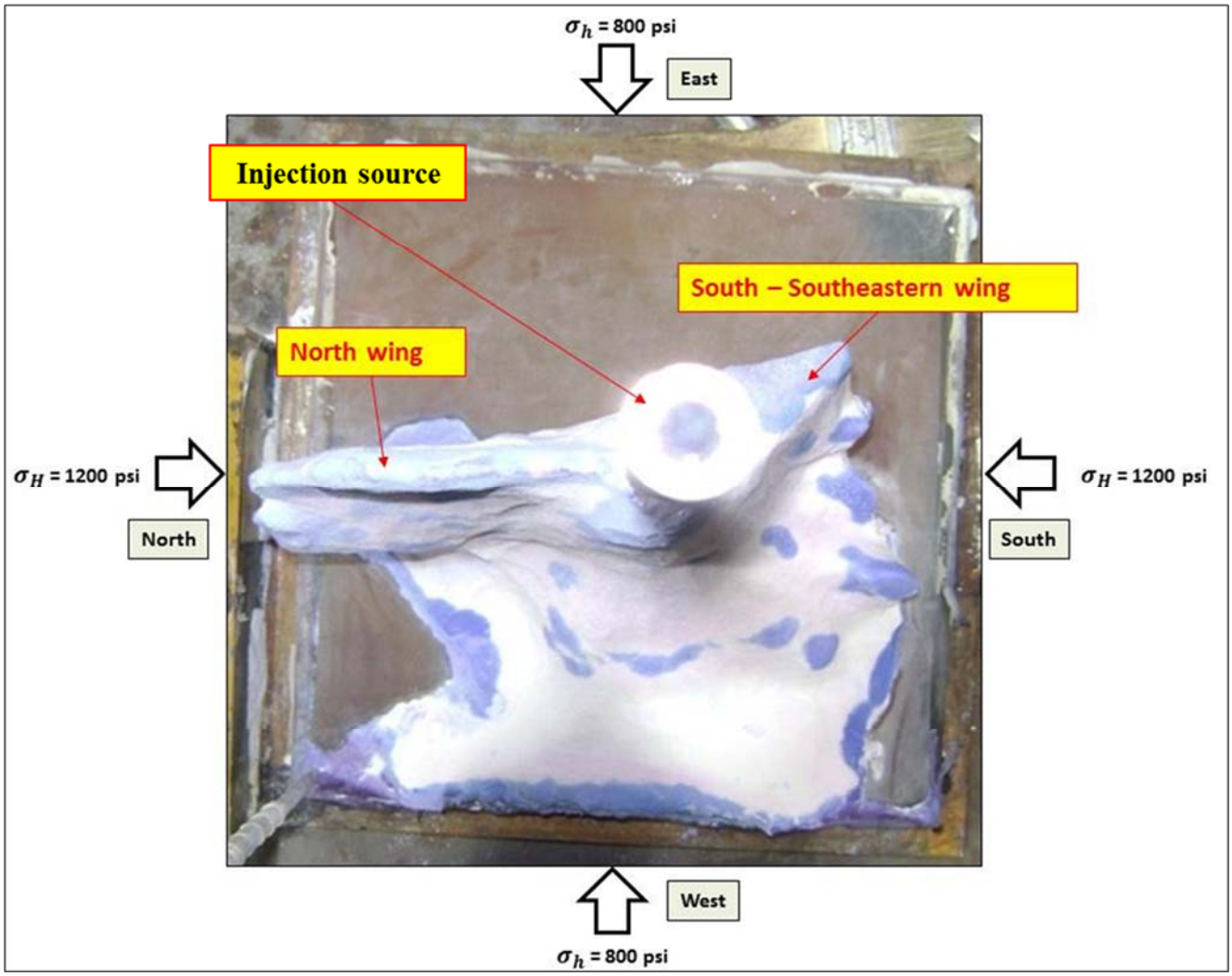

Figure 5.36: View of fracture from top and west side, showing the two wings and their segments.

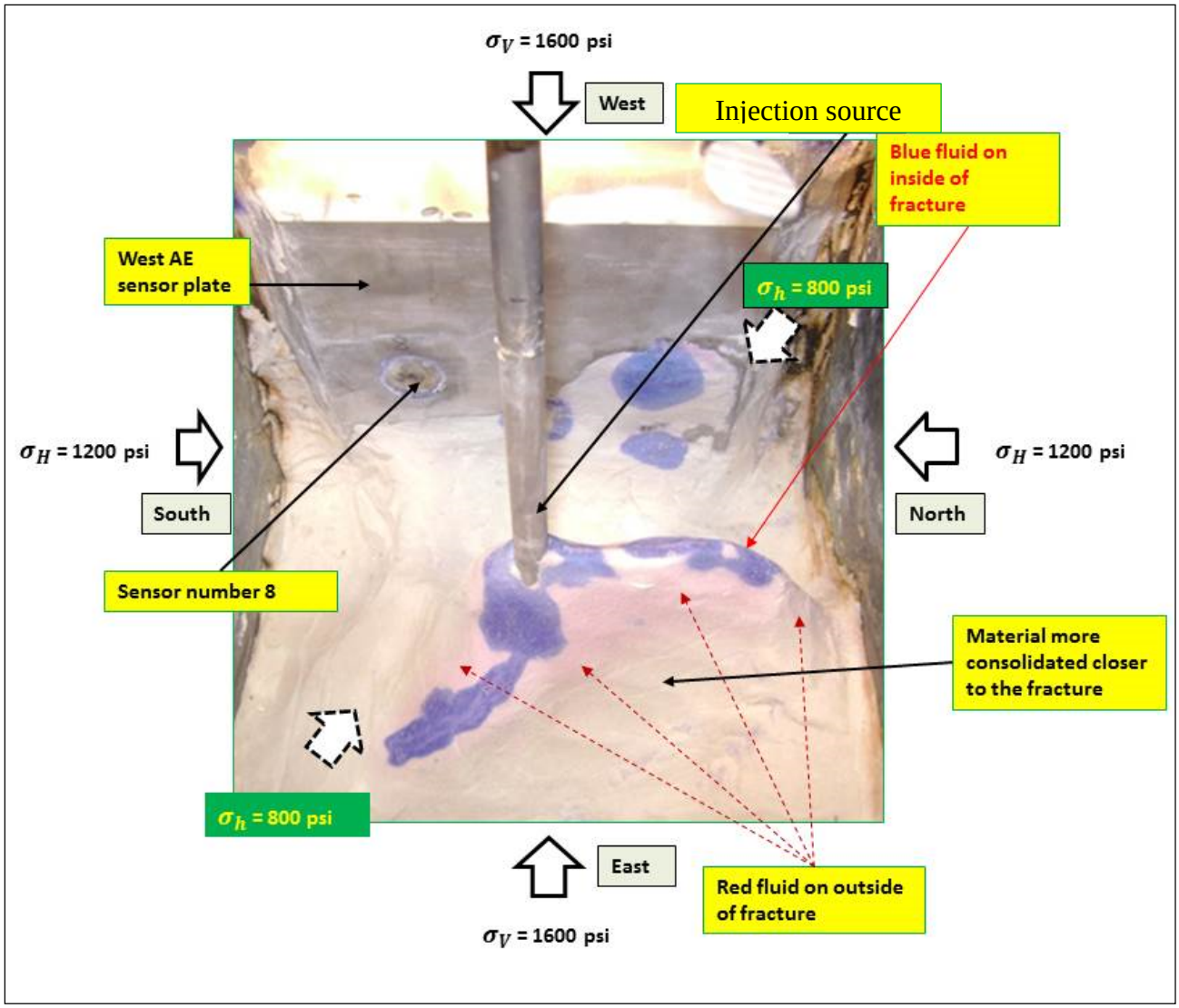

Figure 5.37: East side view from above, showing red and blue fluid localization.

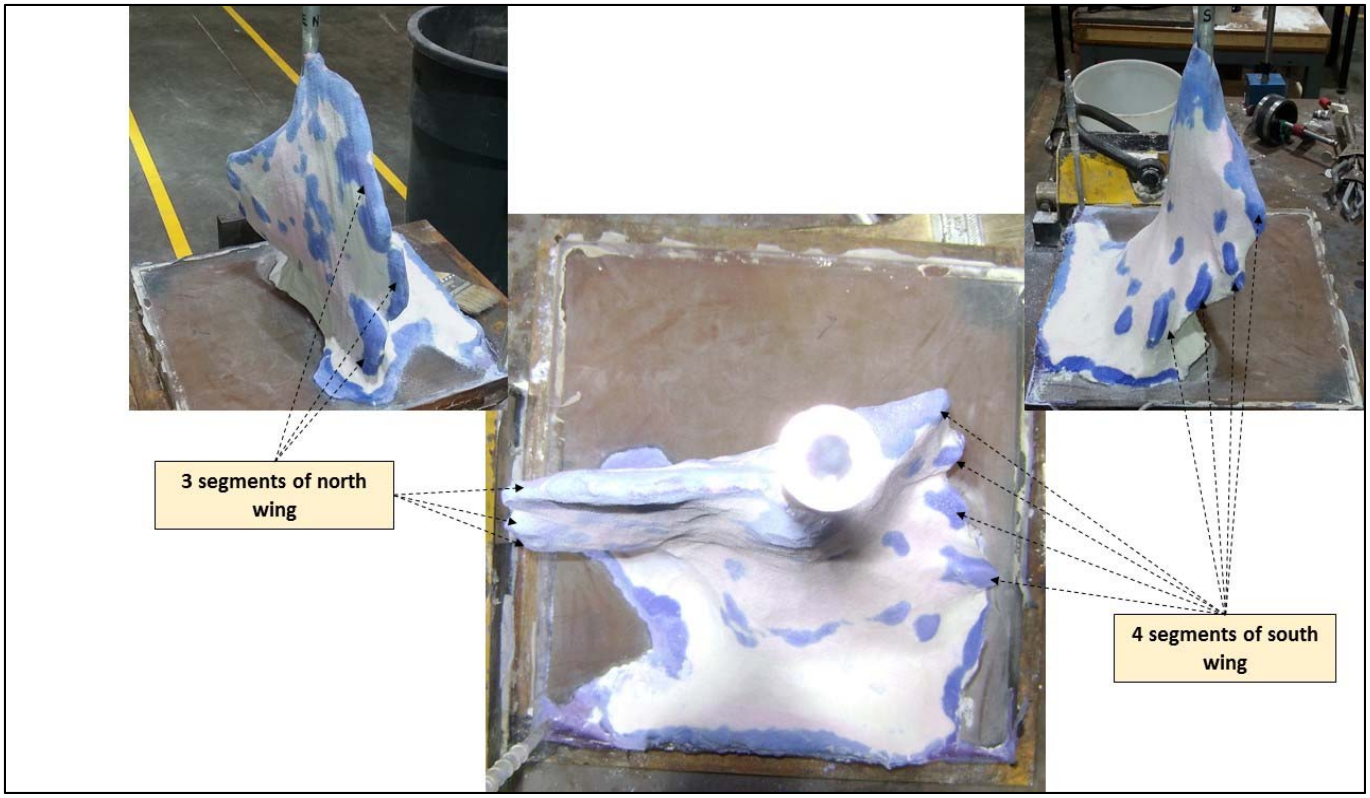

Figure 5.38: View from west side showing multiple segment wings.

Injection pressure signature

The injection pressure signature for test 4 is shown in the **Figure 5.39**. There is a linear rise in the injection pressure preceding the peak pressure. We interpret this generally linear part of the curve as the cavity expansion phase. A small "kink" in the pressure curve was observed at a pressure of 3580 psi. Similar to test 3, this "kink" in the pressure curve may have been caused by a sudden local instability such as shear bands emanating from the expanding cavity or the initiation of a small fracture. The steep rise in the injection pressure is followed by a sharp drop in pressure from a peak value of 5411 psi to approximately 1300 psi. After dropping to 1300 psi, the curve flattens at this level before a moderate increase to 1530 psi and another drop to 1200 psi before the pump is stopped at about 1230 psi. When the pump is stopped, there is a gradual decrease in pressure equal to approximately 200 psi. After that, the pressure curve flattens out and remains approximately constant at approximately 1030 psi.

It appears that after reaching the peak, the pressure drops to a value of 1300 psi, which is greater than σ_2 and yet smaller than σ_1 . The 1300 psi propagation pressure is greater than the σ_3 and therefore sufficient for the fracture tip to open parallel to the σ_3 direction. The pressure behavior is also consistent with a fracture propagating in the direction perpendicular to σ_3 . The pressure then begins to increase to 1530 psi as the fracture front approaches the boundary walls. A total volume of approximately 450 ml of fracturing fluid was injected at a rate of 500 ml/min before the pump was stopped. We interpret the gradual pressure drop of 200 psi after the pump is stopped as the fracture closure pressure (shut-in pressure). The pore pressure was observed to remain fairly uniform during this process, as expected under drained conditions.

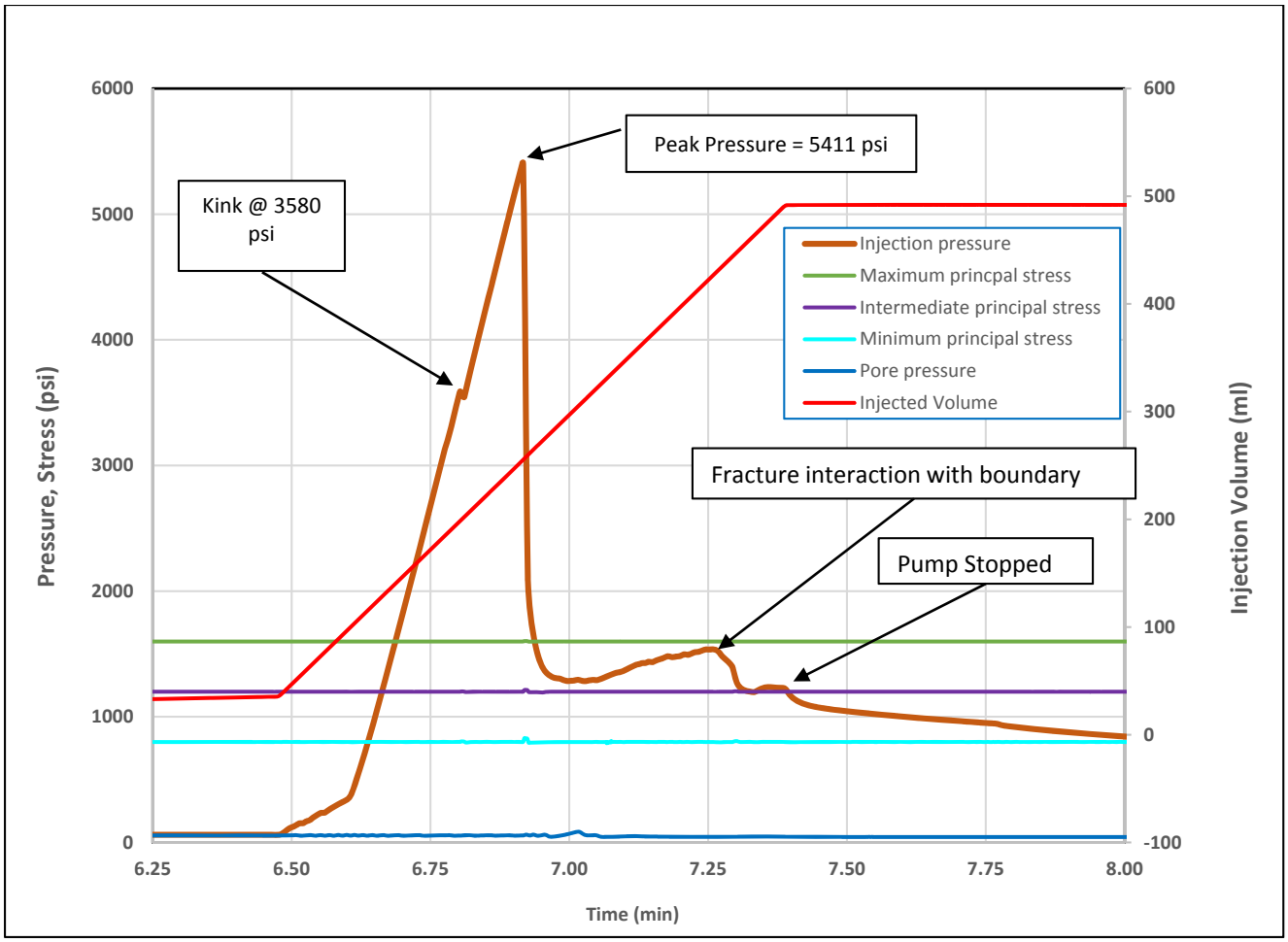

Figure 5.39: Injection pressure-time dependence in test 4.

Flat-jack volume response

The results of the flat-jack (ΔV_2 and ΔV_3) and axial actuator (ΔV_1) volume responses are shown in **Figure 5.40**. As in test 3, there is a slight drop in ΔV_3 at the point coinciding with the "kink" in the injection pressure. The possible causes for this are the same as those discussed in Section 5.4.1. At the injection peak pressure, there are sharp drops in the ΔV_2 and the ΔV_3. This response is similar to that outlined in test 3 (Section 5.4.1). Shortly after the peak pressure, ΔV_3 continues to drop, albeit at a less steep slope, while ΔV_2 begins to increase. This is consistent with a Poisson effect in which the sample expands in σ_3 direction and contracts in the σ_2 direction. These volumetric responses are also consistent with a fracture that propagates in the direction perpendicular to the σ_3. In the propagation zone, as the injection pressure rises

gradually from 1300 psi to approximately 1530 psi, as the fracture tip approaches the boundary, there is a small up and down spike in both ΔV_3 and ΔV_2 . These responses may have been caused by fracture interactions with the boundaries. When the fluid injection is stopped, there is a gradual injection pressure drop of 200 psi, which we interpret as the fracture closure pressure as stated above. The corresponding increases in both ΔV_3 and ΔV_2 may have been an indication of the overall sample contraction during fracture closure. It should be noted that flat-jack data is only a qualitative indicator of the fracture response and should not be taken as numerically precise.

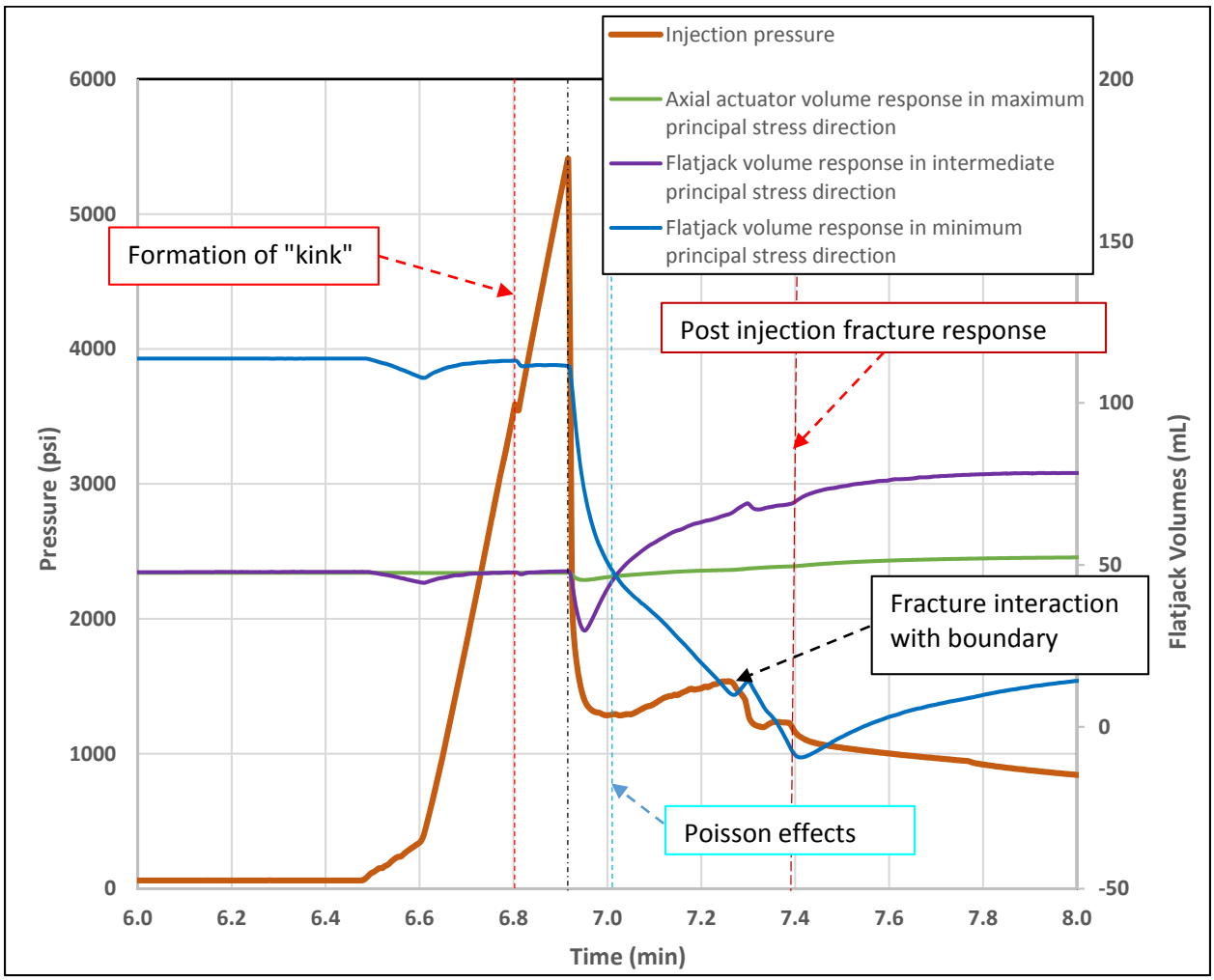

Figure 5.40: Flat-jack and axial actuator volumetric deformation measurements before, during and after fracturing.

Evidence of shear bands and other plastic deformation features in test 4

CT scan images for test 4 are presented in **Figures 5.42** and **5.43**. Features such as shear bands, fracture initiation features, and evidence of cavity expansion are observed in these figures. An injection source made from aluminum alloy 6061 was used in test 4. This facilitated CT scanning of the solidified fracture with the injection source left in place, which minimized the sample disturbance prior to scanning. CT sectioning was performed perpendicular to the injection source. CT data points obtained in this way were utilized for the 3D reconstruction (Appendix B, **Figure A.11)** of the fracture morphology, i.e., the leakoff surface.

Figures 5.42 and 5.43 illustrate the evidence of shear bands observed in our in true-triaxial tests. Shear bands were observed both ahead of the expanding cavity around the injection source, along the length of fracture, as well as at the fracture tip. This observation is consistent with the shear localization effect in strain-softening materials [e.g., Chang et al., 2003; *Chang*, 2004; *Wu,* 2006; *Germanovich et al.,* 2007] such as those used in our experiments. The fact that the shear bands occur both near the expanding cavity and at the fracture tip indicates that both fracture initiation and propagation in our materials are likely to be controlled by inelastic deformation mechanisms. The width and contents of the shear bands could not be measured as they were outside the resolution of the employed CT imaging technique.

It was also observed that the shear bands appeared to form at acute angles relative to the direction of fracture propagation. This observation is consistent with the model of shear banding at the fracture tip [*Chang et al.,* 2003; *Chang,* 2004; *Wu,* 2006; *Germanovich et al.,* 2007]. This model (**Figure 5.41**) explains how fracture propagation may occur in the state of stress, which is compressive everywhere, including near the fracture tip. In order for the fracture to propagate, an inflow volume into which fluid can flow needs to be created at the fracture tip. Yielding of the strain-softening materials near the fracture tip may result in the localized shear bands as shown in **Figure 5.41**. The discontinuity of the shear displacement between the opposing sides of a shear band can generate the necessary volume for the fluid inflow necessary for propagation (**Figure 5.41**).

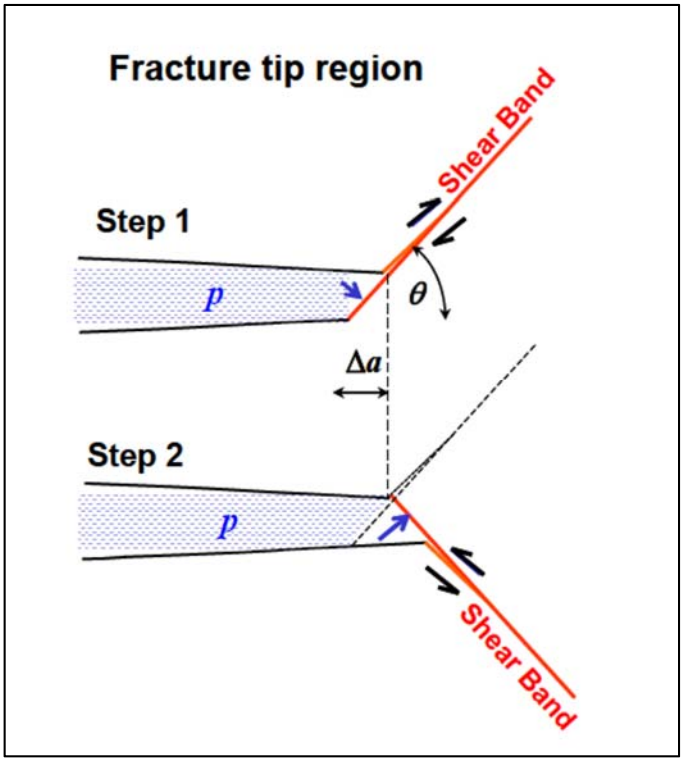

Figure 5.41: Shear band model of hydraulic fracturing in cohesionless particulate materials [*Chang et al.,* 2003; *Chang,* 2004; *Germanovich et al.,* 2007]. Here, P is the injection pressure inside the fracture, θ is the acute angle of the shear band with respect to the fracture direction, and Δa is the incremental advance of the fracture in the fracture direction.

The observed details from CT scans (**Figures 5.33, 5.34, 5.35, 5.42, and 5.43**), are consistent with the following sequence of events [*Chang et al.,* 2003; *Chang,* 2004; *Germanovich et al.,* 2007; *Hurt,* 2012; *Germanovich and Hurt,* 2012; *Hurt and Germanovich,* 2012]. The pressurization of the injection source is followed by the cavity expansion around the injection source. The associated yielding of the softening cohesionless material results in the shear strain localization and one or several shear bands emanating from the expanding cavity. Fracture initiation takes place at one of these shear bands. Subsequent shear bands, then, continuously form and branch ahead of the fracture tip as the fracture propagates (**Figure 5.41**). The shear banding mechanism may be accompanied and even be dominated by the material liquefaction (as the fracturing fluid infiltrates the intact rock and/or more permeable shear bands) and other instability mechanisms near the borehole and at the fracture tip [*Germanovich et al.,* 2007; *Huang et al.,* 2011; *Huang et al.,* 2012; *Zhang and Huang,* 2011; *Zhang et al.,* 2013].

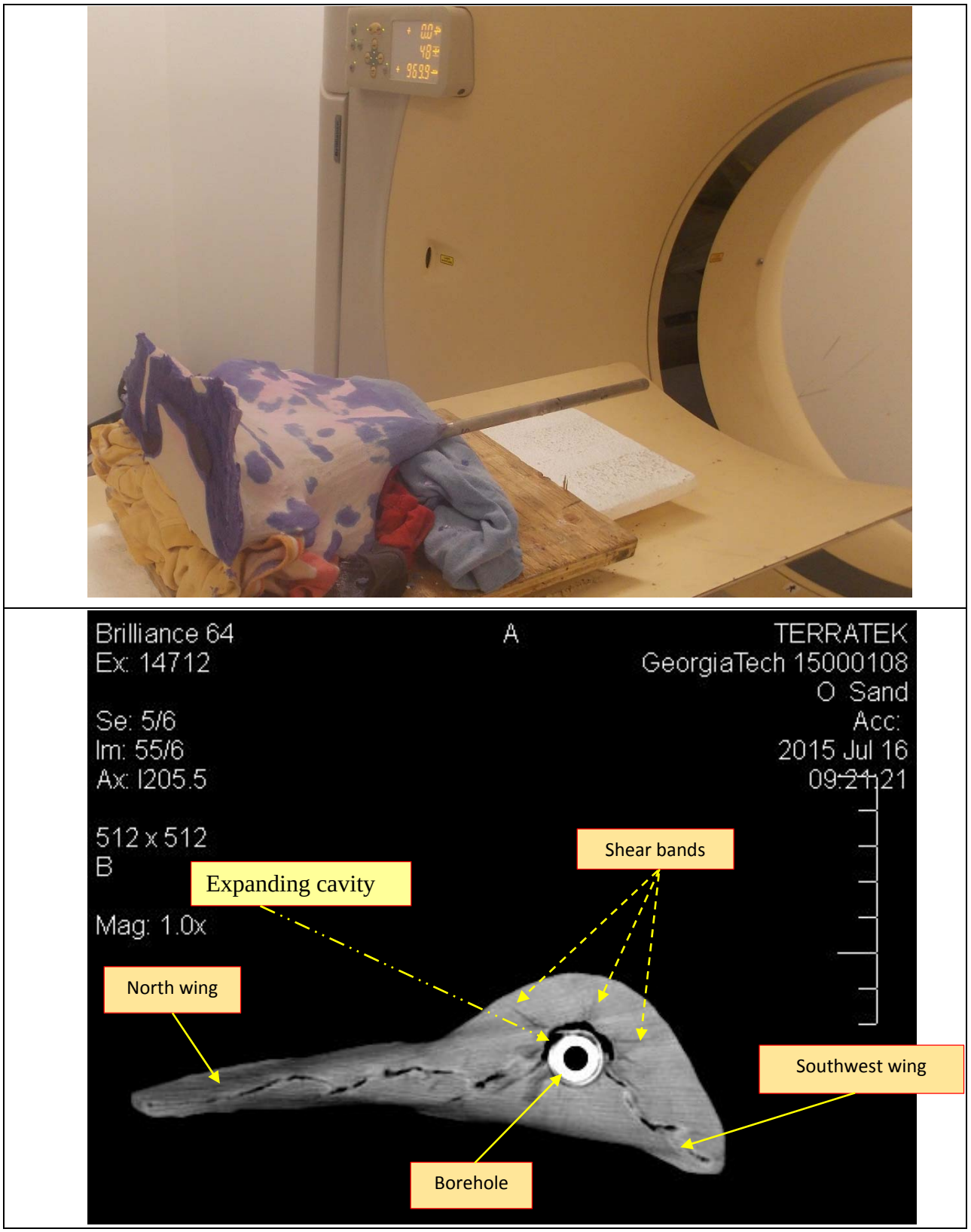

Figure 5.42: CT sectioning perpendicular to the injection source. Features indicating cavity expansion and shear bands are present.

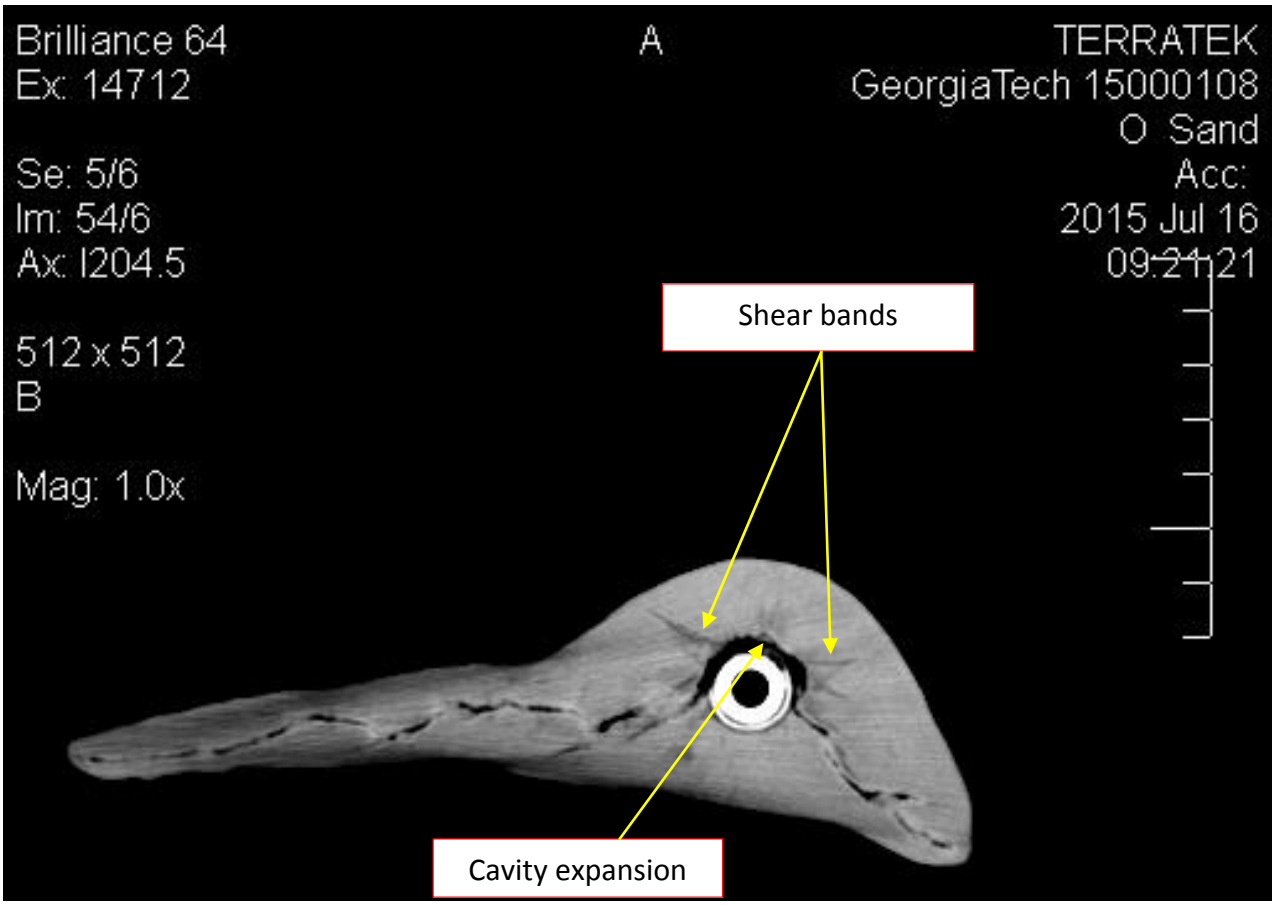

Figure 5.43: CT scan results depicting cavity expansion, shear bands emanating from expanding cavity.

5.4.3. Large block results (Test 2)

Fracture geometry

Results from test 2 evidenced the formation of two fractures (**Figure 5.44**). The major fracture was vertical and consisted of two asymmetrical sub-planar wings perpendicular to the minimum principal stress direction. This is consistent with typical fracture orientation during hydraulic fracturing for the given confining stress configuration. The larger of these two wings propagated north of the injection source and was 5 in in length. The smaller of the two wings propagated south of the injection source and was 3 in in length from the center of the injection source to the tip of the fracture. The larger wing had a height of 6 in while the smaller wing had a height of 4 in. The fracture consisted of a thick leakoff zone with an average thickness of 1 inch across the length of the fracture, and a thin fracture aperture. The minor fracture was sub-horizontal (**Figure**

5.44) and dominantly propagated on the north side of the injection source. It had a thicker leakoff zone than the vertical fracture and consisted of several spheroidal features on its surface. These spheroidal features are not unique to our experiments, but have been reported by other researchers [e.g. *Chang,* 2004; *Dong*, 2010; *Jasarevic et al.,* 2010; and *Hurt,* 2012]. This complex fracture propagated 4 in north of the injection source and was 3 in wide to the east and west of the injection source. **Figures 5.44 – 5.46** highlight the fracture geometry features from test 2.

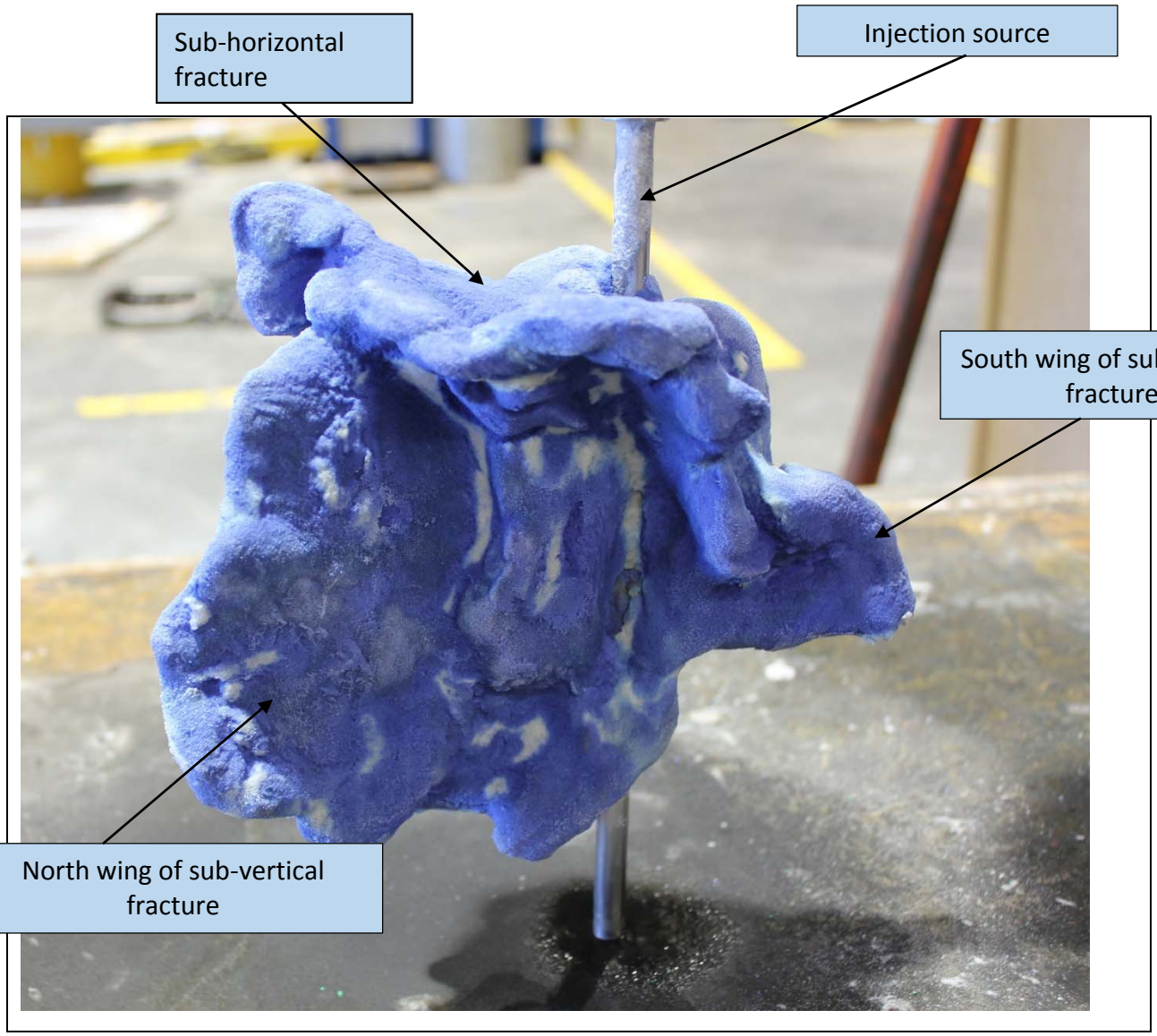

Figure 5.44: A major vertical fracture and a smaller sub-horizontal fracture in close proximity.

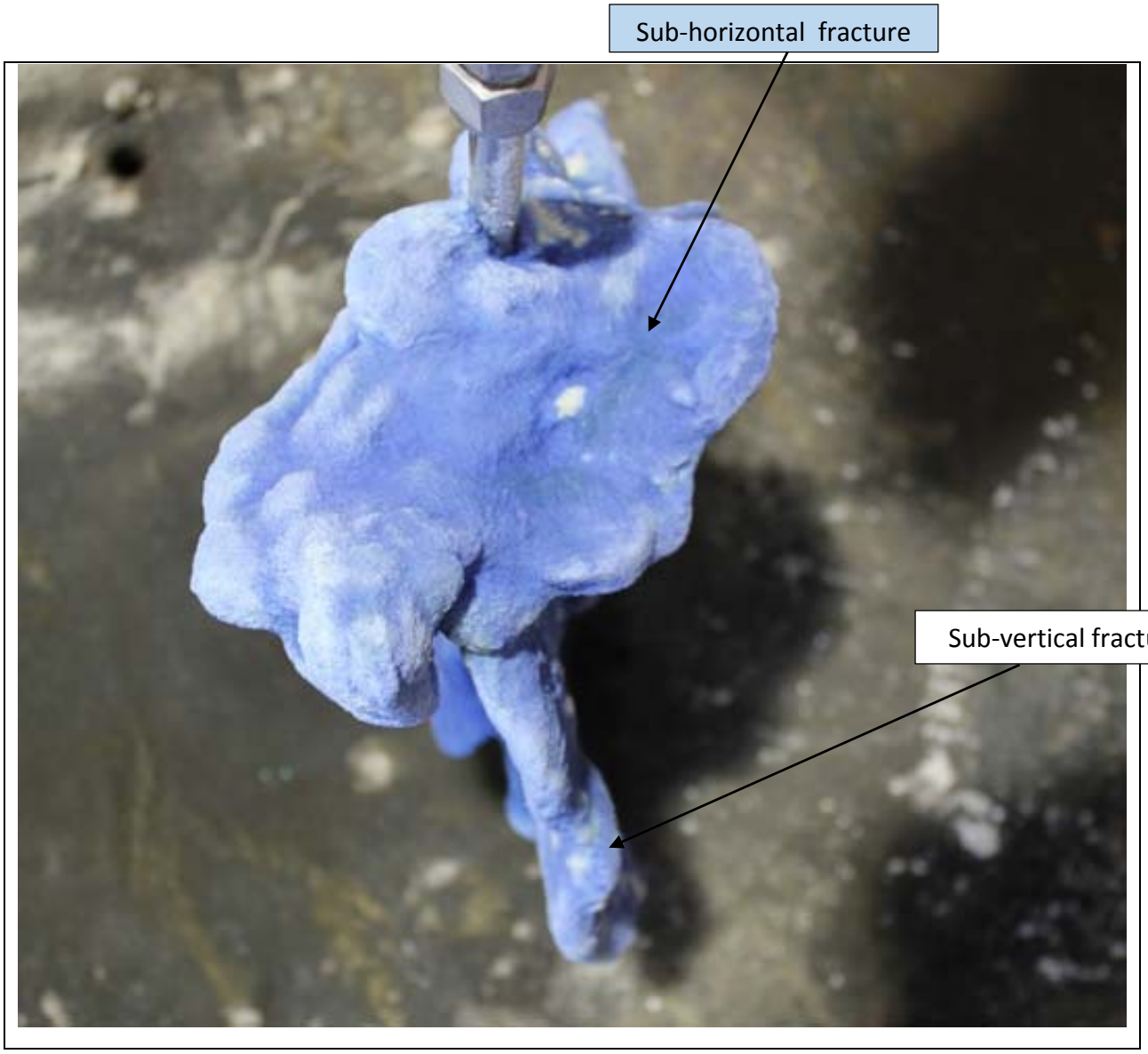

Figure 5.45: Sub-horizontal and sub-vertical fractures from a top view.

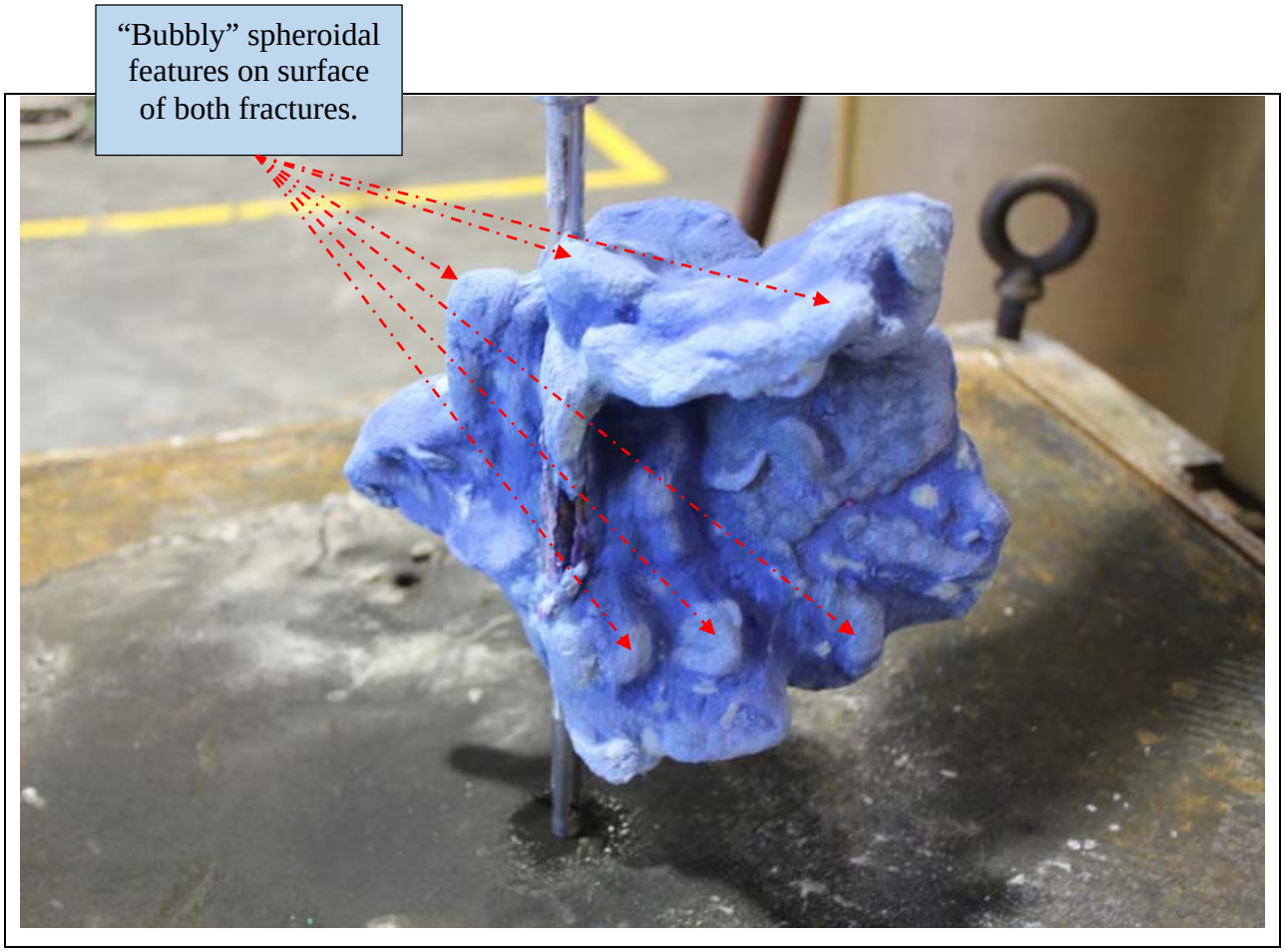

Figure 5.46: "Bubbly" spheroidal features on fracture surfaces.

The major vertical fracture was sectioned at its widest tip to tip point to expose the internal features of the fracture morphology. The sectioned fracture is presented in **Figure 5.47**. Branching was observed in several areas along the length of the fracture and near the fracture tips. The branches were all at an acute angle to each other. Sectioning also allowed us to observe the leakoff zone and the fracture aperture. We observed uniform leakoff thickness throughout the length of the fracture. However, there was significantly more leakoff near the fracture tips than other parts of the fracture. The fracture aperture shown in the image below is the remnant aperture after the fracture closure.

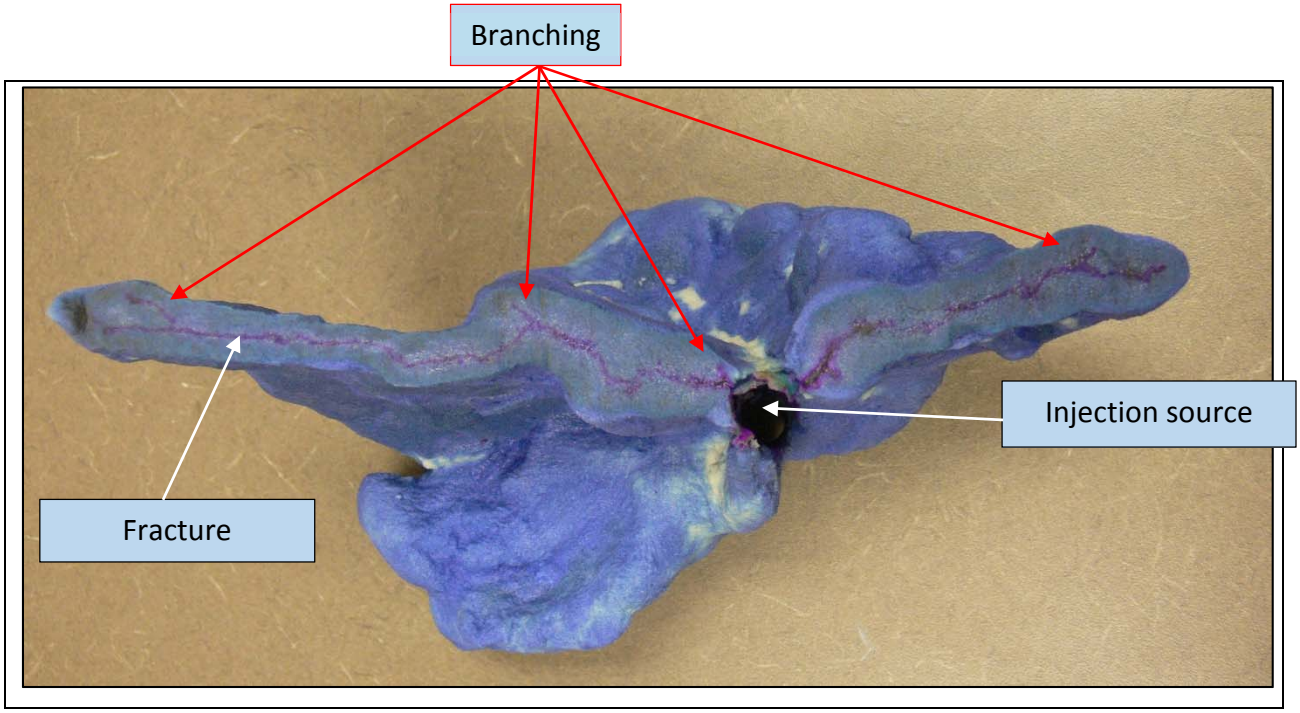

Figure 5.47: Image showing sectioned vertical fracture with evidence of branching. Also showing that most leakoff is at fracture tip.

Injection pressure signature

The recorded fracture injection pressure for test 2 was relatively smooth with a linear rise in pressure followed by a sharp drop after reaching a defined peak pressure (**Figure 5.48**). This is consistent with pressure behavior during hydraulic fracturing. The pressure does not drop below σ_1, however. After dropping to nearly the magnitude of σ_1, the pressure begins to rise again. There was a minor dip in the pressure curve at the point when the pumping system was reset in order to allow for more injection volume. After this the pressure curve rises again until the injection pump is stopped. There is then a gradual decay in the pressure curve until the curve flattens out to a constant value of approximately 2100 psi. We interpret the pressure difference between the point at which the pump is stopped and the flattening of the pressure curve, as the shut-in pressure (closure pressure).

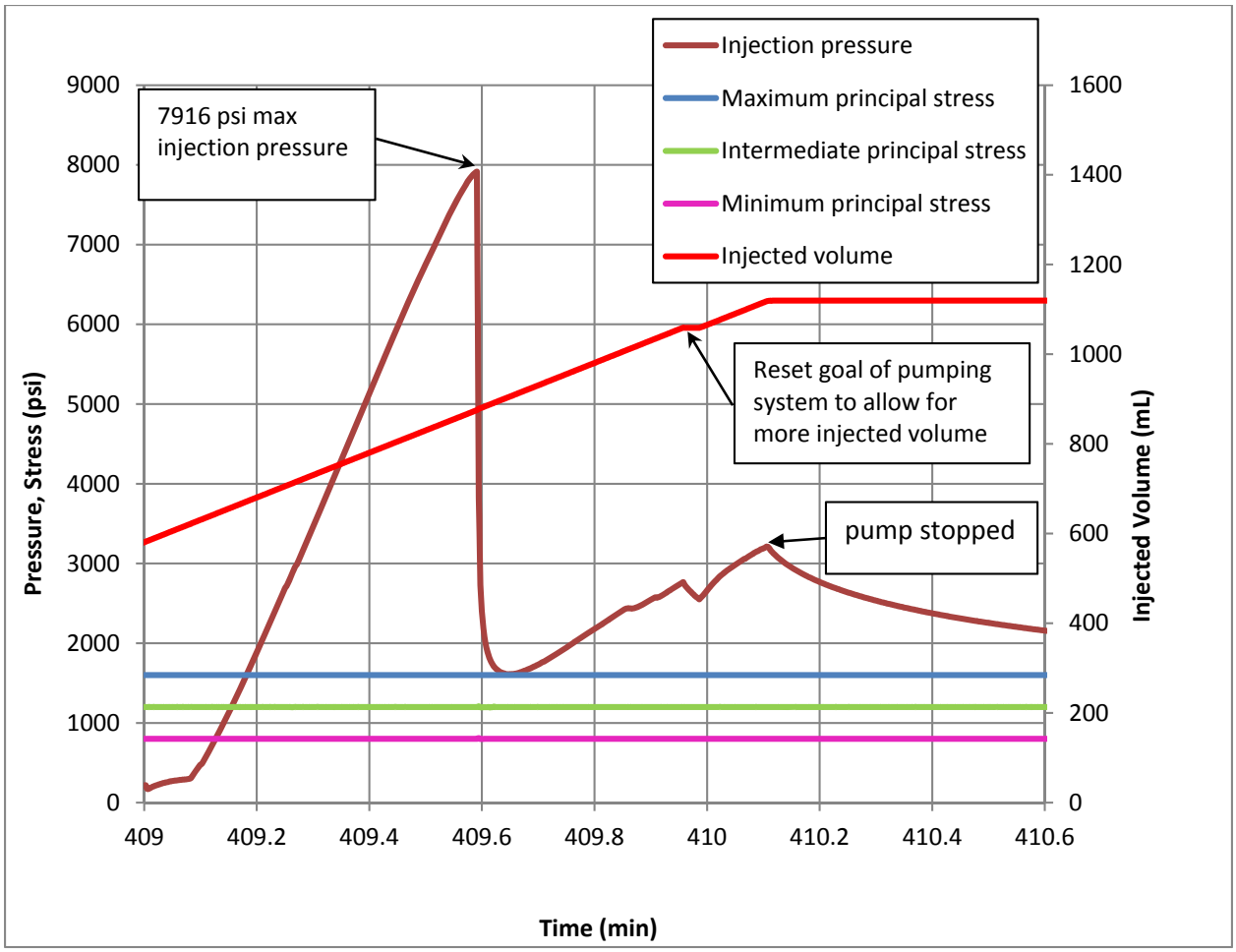

Figure 5.48: Injection pressure versus time during test 2. Injected volume is also shown.

The peak pressure (initiation pressure) in test 2 was 7916 psi. Therefore, the peak pressure to minimum principal stress ratio for test 2 was 9.9. Fluid injection was continued until 500 ml of fracturing fluid was injected into the sample. From the exhumed fracture, we observed that the fracture tip was far from reaching the sample boundaries, which minimized the effect of sample boundaries. From the pressure curve, inference can be made concerning the timing of the fracture initiation for the two fractures. Based on the size and position of the vertical fracture, we conclude that this fracture initiated at the time of the peak pressure. However, it is not clear the exact point at which the horizontal fracture initiated, only that it did so after the vertical fracture had formed. The formation of the vertical fracture is consistent with the orientation of the minimum principal stresses on the block sample. The formation of the horizontal fracture may have been controlled by the newly developed local stress field after the initiation of the main

vertical fracture rather than the remote boundary stresses. This speculation is consistent with the observation that in **Figure 5.52**, the injection pressure does not fall below the maximum vertical principal stress (1600 psi) after the initiation of the main fracture. Pore pressure was monitored throughout the injection process. As the tests were conducted under drained pore pressure conditions, uniform pore pressure readings were recorded over the duration of test 2.

Flat-jack volume response

The flat-jack volumetric responses for test 2 are plotted in **Figure 5.49**. Before the peak pressure, there is a small gradual decrease in ΔV_3. This may be a response to cavity expansion before fracture initiation. Then, there is a sharp drop in ΔV_3 $(\text{and to a small extent in } \Delta V_2)$ coinciding with the peak pressure, showing volume displacement due to the fracture opening in the minimum principal stress direction and propagating perpendicular to the minimum principal stress direction. Shortly thereafter, there is a considerable increase in the volume in the intermediated principal stress direction, possibly associated with the Poisson's effect. This indicates that the flat-jacks were independently able to capture the fracture initiation and growth. After injection stoppage, the flat-jacks continue to show volume increase, indicating fracture contraction during fracture closure.

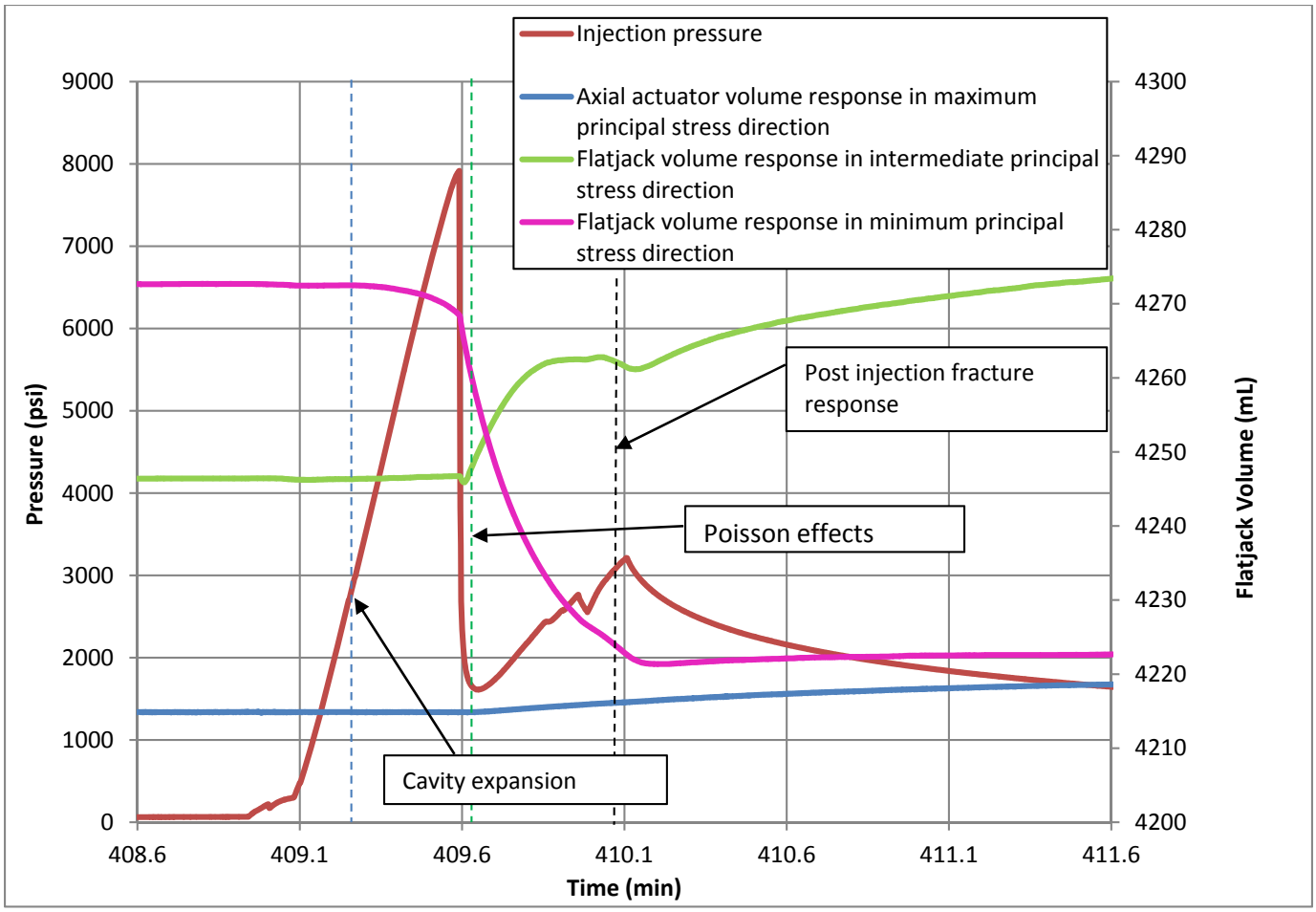

Figure 5.49: Flat-jack volume responses relative to the pressure-time curve.

Evidence of shear bands and other plastic deformation features in test 2

CT scans were performed on the solidified fracture in test 2. The results of the CT scans are presented in **Figure 5.50**. Evidence of branching can be seen along the fracture length. Evidence of plastic deformation features from CT scan images were similar to those from small block samples and described in detail in **Section 5.4.1.**

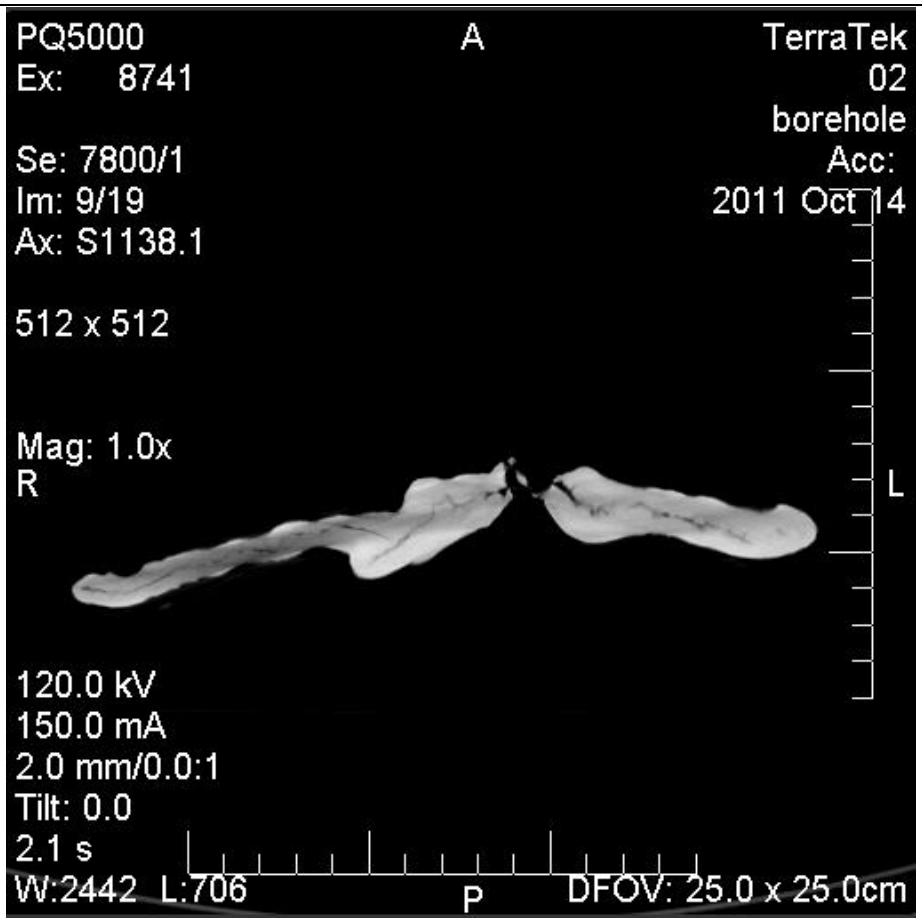

Figure 5.50: (Above) CT scan image with fracture and leakoff from test 2 and (below) the area of sectioning for image above.

5.5. DISCUSSION

Table 5.3 summarizes the similarities and differences between tests 1, 2, 3 and 4. In tests 2, 3 and 4, the block sample was made from (80%) USM100 Sand and (20%) SIL-CO-SIL 106 Silica flour mixtures while test 1 used the F110 Sand (80%) and Silica flour (20%) mixture. In all four tests, the samples were compacted by the rodding method [*Chang,* 2004; *Hurt,* 2012] to a density of approximately 2 g/cm^3. The fracturing fluid type used, the injection rate, and the confining stress conditions were as identical in all four tests as practically possible. In test 4, an aluminum alloy 6061 injection source was used to accommodate CT scanning during the post-test analyses. The internal diameter of this tube was approximately equal to that of the tubes used in tests 1, 2 and 3. The design of the perforation zone was identical in all four tests and is described in detail in *Hurt* [2012]. The volume of fracturing fluid used in test 4 was 450 ml and was less than that used in the other tests in order to minimize the potential of the fluid reaching the boundaries during the test. However, fracturing fluid did reach the sample boundaries in test 4. All tests were conducted under drained pore pressure conditions. The peak pressures and the fracture geometries in tests 2 and 3 were very similar. The peak pressures in tests 4 and 1 were lower than the aforementioned. The peak pressure in test 1 was at about one third of that in test 3, despite the tests being conducted under similar conditions. The similarity in peak pressures between tests 2 and 3 may be an indication that the peak pressure in hydraulic fracturing of unconsolidated particulate materials is independent of scale. Lower initiation pressures in tests 1 and 4 was attributed to the lower levels of saturation that was achieved in the preparation of these samples. Therefore, peak pressure appears to show sensitivity to the saturation levels in the block sample.

The fractures from tests 1 and 4 were generally thick in the middle and more planer away from the middle. The fractures from tests 2 and 3 appear to be thick throughout the lengths of the fracture wings. All four tests had vertical to sub-vertical fractures, which were perpendicular to the minimum principal stress. This result is consistent with hydraulic fracturing in brittle materials. Tests 1 and 4 fractures had two wings with the wings in tests 2, 3 and 4 being asymmetrical relative to the injection source. The asymmetrical nature of the wings may be attributed to variations in pore pressure gradients in the sample during injection source loading.

In tests 2 there was a presence of what appears to be a sub-horizontal offshoot fracture. We suggest that the initiation of this sub-horizontal fracture offshoot may have been controlled by local stress fields that developed near the injection zone sometime after the initiation of the main vertical fracture. Therefore, the orientation of the offshoot fracture was not controlled by the remote boundary stresses.

In the injection pressure plot for tests 3 and 4, there is a kink in the curve before the injection pressure reaches the peak value. In test 3, the kink occurs at approximately 4775 psi (61% of the peak stress) and at 3570 psi (66% of the peak stress) in test 4. In both tests, the kink may be attributed to the development of a local instability such as shear bands emanating from the expanding cavity or the initiation of a small fracture. In all 4 tests there is a sharp drop in pressure after the peak followed by a flattening of the pressure curve. The pressure to which the curve drops after the peak is probably the propagation pressure for the fracture. In tests 2, 3 and 4, this propagation pressure is always greater than the maximum horizontal stress. In tests 3 and 4 this pressure is less than the vertical stress while it is approximately equal to the vertical stress in test 2. During fracture propagation, the fracture front travels perpendicular to the minimum principal stress. It is necessary that the fracture pressure be greater than the minimum principal stress in order for the fracture to propagate perpendicular to that direction. **Figures 5.51** and **5.52** show some comparison details for all four tests.

A comparison of the fracture morphologies of tests in true-triaxial loading conditions (Section 5.4) versus those under triaxial loading conditions (Section 4.3, 4.4, and 4.5) shows important differences. Compared to the triaxial experiments, the resulting morphologies of tests conducted under true-triaxial conditions had thicker leakoff zones and less planar fractures. This is attributed to the high fracture pressures that were developed in tests under high confining stress regimes. Even though the confining stresses in true-triaxial experiments were 10 times greater than those in triaxial experiments, the fracture pressures under the true-triaxial experiments were as much as over 25 times greater than the fracture pressures the under triaxial tests.

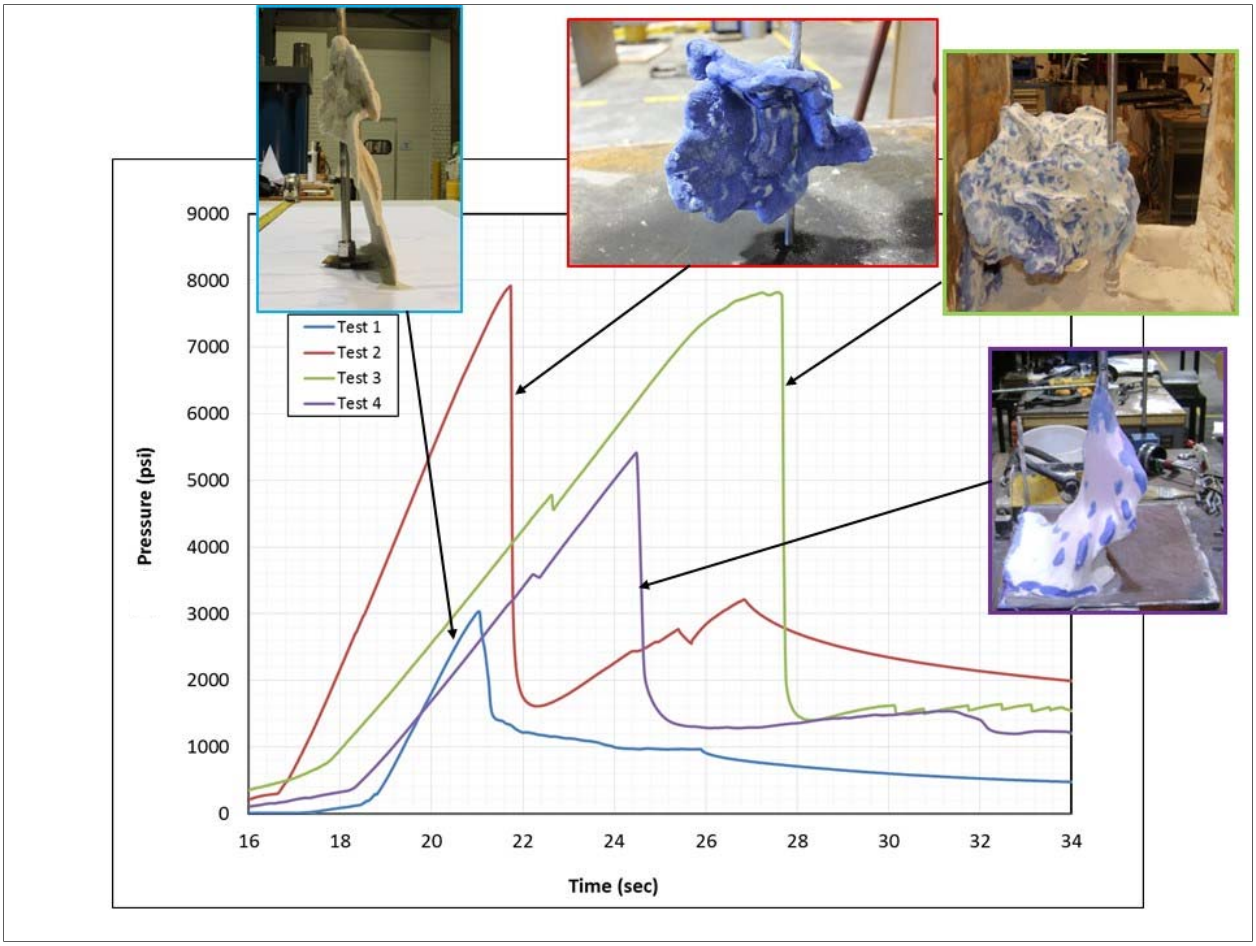

Figure 5.51: Comparison of all 4 test results.

Comparison of slopes

A close look at the plots in **Figure 5.51** shows that the slopes of the curves before the peak pressures for tests 1 and 2 were similar while the slope before the peak pressure for test 3 was similar to that of test 4. These slopes of tests 1 and 2 were approximately equal to 1500 psi/sec and those for tests 3 and 4 were approximately 900 psi/sec. These similarities in slopes between tests 1 and 2 and between tests 3 and 4 and the differences between the first two and the last two tests may be attributed to differences during the sample preparation phase and how tightly the samples were packed. Tests 1 and 2 were compacted to a mass density of 1.9 g/cm^3 while tests 3 and 4 were compacted to a mass density of 2.0 g/cm^3.

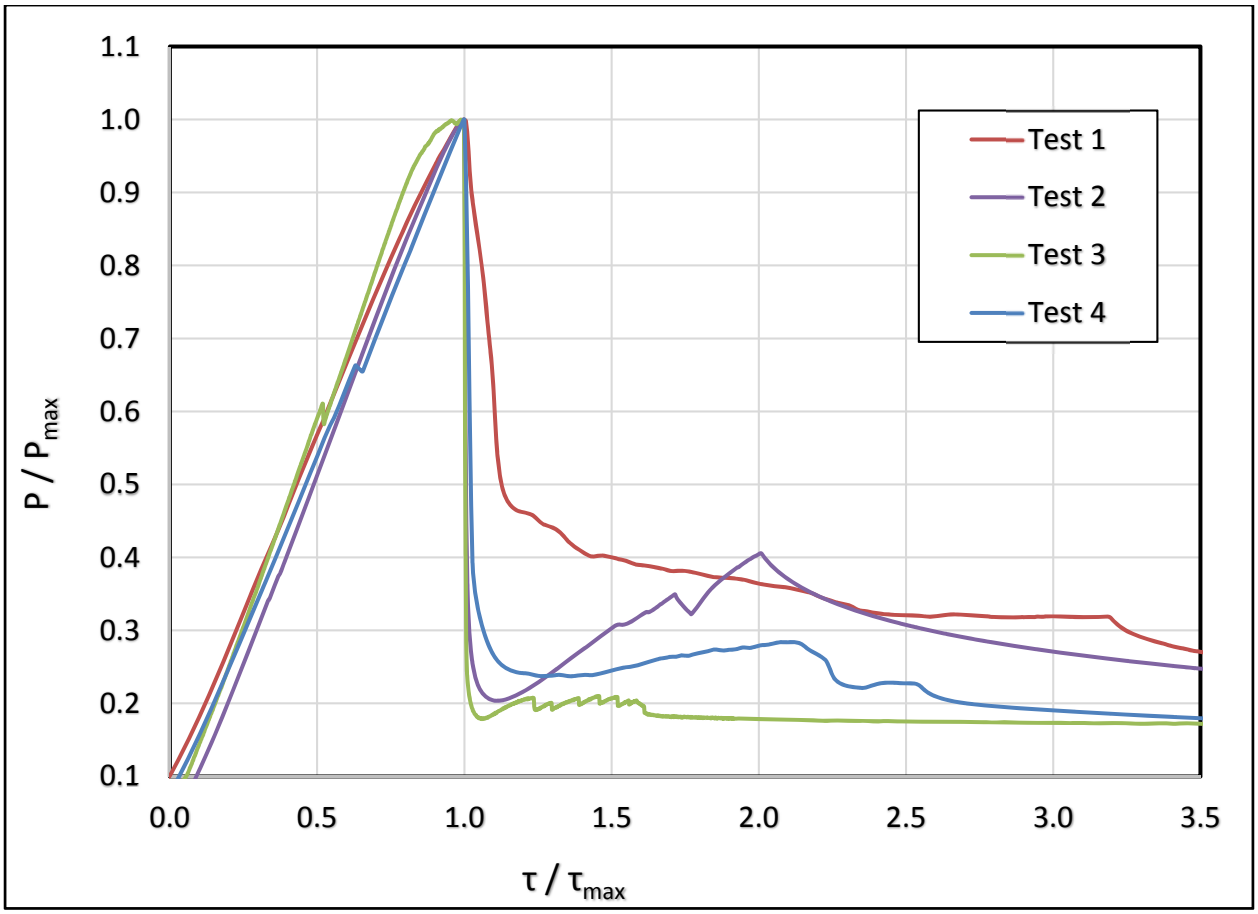

Figure 5.52: Comparison of normalized injection pressure curves.

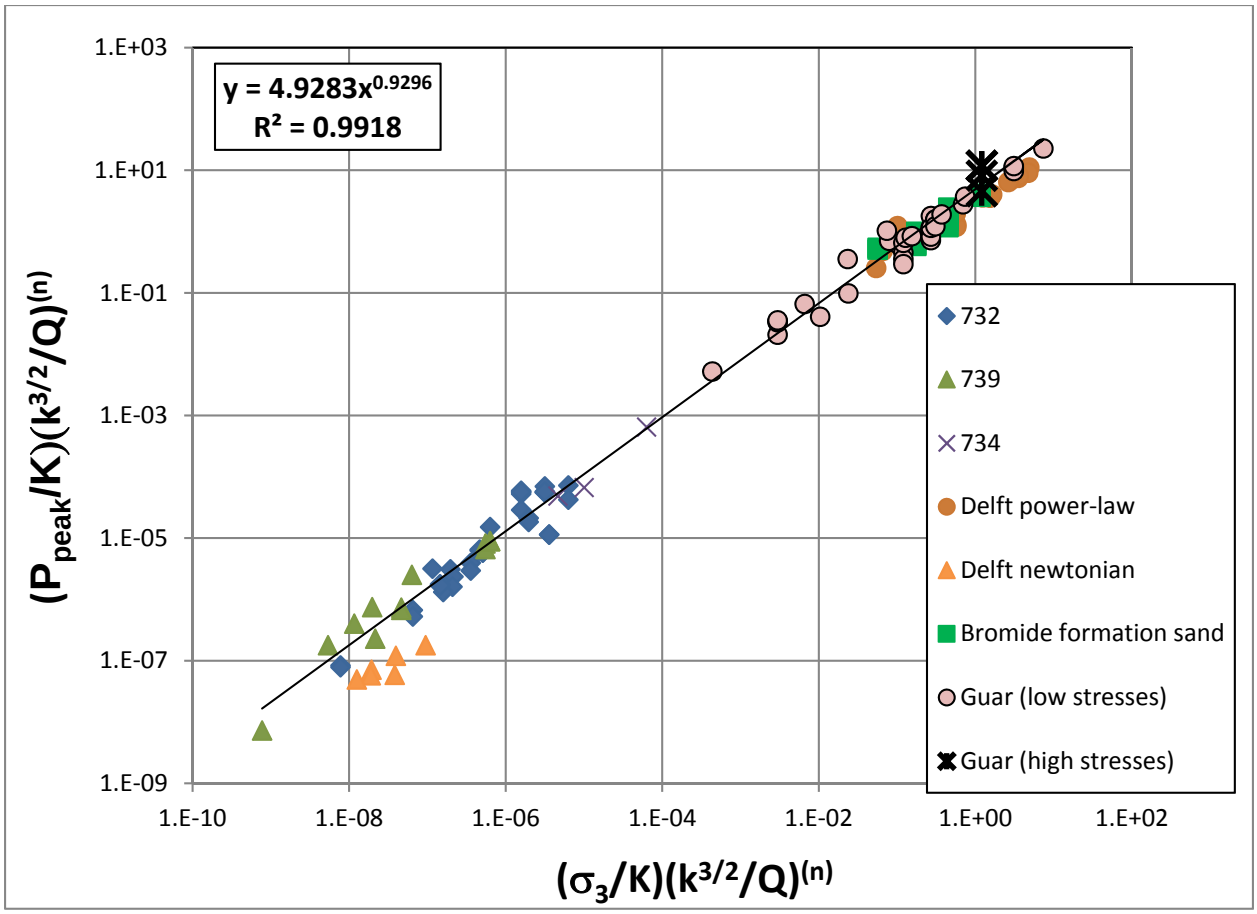

Figure 5.53: Dimensionless peak pressure versus dimensionless confining stress for all triaxial tests at Georgia Tech, tests at Delft [*Bohloli and De Pater,* 2006; *De Pater and Dong,* 2007; 2009; *Dong,* 2010; *Dong and De Pater,* 2008], and true-triaxial tests at TerraTek.

Table 5.2: Ratios of peak pressure to horizontal confining stress in the true-triaxial tests.

Peak Pressure	**Test 1**	**Test 2**	**Test 3**	**Test 4**	**Average**
σ_{peak} (psi)	3032	7916	7800	5411	6040
$\frac{\sigma_{peak}}{\sigma_2}$	2.5	6.6	6.5	4.5	5.0
$\frac{\sigma_{peak}}{\sigma_1}$	3.8	9.9	9.8	6.8	7.6

Table 5.2 compares the peak pressures of tests 1, 2, 3 and 4 to the horizontal principal confining stresses. These ratios are then averaged. Based on these comparisons, we estimate the peak pressure to be larger than the maximum horizontal stress by an average factor of 5 and to be larger than the minimum horizontal stress by an average factor of 7.6.

Given the inherent variability of soil samples, we consider the repeatability of the experiments is reasonably good. Tests 2 and 3 had the most similar peak pressures and fracture geometries. These two tests also had the best saturation levels achieved. The peak pressure in test 4 was lower than that of tests 2 and 3 by about 30 percent. We attribute this to lower saturation levels in test 4 caused by the bottom flow tube being clogged in this test.

Finally, we again applied the dimensionless model of fracture initiation [*Germanovich and Hurt,* 2012; *Hurt and Germanovich,* 2012; *Hurt,* 2012] to our results in order to characterize hydraulic fracturing in triaxial and true-triaxial loading conditions. We plotted all data points from experiments performed by *Hurt* [2012], our low stress triaxial experiments (including Bromide formation sand experiments), our high load true-triaxial tests and experiments conducted by the Delft group (**Figure 5. 53**). A power law correlation between the dimensionless peak pressure and the dimensionless confining stress of all the data is found. Although values of dimensionless groups plotted in **Figure 5.53** vary over six orders of magnitude, there is a correlation between results from synthetic sands, the Bromide formation sand, TerraTek results, and results by others.

Table 5.3: Summary of true-triaxial tests.

Sample Preparation				
	Test 1	**Test 2**	**Test 3**	**Test 4**
Block Sample Size	11"x11"x15"	28 3/8" x 28 3/8" x 35 3/8"	11"x11"x15"	11"x11"x15"
Sample Type	F110 sand (80%) & Silica flour (20%) mixture	USM100 sand (80%) & Silica flour (20%) mixture	USM100 sand (80%) & Silica flour (20%) mixture	USM100 sand (80%) & Silica flour (20%) mixture
Compaction Method	rodding	rodding	rodding	rodding
Porosity	28%	28%	28%	28%
Density	1.9 g/cm^3	1.9 g/cm^3	2.0 g/cm^3	2.0 g/cm^3
Saturation Method	Inlet hole at bottom corner, injection source is the outlet	Inlet hole at top corner, injection source is the outlet	Inlet hole at bottom, outlet hole top diagonally opposite corner	Inlet hole at bottom, outlet hole top diagonally opposite corner (**Figure 5.12a**)
Loading during Saturation	100 psi, 100 psi, 100 psi, no backpressure	600 psi, 300 psi, 300 psi, backpressure 40 psi	700 psi, 500 psi, 500 psi, backpressure 100 psi	800 psi, 600 psi, 400 psi, backpressure 183 psi
Estimated Saturation	Saturation level unknown	Saturation >90%	Saturation >90%	Saturation < 80%

Table 5Table 5.3: Summary of true-triaxial tests (continued).

Fracturing Conditions				
	Test 1	**Test 2**	**Test 3**	**Test 4**
Wellbore	Perforated flow tube 3/8 inch OD & 0.277 in ID (stainless steel tubing)	Perforated flow tube 3/8 inch OD & 0.277 in ID (stainless steel tubing)	Perforated flow tube 3/8 inch OD & 0.277 in ID (stainless steel tubing)	Perforated flow tube 1/2 inch OD & 0.26 in ID (aluminum 6061 alloy tubing)
Fracturing Fluid	Guar based cross-linked fluid, power law, n = 0.41, K = 11 Pa sec^n	Guar based cross-linked fluid, power law, n = 0.41, K = 11 Pa sec^n	Guar based cross-linked fluid, power law, n = 0.41, K = 11 Pa sec^n	Guar based cross-linked fluid, power law, n = 0.41, K = 11 Pa sec^n
Fracturing Fluid Volume	500 ml	500 ml	500 ml	450 ml
Injection rate	500 ml/min	500 ml/min	500 ml/min	500 ml/min
Loading Conditions	1600 psi, 1200 psi, 800 psi	1600 psi, 1200 psi, 800 psi	1600 psi, 1200 psi, 800 psi	1600 psi, 1200 psi, 800 psi
Vertical Loading Direction	From top	From top	From top and bottom	From top and bottom
AE Sensors	Yes	No	No	Yes

Table 5.3: Summary of true-triaxial tests (continued).

Tests Results				
	Test 1	**Test 2**	**Test 3**	**Test 4**
Peak Pressure	3032 psi	7916 psi	7800 psi (kink before peak)	5411 psi (kink before peak)
Fracture Geometry	Sub-vertical, planar, two wings	Sub-vertical with smaller sub-horizontal part, one wing	Sub-vertical with smaller sub-horizontal part, one wing	Sub-vertical, planar, two wings with small sub-horizontal parts
Fracture Morphology	Thicker central region surrounded by thinner planner region	Thick throughout length of fracture wings	Thick throughout length of fracture wings	Thicker central region surrounded by thinner planner region
Fracture Reaching Boundary	Yes	No	Yes	Yes
AE Results	Recorded AE events matching fracturing process, fracture propagation velocity ≈ 50 mm/sec	N/A	N/A	Yes
CT Scans	Yes	Yes	Yes	Yes
CT Scan Results	Leakoff zone, fracture, and fracture initiation zone are clearly seen	Leakoff zone, fracture, and fracture initiation zone are clearly seen	Leakoff zone, fracture, and fracture initiation zone are clearly seen Also plane localization features interpreted as shear bands are observed	Leakoff zone, fracture, and fracture initiation zone are clearly seen Also plane localization features interpreted as shear bands are observed, evidence of cavity expansion
3D Mapping	3D profile mapped by goniometric technique [*Hurt*, 2012]	3D profile mapped by high resolution video technique	No	Full CT scan used to produce 3D fracture mapping **(Figure A.11)**

5.6. CONCLUSIONS

In this chapter, we present results of hydraulic fracturing experiments in cohesionless particulate materials that were conducted in an industrial laboratory under high stresses (up to 1600 psi). Three tests were performed in a small block sample (11 x 11 x 15 cubic in) and one test in a large block (28.5 x 28.5 x 35.5 cubic in). The main points of this chapter can be summarized as follows.

1. The prevalence of shear bands near the cavity expanding around the injection source and near the fracture tips confirmed that both hydraulic fracture initiation and propagation in cohesionless, sediment-like, particulate media is associated with inelastic deformation mechanisms.
2. Using three independent monitoring methods, namely, injection pressure signatures, flat-jack volumetric responses, and post-test CT scans, we concluded that hydraulic fracturing in particulate, cohesionless materials takes place in the following sequence. The pressurization of the injection source is followed by the cavity expansion around the injection source. As a result of the yielding associated with cavity expansion of the softening cohesionless materials, shear strain localization takes place. This localization manifests itself as one or several shear bands emanating from the expanding cavity [*Chang et al.,* 2003; *Chang,* 2004; *Germanovich et al.,* 2007; *Hurt,* 2012; *Germanovich and Hurt,* 2012; *Hurt and Germanovich,* 2012]. Fracture Initiation follows at one of these shear bands. Consequent shear bands, continuously form and branch ahead of the fracture tip as the fracture propagates.
3. The shear banding mechanism may be accompanied and even be dominated by the material liquefaction (as the fracturing fluid infiltrates the block sample and/or more permeable shear bands) and other instability mechanisms near the borehole and at the fracture tip [*Germanovich et al.,* 2007; *Huang et al.,* 2011; *Huang et al.,* 2012; *Zhang and Huang,* 2011; *Zhang et al.,* 2013].

4. The geometries of hydraulic fractures in saturated cohesionless particulate media show complexity with thick fractures that were perpendicular to the minimum principal confining stress direction. The presence of a sub-horizontal fracture offshoot from the main vertical fracture was observed in test 2. The formation of this sub-horizontal offshoot may have been controlled by the new local stress field, created after formation of the main fracture, and not necessarily by the remote boundary confining stresses. The fracture also had wings that were asymmetrical, relative to the injection source.
5. Fracture initiation results from the true-triaxial experiments showed a power law dependence of the dimensionless peak pressure versus the dimensionless confining stress, that was consistent with previous studies [*Germanovich and Hurt*, 2012; *Hurt and Germanovich,* 2012; *Hurt,* 2012]. Further, it was found that the ratio of the peak pressure to the confining minimum principal stress was nearly 10 for fully saturated cohesionless particulate materials. In addition, it was found that the initiation pressure in our true-triaxial experiments was sensitive to the degree of saturation of the block samples.
6. Differences in sample size did not show significant impact on the hydraulic fracture initiation and propagation behavior in saturated cohesionless particulate media. There was, also, no significant impact of scale on the fracture morphology in this work. The large block sample was 16 times larger in terms of mass and volume, yet pressure signatures and fracture morphologies were nearly identical in fully saturated samples. Although there were some boundary effects in the small sample, it appears these did not impact the overall pressure signature and fracture morphology.
7. Compared to the triaxial tests in low stress (up to 160 psi) regime experiments, the resulting morphologies of tests conducted under true-triaxial conditions and high stress regimes (up to 1600 psi) had thicker leakoff zones and less planar fractures. This is attributed to the high fracture pressures that were developed in tests in high confining stress regimes. For example, even though the confining stresses in high stress regime experiments were 10 times greater than those in low stress regimes, the fracture pressures under high stress regime experiments were as much as over 25 times greater than the fracture pressures under low stress regimes.

8. One of the most important findings of this work was that acoustic emission techniques can be used to characterize the hydraulic fracturing process in saturated, cohesionless, particulate media. This finding is presented in detail in Chapter 6 of this work.

6. ACOUSTIC MONITORING OF HYDRAULIC FRACTURING IN PARTICULATE MATERIALS

6.1. INTRODUCTION

In this work we show, for the first time, that hydraulic fracturing in cohesionless particulate media can be successfully monitored in the laboratory by means of passive acoustic emission and active ultrasonic transmission measurements. Conventional wisdom suggests that it is not possible to monitor hydraulic fracturing in cohesionless materials using acoustic emission (AE) or ultrasonic transmission (UT) measurements. Yet, in this chapter, we demonstrate that:

1. Acoustic monitoring can be used to observe hydraulic fracturing in unconsolidated sediment-like materials.
2. Ultrasonic transmission techniques can be used to monitor hydraulic fracturing in unconsolidated sediment-like materials.
3. AE hypocenter location can be used to map the geometry of fractures in cohesionless particulate media.
4. Statistical acoustic data, like acoustic emission count rate, can be used to independently isolate fracture initiation.
5. AE and UT measurements show sensitivity to plastic deformation during the early stages of hydraulic fracturing in cohesionless particulate media (e.g., cavity expansion).

In Section 6.2 of this chapter, a literature review of acoustic monitoring in geomechanics is presented. The acoustic monitoring procedure is described in Section 6.3. The passive acoustic emission results are presented in Section 6.4 followed by the results of active ultrasonic transmission measurements in Section 6.5. Finally, conclusions are drawn in Section 6.6.

6.2. LITERATURE REVIEW

Acoustic emissions are transient elastic waves produced by a sudden redistribution of stress in a material caused by changes in the internal structure [*Reiweger et al.,* 2015]. Cracking in a solid material is accompanied by the release of elastic energy generating elastic waves, which propagate to the surface and are recorded by sensors as acoustic signals. Recording AE can be used for detecting cracks, fractures, and their growth [e.g. *Lockner,* 1993]. Sources of AE vary from natural events like earthquakes and rockbursts to the initiation and growth of fractures, to slip and dislocation motions. In granular geological media several classes of AE source mechanisms exist, namely, grain contact network rearrangement, motion of liquid-gas interfaces, friction between grain surfaces, grain crack formation, and other grain-scale motions [*Reiweger et al.,* 2015].

In various original publications [e.g., *Kino*, 1987; *Grosse and Ohtsu*, 2008] and reviews [e.g., *Swindlehurst*, 1973; *Scruby*, 1987; *Boyd and Varley*, 2001], theoretical aspects of AE have been summarized. In geosciences, there is an increasing amount of research on the use of AE as an early warning to signals in real time landslide monitoring systems. For example, measured AE from soils and sands was used to assess stability of slopes [*Lord and Koerner*, 1974, 1975; *Koerner* et al., 1976, 1977; *Huck and Koerner*, 1981; *Koerner et al.,* 1981a].

Ishida [2001] used AE monitoring both in the laboratory and in the field to study mechanisms of hydraulic fracturing in rocks. In laboratory experiments, he investigated the effects of the texture properties of rock on hydraulic fracturing mechanisms. The fault plane solutions of AE source mechanisms indicated that the shear fracturing is dominant in the specimens having larger grains whereas the tensile fracturing is dominant in those having smaller grains [*Ishida*, 2001]. The experiments were also conducted in the same granitic rock type, with three different conditions being applied, namely, (1) water injection, (2) injection of viscous oil, and (3) pressurization via a urethane sleeve. AE monitoring indicated that shear fracturing was dominant during water injection and pressurization via a urethane sleeve whereas the tensile fracturing was dominant during viscous oil injection [*Ishida,* 2001]. *Ishida* [2001] states that the results of these laboratory experiments suggest that AE monitoring in field operations of

hydraulic fracturing is effective to study fracturing mechanisms or crack behavior. A borehole sonde was made and AE events were monitored during hydraulic fracturing in the field to measure rock stress at the construction site of an underground power station [*Ishida*, 2001]. The results indicated that AE count rates increased with the closing and reopening of a hydraulically induced crack. This fact suggests that AE monitoring could improve the reliability and accuracy of hydraulic fracturing stress measurements.

Matsunaga et al. [1993] conducted laboratory hydraulic fracturing experiments in cubic blocks, with a side of 20 cm, to investigate the fracturing mechanism using AE. They evaluated the effect of fluid permeation on the fracture mechanism by using different fracturing fluids and different rock types. It was reported that the fracture plane inferred from the distribution of AE hypocenters matched quite well with the fracture location observed directly in a core and on the surfaces of the block. It was also reported that the AE events defined a diffuse planar feature whose orientation coincided with the maximum stress direction. *Matsunaga et al.* [1993] concluded that the results of their experiments suggested that the initiation and extension mechanisms of hydro-fractures were strongly affected by rock permeability and texture, as well as by the viscosity of the fracturing fluid. They suggested that AE observations can be used to define both the geometry of hydraulic fractures and the in situ stress state.

Barriere et al. [2012] studied experimentally the effect of partial saturation on direct P-wave velocity and attenuation by monitoring a sand-filled tank during two imbibition/drainage cycles. The sand was highly permeable, homogenous, with grain size diameters around 250 μm. The low velocity of P-waves enabled them to observe the wave propagation along 10 wavelengths in their 1 m long apparatus. They concluded from the inverted poro-visco-elastic models that V_P (P-wave velocity) strongly depends on the mechanical properties of the effective fluid and on the effective pressure. Specifically, during imbibition, the fluid injection increases P_f (pore fluid pressure) and V_P decreases as a function of saturation. During drainage, V_P still decreases with increasing saturation, but less rapidly since effective stress is negligible. This study also shows that fluid distribution at microscopic scale has a strong influence on the attenuation of direct P-waves at macroscopic scale and confirms that seismic prospection may be a powerful

tool for the characterization of transport phenomena in porous media [*Barriere et al.,* 2012]. Further details on this are given below in the Signal Attenuation Section (page 223).

Reiweger et al. [2015] studied the characteristics of ultrasonic wave propagation in snow and measured AE signals during snow loading experiments in a cold laboratory (at constant temperature of -5 °C). They found that the wave velocity was of the order of the speed of sound (300 to 350 m/s) in air for the lower densities of snow (about 270 kg/m^3) and significantly increased with increasing snow density to about 500 m/s for a density of 300 kg/m^3. During the loading experiments with layered samples, they succeeded, to show that the AE stem from fracturing a weak snow layer where most of the deformation was concentrated. In all experiments that led to catastrophic failure, analysis of the acoustic data revealed a decrease of the exponent β of the complementary cumulative size frequency distribution of event energy ("survival curve") during and before catastrophic failure, at least, for laboratory size samples. This exponent is defined by

$$p(E) \propto E^{-\beta} \quad (E \propto A^2) \tag{6.1}$$

where $p(E)$ denotes the probability that the energy of an event is greater than E. In turn, the energy is proportional to the square of the wave amplitude, A. *Reiweger et al.* [2015] concluded that this drop of exponent β at and before failure has the potential to serve as an indicator of unstable conditions, i.e., to indicate a snowpack state when the avalanche release probability is high. Understanding failure localization and the change in exponent β are considered important steps towards recognition of precursors to snow failure with respect to dry-snow slab avalanche release [*Reiweger et al.,* 2015].

Stanchits et al. [2012] report results of laboratory experiments they conducted to study the effect of discontinuities on hydraulic fracture propagation initiated by injection of different viscosity fluids in low permeability sandstone blocks. They used acoustic emission and ultrasonic transmission techniques to monitor these processes and to identify various stages of the process, including fracture initiation, fracture interaction with the pre-existing discontinuities, and fracture closure. AE analysis confirmed the orientation of the hydraulic fracture propagation in the direction perpendicular to the minimum horizontal stress and crossing the interfaces of the

pre-existing discontinuities. Further, *Stanchits et al.* [2012] report that the onset of borehole peak pressure correlates to the time, when the fracture crosses the discontinuity interface. They conclude that the analysis of the combined AE and UT data provides insight into the fracturing process and that it gives significant information that improves understanding of the dynamics of hydraulic fracture propagation and also gives a reference for interpreting microseismic data recorded in the field.

Acoustic measurement tools usually consist of sensors, preamplifiers, amplifiers with filters, acquisition boards, AE signal processors, and data display and storage equipment. The sensors are AE piezoelectric transducers, geophones, accelerometers or hydrophones, which are in direct contact with the material to be tested. The mechanical movements at the sensors surface are transformed into voltage signals that are amplified by preamplifiers before being transmitted to acquisition boards. This amplification is often 100 to 1000 times (40 or 60 dB gain), but can be significantly greater [*Koerner et al.*, 1981a]. The system also includes filters, which eliminate part of an AE signal based on its frequency. High pass filters can eliminate background noise with frequencies lower than a selected value. Low pass filters can eliminate signals with frequencies greater than the sensor's resonance. Amplifiers, placed after the filters increase the signal strength for subsequent processing. Other tasks such as the discrimination between real and false signals (noise) and the collection of statistical information about the parameters of each signal are also common to most AE systems [http://www.nde-ed.org]. Materials that are more susceptible to attenuation are tested at lower frequencies for better distinction of AE signals.

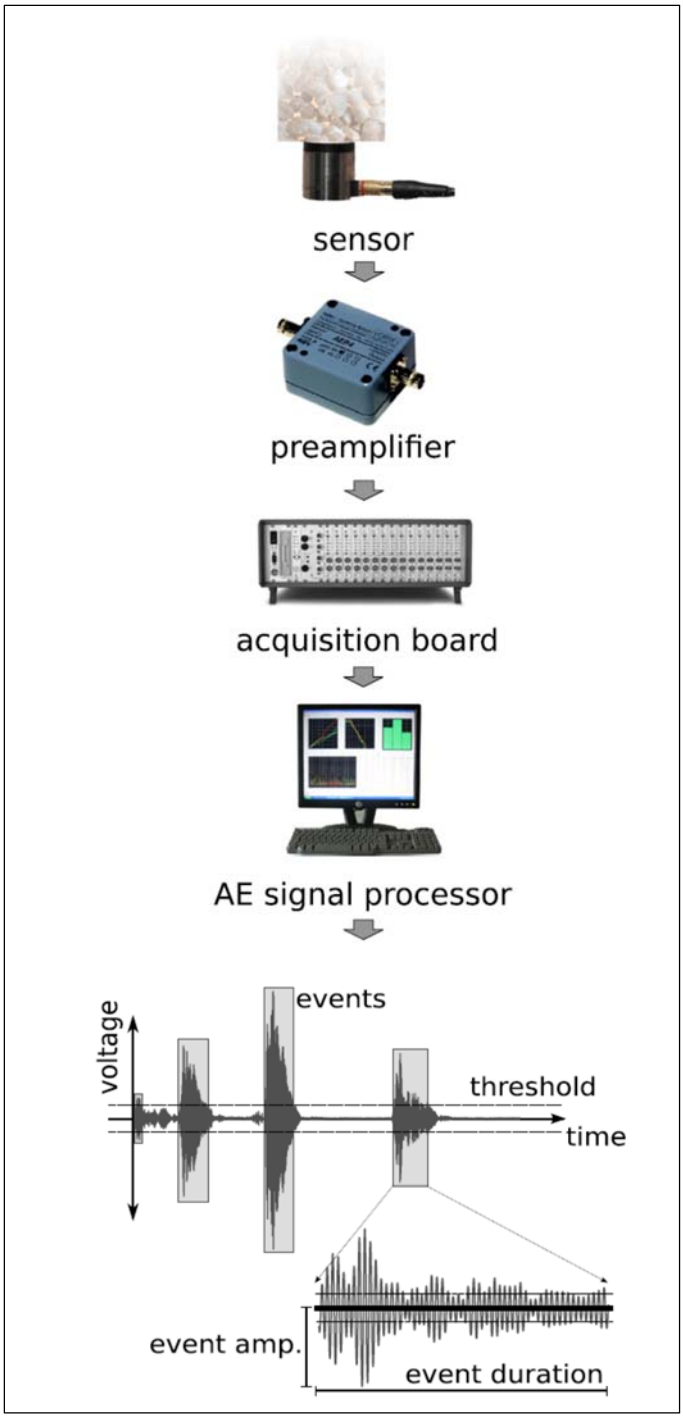

Figure 6.1: A summary of the principle of acoustic emission technique: various tools and systems that are used in the data acquisition and analysis of acoustic monitoring [*Michlmayr et al.,* 2012].

Acoustic emissions in materials may be produced by a variety of several failure mechanisms including but not limited to the release of force chains (formation of shear bands), grain collisions and contact rearrangements, grain friction, crack formation and fluid motion. The characteristics and statistics of AE from these mechanisms can be used to identify deformation events. The literature presents at least four major sources of AE in granular media.

1. AE induced by grain contact network rearrangement.

   According to *Rioul et al.* [2000] grain contact rearrangement is the grain-to-grain collisions and the rapid removal of contact points. Within a particle network in a body, only a small fraction of the grains are bearing disproportionally high loads and the load bearing particles are usually aligned in the direction of principal stresses called force chains [*Michlmayr et al.,* 2012]. *Radjai et al.* [1998] and *Majmudar* and *Behringer* [2005] state that characteristic patterns of grain rearrangement, namely, the promotion of a strong contact network (force chains) bearing disproportionately high loads, appearance of rolling and sliding particle contacts leads to the formation of shear bands. It has been suggested that once a shear zone is formed, episodic fluctuations of the average number of grain contacts (coordination number) and the local density within the shear zone would be accompanied by sequences of shear flow within the mobilized layers of the material and hindered shear zones [e.g., *Cain et al.,* 2001; *Aharonov and Sparks,* 2004]. Therefore, when shear zones are formed within a granular material, they have a potential for emission of elastic waves due to the intermittent destruction and formation of contact points [*Michlmayr et al.,* 2012].

2. AE from grain friction.

   Granular materials exhibit friction interaction at particle contacts when under loading. The importance of grain-to-grain friction in geological materials is widely recognized. *Tordesillas* and *Muthuswamy* [2009] have shown that frictional slip events exert a large influence on the collapse of force chains because they typically affect the weak contacts delivering support for grains holding high loads. When surfaces of granular materials are in contact and slide relative to each other, frictional processes such as abrasion and deformation of asperities, grinding and wear of debris between the surfaces,

and unlocking of the contact asperities may result. These frictional processes are associated with elastic waves, vibrations, and acoustic emission [*Akay,* 2002; *Yabe*, 2008].

3. AE resulting from crack formation.

   Michlmayr et al. [2012] note that cracks and fractures in granular earth materials occur within solid cohesive grain bonds or during abrasive wear or splitting of single particles. They also note that the formation and growth of cracks is a hallmark of brittle failure, and is the most common type of material damage monitored by acoustic emissions. These authors further state that elastic waves generated during fracturing of brittle solids depend on the failure plane orientation, the material elasticity, and the failure mode (I, II, or III).

4. AE from pore fluid motion

   Acoustic emissions can also be produced by rapid flow of fluid through a porous material. It was observed by *DiCarlo et al.* [2003] that considerable elastic waves could be generated during the imbibition and drainage of sand columns. *Goren et al.* [2010, 2011] showed the presence of considerable and fast liquid pressure fluctuations due to mechanical coupling of pore fluid and grains during shear deformation. From this observation, *Michlmayr et al.* [2012] makes the inference that fluctuations of pore liquid pressure may present a further mechanism that generates acoustic emissions.

Koerner et al. [1981a] conducted a comparison of AE characteristics in different soil types, namely, sand, silt, and clay. Soils of varying moisture contents and wet densities were placed in a direct shear box and deformed by applying similar stresses to each specimen. They found that acoustic emission levels are always much less in clay than in sand samples. *Koerner et al.* [1981a] attributed this to the general behavioral differences between sand and clay. Granular sand soils have larger particle sizes, approximately equidimensional shapes, close interlocking of particles, and their strength is mobilized by friction. Fine grained soils like clays have small particle sizes, flat plate-like shapes, separation of particles, and their strength is often mobilized by cohesion. Sand has the highest (the most emittive) AE response. Silt has an intermediate AE response, and clay the lowest (the least emittive) [*Koerner et al.,* 1981a].

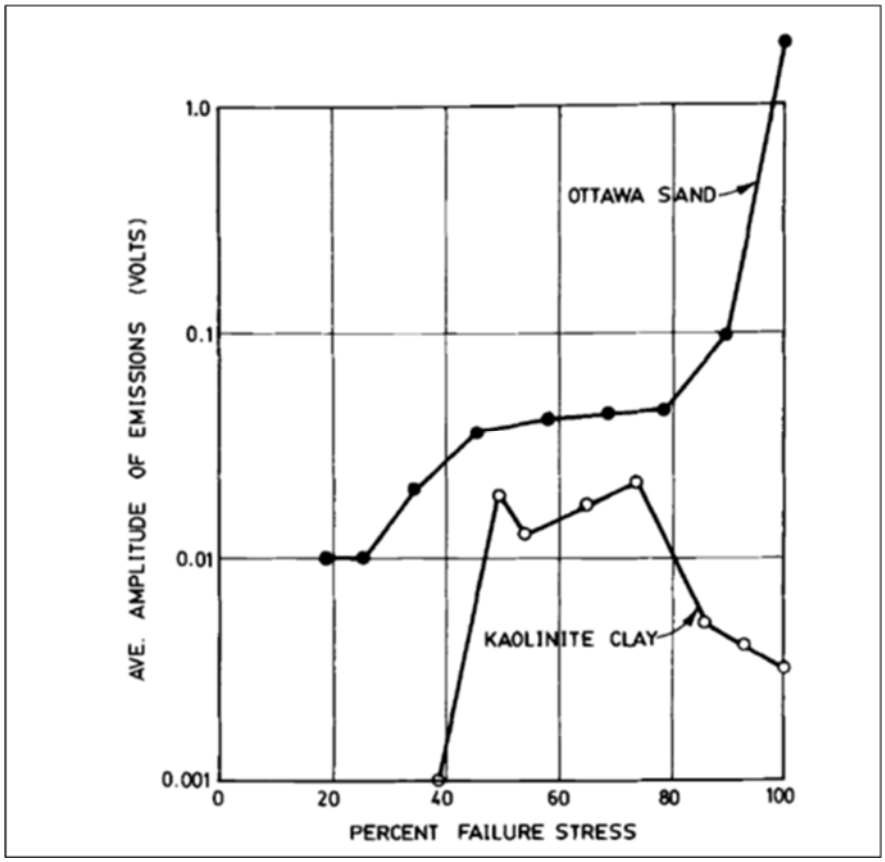

Figure 6.2: Amplitude of emissions (i.e. signal strength in volts) versus percent failure stress of granular soil and a fine grained soil [*Koerner et al.,* 1981]. The percent failure stress is defined as current stress level divided by the shear strength multiplied by 100.

A sand and a clay were identically tested in the shear box with normal stresses of 11 psi (76 kN/m^2) for failure and their emission amplitudes compared [*Koerner et al.,* 1981a]. **Figure 6.2** shows a gradually increasing AE behavior in sand followed by a sharp rise at failure while there is an initial increase in AE behavior for clay followed by a general flattening of the curve before AE amplitude begins to fall at failure. *Koerner et al.* [1981a] explain that the clay sample failed by mobilizing the flat particles into an orientation parallel to the maximum shear stress, which, during failure, is relatively "quiet." This phenomenon is known as "slicken-sides."

Lord and Koerner [1975] conducted experiments on the acoustic emission response on soils, which included the effects of axial compressive stresses and soil water content on the AE count. Axial loading was applied with a hand operated hydraulic press and no lateral stresses were applied to the samples (unconfined compression). The loading was applied in increments of 2 psi with the load being held constant while emissions were counted at each new stress level. Samples of varying water content were studied. *Lord and Koerner's* [1975] findings are presented in **Figure 6.3**. It can be seen that increasing the water content decreases the AE count.

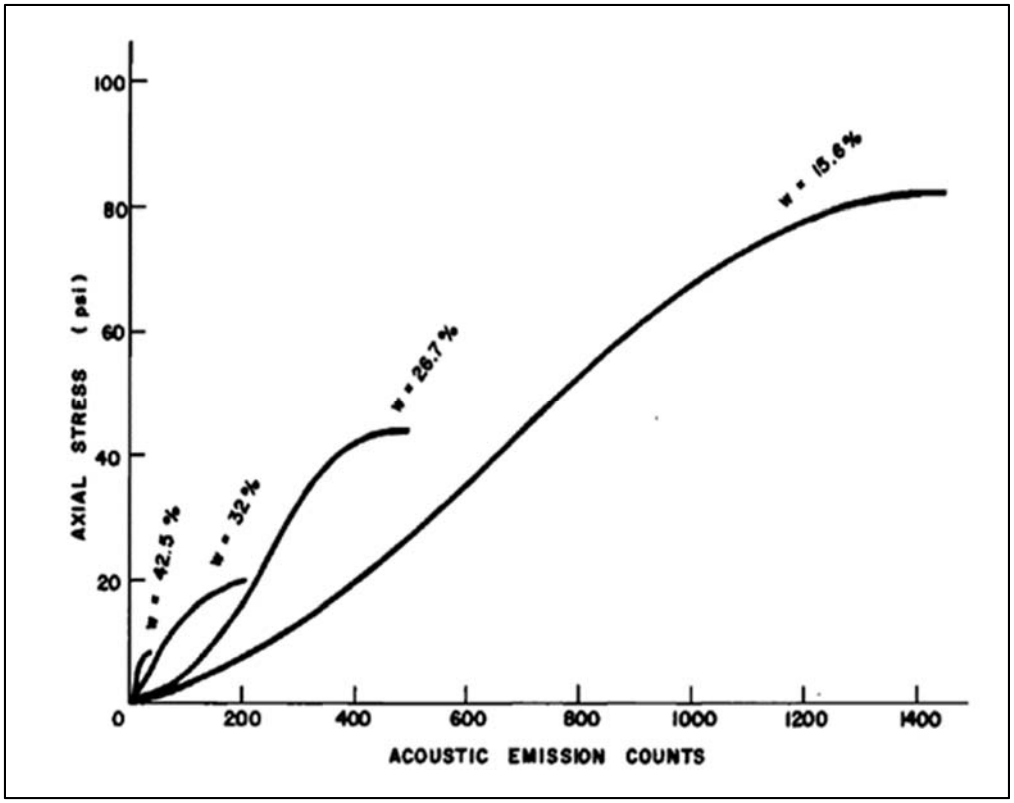

Figure 6.3: Unconfined compression test response of varying water content clayey-silt soil, showing stress verses AE counts [*Lord and koerner,* 1975]. All soils were partially saturated as indicated by the water contents ($w = eS/G_s$, w is the water content, e is the void ratio, S is the degree of saturation, and G_s is the specific gravity).

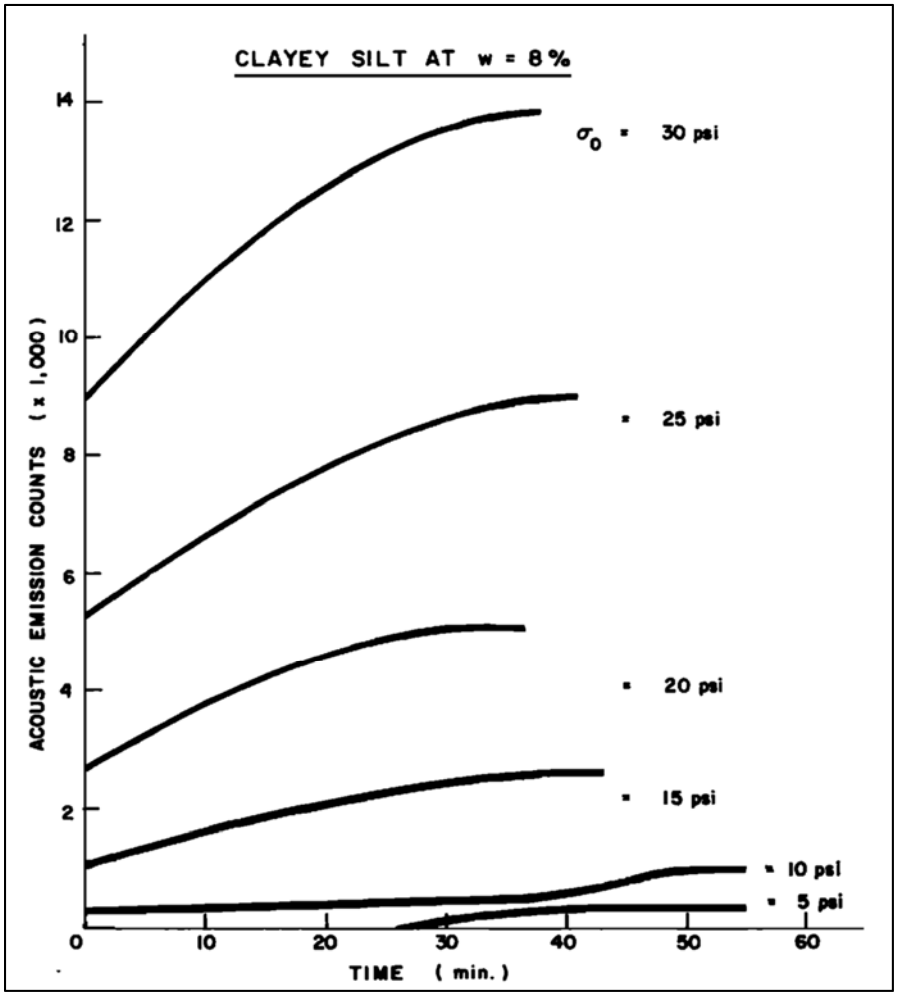

Figure 6.4: Hydrostatic (isotropic) test response of an 8% water content clayey silt at various confining pressures, showing time versus AE counts [*Lord and Koerner*, 1975].

The effect of confining pressure on AE counts was also studied. A clayey silt with a moisture content of 8 percent was used for experiments. The results are shown in the AE count versus time curve in **Figure 6.4**. *Lord and Koerner* [1975] concluded that the higher the confining stress the higher the AE count in particulate media.

Signal Attenuation

The amplitude (and strength) of an AE wave decreases as it travels through a structure. Attenuation is the loss of amplitude of a wave as it travels outward from a source. Factors that cause attenuation include geometric spreading, wave scattering at structural boundaries, and the wave energy absorption by the host material. Geometric spreading is the type of wave

amplitude decay whereby a finite amount of energy of the wave is spread out over a wave front having ever-increasing area [*Jaeger et al.*, 2007]. Here the energy of the wave is not lost but is simply spread over a larger area. Because the energy flux is proportional to the amplitude squared, as an AE spreads from its source, its amplitude decays as the inversed distance from the source in 3-D and as inversed square root of the distance to the source in 2-D. Wave scattering causes attenuation when material discontinuities (e.g. grain boundaries, inclusions) and boundaries reflect some of the energy that was initially transmitted. Absorption or material dumping occurs when the kinetic and elastic energies of AE waves are absorbed and converted into heat. In this type of attenuation, energy is "lost" or "dissipated" as heat from a mechanical stand point. Absorption (dumping) mechanisms include friction on the grain contacts where the relative grain slip takes place and viscous dissipation in the fluid in the porous space (between the grains).

P-wave (V_p) and S-wave (V_S) velocities are defined by the Biot-Gassmann theory [e.g., *Jaeger et al.,* 2007] as

$$V_p = \sqrt{\frac{K + \frac{4}{3}G}{\rho}} \tag{6.2}$$

and

$$V_S = \sqrt{\frac{G}{\rho}} \tag{6.3}$$

respectively, where K is the material bulk modulus (stiffness), G is the shear modulus (stiffness), and ρ is the bulk density. Hence, V_p reflects the bulk stiffness, K, and shear stiffness, G, of the medium, while the V_S only depends on the shear stiffness, G. Our true-triaxial experiment was conducted at relatively low frequencies such that the movement of the saturation fluid relative to the solid particles was minimal during the wave propagation. This condition is necessary for the Biot-Gassmann theory to be applicable [e.g., *Emerson and Foray,* 2006]. Wave parameters like frequency, wavelength, amplitude, and mode of propagation (compressional or shear) affect

propagation of elastic waves in particulate materials. Also, soil parameters like the skeleton stiffness, porosity, and degree of saturation influence wave propagation behavior. The bulk stiffness of the soil mass is not sensitive to the stiffness of the skeleton, in fully saturated soils [e.g., *Santamarina*, 2001]. It is a function of the bulk grain stiffness, K_g, the porosity, and the bulk stiffness, K_f , of the fluid. If air is present in the soil voids, then K_f, is drastically reduced. In this case the P-wave velocity becomes mainly a function of the stiffness of the skeleton. *Emerson* and *Foray* [2006] measured P-wave velocities in well controlled samples of both dry and saturated sands at shallow depths (3 – 5 m) and their results concurred with the Biot-Gassmann theory, which predicts that for $0 < S_r < 0.985$ (where S_r denotes the degree of saturation as the fraction of the volume occupied by liquid), V_p in a partially saturated medium is less than V_p in a dry medium (**Figure 6.5**). At 100 percent saturation, the V_p largely exceeds that in dry and partially saturated sand. These results show that, for the saturation to significantly alter the P-wave velocity, a high degree of saturation is required [*Emerson and Foray,* 2006].

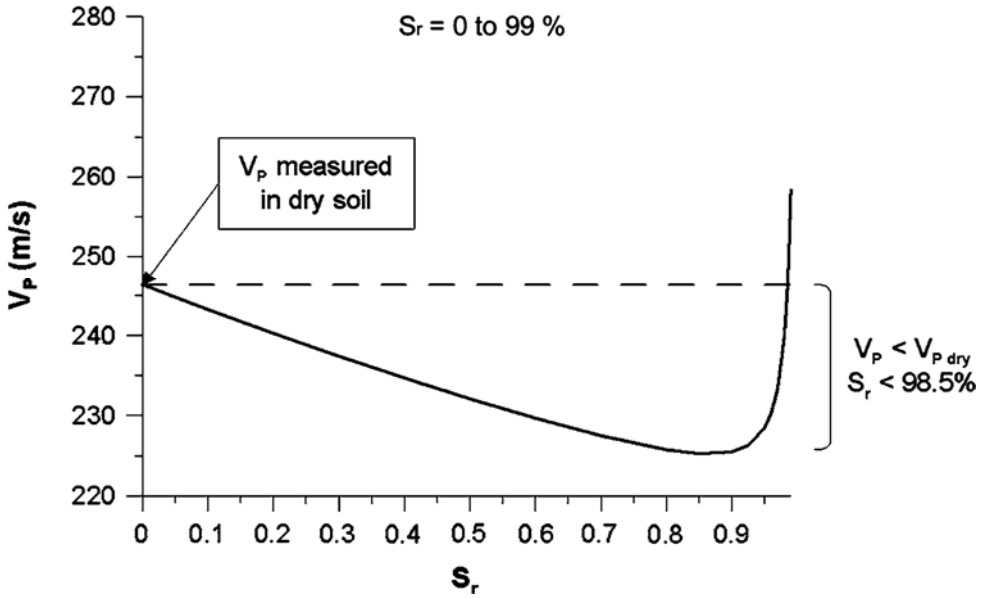

Figure 6.5: Theoretical evolution of P-wave velocity with saturation calculated from measured seismic velocities in dry Hostun S28 sand [*Emerson and Foray*, 2006].

The dimensionless quality factor *Q* is used to measure elastic wave attenuation. Factor *Q* is a measure of the relative wave energy loss per one wave cycle [e.g., *Knopoff,* 1964] given by

$$\frac{1}{Q} = \frac{c\alpha}{\pi f} \tag{6.4}$$

where *c* is the wave velocity (V_p or V_S), *f* is the frequency, and α is the logarithm of the ratio of two amplitudes measured at two different distances from the source. From this equation it can be deduced that attenuation decreases with decreasing frequency, increasing confining stress, increasing velocity, and decreasing fluid saturation [*Santamarina*, 2001].

6.3. ACOUSTIC MONITORING PROCEDURE

A robust active acoustic monitoring system was utilized in the true-triaxial test 4 described in Sections 5.3.1 and 5.4.3. We employed the acoustic monitoring system, comprised of 12 acoustic SE-150_M sensors (made by the Dunegan Engineering Consultants, Inc. [www.deci.com]), 2 aluminum plate, 12 AEP3 signal pre-amplifiers [www.valen.de/products/preamplifiers], and an AMSY-6 data acquisition system (manufactured by Vallen Systems, Inc. [www.vallen.de]). AE monitoring was performed by the placement of a system of receiver sensors in advantageous positions from which small deformation events induced by the injection of fluid into the block sample could be detected and located to provide geometric and behavioral information about the hydraulic fracturing process. The sensor array was placed perpendicular to the anticipated direction of propagation of the fracture and is described in detail in Chapter 5 (Section 5.2.5) of this work. Algorithms, described by *Stanchits et al*. [2014b], were used to locate the AE hypocenters of deformation "events." These algorithms are based on an assortment of information obtained from compressional (P-wave) arrivals detected by the array and on the characteristic velocity of the block sample.

A total of 14,397 AE events were utilized for fracture geometry mapping in test 4. A 5 MHz sampling rate and 16-bit amplitude resolution were selected for test 4. The objectives of this acoustic monitoring system were to record reliable signals and AE data that could be used to reproduce the AE spatial and temporal evolution, to independently determine the moment of

fracture initiation, to map the fracture geometry, and to evaluate hydraulic fracturing dynamics during the early stages of fracture growth. After the test, all AE and UT signals were automatically separated into three data sets: (I) auto-calibration signals to determine the velocity model of the block sample (which is required for calculations of AE hypocenter coordinates), (II) AE signals monitored during injection, and (III) ultrasonic transmissions performed along 36 ray-paths once per s to monitor variations of waveforms, velocities, and amplitudes related to fluid injection into the unconsolidated block sample.

Two kinds of ultrasonic transmission measurements were performed during this test. (A) Before the beginning of fluid injection, ultrasonic transmissions were performed using a built-in function of the Vallen data acquisition, called "auto-calibration" [*Stanchits et al.,* 2014a, b; www.vallen.de]. During this procedure, each transducer was excited by an electric pulse of 450 V to generate an acoustic wave, and the remaining 11 transducers received this signal. The procedure allowed us to calculate the velocity in the block along multiple ray path directions. (B) During the fluid injection interval, a different ultrasonic transmission system was used. This system applied a 200 V pulse from a pulse generator to sensors 1-6, which were installed on the east face of the block (the east face was perpendicular to the σ_3 direction as shown in **Figure 5.1b**). Included in this were six relays disconnecting AE sensors from preamplifiers, and after triggering of the external pulse generator, relays were returned back to AE registration mode. The full cycle of sending pulses by six senders took approximately 0.8 s, and transmissions were repeated once per s.

Figure 6.6 shows measurements during the auto-calibration procedure as the plot of distances between different sensor pairs versus automatically determined onset time. In total, 124 ultrasonic transmission signals were analyzed, providing reliable measurements of onset time, but only 71 ultrasonic transmission signals crossing the block between opposite faces were selected (red dots). Ultrasonic transmission signals located within single faces of the block (west or east) were excluded from calculation of velocity (gray dots).

It appears that most of the excluded signals had a much higher velocity than those expected in unconsolidated sand. P-wave velocities in wet sand have been measured to be

typically 1.5 to 2.0 km/s [e.g. *Bourbie et al.,* 1987]. It is possible that these exhibited propagation of ultrasonic waves within the aluminum plate that the sensors were embedded in (P-wave velocity in aluminum is about 6 km/s). Therefore, only transmissions between the opposite eastern and western faces of the block were taken into account. The slope of the best fit straight line to the distances between sensor pairs versus onset time, provides the characteristic velocity of the block. Thus, 2.16 km/s was selected as the characteristic velocity for this block and was utilized for localization of AE hypocenters (in test 1, the sample block velocity was approximately 1 km/s).

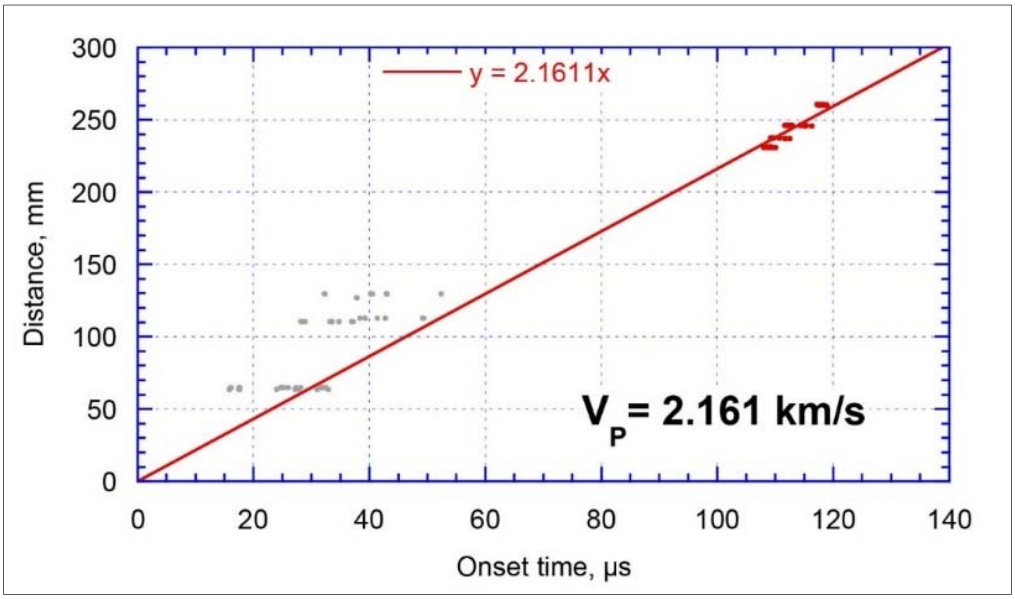

Figure 6.6: Distance between sensor pairs versus onset time. Gray dots indicate ultrasonic transmission traces located within single face of the block and are excluded from analysis. Red dots indicate ultrasonic traces corresponding to transmissions between eastern and western faces of the block, providing calculation of characteristic velocity of unconsolidated sand pack.

6.4. ACOUSTIC EMISSION RESULTS

This section presents acoustic emission results from test 4 of the true-triaxial experimental series described in Chapter 5. First, the injection pressure signature during fluid injection is correlated to the acoustic emission count rate. Secondly, the AE hypocenter locations are mapped and compared to the excavated fracture geometry. Then the AE cloud spread with time, in the

principal stress directions is discussed. Finally, the AE hypocenter spatial and temporal evolution is presented for the pre-peak, post-peak, and post-shut-in stages of injection defined below.

6.4.1. Correlation between injection pressure and AE count rate

In **Figure 6.7** the injection pressure is shown in red and the cumulative number of AE events is shown in green. The injection volume and the AE activity count rate as functions of time are shown in blue and pink, respectively. The AE activity count rate as a function of time is calculated as a derivative of the cumulative number of AE events shown in green in **Figure 6.7**. The flat-jack and axial actuator volume responses are shown in **Figure 6.7** indicating volumetric deformation of the block sample. For the σ_1 direction (cyan), the change in the axial actuator volume (ΔV_1) is shown. For the σ_2 (purple) and σ_3 (green) directions, the changes in flat-jack volumes (ΔV_2 and ΔV_3) are shown (see Section 5.1 for the definitions of ΔV_1, ΔV_2, and ΔV_3). **Figure 6.7** also shows the block configuration and the applied stress conditions. There appears to be a correlation between the injection pressure curve and the AE activity count rate curve**.** First, there is a general rise in the AE activity count that corresponds to the rise in injection pressure before the peak pressure is reached. At the peak pressure, there is a steep drop both of the pressure and the AE count rate. After this steep drop, there is a general flattening in both the pressure curve and the AE count rate curve. Finally, there is a drop in both curves as the fracture tip approaches the boundaries (Section 5.4.3). Therefore, it seems possible to characterize the hydraulic fracturing process by independently analyzing the AE count rate versus time plot. Specifically, it seems possible to identify the point at which the hydraulic fracture peak pressure is reached in cohesionless particulate materials by using AE count rate data. The correlation between the injection pressure curve and the AE count rate also appears to be consistent with the ΔV_3 behavior shown in **Figure 6.7** and explained, in detail, in Section 5.4.3.

Throughout Sections 6.4 and 6.5 the injection loading is divided into 5 time intervals, (a) through (e), as shown in **Figure 6.7.** Time interval (a) ranges from the start of injection to the point of the "kink" (injection pressure p = 3580 psi) in the injection pressure curve. Interval (b) ranges from the "kink" to the peak pressure (p = 5411 psi) while interval (c) represents the time period from the peak pressure to the local pressure minimum (p = 1300 psi) immediately after

the peak. During the interval (d) the pressure changed from p = 1300 psi to the local pressure maximum p = 1500 psi followed by a drop to 1200 psi when injection was stopped. In the final interval (e) there was a gradual decrease in pressure to a constant value of approximately 1000 psi. **Figure 6.8** shows zoom-in plots of time intervals (c) through (f).

6.4.2. Fracture geometry mapping

One of the most important findings of this work was that the fracture footprint can be mapped in the laboratory using passive acoustic sensors. The array of 12 sensors placed on the eastern and western faces of the block sample was used to locate and map source coordinates of seismic events produced by the fracturing process in the block sample. **Figure 6.9**, shows a comparison of the geometry of the excavated fracture for test 4 and the 2D cumulative AE hypocenter mapping at the end of the fracturing process. A clear match between the two images was obtained. Using this technique, we were able to ascertain the 2D fracture geometry in cohesionless, particulate materials without having to physically open the block sample. It was also possible to observe the extent of the fracture and the fracturing direction where it may otherwise have been, visually, impractical to observe. Therefore, we conclude that not only is it possible to map the fracture geometry in cohesionless, sediment like materials using AE mapping, but that it is an effective technique that can produce detailed information about the fracturing process.

In **Figure 6.9**, each of the dots in the fracture mapping, represents an AE event source location. To localize the AE signals we used a localizing algorithm employed by *Stanchits et al.* [2012] and *Stanchits et al.* [2014a, b]. The localization algorithm is based on the different arrival times of the AE signal at different sensor locations. The source localization of AE events is described in *Grosse et al.* [2003], and *Grosse and Ohtsu* [2008] and is analogous to the determination of earthquake hypocenters in seismology. In seismology, several techniques are used to locate sources of seismic events including basic triangulation of arrival times from at least three seismometers and the evaluation of distances to the seismic source from the arrival times of the first and second precursors of the compression (P-wave) and shear (S-wave) waves [*Grosse et al.,* 2003]. However, in laboratory conditions, the S-wave usually arrives during the remaining

coda of the P-wave and therefore, the time interval between the arrival of the P and S waves is very short [*Stein and Wysession*, 2003]. Consequently, it is typically not possible to reliably select the S-wave arrival time.

In our tests, to localize the source coordinates of the AE events, we first characterized the P-wave velocity of the block sample as discussed in Section 6.3 (see **Figure 6.6**). Picking the P-wave onset time was based on the Akaike Information Critterion (AIC criterion) [*Leonard and Kennett,* 1999; *Stanchits et al.*, 2014b]. From the P-wave arrival times and the characteristic P-wave velocity of the block sample, the distance from the source to the sensor was calculated. Application of this method allowed for an accuracy in the AE hypocenter localization of ≈ 5 mm. A total of 14,397 AE signals were processed for fracture geometry mapping in test 4.

6.4.3. Spatial and temporal AE cloud growth in the principal stress directions

Figure 6.10 shows the projections of the AE hypocenters onto the three principal stress directions as a function of time. The injection pressure and the cumulative AE number curves are also presented to correlate AE spatial and temporal evolution with the pressure. The AE projections along σ_1 direction are shown by green dots in **Figure 6.10 (b).** The AE projections along σ_2 direction are shown by purple dots in **Figure 6.10 (c)** and the AE projections along σ_3 are shown by cyan dots in **Figure 6.10 (d).** Initially, the AE cloud in all three principal stress directions was clustered very close to the injection source in the center of the sample block. Then, the AE cloud began to spread and expand away from the center. At the moment just before the peak pressure (**Figure 6.10,** interval (e)), the extent of the AE cloud in σ_3 direction was approximately 40 mm (**Figure 6.10 (b)**), approximately 55 mm (**Figure 6.10 (c)**) in the σ_2 direction, and approximately 110 mm (**Figure 6.10 (d)**) in the σ_1 direction. This asymmetrical spatial growth in AE hypocenters in these directions may be a manifestation of the cavity expansion process that starts out in a circular cross sectional shape and grows into an elliptical cross sectional shape just before peak pressure **(Figures 6.11 and 6.12).** The speed of growth of the AE cloud in the three principal directions was also estimated based on the slope of the AE cloud spatial and temporal evolution**.** The AE cloud extended in the σ_1 direction with a uniform speed of approximately 2 mm/s (**Figure 6.10 (d)**) and a uniform speed of 1.2 mm/s (**Figure 6.10 (c)**) in the σ_2 direction. The speed of the

AE cloud growth in the σ_3 direction was approximately 0.5 mm/s (**Figure 6.10** (b)). Immediately following peak pressure, there was a significant drop in the AE cloud density during interval (f) (**Figure 6.10**). After that, there was a slight increase in the spread in the locations of AE hypocenters. AE signals were spread in a significantly larger volume and not clustered in the central part of the sample like at the beginning of injection. This was consistent with the propagation of a large volume of fracturing fluid into the block sample immediately after peak pressure.

There appears to be an increase in the AE hypocenter density in all three directions during the fracture propagation stage in interval (g) (**Figure 6.10**). Then, there appears to be another drop in the AE hypocenter density towards the end of interval (g) as the fracture reaches the boundaries. Finally, there is another increase in the AE hypocenter density after the end of interval (g) when injection is stopped. This increase in the AE density can be attributed to the sample contraction during fracture closure. These observations illustrate the sensitivity of AE monitoring to the cycle of the fracturing process in cohesionless particulate materials.

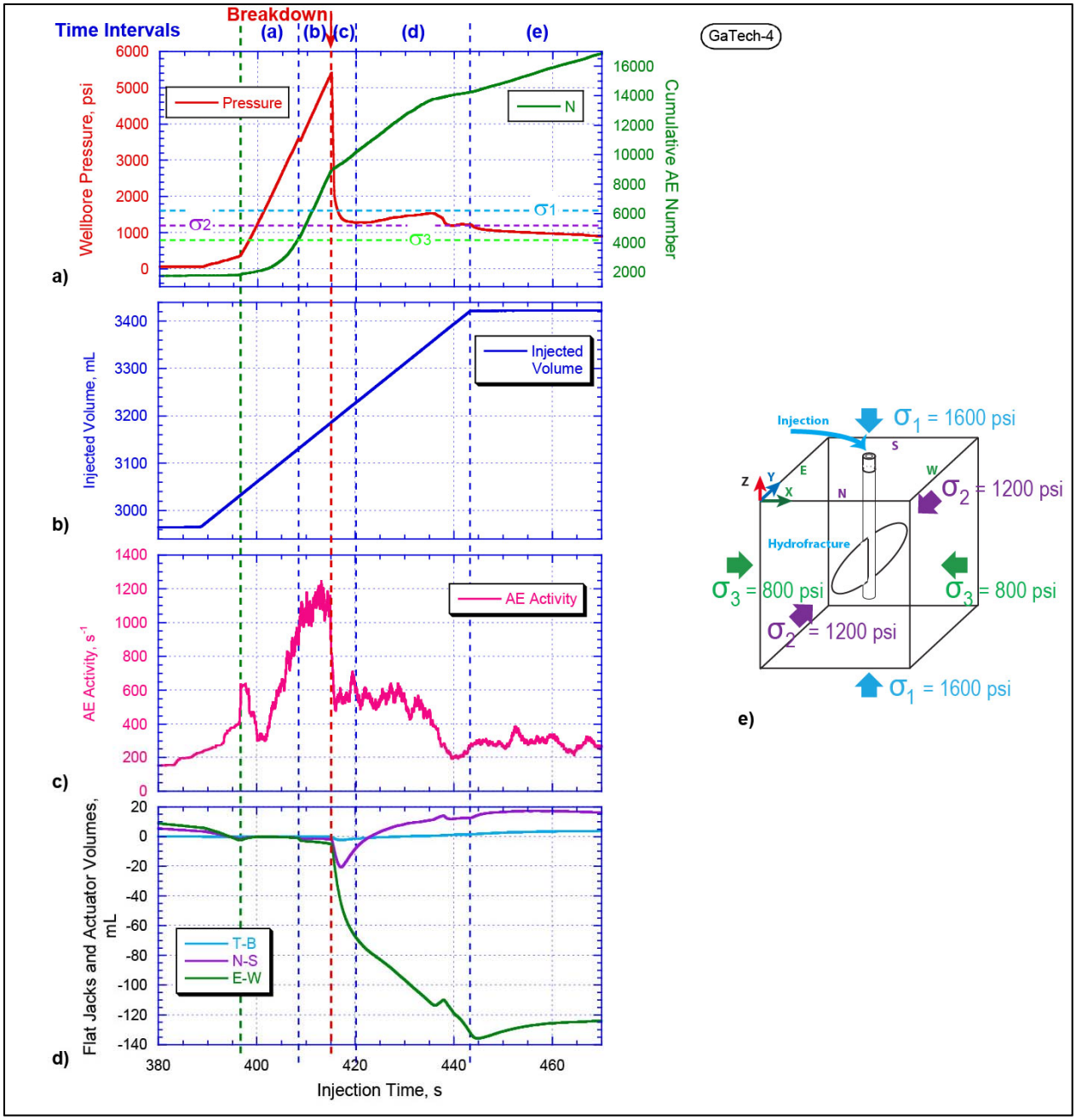

Figure 6.7: (a) Applied injection pressure (red) and cumulative number of AE events (green). (b) Injected fluid volume (blue). (c) AE activity count, calculated as a derivative of the cumulative number of AE events, presented as green curve in (a). (d) Change in flat-jack and axial actuator volumes, indicating block deformations ΔV_1(cyan), ΔV_2 (purple), and ΔV_3 (green). (e) The block configuration and the applied stress conditions.

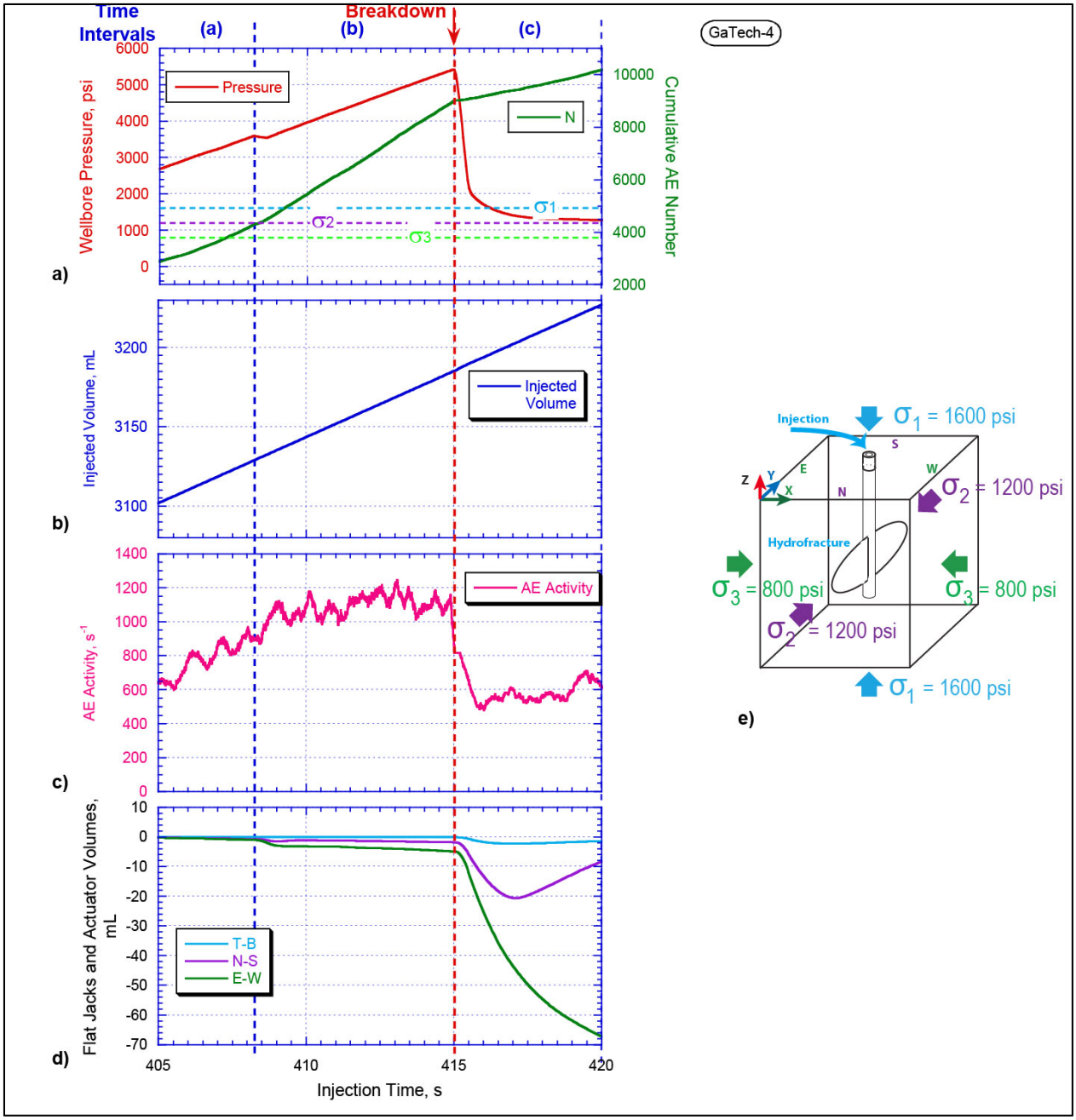

Figure 6.8: (a) A detailed view of the applied injection pressure (red) and cumulative number of AE events (green). (b) Injected volume (blue). (c) AE activity count, calculated as a derivative of the cumulative number of AE events, presented as green curve in (a). (d) Change in flat-jack and axial actuator volumes, indicating block deformations ΔV_1 (cyan), ΔV_2 (purple), and ΔV_3 (green). (e) The block configuration and the applied stress conditions.

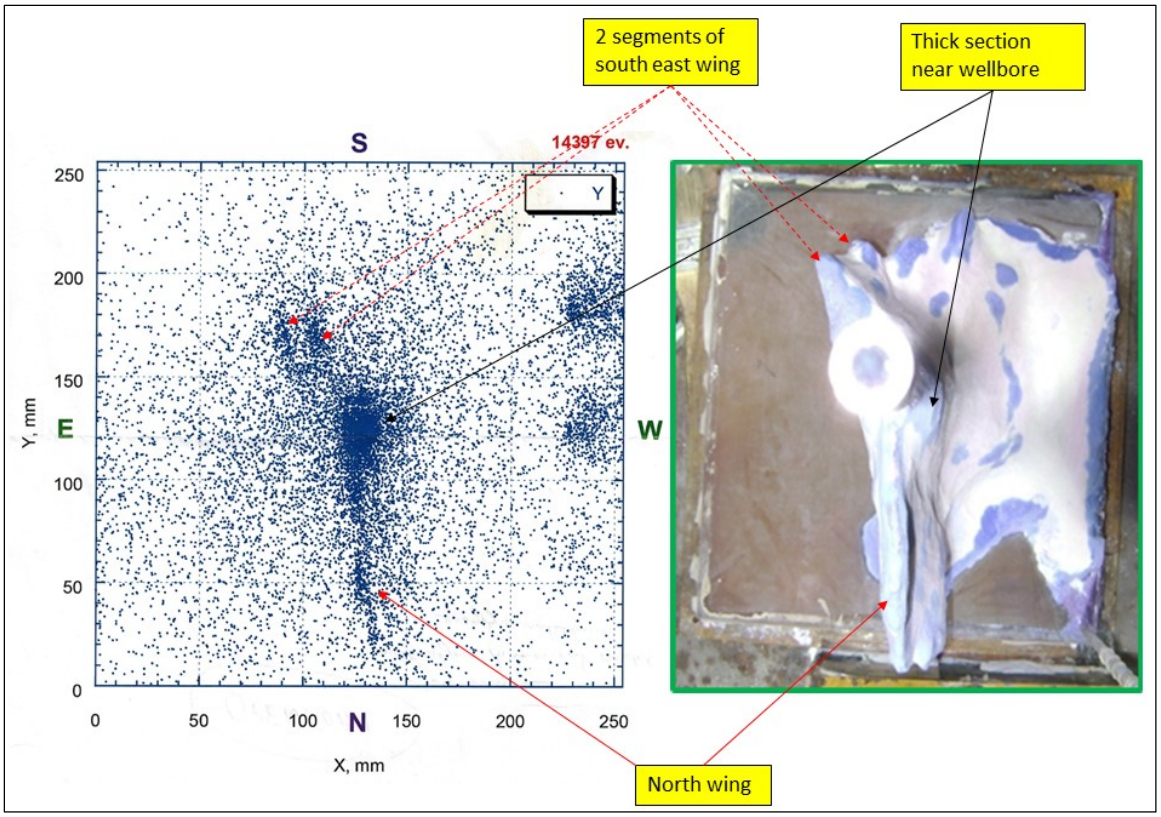

Figure 6.9: Matching the acoustic emission mapping and the geometry of the hydraulic fracture. A total of 14,397 AE signals were used.

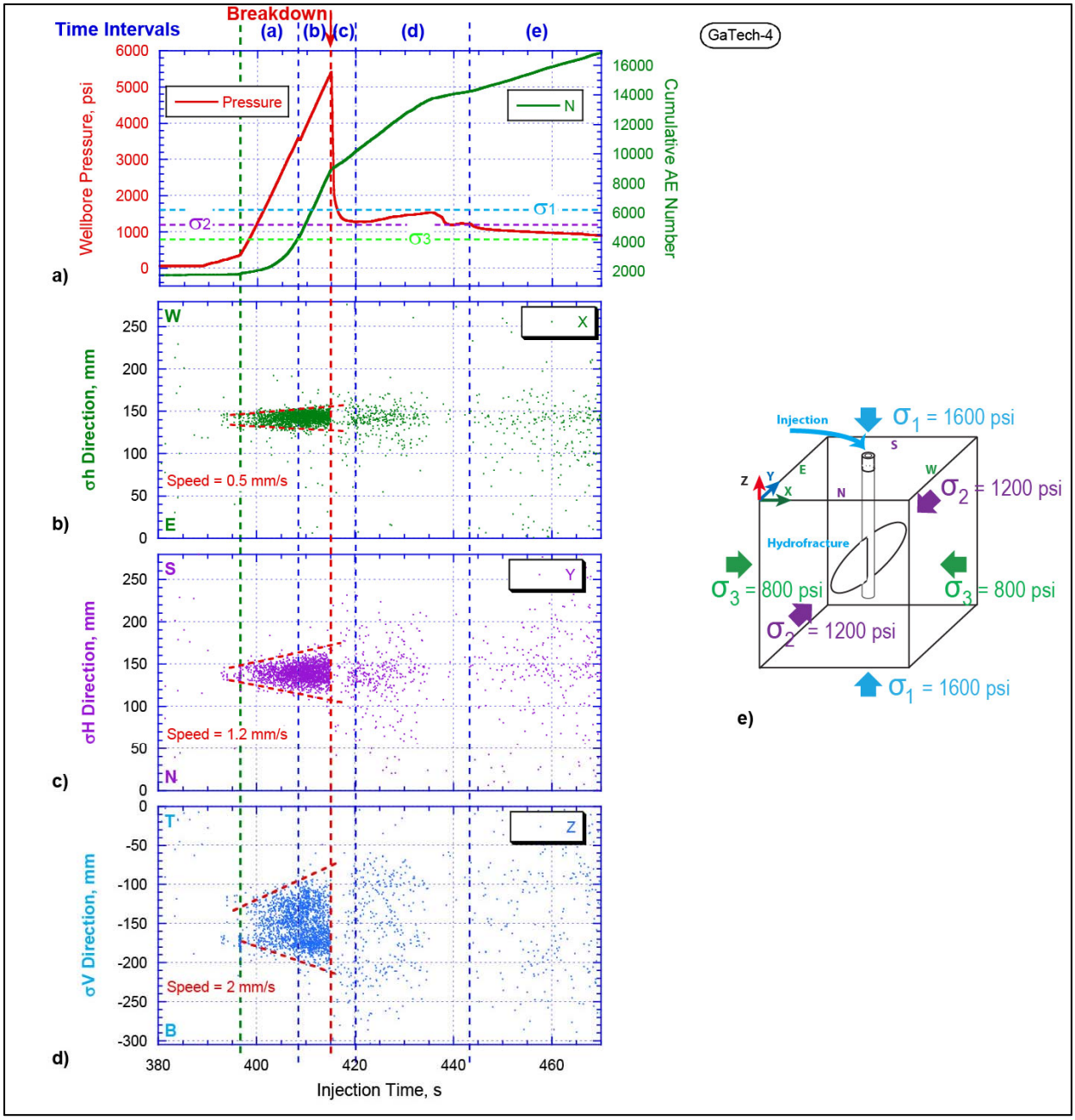

Figure 6.10: (a) Injection pressure and cumulative number of AE during all stages of fracture propagation as a function of time. (b) AE spread along the σ_3 direction as a function of time. (c) AE spread along the σ_2 direction as a function of time. (d) AE spread along the σ_1 direction as a function of time. (e) Insert showing the block configuration and the stress conditions.

6.4.4. Correlation between AE evolution and hydraulic fracturing

This section presents and discusses stage by stage snapshots of the AE hypocenter spatial and temporal distributions. **Figures 6.11** through **6.15** show AE data results measured from the beginning of the injection of the fracturing fluid to a few minutes after the injection was stopped. This presentation and analysis is divided into three stages, namely, (1) pre-peak stage which combines time intervals (a) and (b) defined above, (2) post-peak stage combining time intervals (c) and (d), and (3) post-shut-in stage i.e., time interval (e). The pre-peak stage is defined as the time period from the beginning of fluid injection to the moment of the peak injection pressure. The post-peak stage is defined as the time period from the peak (p = 5411 psi) to when the injection is stopped. The post-shut-in stage is defined as the time after the injection is stopped.

Each figure discussed in these stages is presented in three sections: upper, middle, and lower. The upper sections of the figures show three orthogonal projections of AE hypocenters. The σ_2 direction (north view), σ_3 direction (east view), and σ_1 direction (top view) projections are shown. The magnitudes of the applied stresses are provided in the text in the top of the upper section of the figure. Colors are used to represent the σ_1 (cyan), σ_2 (pink), and σ_3 (green) stresses. The orientation of these stresses is displayed with arrows of the same colors in the orthogonal projection plots.

The middle sections of each figure show the time progression of the injection pressure (red), the cumulative AE number (purple), and the volumetric deformations along the three principal stress directions of the block (ΔV_1, ΔV_2, $\text{and}\ \Delta V_3$). These deformations are shown as dotted blue, purple, and green curves, correspondingly. The color bar at the base of the plot highlights the portions of these curves associated with the time interval investigated ((a) through (g)). The colors in this highlighted region differentiate the early acoustic events (purple, blue, and green) from the late acoustic ones (yellow, red, and dark red), and provide the same information in the orthogonal projection plots.

The bottom section of each figure shows the corresponding AE hypocenter density plots. These are calculated as the averaged AE density within a sliding cube of dimensions 10 x 10 x 10

mm^3, and the result is plotted as normalized fractions of the maximum number counted, on each orthogonal projection.

Pre-peak stage

Figures 6.11 and **6.12** show AE cloud spatial and temporal evolution during the pre-peak stage of the injection. A general increase in AE activity rate is observed from the beginning of injection to the end of this stage. The AE cloud starts out confined to the zone close to the injection source in the center of the block sample but gradually spreads out in all directions. It can also be seen that the spread of the AE cloud is asymmetrical. The top view along σ_1 direction in the normalized density plots at the bottom sections of **Figures 6.11** to **6.12** show this asymmetrical growth. We found that the AE cloud evolves from a circular shaped cross section at the beginning (**Figure 6.11**, bottom row, top view) to an elliptical cross section just before the peak pressure (**Figure 6.12**, bottom row, top view), with the longer axis of the ellipse perpendicular to the σ_3 direction. The evolution of the AE cloud also shows more extension towards the north side of the sample than to the south side. These observations are consistent with the results presented in Section 6.4.2 and the excavated fracture (**Figure 5.40**). We interpret this AE cloud evolution with time as a manifestation of the cavity expansion process preceding fracture initiation. The elliptical shape of the expanding cavity is a demonstration of the deformation sensitivity to the true-triaxial remote stress state.

A total of 5318 AE events were recorded during the pre-peak stage of the wellbore pressurization (**Figure 6.16**). The AE activity rate was measured to be 67 per s at the beginning of the pre-peak stage. It increased to 371 events per s in the mid part of this stage to 504 AE events per s just before the peak pressure was reached. This represents a 36 percent jump in AE count rate just before fracture initiation. A sharp jump in AE activity rate like this may be a precursor to fracture initiation. However, this analysis is too basic and a more robust AE statistical analysis is required to model the eminence of hydraulic fracturing in particulate media using AE statistical data.

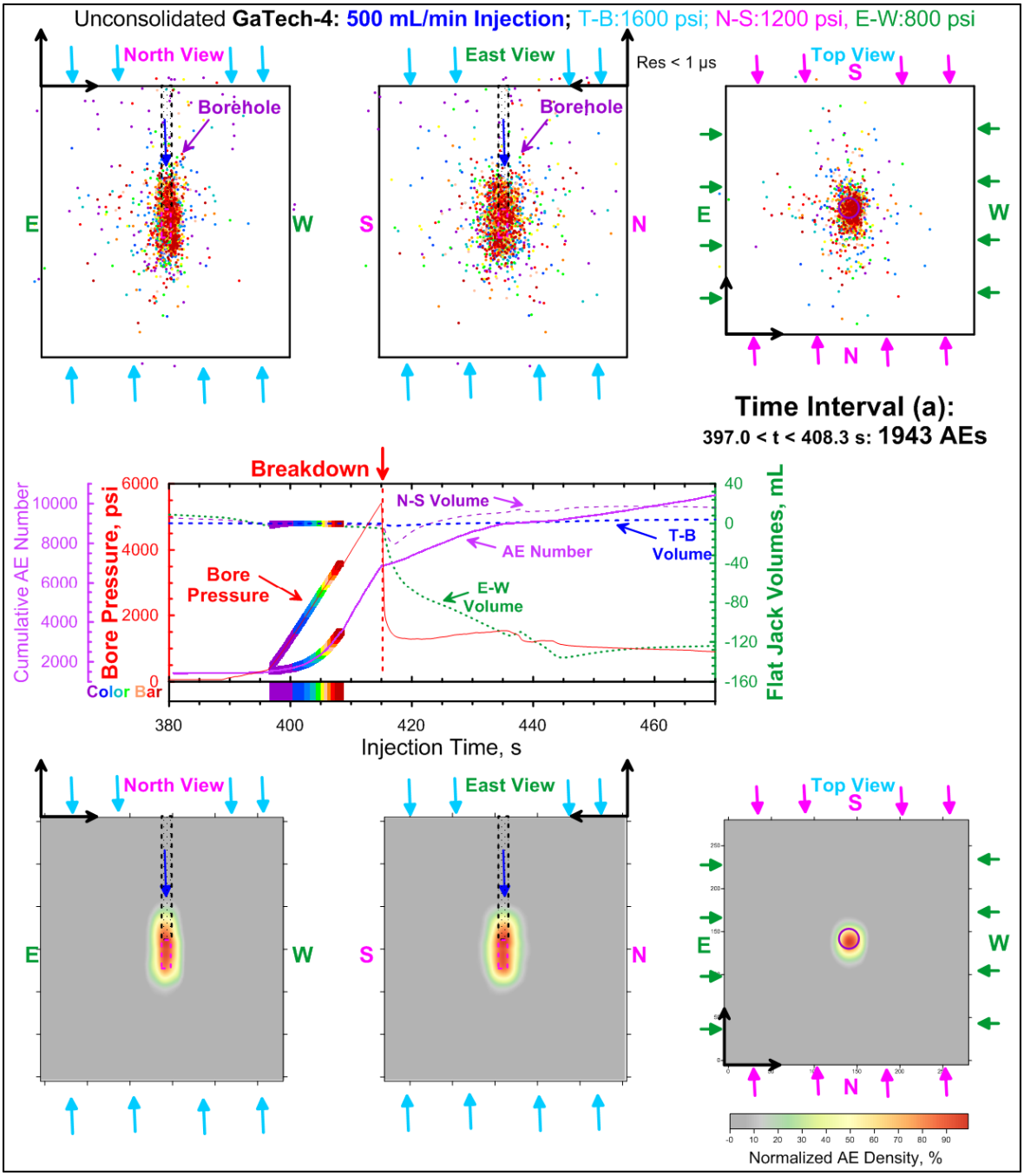

Figure 6.11: (Top) Three orthogonal projections of AE hypocenters. (Middle) Loading history recorded during injection interval (a) (i.e., the first part of the pre-peak injection stage). The color of the dots corresponds to the time sequence of AE events according to the color bar at the bottom of the figure. (Bottom) Three orthogonal projections of the normalized density of AE hypocenters.

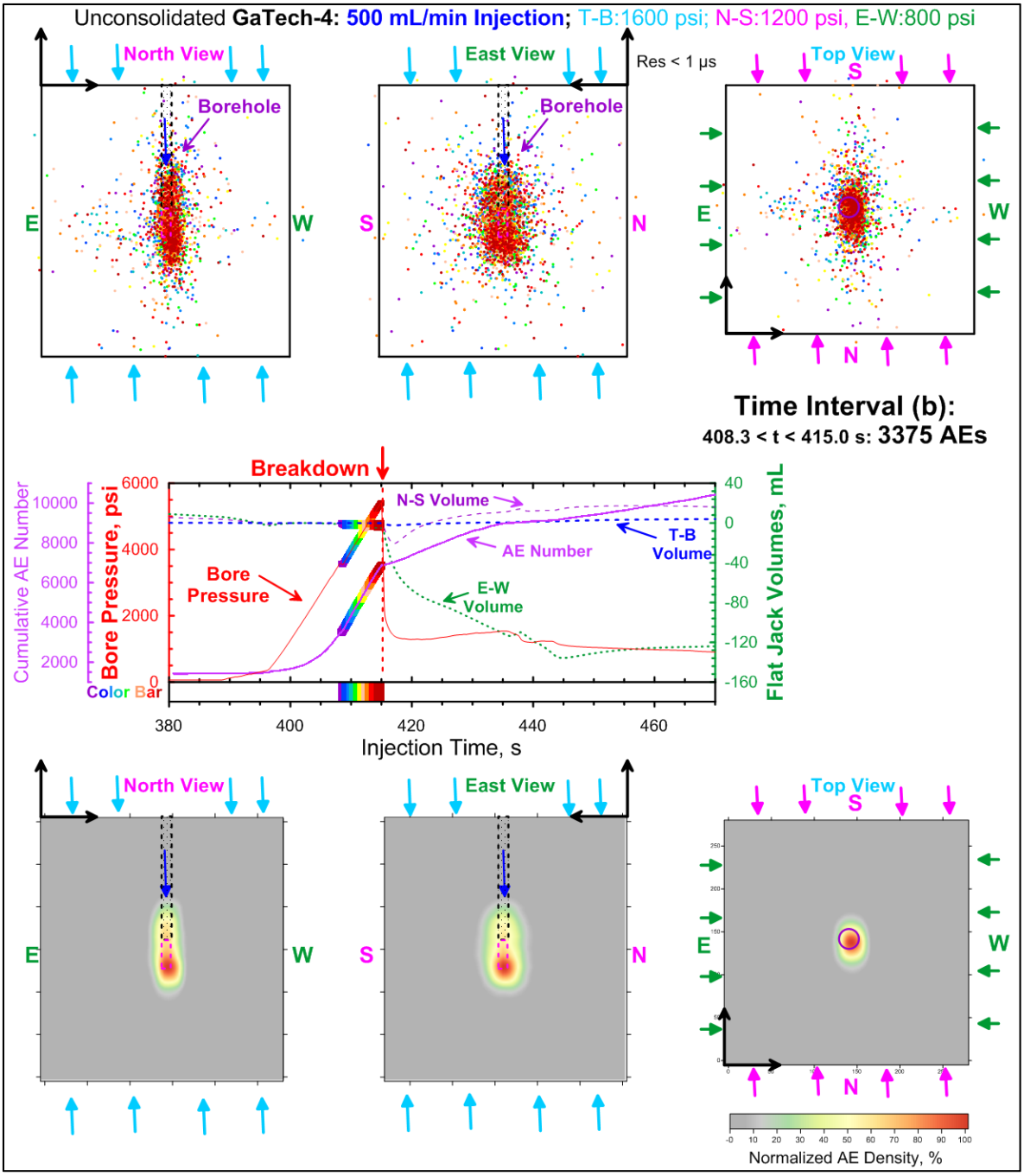

Figure 6.12: (Top) Three orthogonal projections of AE hypocenters. (Middle) Loading history recorded during injection interval (b) (i.e., the second part of the pre-peak injection stage). The color of the dots corresponds to the time sequence of AE events according to the color bar at the bottom of the figure. (Bottom) Three orthogonal projections of the normalized density of AE hypocenters.

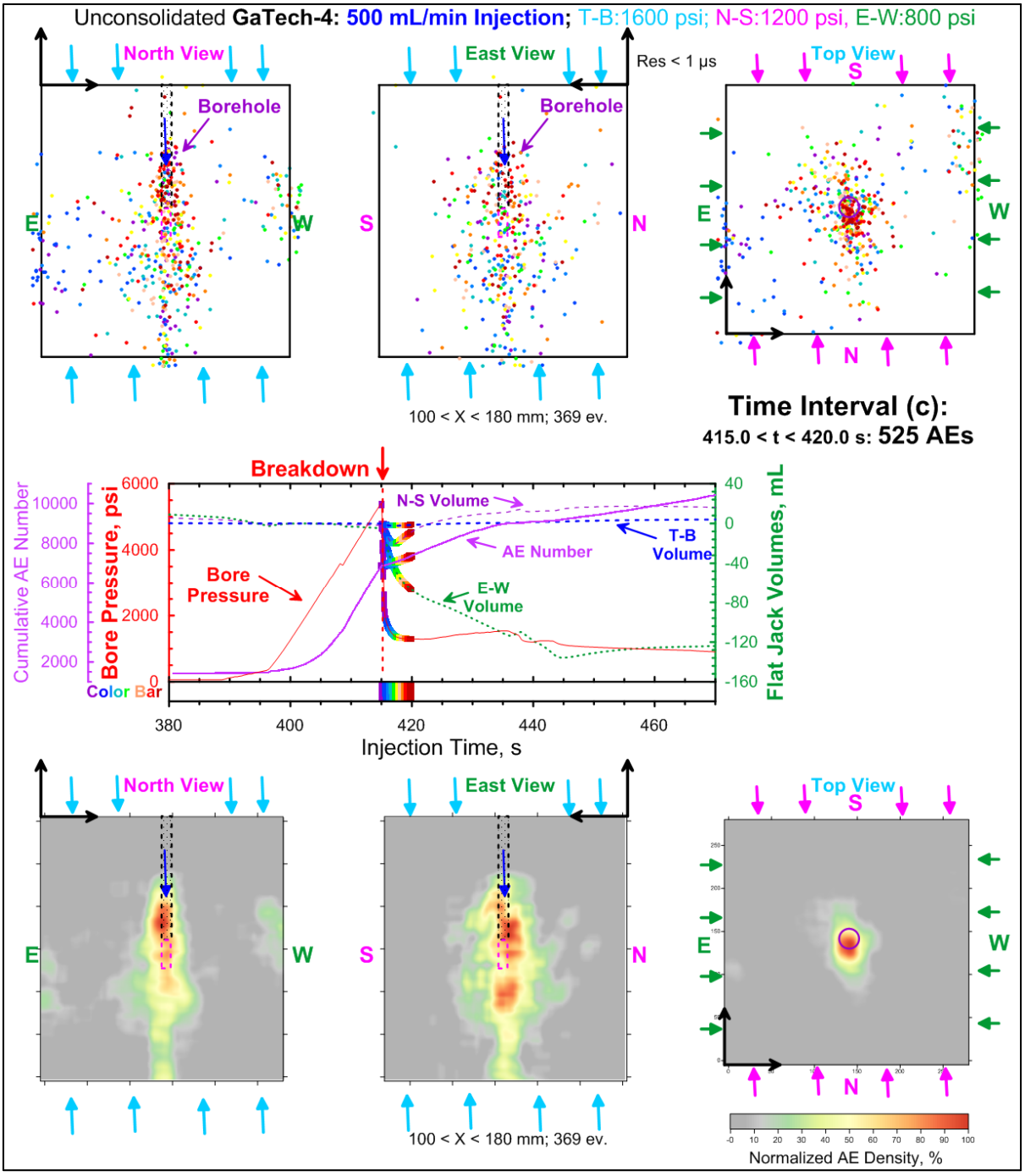

Figure 6.13: (Top) Three orthogonal projections of AE hypocenters. (Middle) Loading history recorded during injection interval (c) (i.e., the first part of the post-peak injection stage). The color of the dots corresponds to the time sequence of AE events according to the color bar at the bottom of the figure. (Bottom) Three orthogonal projections of the normalized density of AE hypocenters.

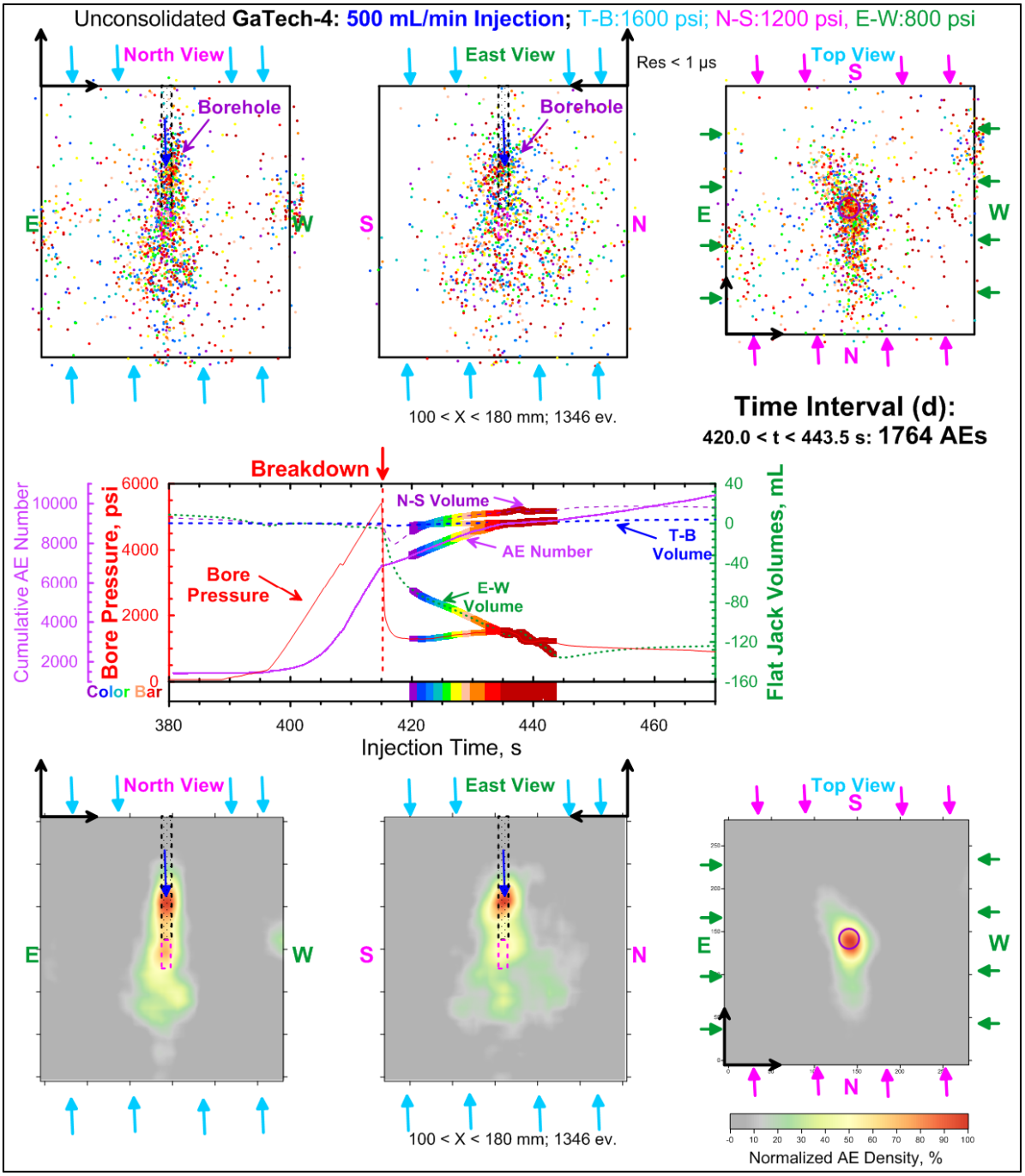

Figure 6.14: (Top) Three orthogonal projections of AE hypocenters. (Middle) Loading history recorded during injection interval (d) (i.e., the second part of the post-peak injection stage). The color of the dots corresponds to the time sequence of AE events according to the color bar at the bottom of the figure. (Bottom) Three orthogonal projections of the normalized density of AE hypocenters.

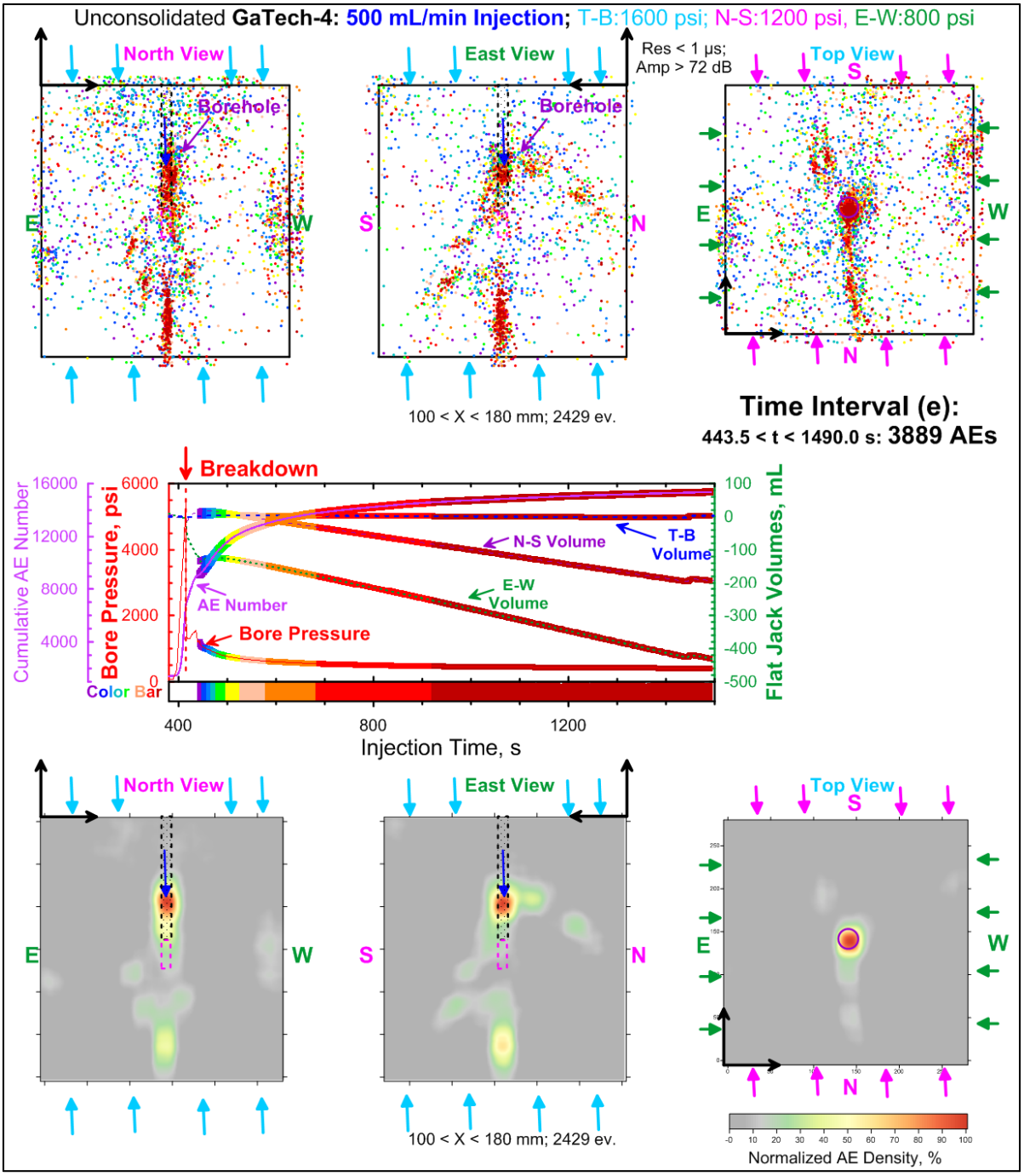

Figure 6.15: (Top) Three orthogonal projections of AE hypocenters. (Middle) Loading history recorded during injection interval (e) (i.e., the post-shut-in injection stage). The color of the dots corresponds to the time sequence of AE events according to the color bar at the bottom of the figure. (Bottom) Three orthogonal projections of the normalized density of AE hypocenters.

Post-peak stage

Figures 6.13 and **6.14** show the AE cloud spatial and temporal evolution during the post-peak stage. There is a sharp drop in the AE activity during this interval (c). Specifically, the AE count rate drops from 504 per s to 105 per s. This represents a 79 percent drop in AE count rate. During this same period there is a corresponding injection pressure drop of 76 percent from 5411 psi to 1300 psi. As stated before, a steep drop in injection pressure after the peak pressure, like this, is consistent with hydraulic fracture initiation. From this observation, we see that it may be possible to independently isolate the time of fracture initiation using AE statistical data. Also, from the normalized AE hypocenter density mapping (**Figure 6.13**, bottom row, top view, and east view), it appears that fracture initiation occurred first on the north side of the borehole. **Figure 6.13**, bottom row shows the red color density plots extending more towards the north face in relation to the wellbore position. This observation is also supported by the fact that the excavated fracture (**Figure 5.40**) had a much larger wing on the north side than the one on the southeast side. Side view projections of AE density plots (north view and east view of the lower row) also indicate spreading of the AE cloud towards the bottom face of the block. Comparison of east view and north view projections in the bottom row shows a larger spread of the AE cloud in σ_2 direction, than in σ_3 direction. These observations are consistent with a fracture that propagates in the direction perpendicular to σ_3 direction.

Figures 6.14 shows the AE cloud spatial and temporal evolution during the second part of the post-peak stage (interval (d)). The σ_1 direction (top view) projection shows significant asymmetry of the created cloud, with propagation more towards the northern face of the block than towards the southern face. At the end of the post-peak stage, the top view of the normalized AE density mapping is consistent with the geometry of the actual excavated fracture (**Figure 5.40**). The fracture has a main wing from the injection source towards the north face and a smaller wing in the southeastern direction. Therefore, it appears AE monitoring may even detect fracture geometry details such as fracture asymmetry. There was a moderate decrease in AE count rate from 105 per s in interval (c) to 74 per s during interval (d). A total of 2,289 AE signals were utilized in the analyses of the post-peak stage.

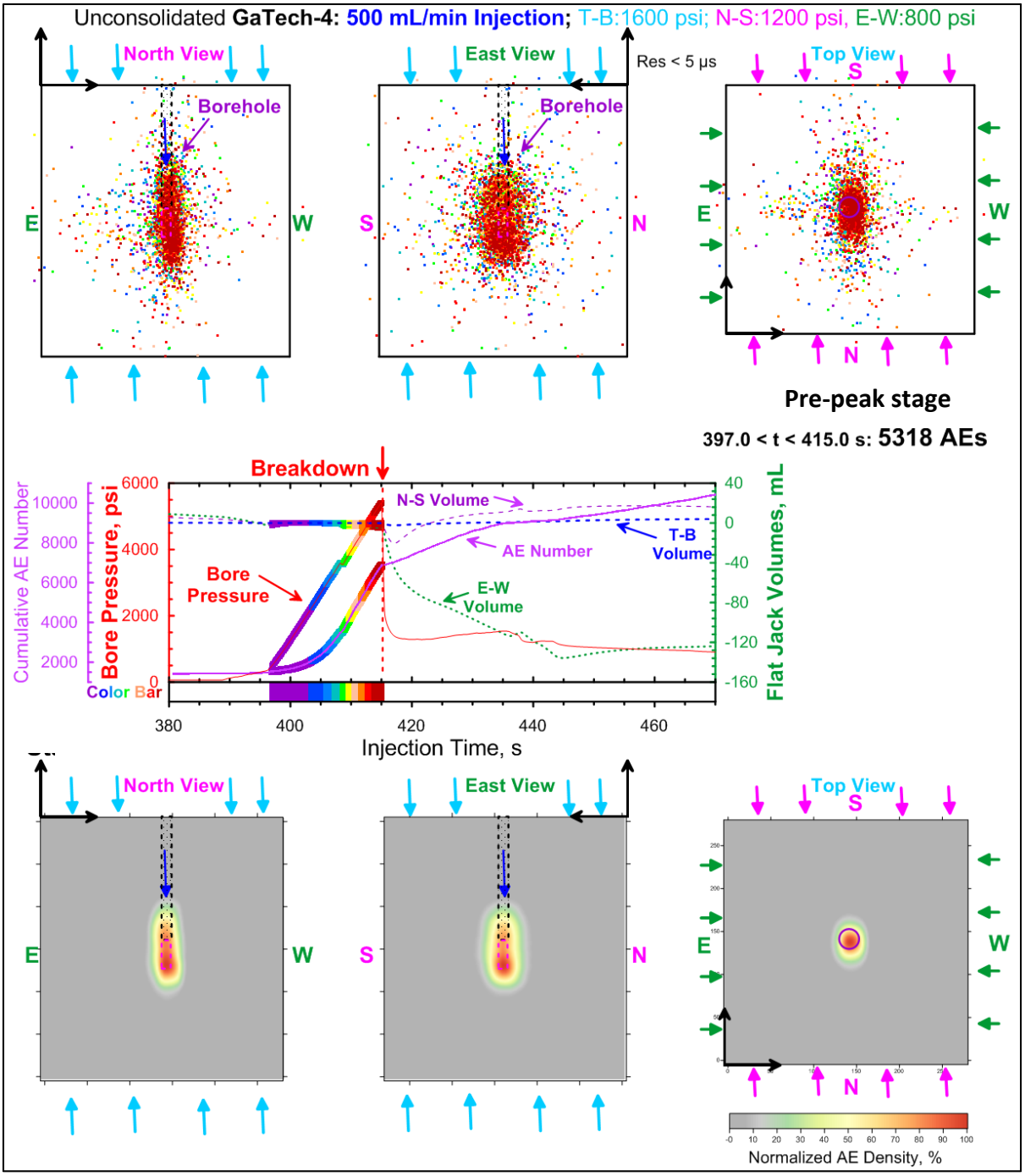

Figure 6.16: Cumulative AE of time intervals (a) and (b) in the pre-peak stage. (Top) Three orthogonal projections of AE hypocenters. (Middle) Loading history recorded during injection intervals (a) and (b). The color of the dots corresponds to the time sequence of AE events according to the color bar at the bottom of the Figure. (Bottom) Three orthogonal projections of the normalized density of AE hypocenters.

Post-shut-in stage

Figures 6.15 shows the AE cloud spatial and temporal evolution during the post-shut-in stage. This stage captures the AE data recorded 20 minutes after the injection is stopped. This plot shows the sensitivity of AE to the fracture closure process that takes place after injection is stopped. From the north view, east view, and the top view in the upper row of **Figure 6.15**, it was observed that the red dots were mostly within the margins of the fracture, indicating that the AE activity during this stage may have been related to fracture closure. The average rate of AE during this period was approximately 4 per second. A total of 3889 AE signals were utilized in the analysis of the post-shut-in stage.

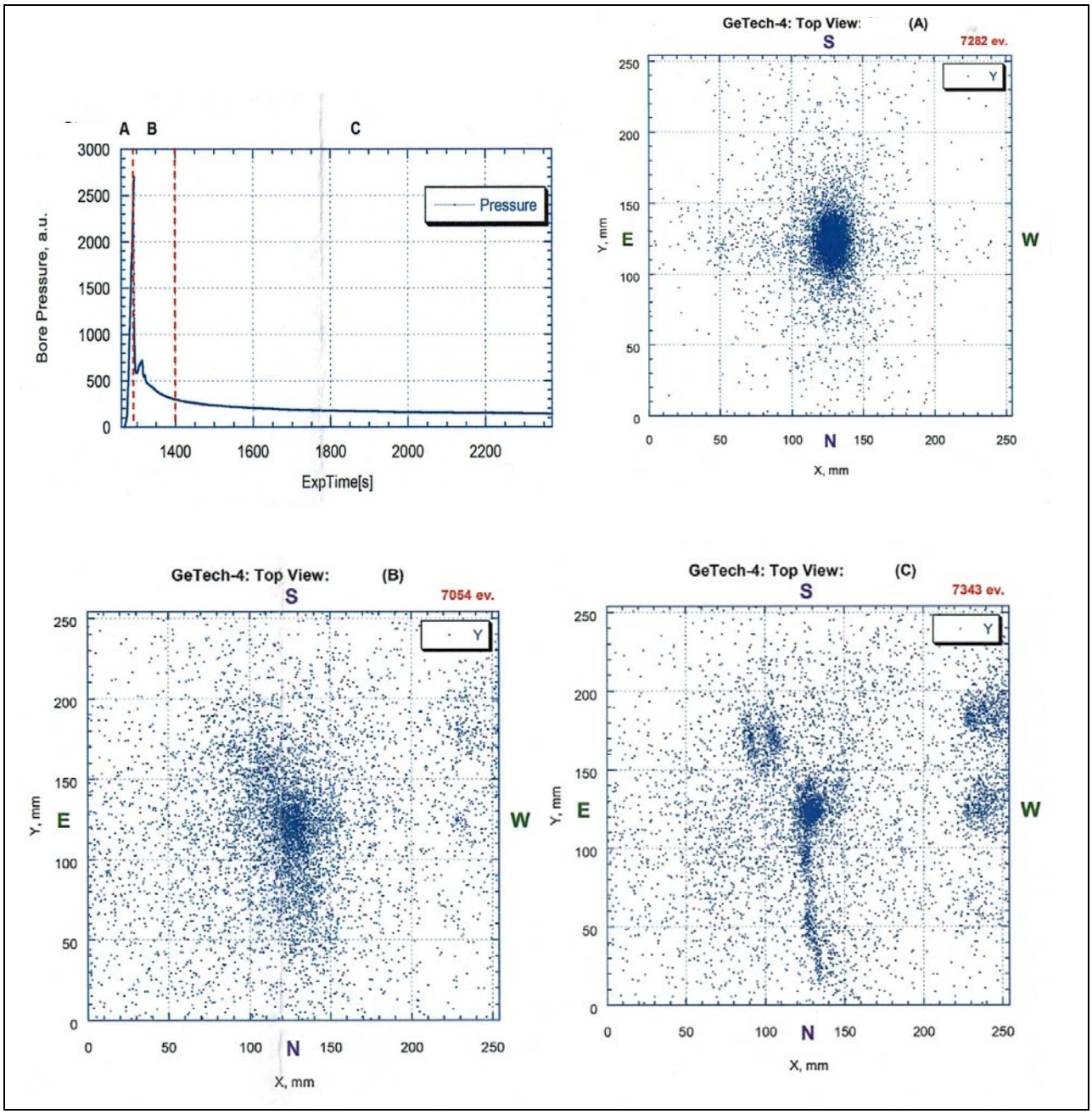

Figure 6.17: Spatial and temporal evolution of AE.

6.5. ULTRASONIC TRANSMISSION RESULTS

Ultrasonic transmissions were performed between sensors on opposite faces along the σ_3 direction. During the injection process, an internal pulse generator transmitted signals from sensors 1 to 6 on one plate to each of the 6 sensors (acting as receivers) on the other plate. Therefore, ultrasonic transmissions were made across 36 ray paths once per s to measure variations in velocity, amplitude, and waveform across the block sample and the expected fracture plane. **Figure 6.18** shows a typical representation of some ultrasonic transmission ray paths during the injection process. The following is a brief description of the variations in velocities, amplitudes, and waveforms across all the ray paths.

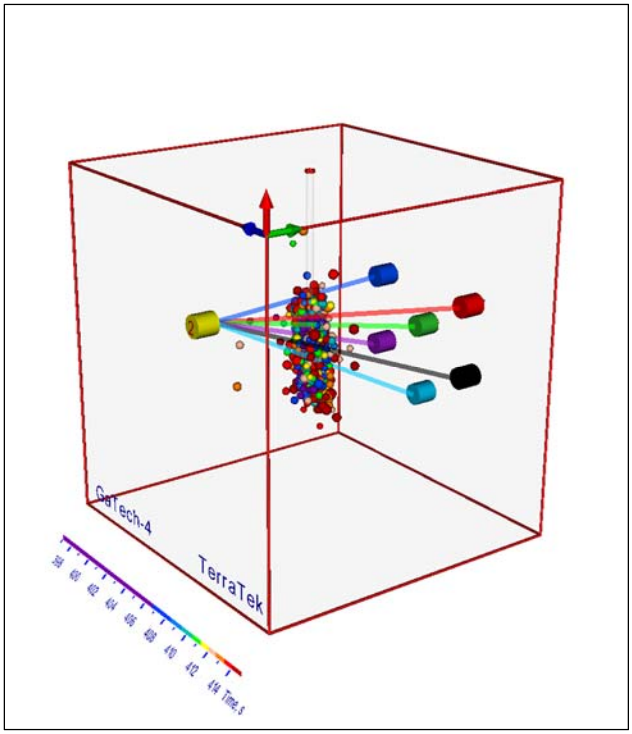

Figure 6.18: Typical representation of UT ray paths during the injection process.

6.5.1. Ultrasonic transmission velocity

Figures 6.19 and **6.20** show various P-wave velocity versus time plots calculated along all 36 ultrasonic transmission ray-paths between the eastern and western faces in the σ_3 direction of the block. The figures indicate that during interval (a) of fluid injection, marked by vertical green

dash line, P-wave velocities measured along all ray paths ranged from 2.14 km/s to 2.19 km/s. The signals with the lowest velocities were along ray paths 1-9, 2-11, 3-10, 4-11, 5-7, 6-9, and 6-12. The variations in signal velocities along various ray paths in time interval (a) are attributed to the variations in pore saturation in the sample. As discussed in Chapter 5, the saturation of the block sample in test 4 may not have been homogeneous due to a clogged inflow tube in the bottom north west corner. It appears that some pore spaces may have been partially saturated while others may have been fully saturated. The Biot-Gassmann theory predicts that, for $0 < S_r < 0.985$, V_p in a partially saturated medium decreases as a function of the degree of saturation and that V_p in dry sand is greater than in partially saturated sand (see **Figure 6.5**, Section 6.2). Therefore, the signals with the lower P-wave velocities may have been those whose ray paths encountered more partially saturated pore spaces while signals with the relatively higher P-wave velocities may have been those whose ray paths encountered more dry sand pore spaces.

Table 6.1: Summary of fastest and slowest ray paths for interval (a) of borehole pressurization.

Lowest velocity ray paths during interval (a) of injection.	Highest velocity ray paths during interval (a) of injection.
1 – 9 2 - 11 3 – 10 4 – 11 5 – 7 6 – 9 6 - 12	1 – 11 2 – 10 3 – 9 4 – 8 5 – 8 6 - 7

During interval (b), some ultrasonic transmission signals demonstrate a sudden increase of velocities of up to 5 percent, while velocities in most signals remained unchanged. From **Figures 6.19** and **6.20,** it is shown that the 5 percent increase in V_p occurred in signals 1-7, 1-10, 2-8, 2-9, 3-7, 3-9, 3-10, 4-8, 4-11, 5-9, 5-10, 6-9, and 6-11. These signals all passed through the region closest to the injection source in the center of the block sample which are estimated to have achieved better or even full saturation (Chapter 5). Biot-Gassmann theory predicts that, at full saturation the P-wave velocity sharply exceeds that in dry and partially saturated sand (see **Figure 6.5**, Section 6.2). Therefore, the spike in some V_p in interval (b) may be attributed to these

signals encountering fully saturated pore spaces near the injection zone. Another possible explanation for the spike in some V_p may have been that this was caused by an increase in the bulk stiffness of the pore fluid and the grain particles as the area near the injection zone underwent consolidation and a decrease in porosity due to the increased pressure levels in the expanding cavity around the injection source. The formation of shear bands outside the expanding cavity near the injection zone may also have caused the spike in some V_p in signals that encountered these strain localization features.

In interval (c), there is a sharp decline in velocity almost in all wave signals. During this time interval fracture initiation occurs and a significant amount of the fracture fluid ruptures into the sample. Therefore, the sharp decline in velocity in several signals passing through the injection zone may be attributed to the P-wave signal crossing the fracture plane, which is depressurized at this stage as the fluid flows into a larger volume and spreads inside the sample. This volume may also have undergone softening due to fluidization mechanisms during this time interval.

There is a general increase in velocity along all signals in interval (d) as the fracture zone is re-pressurized and P-wave transmissivity is increased again. Towards the end of this interval there is small drop in P-wave velocities generally in all signals as the fracture reaches the boundaries, depressurizing the fracture plane. There is another increase in velocity along all signals in interval (e) as the sample contracts during fracture closure.

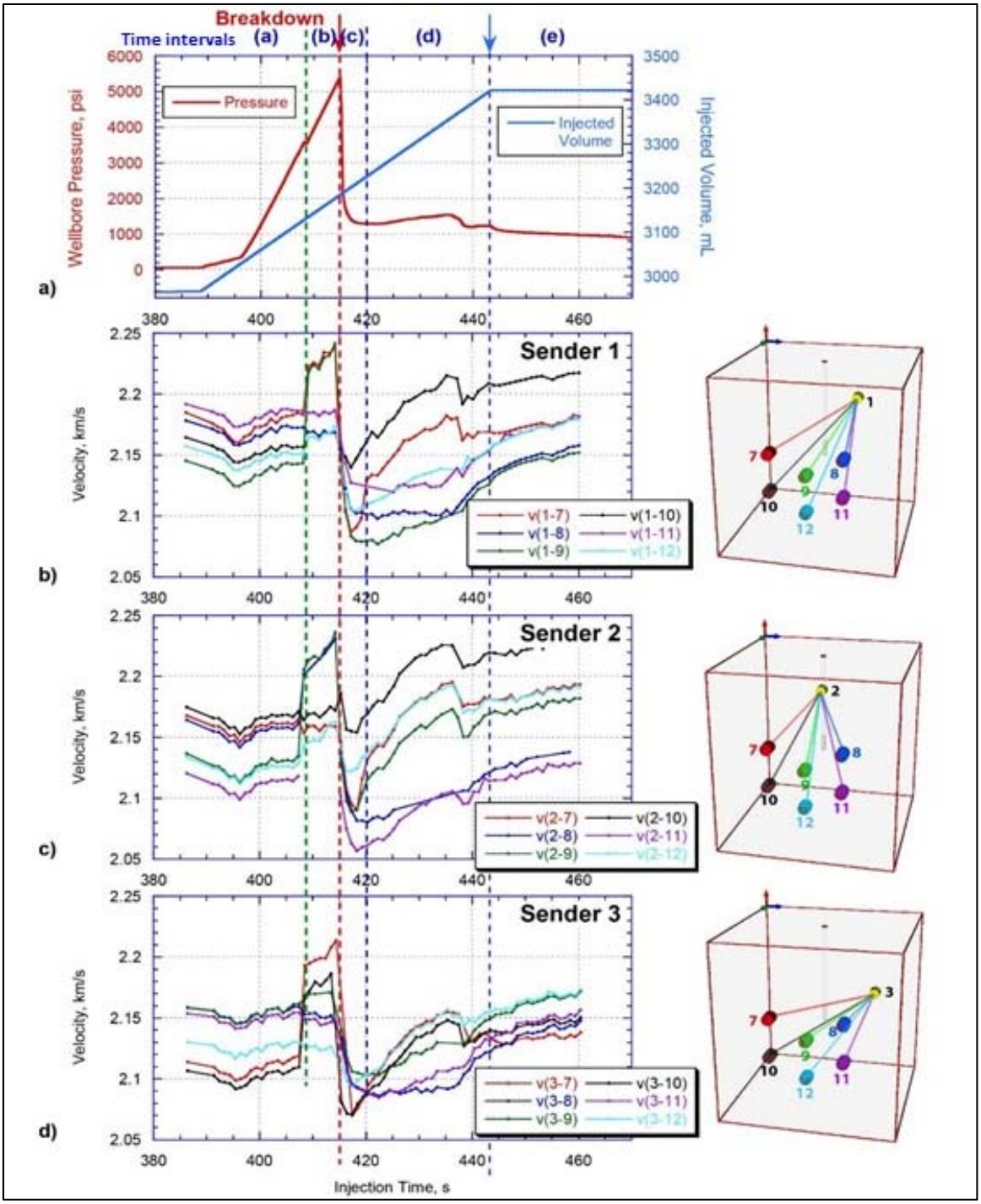

Figure 6.19: (a) Applied injection pressure (red) and injected volume (blue). (b), (c), and (d) P-wave velocities calculated for ray-paths located between east and west faces of the block with sensors 1, 2, and 3 acting as the senders, respectively.

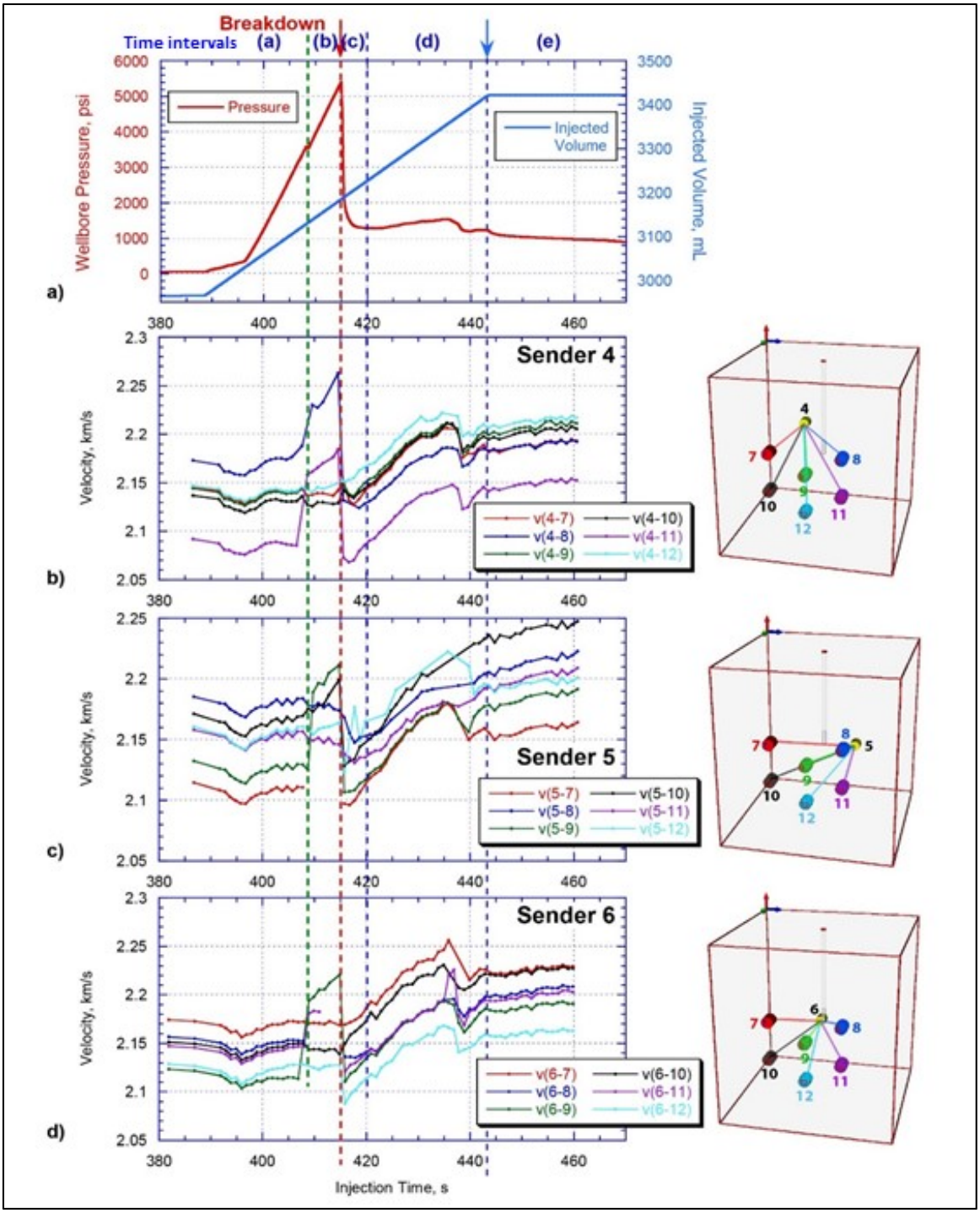

Figure 6.20: (a) Applied injection pressure (red) and injected volume (blue). (b), (c), and (d) P-wave velocities calculated for ray-paths located between east and west faces of the block with sensors 4, 5, and 6 acting as the senders, respectively.

6.5.2. Ultrasonic transmission first motion amplitude

The UT relative first motion amplitude results for the 36 ray paths along the σ_3 direction are shown in **Figures 6.21** and **6.22**. Analysis of the relative first motion amplitude variations shows that most of these amplitudes remained almost uniform during interval (a) of the injection. During interval (b), there were significant sudden decreases in amplitudes of P-waves along signals 1-7, 1-12, 1-9, 1-10, 2-9, 2-8, 2-12, 3-10, 3-7, 4-11, 4-12, 5-9, 5-7, 6-11, and 6-9. It was observed that these signals ray paths passed near the injection source zone where the degree of water saturation was relatively higher. The sharp drop in relative first motion amplitude in interval (b) may be attributed to high attenuation that these signals went through as they encountered this saturated zone.

During interval (c) indicated by the red arrow and the vertical red dash line, the relative first motion amplitudes show some complicated behavior. A few of the signals show a significant relative first motion amplitude increase while most signals show unchanged amplitude sizes to very small increases in amplitudes. Signals 1-7, 1-10, 2-9, 4-8, 6-12, and 6-9 had the highest jumps in relative first motion amplitudes. These signals also passed near the injection source zone that had the higher degree of saturation. There where yet a few more signals that exhibited amplitude decay during this interval. This complex signal amplitude behavior could be related to the complex geometry of the fracture as it propagates and grows in its plane. Signals that intercepted the fracture plane may have undergone attenuation and therefore recorded a drop in relative first motion amplitude. There may also have been a consolidated zone ahead of the fracture tip which may have had multiple shear bands. The signals that intercepted these shear bands may have undergone upward jumps in relative first motion amplitudes. The signals that did not intercept the fracture plane or the shear bands ahead of the fracture tip may have showed little to no change in amplitudes.

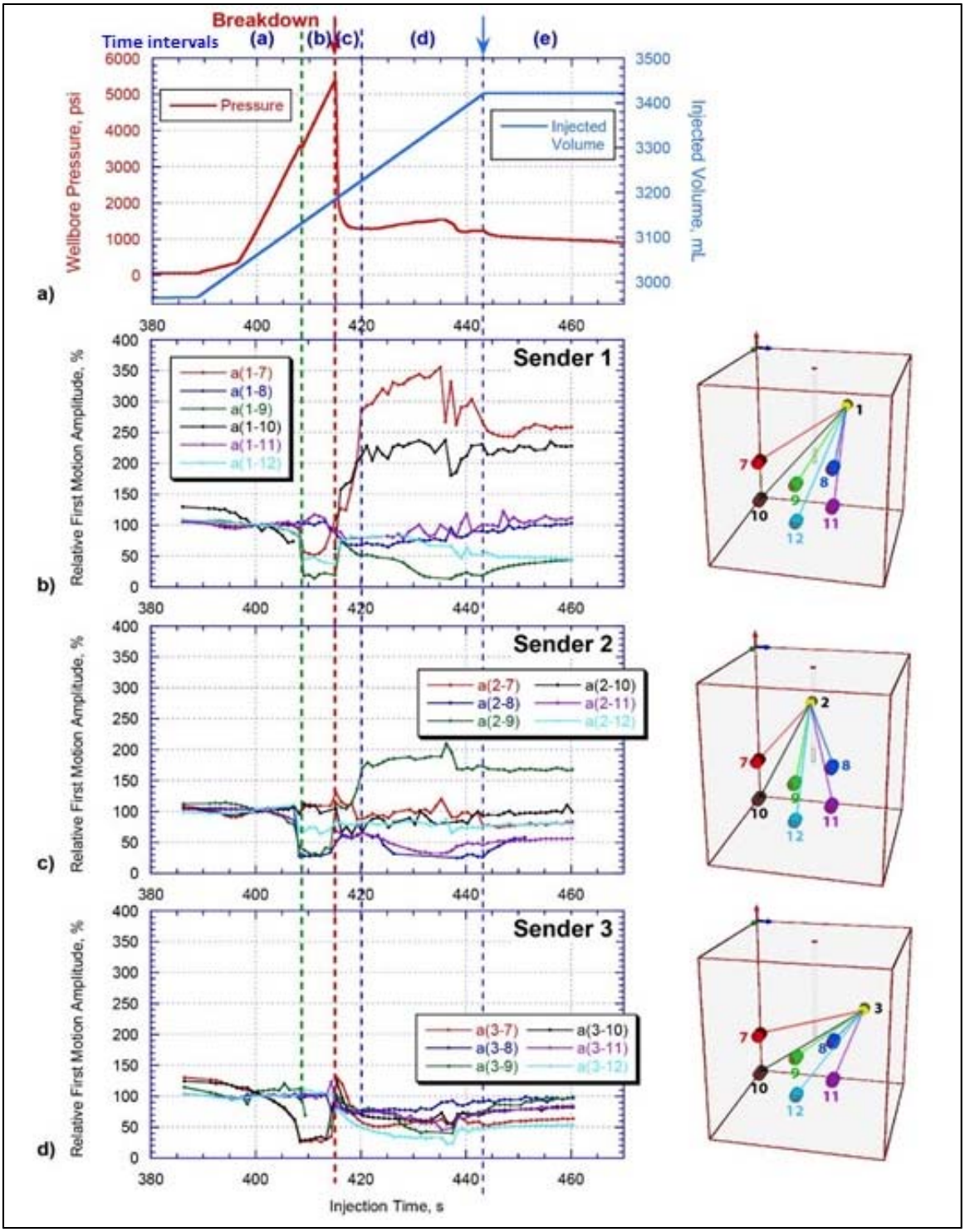

Figure 6.21: (a) Applied injection pressure (red) and injected volume (blue). (b), (c), and (d) P-wave relative first motion amplitudes normalized for the mean values measured during Interval (a) of injection for ray-paths along the σ_3 direction with sensors 1, 2, and 3 acting as the senders.

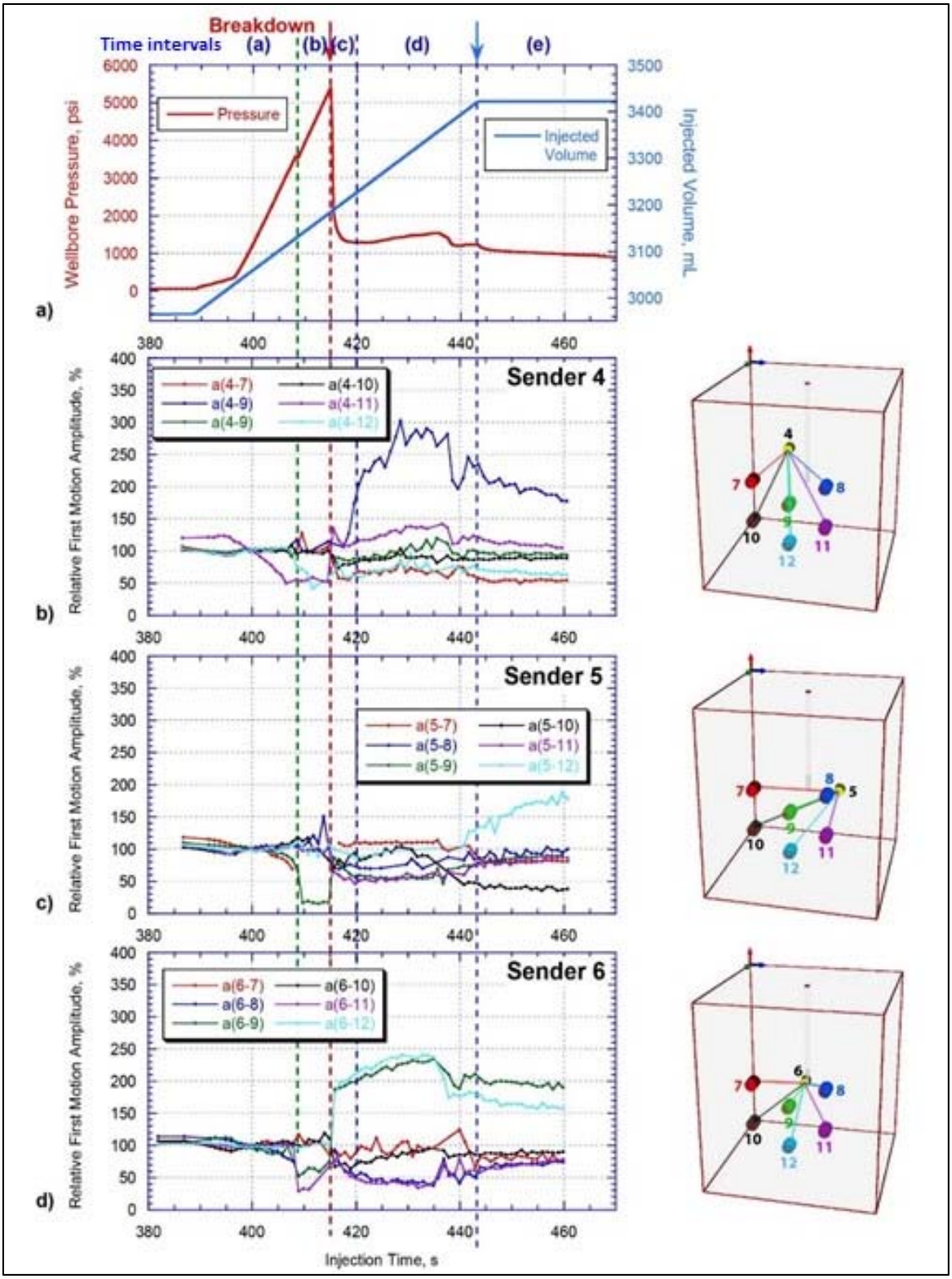

Figure 6.22: (a) Applied injection pressure (red) and injected volume (blue). (b), (c), and (d) P-wave relative first motion amplitudes normalized for the mean values measured during Interval (a) of injection for ray-paths along the σ_3 direction with sensors 4, 5, and 6 acting as the senders.

6.5.3. Ultrasonic transmission waveform

Figures 6.23 through **6.28** show variations of waveforms of ultrasonic transmissions radiated by senders 1 through 6 along σ_3 direction. Transmissions were performed during intervals (a) through (e) of fluid injection by senders located on the eastern face of the block and waveforms were recorded by receiver 9, located in the center of the western face of the block. For the purpose of easier comparisons of waveforms, the negative motions of all waveforms are highlighted by a solid color, and the onset times are indicated by open circles. From **Figures 6.23** and **6.24** signals 1-9 and 2-9, there is a decrease in onset arrival times of the waveforms from interval (a) to interval (b), indicating an increase in P-wave velocities. During this time, there is a decrease in the waveform amplitudes. The increase in P-wave velocities in this interval may have occurred in signals that may have intercepted fully saturated pore spaces near the injection zone or possible shear bands emanating from the expanding cavity. The lower amplitudes in some signals in interval (b) may be attributed to the signals that may have undergone attenuation as they intercepted partially saturated pore spaces.

In signals 1-9 and 2-9, there is a drop in the P-wave velocity and a general increase in the waveform amplitude after the peak pressure (interval (c)). The hydraulic fracture was initiated and propagated in a plane perpendicular to the σ_3 direction and therefore perpendicular to the UT signals 1-9 and 2-9. A large volume of the sample may have undergone softening due to fluidization mechanisms in the plane of the fracture. The drop in velocity in these signals may have been due to the signal crossing the fluidized and depressurized fracture plane. After peak pressure, the fracture underwent re-pressurization as injection continued.

In UT signals 3-9 and 4-9 shown in **Figures 6.25** and **6.26** the amplitudes of the signals during all intervals of the injection process were generally constant. There was a slight drop in P-wave velocities in these signals just after the peak pressure. As noted above, this slight drop in velocity may have been due to the signals crossing the fluidized and depressurized fracture plane during the interval after peak pressure.

Figures 6.27 and **6.28** show velocity and amplitude variations of UT ray paths 5-9 and 6-9. There was a slight decrease in the first motion onset time from interval (a) to (b) in signals 5-9 and 6-9 as shown in **Figures 6.27** and **6.28**. This indicates an increase in velocity during this time frame. This is followed by an increase in the first motion onset time after peak pressure indicating a decrease in P-wave velocities in these UT signals. Finally, there is a gradual decrease in first motion onset time (increase in P-wave velocity) until the end of fluid injection. The initial increase in P-wave velocities from interval (a) to (b) may have been the result of the signals encountering pore spaces with higher bulk stiffness of the pore fluid and the grain particles due to higher confining stresses from the injection loading. It may also have been due to the signals encountering fully saturated pore spaces near the injection zone. The drop in P-wave velocities from interval (b) to (c) may be attributed to the signal crossing the fluidized and softened fracture plane after peak pressure. The final recovery in P-wave velocities may be due to the recovery in pressure in the fracture as injection loading continued.

There is also a decrease in P-wave amplitude from interval (a) to (b) in signal 5-9, while this remains fairly uniform during the same intervals in signal 6-9 as shown in **Figures 6.27** and **6.28**. This is followed by an increase in P-wave amplitudes at the peak pressure period. The decrease in amplitude from interval (a) to (b) in signal 5-9 may be due to the attenuation of the signal as it encounters partially saturated pore spaces. After peak pressure, the fracture underwent re-pressurization as the injection loading continued. Therefore, the re-pressurization of the fracture may have resulted in increased wave amplitudes in signals that intercepted the fracture plane.

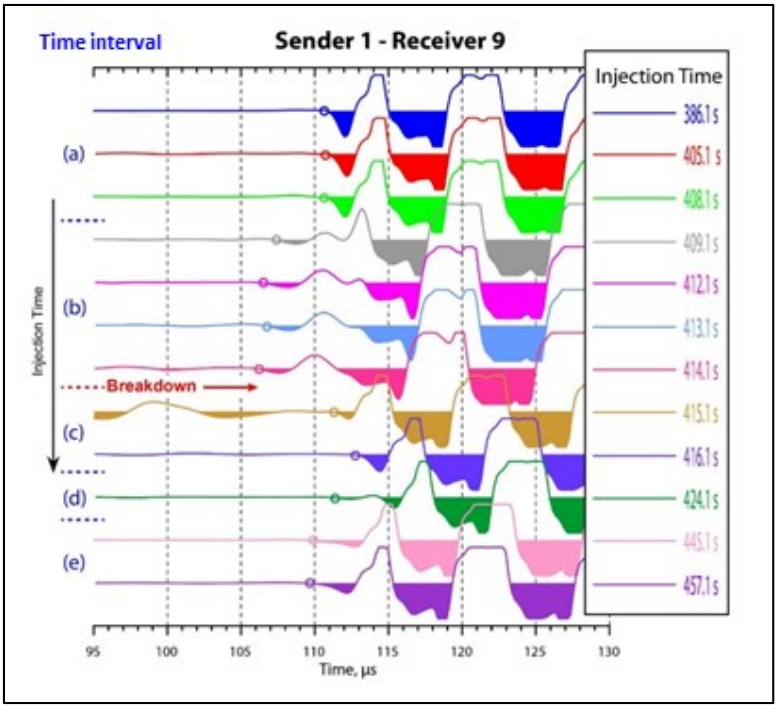

Figure 6.23: Waveforms of ultrasonic transmissions performed by sender 1 recorded by receiver 9 (Insert in **Figure 6.21**). The red arrow indicates the moment of peak pressure.

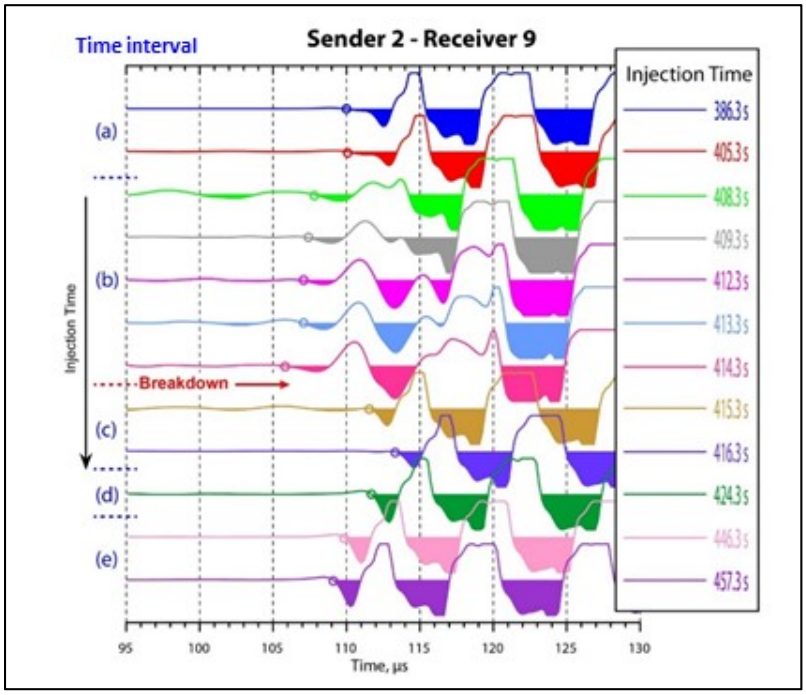

Figure 6.24: Waveforms of ultrasonic transmissions performed by sender 2 recorded by receiver 9 (Insert in **Figure 6.21**). The red arrow indicates the moment of peak pressure.

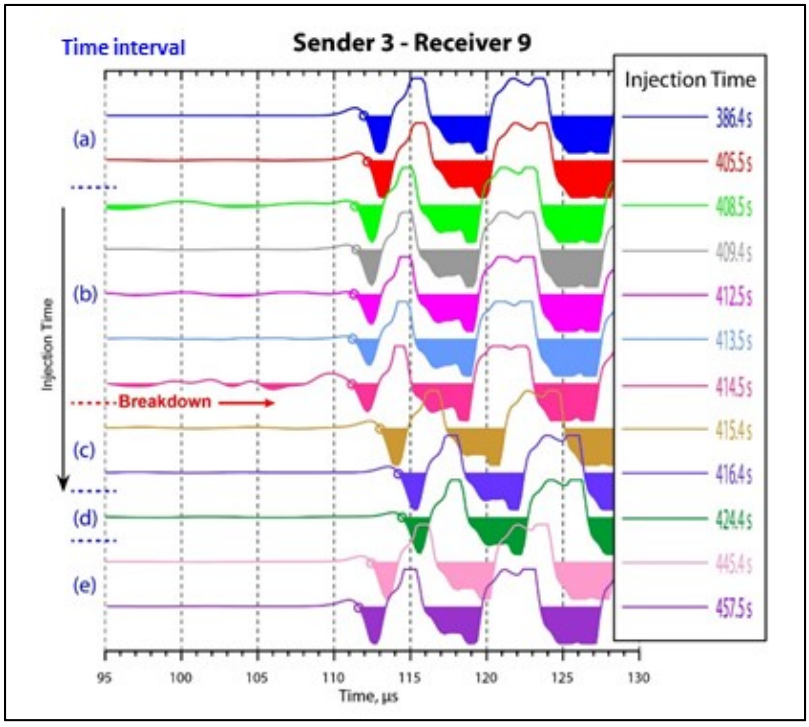

Figure 6.25: Waveforms of ultrasonic transmissions performed by sender 3 recorded by receiver 9 (Insert in **Figure 6.21**). The red arrow indicates the moment of peak pressure.

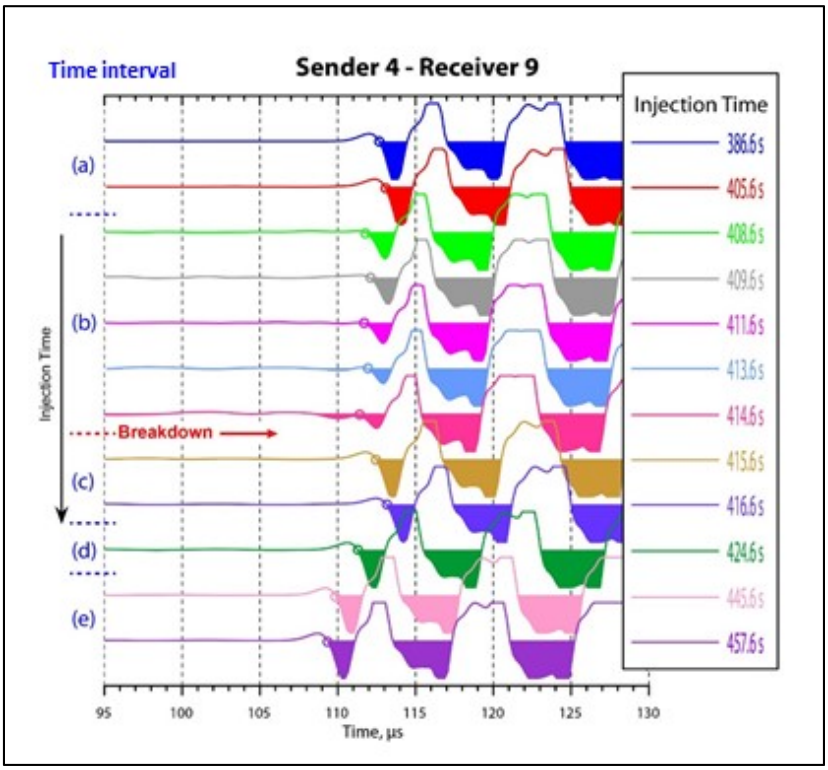

Figure 6.26: Waveforms of ultrasonic transmissions performed by sender 4 recorded by receiver 9 (Insert in **Figure 6.22**). The red arrow indicates the moment of peak pressure.

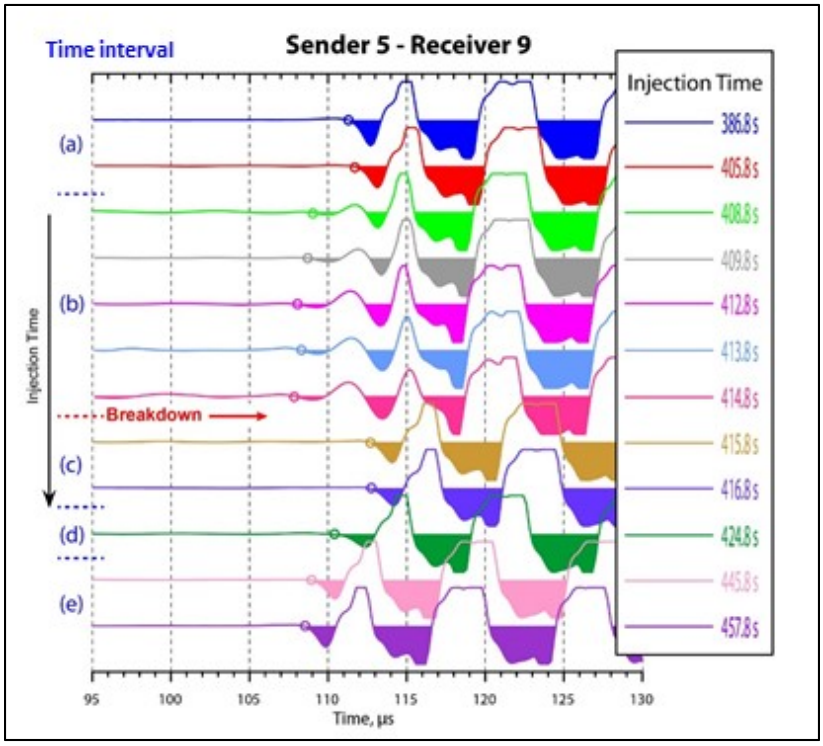

Figure 6.27: Waveforms of ultrasonic transmissions performed by sender 5 recorded by receiver 9 (Insert in **Figure 6.22**). The red arrow indicates the moment of peak pressure.

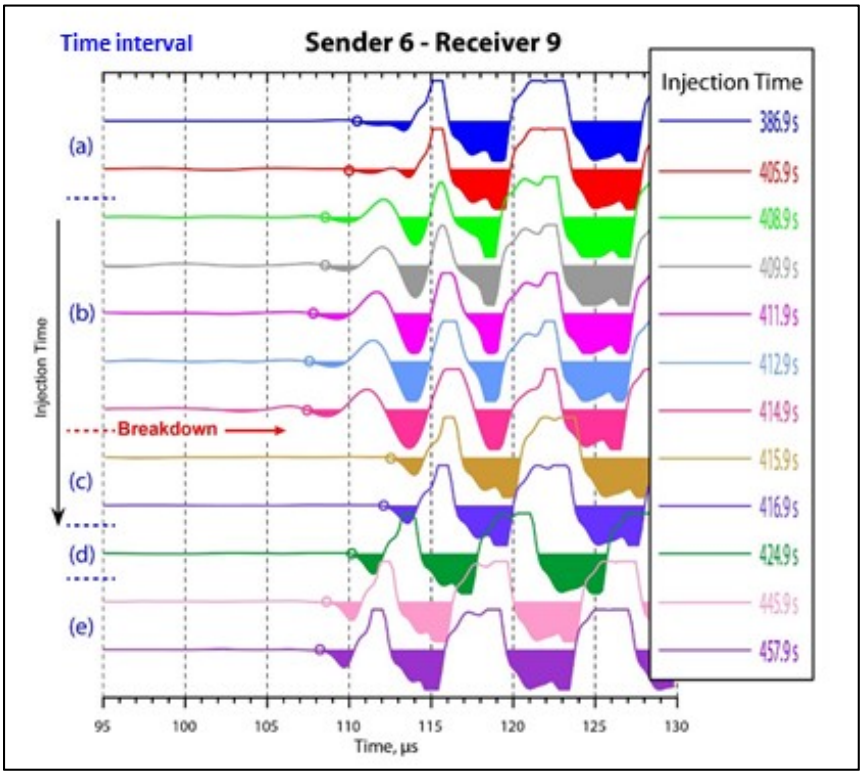

Figure 6.28: Waveforms of ultrasonic transmissions performed by sender 6 recorded by receiver 9 (Insert in **Figure 6.22**). The red arrow indicates the moment of peak pressure.

6.5.4. Ultrasonic transmission velocity and relative amplitude mapping

Figures 6.29 through **6.32** show density mappings of P-wave velocities and first motion amplitudes spatial distributions calculated for the 36 ultrasonic transmission signals during various fluid injection intervals. Amplitudes were normalized using the mean values measured during interval (a) of the injection and variations of the results are shown on a percentage scale, relative to the initial values. **Figure 6.29,** shows almost symmetric distribution of velocities with slightly lower velocities in the vicinity of the injection source and higher velocities further away from the injection source. As shown in **Figure 6.29 (c)** relative amplitudes are equal to 100 percent during injection Interval (a) because of normalization. The lower velocities in the vicinity of the injection zone may be attributed to the partially saturated pore spaces in some parts of the block sample in this zone while some velocities may have been higher in some dry areas further away from the injection zone.

Figure 6.30 shows density maps of P-wave velocities and first motion amplitudes spatial distributions calculated for 36 ultrasonic transmission signals during interval (b), before the point of peak pressure. **Figure 6.30,** shows an increase of velocities especially in the upper central part of the block. **Figure 6.30** also shows a significant decrease of the first motion amplitude in the southern and central parts of the block (first motion amplitude is greater on north side than on the south side of injection zone). The increase in velocities may be attributed to signals encountering fully saturated pore spaces and higher bulk stiffness of the pore fluid and consolidated grain particles. The decrease in first motion amplitudes in the central zone of the block sample may be attributed to signal attenuation as the signals encountered some partially saturated pore spaces.

Figure 6.31 shows density mappings of P-wave velocities and first motion amplitudes spatial distributions calculated for 36 ultrasonic transmission ray-paths during interval (c). **Figure 6.31** also shows a decrease of velocities in most regions near the injection zone. This may be attributed to the signals crossing the fluidized and softened fracture plane. In addition to this **Figure 6.31** shows an increase of the first motion amplitudes mostly in the central to northern part of injection source. The density mapping of areas with high and low relative first motion

amplitudes may be a reflection of the geometry complexity of the fracture at this interval. Signals that may have intercepted the fluidized and softened fracture plane may have undergone signal attenuation with resulting lower amplitudes while those signals that did not intercept the fracture plane but intercepted the consolidated regions ahead of the fracture boundaries may have had elevated first motion amplitudes.

Figure 6.32 shows density mappings of P-wave velocities and first motion amplitudes spatial distributions calculated for 36 ultrasonic transmission ray-paths during interval (d). it also shows a significant increase of P-wave velocities mostly in the northern part of the block. There seems to be a corresponding increase in the first motion amplitudes mostly in the northern part of the block as shown. The P-wave velocity and first motion amplitude mapping in **Figure 6.32** may be a reflection of the fracture geometry complexity and the internal fracture pressure at this interval of injection. Signals that may have intercepted the re-pressurized fracture plane, may have had increased velocities and increased amplitudes.

A comparison of density maps presented in **Figures 6.29** through **Figure 6.32** suggests that both velocities and first motion amplitudes of elastic waves are sensitive to the deformation changes associated with the hydraulic fracturing process in cohesionless particulate materials. The results from the velocity and amplitude density mappings are consistent with those from the ultrasonic transmission velocities, relative first motion amplitudes, and waveforms, described previously in this section.

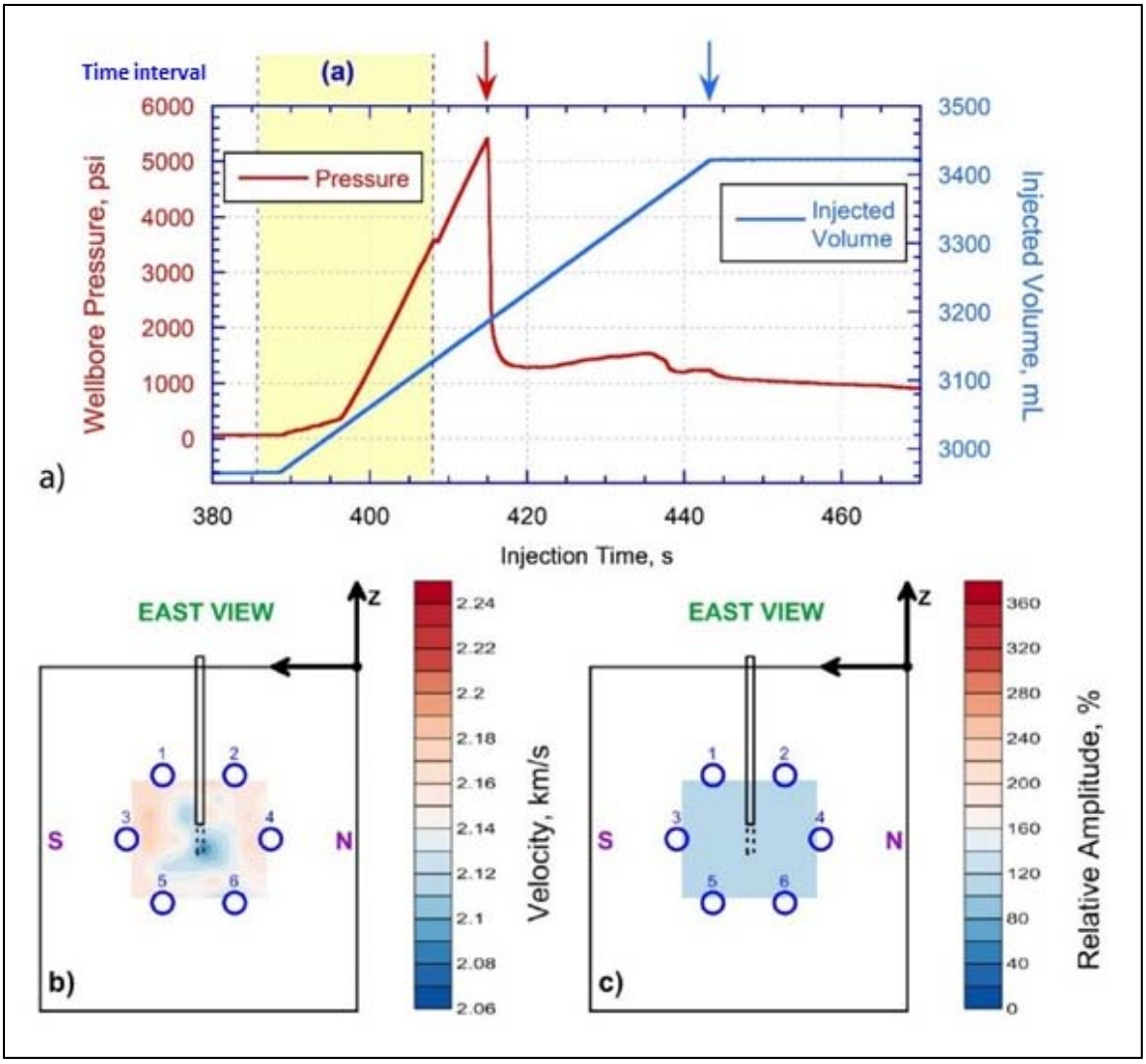

Figure 6.29: (a) Applied injection pressure (red) and injected volume (blue). Yellow rectangle highlights interval of analysis. (b) Map of P-wave velocity spatial distributions calculated for 36 ultrasonic transmission ray-paths during interval (a) of injection. (c) Map of normalized P-wave amplitude spatial distributions calculated for 36 ultrasonic transmission ray-paths. Normalization was performed using the mean values measured during interval (a), therefore (c) indicates a constant value equal 100 percent.

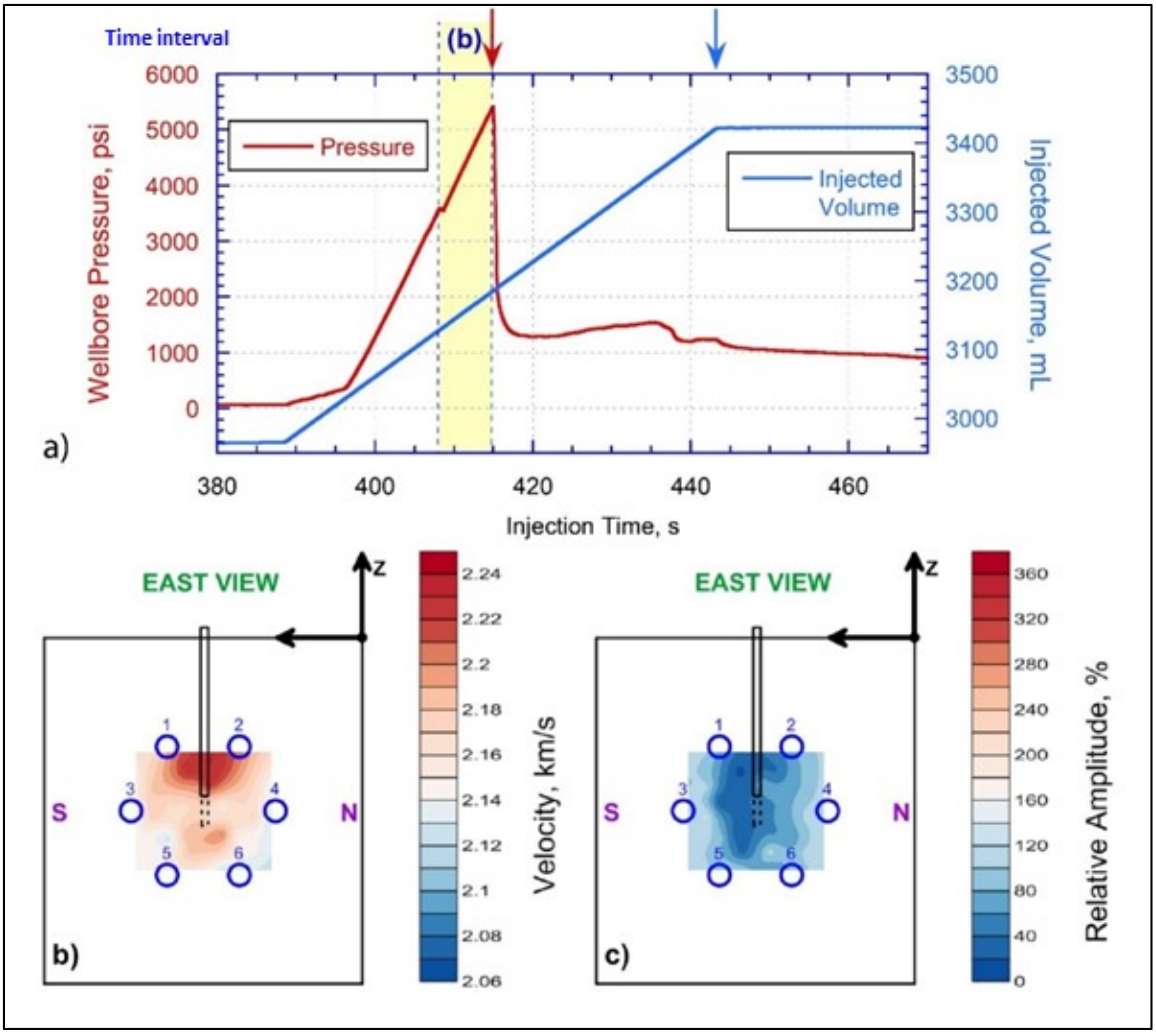

Figure 6.30: (a) Applied injection pressure (red) and injected volume (blue). Yellow rectangle highlights interval of analysis. (b) Map of P-wave velocity spatial distributions calculated for 36 ultrasonic transmission ray-paths during interval (b) of injection. (c) Map of normalized P-wave amplitude spatial distributions calculated for 36 ultrasonic transmission ray-paths during interval (b) of injection. Normalization was performed using the mean values measured during interval (a).

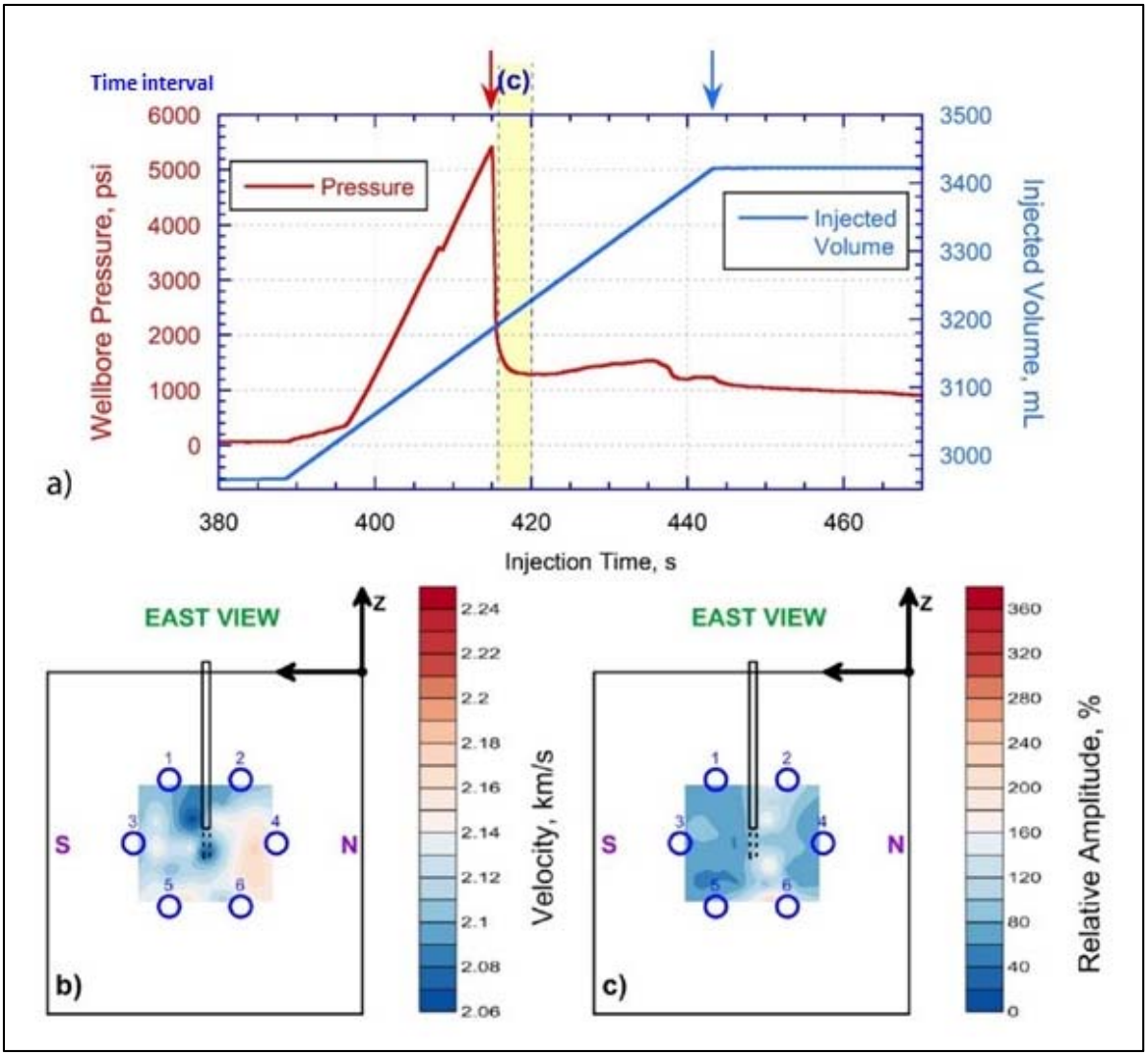

Figure 6.31: (a) Applied injection pressure (red) and injected volume (blue). Yellow rectangle highlights interval of analysis. (b) Map of P-wave velocity spatial distributions calculated for 36 ultrasonic transmission ray-paths during interval (c) of injection. (c) Map of normalized P-wave amplitude spatial distributions calculated for 36 ultrasonic transmission ray-paths during interval (c) of injection. Normalization was performed using the mean values measured during interval (a).

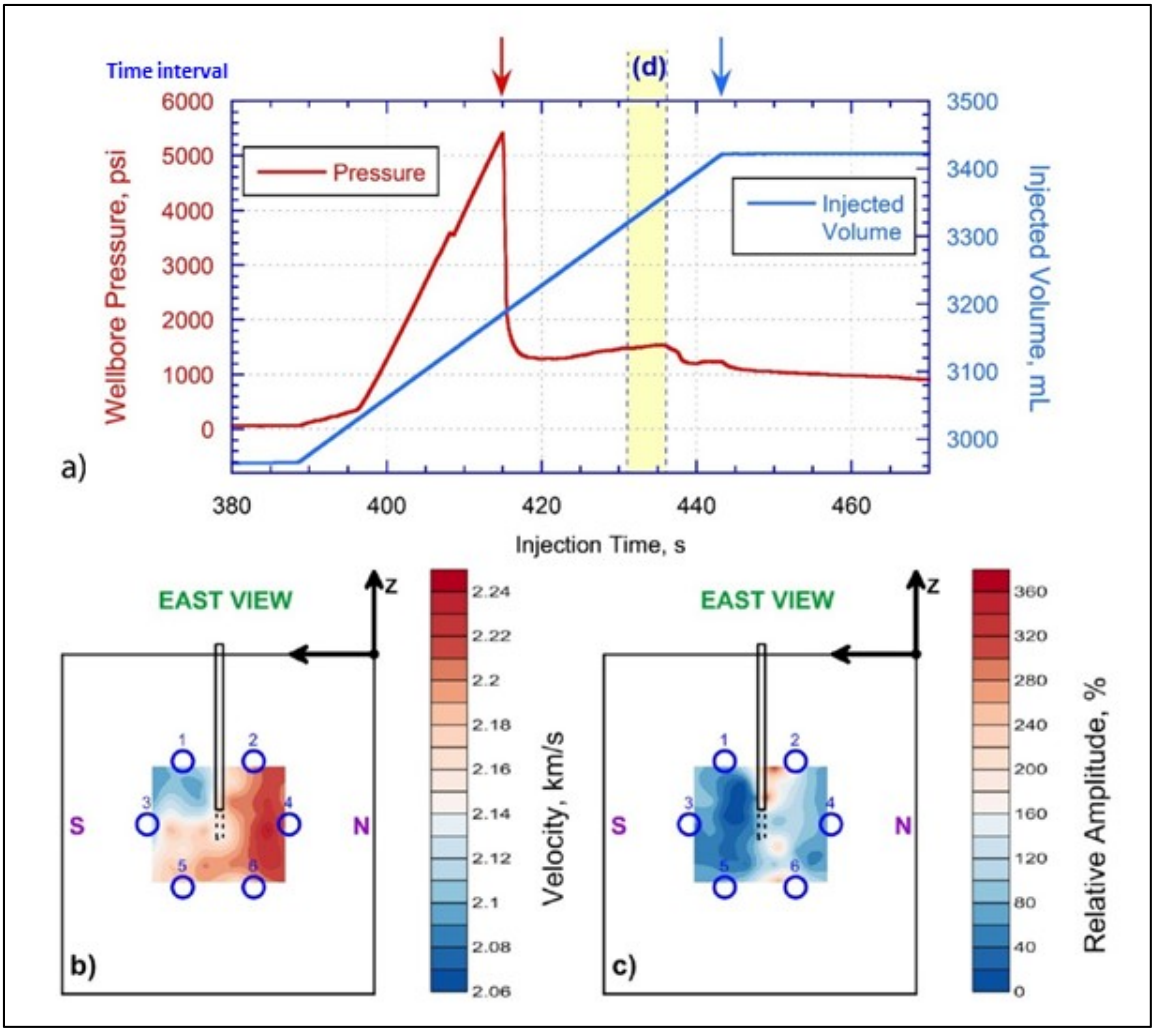

Figure 6.32: (a) Applied injection pressure (red) and injected volume (blue). Yellow rectangle highlights interval of analysis. (b) Map of P-wave velocity spatial distributions calculated for 36 ultrasonic transmission ray-paths during interval (d) of injection. (c) Map of normalized P-wave amplitude spatial distributions calculated for 36 ultrasonic transmission ray-paths during interval (d) of injection. Normalization was performed using the mean values measured during interval (a).

6.6. CONCLUSIONS

In this chapter, the results of passive acoustic emission and active ultrasonic transmission measurements to characterize hydraulic fracturing in cohesionless, particulate materials are presented. The main conclusions of this chapter are as follows.

1. For the first time, acoustic monitoring and ultrasonic transmission measurements were successfully applied to observe hydraulic fracturing mechanisms in saturated cohesionless, sediment-like particulate materials.
2. Through acoustic emission (AE) event source localization, we were able to map the footprint of the fracture geometry. The characteristic P-wave velocity and P-wave arrival times were used in algorithms similar to those employed by *Stanchits et al.* [2014] to localize AE source hypocenters. It was also possible to observe the extent of the fracture and the fracturing direction. Therefore, we conclude that not only is it possible to map the fracture geometry in cohesionless, sediment like materials using AE, but that it is a very effective technique that can produce detailed information about the fracturing process.
3. The AE monitoring technique for hydraulic fracturing in particulate block samples can be used as a reference for field scale microseismic monitoring of hydraulic fracturing. For example, seismic hypocenter localization algorithms can be calibrated and improved using this technique.
4. A correlation between the growth of the AE count rate and the injection pressure was observed. It appears that fracture initiation and propagation can be isolated using the growth of the AE count rate. The highest rate of AE activity was just before peak pressure. The acoustic emission count rate dropped sharply (nearly 5 times) immediately after the moment of peak pressure. During this same period, there was a corresponding pressure drop (more than 4 times). There was also a sharp rise (by nearly 2 times) in AE activity rate in the time period just before fracture initiation. Therefore, we suggest that the changes in the rate of AE events may be used as a precursor to fracture initiation in unconsolidated sediments.

5. Cavity expansion just before fracture initiation was captured using AE measurements. It was observed that this cavity expansion was sensitive to the configuration of the remote confining stresses. By analyzing the spatial evolution of the AE cloud with time, it was observed that the cavity grew with a circular cross section at the beginning, to an elliptical cross section at the moment of fracture initiation. The velocity of cavity expansion in σ_1 direction was approximately twice that in σ_2 direction, which, in turn, was twice the rate of expansion in σ_3 direction. Therefore, AE measurements showed qualitative sensitivity to plastic deformation evolution during the early stages of hydraulic fracturing in cohesionless particulate media.
6. Through AE monitoring, we were able to spot the first fracture wing to initiate. Asymmetrical fracture growth relative to the injection source was also observed acoustically.
7. Ultrasonic transmission measurements also demonstrated sensitivity to the process of hydraulic fracturing in cohesionless particulate media. Ultrasonic transmissions were processed along 36 ray paths and showed sensitivity to sample saturation and shear band formation. There was an agreement between UT velocity, relative first motion amplitude, and waveforms in characterizing the hydraulic fracturing process.

7. CONCLUSIONS

The main conclusions derived in this work are synthesized below.

1. We have designed an experimental approach that aims to activate faults in-situ at scales of $\sim$ 10 - 100 m using fluid injection and thermal techniques to modify in-situ stresses and the fault strength to the point where the rock fails. Deep underground mines, like the Homestake mine in the Black Hills of South Dakota, present an opportunity to conduct such experiments as they have sufficient in-situ stresses to drive faulting.
2. We apply the model of *Garagash and Germanovich* [2012] to evaluate the potential slip patch size at the onset of dynamic propagation. For the Homestake mine conditions, a minimum patch size of 3 m and a maximum patch size of 17 m were estimated for mine depths of 8000 ft and 3000 ft, correspondingly. Therefore, our (scale) analyses for the Homestake fault conditions indicate that the onset of dynamic slip occurs for a patch size on the order of 1 m to 10 m. Creating a dynamic patch of this size requires an experimental configuration of at least 10 m to 100 m. This appears feasible under field conditions in the Homestake mine, but it demonstrates why the characterization of a dynamic slip patch is beyond the reach of laboratory experiments. This result is significant, also because the Homestake fault conditions of 1 to 3 km (3280 to 9840 ft) depth are representative of many mines around the world.
3. The nucleation length is largely controlled by the proximity of the fault loading to the static strength, quantified by the understress parameter $\left(\tau_p - \tau^b\right)/\tau_p$. In other words, the nucleation length is weakly dependent on the fluid pressure but strongly dependent on the proximity of the fault loading to the static strength.
4. We propose two methods for mine-based earthquake nucleation and rock faulting field experiments. In the first method, we propose pore pressure perturbation of a fault by fluid injection on the fault to reactivate it. In the second method, a robust approach for creating new faults would be to circulate chilled fluid through arrays of boreholes drilled along vertical planes; boreholes could be either horizontal or vertical. This will reduce the horizontal compression normal to the planes of the boreholes while the vertical stress

remains unchanged. Our scaling and numerical analyses of these designs show that the thermal technique can create differential stresses sufficient to induce faulting within a period of approximately 11 days. The thermal technique can be used to create new faults in intact rock and can therefore be used to study how faults form. This research also suggests that the two methods can be used together to reactivate an existing fault in a controllable manner.

5. Hydraulic fracture behavior in the natural Bromide formation sand is similar to that in man-made cohesionless particulate materials, in terms of fracture pressure signatures, fracture morphologies, and geometries. Therefore, it appears that experiments with synthetic sands are sufficiently representative.
6. Dimensional analysis of results from both synthetic sands and natural Bromide formation sand shows a power law dependence of the dimensionless peak injection pressure to the dimensionless confining stress.
7. Hydraulic fracturing in the Bromide formation sand showed that the initiation pressure (peak pressure) was sensitive to the fracturing fluid injection rate. The peak pressure was monitored over variations of the injection flow rate of three orders of magnitude. It was observed that the higher the flow rate, the higher the corresponding peak pressure. This relationship was consistent with experiments in synthetic mixtures.
8. In our experiments under true-triaxial loading conditions, the prevalence of shear bands near the cavity expanding around the injection zone and near the fracture tips confirmed that both hydraulic fracture initiation and propagation in cohesionless, sediment-like, particulate media is associated with inelastic deformation mechanisms.
9. Using three independent monitoring methods, namely, injection pressure signatures, flat-jack and axial actuator volumetric responses, and post-test CT scans, we concluded that hydraulic fracturing in particulate, cohesionless materials takes place in the following sequence. The pressurization of the injection source is followed by the cavity expansion around the injection zone. As a result of the yielding associated with cavity expansion of the softening cohesionless materials, shear strain localization takes place. This localization manifests itself as one or several shear bands emanating from the expanding

cavity [*Chang et al.,* 2003; *Chang,* 2004; *Germanovich et al.,* 2007; *Hurt,* 2012; *Germanovich and Hurt,* 2012; *Hurt and Germanovich,* 2012]. Fracture Initiation follows at one of these shear bands. Then subsequent shear bands, continuously form and branch ahead of the fracture tip as the fracture propagates.

10. The shear banding mechanism may be accompanied and even be dominated by the material fluidization (as the fracturing fluid infiltrates the block sample and/or more permeable shear bands) and other instability mechanisms near the borehole and at the fracture tip [*Germanovich et al.,* 2007; *Huang et al.,* 2011; *Huang et al.,* 2012; *Zhang and Huang,* 2011; *Zhang et al.,* 2013].
11. Fracture initiation results from the true-triaxial experiments showed a power law dependence of the dimensionless peak pressure versus the dimensionless confining stress, that was consistent with previous studies [*Germanovich and Hurt*, 2012; *Hurt and Germanovich,* 2012; *Hurt,* 2012]. Further, it was found that the ratio of the peak pressure to the confining minimum principal stress was nearly 10 for fully saturated cohesionless particulate materials. In addition, it was found that the initiation pressure in our true-triaxial experiments was sensitive to the degree of saturation of the block samples.
12. One of the most important findings of this work was that for the first time, passive acoustic emission and active ultrasonic transmission measurements were successfully used to characterize the hydraulic fracturing process in saturated cohesionless particulate materials. Through AE source localization algorithms employed by *Stanchits et al.* [2012] and *Stanchits et al.* [2014a] we were able to map the footprint of the fracture geometry.
13. A correlation was observed between the growth of the AE activity count rate and the growth of the injection pressure. From this observation, we suggest that it may be possible to isolate the moment of fracture initiation using the AE count rate independent of the injection pressure signature. It may also be possible to model the changes in AE count rate as a precursor to fracture initiation.
14. The AE monitoring technique for hydraulic fracturing in particulate block samples can be used as a reference for field scale microseismic monitoring of hydraulic fracturing. Microseismic monitoring techniques can be studied and improved in the laboratory. For

example, seismic hypocenter source localization algorithms can be developed and improved using this technique.

15. Fracture wing asymmetrical geometries relative to the injection source were observed both in triaxial low stress regime experiments and true-triaxial high stress regime experiments. We conclude that similar to cohesive materials, asymmetrical wing geometries in hydraulic fracturing of cohesionless materials may be more common than symmetrical wings.

APPENDIX A. EXPERIMENTAL CONDITIONS

Test	Date	Conf. Stress	Injection	Sample	Injection rate	Permeability	Saturation
		psi	Fluid		ml/min	mD	%
1	11/23/2011	10	Guar	Silica flour	1000	25	Dry
3	12/29/2011	10	Guar	Silica flour	500	25	Dry
7	8/2/2012	12	Guar	Silica flour	500	25	Dry
9	11/21/2012	10	Guar	Silica flour	500	25	Dry
12	2/6/2013	10	Guar	Bromide formation sand	500	3500	90
13	2/12/2013	10	Guar	Bromide formation sand	500	3500	89
15	11/8/2013	80	Guar	20% silica/ 80% USM100	500	200	95
17	2/24/2014	80	Guar	20% silica/ 80% USM100	500	200	80
18	2/27/2014	80	Guar	USM100	10000	1800	92
19	3/8/2014	80	Guar	USM100	5000	1800	90
20	3/12/2014	80	Guar	Silica flour	5000	20	Dry
21	3/16/2014	80	Guar	Bromide formation sand	5000	1200	90
23	3/22/2014	80	Guar	Bromide formation sand	500	1200	92
24	4/4/2014	80	Guar	F110	500	1300	79
25	4/7/2014	80	Guar	F110	500	1300	90
26	4/9/2014	80	Guar	Bromide formation sand	5000	1200	90
27	4/23/2014	80	Guar	F110	500	1300	90
28	2/29/2014	80	Guar	F110	500	1300	90

Test	Date	Conf. Stress	Injection	Sample	Injection rate	Permeability	Saturation
		psi	Fluid		ml/min	mD	%
29	5/2/2014	80	Guar	F110	500	1300	93
30	7/7/2014	80	Guar	Bromide formation sand	500	1200	90
32	7/14/2014	80	Guar	Bromide formation sand	500	1200	91
33	7/22/2014	80	Guar	F110	500	1300	92
34	10/7/2014	80	Guar	Bromide formation sand	500	1200	90
35	10/12/2014	80	Guar	Bromide formation sand	500	1200	91
36	10/4/2014	80	Guar	Bromide formation sand	500	1200	90
37	11/17/2014	80	Guar	Bromide formation sand	50	1200	90
38	1/2/2015	80	Guar	F110	500	1300	92
39	3/3/2015	80	Guar	20% silica/ 80% USM100	500	200	89
40	3/27/2015	80	Guar	20% silica/ 80% USM100	500	200	90
41	2/7/2016	80	Guar	Bromide formation sand	5000	1200	94
42	6/17/2016	80	Guar	Bromide formation sand	50	1200	95
43	7/4/2016	80	Guar	Bromide formation sand	5000	1200	94
44	7/19/2016	80	Guar	USM100	50	1800	90
45	9/11/2016	80	Guar	20% silica/ 80% USM100	500	200	88
46	10/20/2016	80	Guar	Silica flour	500	20	Dry
49	12/2/2016	10	Guar	Silica flour	500	20	Dry

APPENDIX B. EXPERIMENTAL RESULTS

Test	Date	P_{peak}	P_{drop}	$P_{propagation}$	Fracture reached boundary	Rate of pressure increase before breakdown	Ratio of peak pressure to conf. stress	Wing asymmetry ratio*
		psi	psi	psi		psi/sec		
1	11/23/2011	130	5	125	Yes	32.5	13.0	0.2
3	12/29/2011	120	N/A	120	yes	60.0	12.0	0.2
7	8/2/2012	114	N/A	110	yes	215.1	11.4	0.5
9	11/21/2012	68	23	45	yes	7.6	6.8	0.4
12	2/6/2013	88	29	59	No	4.4	8.8	0.8
15	11/8/2013	447	222	225	yes	44.7	5.6	0.5
17	2/24/2014	342	32	310	No	13.7	4.3	0.8
18	2/27/2014	702	332	370	no	140.4	8.8	1.0
19	3/8/2014	463	213	250	no	154.3	5.8	0.9
20	3/12/2014	325	224	101	no	65.0	4.1	N/A
21	3/16/2014	285	115	170	No	190.0	3.6	0.8
23	3/22/2014	209	34	175	No	10.5	2.6	0.8
24	4/4/2014	247	16	231	No	7.3	3.1	0.6
25	4/7/2014	532	75	457	yes	15.6	6.7	N/A
27	4/23/2014	210	88	122	no	8.1	2.6	0.6
28	2/29/2014	325	25	300	no	12.5	4.1	1.0
29	5/2/2014	318	118	200	no	13.7	4.0	0.9
30	7/7/2014	278	54	224	No	11.1	3.5	0.3
32	7/14/2014	215	15	200	Yes	14.3	2.7	0.3
33	7/22/2014	308	58	250	no	13.8	3.9	0.9
34	10/7/2014	432	82	350	no	19.0	5.4	0.4
35	10/12/2014	258	61	197	no	12.9	3.2	0.3
36	10/4/2014	322	N/A	N/A	no	10.7	4.0	0.9
37	11/17/2014	252	21	231	no	2.2	3.2	1.0
38	1/2/2015	295	45	250	no	11.4	3.7	0.7
39	3/3/2015	195	15	180	yes	11.3	2.4	0.5
40	3/27/2015	236	10	226	no	11.8	3.0	0.4
41	2/7/2016	330	N/A	230	yes	33.0	4.1	0.5
42	6/17/2016	284	4	280	no	4.7	3.6	0.1
43	7/4/2016	250	70	180	no	83.3	3.1	0.5
44	7/19/2016	320	85	235	no	16.0	4.0	0.3
45	9/11/2016	302	100	202	no	60.8	3.8	0.4
46	10/20/2016	330	50	280	yes	16.5	4.1	0.3

*The asymmetry ratio is the length of the smallest wing divided by the length of the largest wing.

Some experimental plots and sample images are given below (**Figures A1 – A11**).

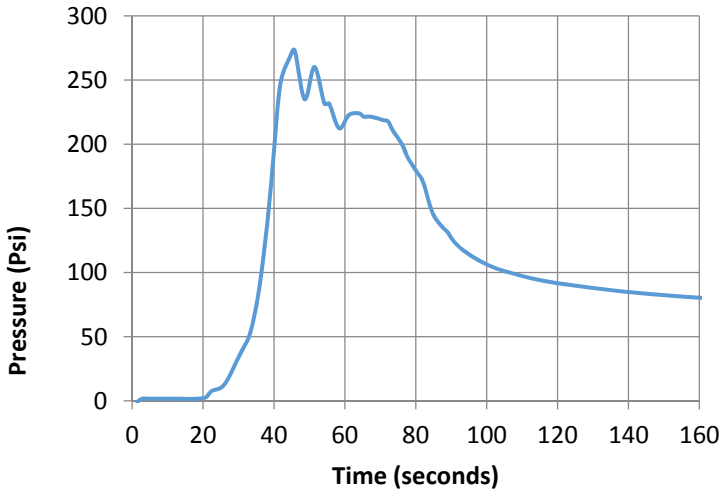

(a)

- Sample: Bromide Formation Sand.
- k = 3.6 D
- Applied confining stress 80/160 psi.
- Guar fluid,
- Injection rate 500 ml/min.
- K = 75 Pa × sec^{n}, n = 0.17

(b) (c)

Figure A.1: Test 30R. (a) Pressure – time dependence, (b) test conditions, and (c) fracture images.

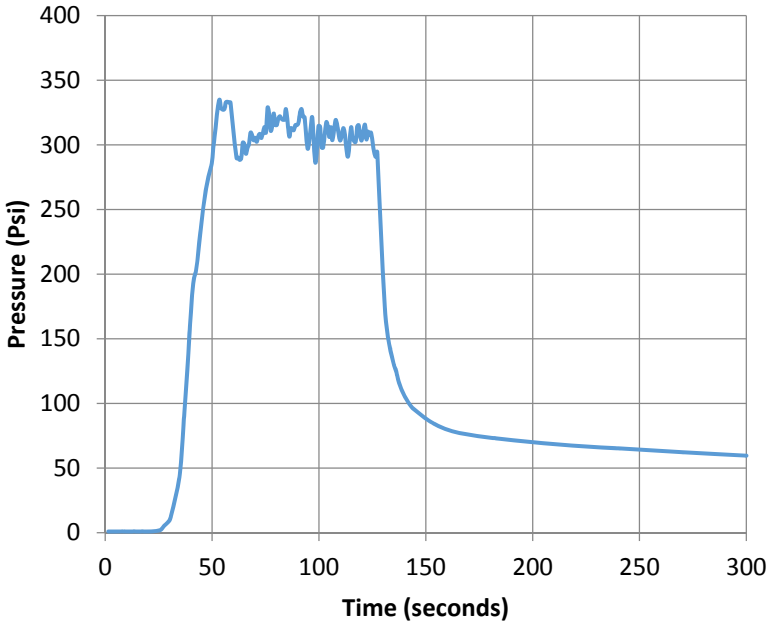

(a)

- Sample: 20/80 Silica flour/ USM100 mixture
- k = 0.2 D
- Applied confining stress 80/160 psi.
- Guar fluid,
- Injection rate 500 ml/min.
- K = 75 Pa × sec^{n}, n = 0.17

(b)

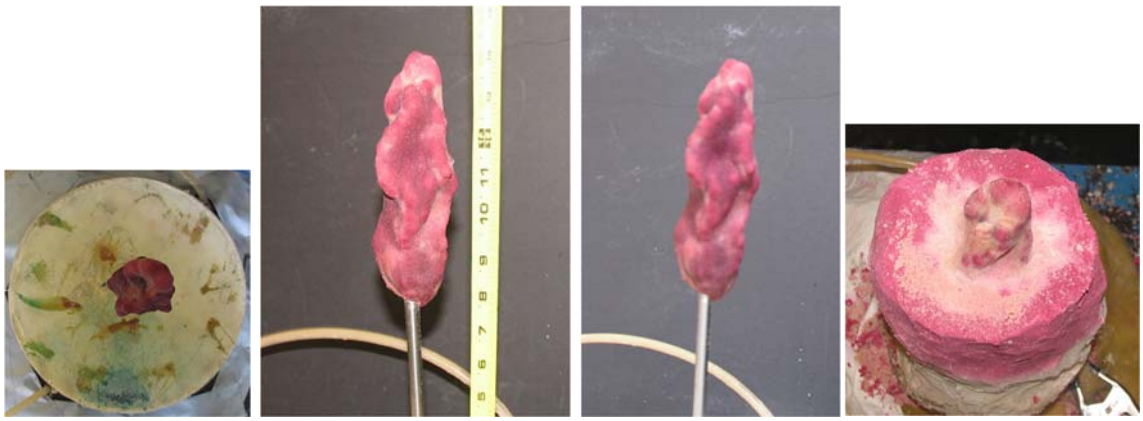

(c)

Figure A.2: Test 17. (a) Pressure – time dependence, (b) test conditions, and (c) fracture images.

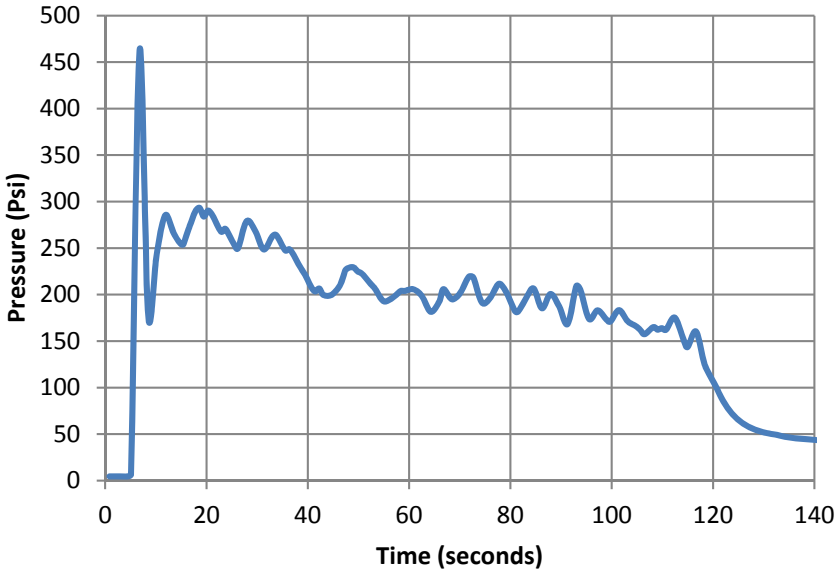

(a)

- Sample: 20/80 Silica flour/ USM100 mixture
- k = 0.2 D
- Applied confining stress 80/160 psi.
- Guar fluid,
- Injection rate 5000 ml/min.
- K = 75 Pa × sec^{n}, n = 0.17

(b)

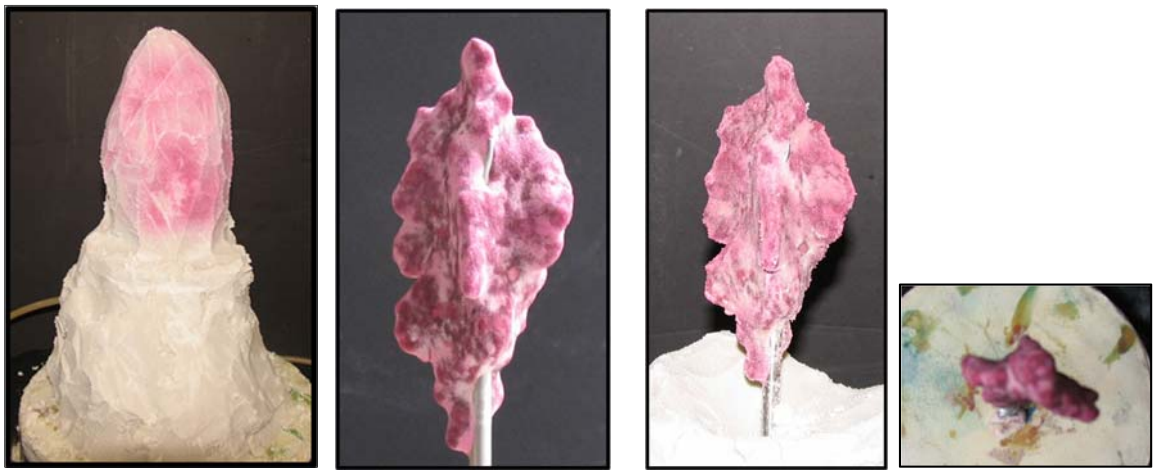

(c)

Figure A.3: Test 19. (a) Pressure – time dependence, (b) test conditions, and (c) fracture images.

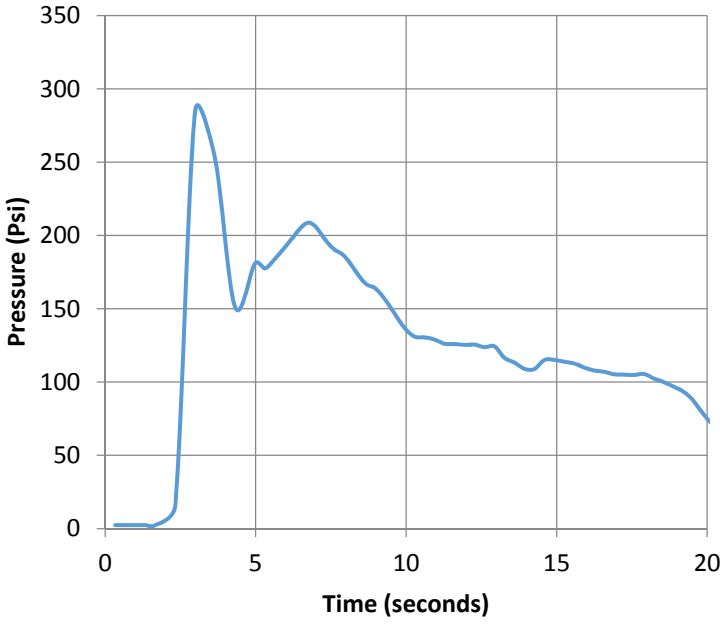

(a)

- Sample: Bromide Formation sand
- k = 3.6 D
- Applied confining stress 80/160 psi.
- Guar fluid,
- Injection rate 5000 ml/min.
- K = 75 Pa × sec^{n}, n = 0.17

(b)

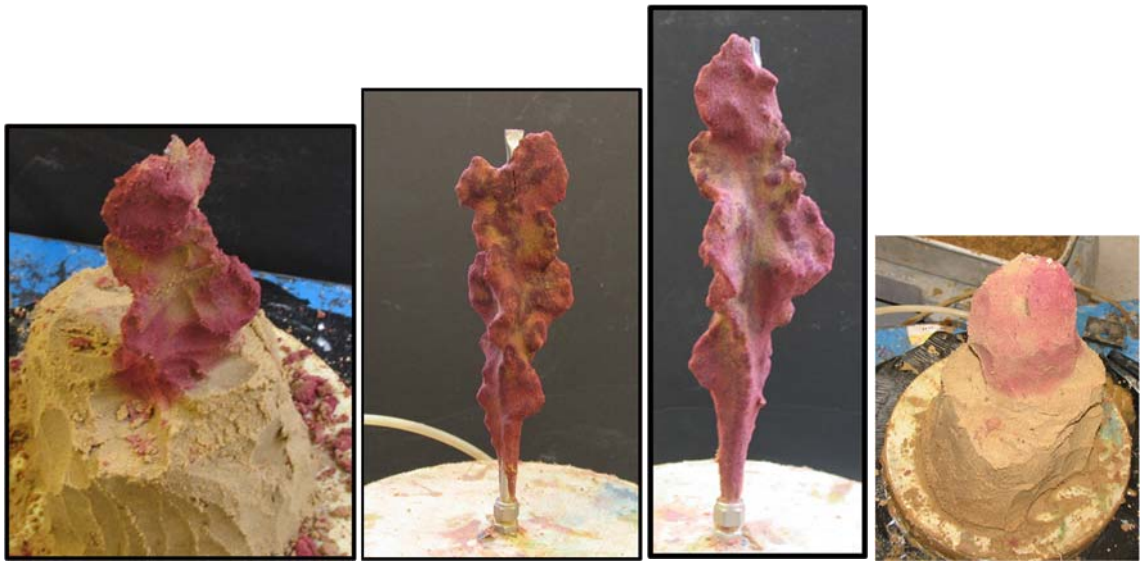

(c)

Figure A.4: Test 21. (a) Pressure – time dependence, (b) test conditions, and (c) fracture images.

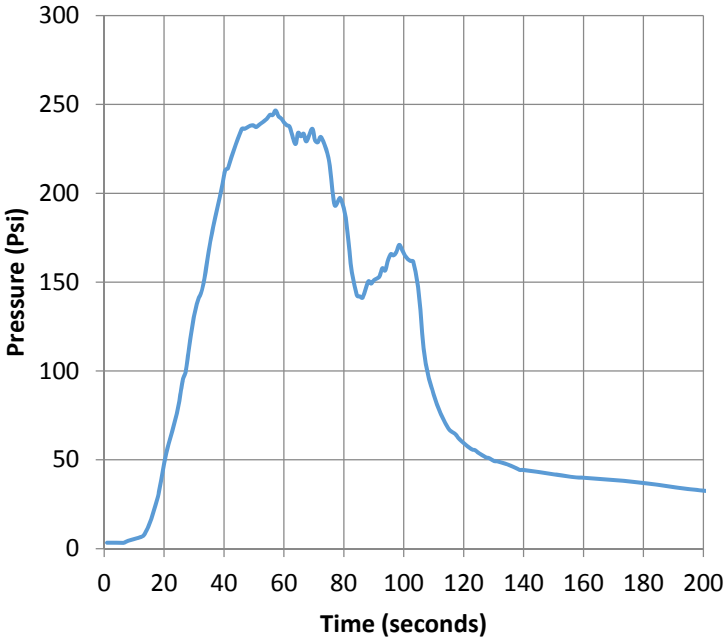

(a)

- Sample: F110 sand
- k = 1.3 D
- Applied confining stress 80/160 psi.
- Guar fluid,
- Injection rate 500 ml/min.
- K = 75 Pa × sec^{n}, n = 0.17

(b)

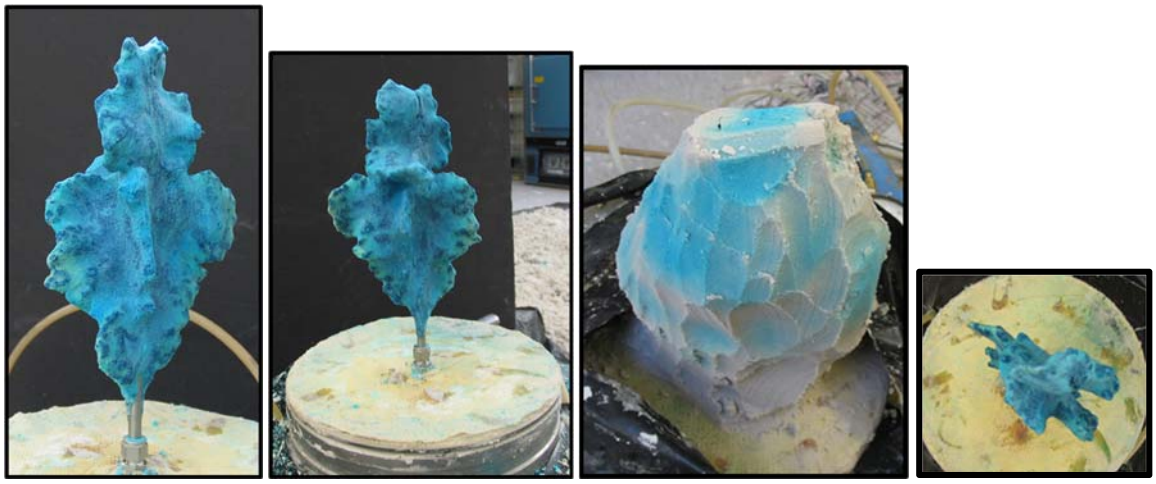

(c)

Figure A.5: Test 24. (a) Pressure – time dependence, (b) test conditions, and (c) fracture images.

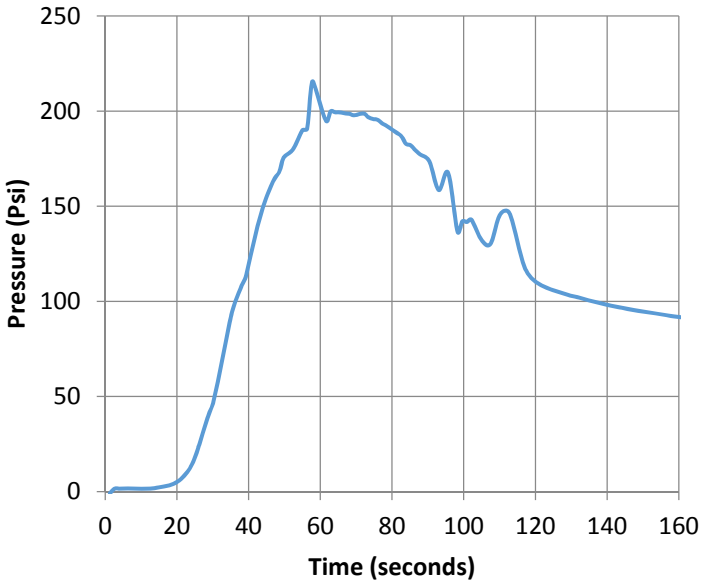

(a)

- Sample: Bromide Formation sand
- k = 3.6 D
- Applied confining stress 80/160 psi.
- Guar fluid,
- Injection rate 500 ml/min.
- K = 75 Pa × sec^{n}, n = 0.17

(b)

(c)

Figure A.6: Test 32. (a) Pressure – time dependence, (b) test conditions, and (c) fracture images.

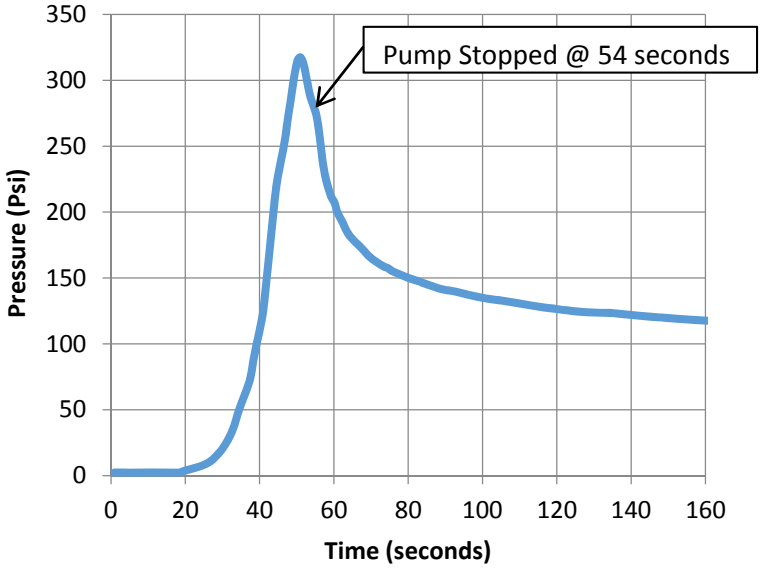

(a)

- Sample: Bromide Formation sand
- k = 3.6 D
- Applied confining stress 80/160 psi.
- Guar fluid,
- Injection rate 500 ml/min.
- K = 75 Pa × $\sec^{n}$, n = 0.17

(b)

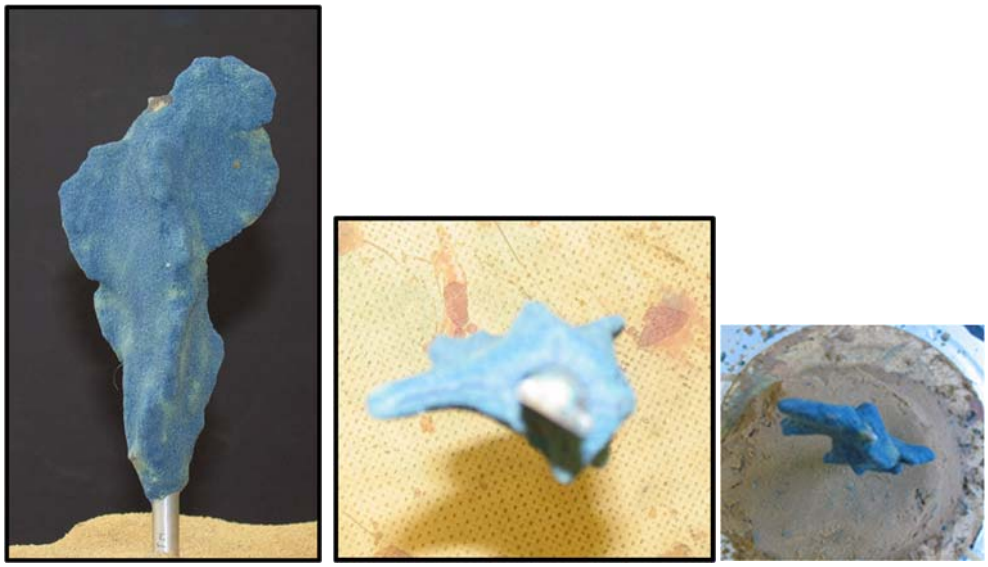

(c)

Figure A.7: Test 36. (a) Pressure – time dependence, (b) test conditions, and (c) fracture images.

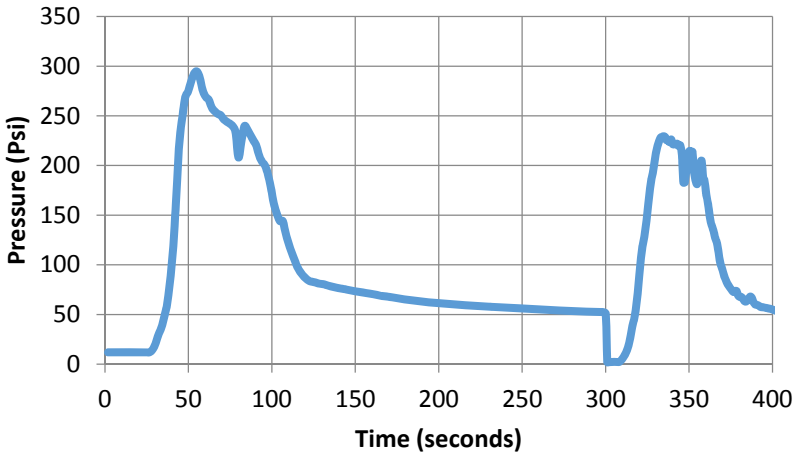

(a)

- Sample: F110 Ottawa fine sand
- k = 1.3 D
- Applied confining stress 80/160 psi.
- Guar fluid,
- Injection rate 500 ml/min.
- K = 75 Pa × sec^{n}, n = 0.17

(b)

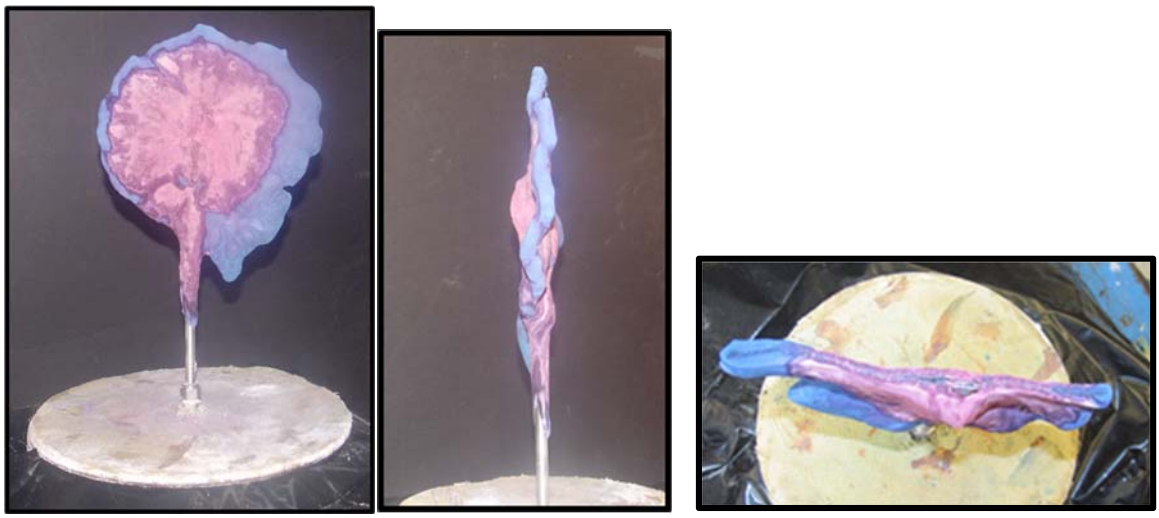

(c)

Figure A.8: Test 38. (a) Pressure – time dependence, (b) test conditions, and (c) fracture images.

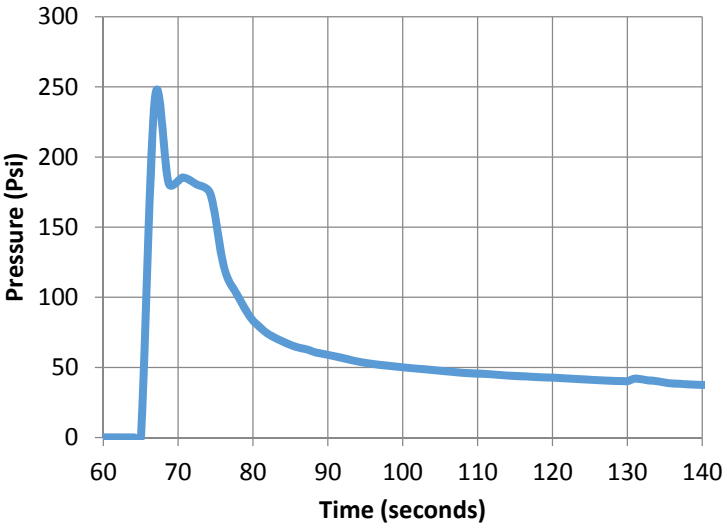

(a)

- Sample: Bromide formation sand
- k = 3.6 D
- Applied confining stress 80/160 psi.
- Guar fluid,
- Injection rate 500 ml/min.
- K = 75 Pa × sec^{n}, n = 0.17

(b)

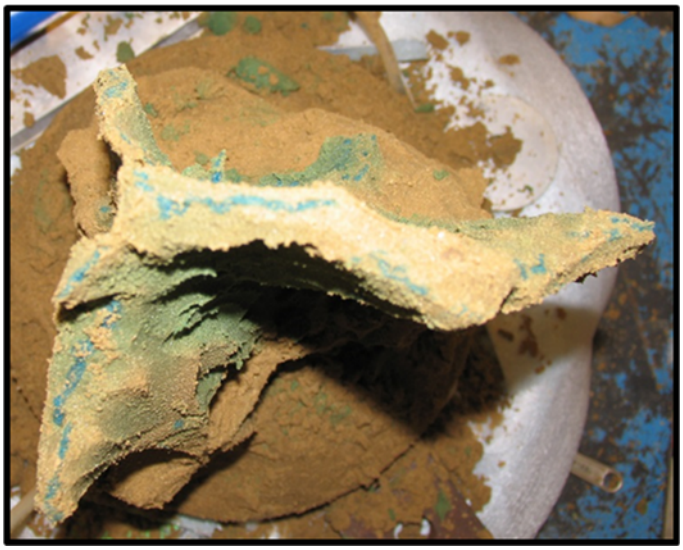

(c)

Figure A.9: Test 43. (a) Pressure – time dependence, (b) test conditions, and (c) fracture images.

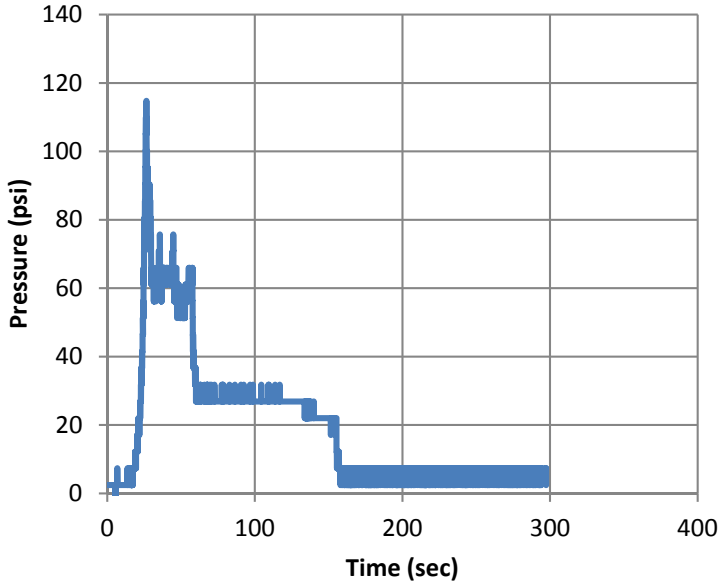

(a)

- Sample: Pure Silica Flour
- k = 0.02 D
- Applied confining stress 10/20 psi.
- Guar fluid,
- Injection rate 500 ml/min.
- K = 75 Pa × sec^{n}, n = 0.17

(b)

(c)

Figure A.10: Test 5. (a) Pressure – time dependence, (b) test conditions, and (c) fracture images.

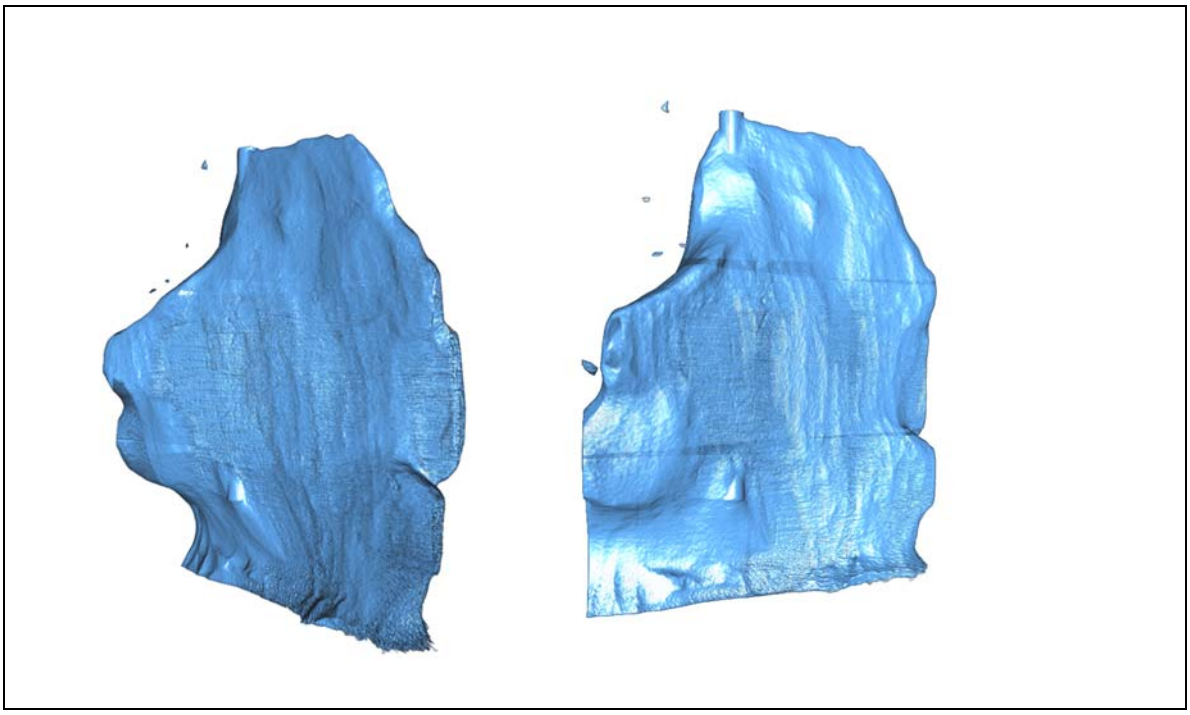

Figure A.11: Two views of 3-D reconstruction image for true-triaxial test 4 (Section 5.4).

APPENDIX C. DATA AQUISITION

The pressure transducer was connected to the injection source near the elbow joint, connecting the injection chamber to the injection source. The transducer is in-turn connected to the multi-channel DAQ module device (www.mccdaq.com/solutions/USB-Data-Acquisition.aspx) which converts the pressure reading in the borehole to a voltage. Matlab files were written to convert voltage readings to pressure and to plot the pressure versus time graph in real time. The DAQ module device also uses DAQ software and InstaCal software.

Figure B1: Daq module device

The Matlab programmes used with this device are presented below. Codes daq_1000psi.m, daq_continous_2.m, and daq_continous_timer_callback_2.m are used to check the data acquisition hardware and to record the data and present them in real time on a PC (x86) monitor. Code daq_1000psi.m is run from Matlab. It automatically calls for daq_continous_2.m and daq_continous_timer_callback_2.m, which need to be loaded in the same folder as daq_1000psi.m. All other details are given in the codes as comments.

Matlab R2015b code: daq_1000psi.m

```
clc
clear all
global time_backup pres_backup;

% This file is for checking the data aquesition hardware. Run this before
% every test so that the offset voltage is aquired. Press the test button
% on the pressure gauge during the second data aquesition phase. This
% should be 1 volt and it represnts 2500 psi on the 5000psi gauge.

ai = analoginput('mcc',0);          % find daq device
chan = addchannel(ai,0);            % Add channel from said device
duration = 5;                       % Accquisition time in seconds
set(ai,'SampleRate',500)            % Nummber of points per second
ActualRate = get(ai,'SampleRate');
set(ai,'SamplesPerTrigger',duration*ActualRate); % This sets the trigger time
set(ai,'TriggerType','Manual');
blocksize = get(ai,'SamplesPerTrigger');
Fs = ActualRate;
% Initial Test for minimum voltage
start(ai)                           % Starts the data aqu.
trigger(ai)
wait(ai,duration + 1)               % Wait comand to give enough time for data
storage
data_low = getdata(ai);             % gets data from storage to workspace
%%%%%%%%%%%%%%%%%%%%%%%%%%%%%%%%%%%%%%%%%%%%%%%%%%%%%%%%%%%%%%%%%%%%%%%
% Plot of initial Voltage should be close to zero volts
%%%%%%%%%%%%%%%%%%%%%%%%%%%%%%%%%%%%%%%%%%%%%%%%%%%%%%%%%%%%%%%%%%%%%%%
figure(1)
subplot(2,1,1)
plot(data_low)
grid on
ylabel('V')
xlabel('# of Samples')
title('low data 0-Volts 0-psi')
%Pause comand to give enough time for gauge test
display ('PRESS and HOLD test button on gauge, then press any key to contiue')
pause
% Second Test for mid value, should be 1 volt (2500psi on 5000psi gauge
start(ai)
trigger(ai)
```

```
    wait(ai,duration + 1)
    data_high = getdata(ai);
    %%%%%%%%%%%%%%%%%%%%%%%%%%%%%%%%%%%%%%%%%%%%%%
%%%%%%%%%%%%%%%%%%%%%%%%%%%%%
    % Plot of 'Test' Voltage should be close to one volt
    %%%%%%%%%%%%%%%%%%%%%%%%%%%%%%%%%%%%%%%%%%%%%%
%%%%%%%%%%%%%%%%%%%%%%%%%%%%%
    subplot(2,1,2)
    plot(data_high)
    grid on
    ylabel('V')
    xlabel('# of Samples')
    title('High data 1-Volt 2500-psi')
    % These are averages for test voltage values
    ZERO_VOLT = mean(data_low)
    ONE_VOLT = mean(data_high)
    %Pause comand to give enough time for test setup
    display ('press any key when test is ready')
    pause
    %%%%%%%%%%%%%%%%%%%%%%%%%%%%%%%%%%%%%%%%%%%%%%
%%%%%%%%%%%%%%%%%%%%%%%%%%%%%
    % START OF DATA AQU
    %%%%%%%%%%%%%%%%%%%%%%%%%%%%%%%%%%%%%%%%%%%%%%
%%%%%%%%%%%%%%%%%%%%%%%%%%%%%
    ai = analoginput('mcc',0);
    addchannel(ai,0);
    %To continuously acquire data set the SamplesPerTrigger property to Inf.
    % Use the stop command (Ctrl+C) then "STOP_AQU" in comand Window to stop
the device.
    set(ai,'SamplesPerTrigger',Inf);
    set(ai,'SampleRate',50);
    %Use the getdata command to bring the data back periodically into MATLAB.
    %This is important when you set the SamplesPerTrigger property to Inf to
    %avoid draining system resources. Use the daqmem command to check the
    %system resources for the Data Acquisition Toolbox software:
    %The TimerFcn property of the analog input object is used to periodically
    %monitor the data. You can assign a callback function to the TimerFcn
    %property that will execute each time the time specified by the
    %TimerPeriod property passes.
    %Set the TimerPeriod property to 0.5 seconds. Set the TimerFcn to the
    %callback function demoai_continuous_timer_callback to get the data,
    %update the figure and send a stop signal to the object once the condition
    %is met.
    offset=ZERO_VOLT; % This is the offset from the initial voltage test run
```

```
        set(ai,'TimerPeriod',.5);
        %Set up the Plot for real time pressure display
        figure(2);              % Setting up the plot
        maximize(2);            % This maximizes the figure window for plot
        P = plot(zeros(1000,1));    % Initially blank plot
        T = title(['Number of callback function calls: ', num2str(0)]);
        xlabel('TIME (sec)')
        ylabel('PRESSURE (psi)')
        grid on;
        set(ai,'TimerFcn',{@daq_continuous_timer_callback_2,P,T,offset});
        % This is call to the callback function for real time plotting
        tic         %Starts an independent timer for data aqu
        start(ai);     %Starts the data aqu
        while(strcmpi(get(ai,'Running'),'On')) % To keep the code running till the callback
issues a stop
          pause(0.5);
        end
        toc % This ends the independent timer after data aqu ends should be close to
time record

        %The callback function, daq_continuous_timer_callback, uses getdata to
        %bring the data into MATLAB. The functiona also calls a custom
        %daq_continuous function that returns a boolean signifying whether
        %the timmer has been reached. If the result is true, then the
        %function copies the data to the UserData property of the analog object
        %and issues a stop command to the object.

        % This is the final plot of the data
        % The data is available under the allData variable
        allData = get(ai,'UserData');
        figure(3);
        maximize(3);
        plot((allData.time/60),((allData.data-offset)/.002));
        xlabel('Time (min)')
        ylabel('Pressure (psi)')
        title('Total Data captured');
        grid on;
        A = allData.time;
        B = allData.data;
        R = input('Input time file name (include txt extension)','s');
        S =input('Input voltage file name (include txt extension)','s');
        save (R, 'A', '-ascii');
        save (S,  'B', '-ascii');
```

Matlab R2015b code: daq_continous_2.m

```
function condition = daq_continuous_2(data,time,plotHandle,offset)
% This function plots the data in real time. You MUST set the time of
% experemnt by the THRESHOLD value before. This ends up being close to one
% second per threshold value. So set this to the number of seconds you wish
% to record
global time_backup pres_backup;
% lengthofData = length(data);
% lengthofTime = length(time);
%%%%%%%%%%%%%%%%%%%%%%%%%%%%%%%%%%%%%%%%%%%%%%%%%%%%%%%%%%%%%%%%%%%%%%%%%%%%
%%%%%%%%%%%%%%%%%%%%%%%%%%%%%%%%%%%%%%%%%%%%%%%%%%%%%%%%%%%%%%%%%%%%%%%%%%%%
% SET THIS VALUE TO THE NUMBER OF SECONDS YOU WANT TO AQUIRE DATA%%%%%%%%%
threshold = 300; % this value should be a multiple of 100 also check that the code will record for the time of experiment
%%%%%%%%%%%%%%%%%%%%%%%%%%%%%%%%%%%%%%%%%%%%%%%%%%%%%%%%%%%%%%%%%%%%%%%%%%%%
%%%%%%%%%%%%%%%%%%%%%%%%%%%%%%%%%%%%%%%%%%%%%%%%%%%%%%%%%%%%%%%%%%%%%%%%%%%%
pres = ((data-offset)/.002); % CONVERTS VOLTAGE DATA TO PRESSURE
% abs_time = time;
set(plotHandle, 'ydata',pres,'xdata',time); % Updating the plot
drawnow; % Update the plot
time_backup=time;     % This is backup data in case the script crashes
pres_backup=pres;     % This is backup data in case the script crashes
val = max(time);      % Checking the time stamp
if (val > threshold)
   condition = 1;
else
   condition = 0;
end
```

Matlab R2015b code: daq_continous_timer_callback_2.m

```
function daq_continuous_timer_callback_2
% This callback function executes each time the time specified by
% TimerPeriod passes. The input parameters obj and event are passed implicitly
in the callback
% function.
% * obj is the analog input object ai
% * event is a variable that stores the data contained in the EventLog
%   property
% This function calls the daq_continuous function to check whether the timer is
reached.
% If timer is over the threshhold value then the callback issues a stop command
to
% the analog input object.

persistent count;
persistent totalData;
if isempty(count)
    count =0;
end
count = count + 1;
% Get only the number of samples that are available
[data,time] = getdata(obj,ceil(obj.SamplesAvailable));
% First time through assign the data to totalData, else append it.
if isempty(totalData)
   totalData.time = time;
   totalData.data = data;
else
   totalData.time = [totalData.time;time];
   totalData.data = [totalData.data;data];
end
% Call daq_continuous to check timer is detected. If detected,
% transfer the data to UserData property of the object and stop the object
if(daq_continuous_2(totalData.data,totalData.time,plotHandle,offset))
   set(obj,'UserData',totalData);
   stop(obj);
end
% Update the title of the graph
set(titleHandle,'String',['Number of callback function calls: ',
num2str(count)]);
```

REFERENCES

Aharonov, E., and D. Sparks (2004), Stick-slip motion in simulated granular layers, *Journal of Geophysical Research, vol. 109,* B09306, doi: 10.1029/2003JB002597.

Akay, A. (2002), Acoustics friction, *Journal of the Acoustical Society of America, vol. 111,* 4*,* pp. 1525 – 1548, doi: 10.1121/1.1456514.

Al-Shaikh-Ali, M.M.H., A.G. Davis, and M.J. Lloyd (1981), In situ measurement of K_0 in a stiff fissured glacial till by hydraulic fracturing, *Ground Engineering, vol. 14,* pp. 19 - 25.

Amsden, T.W. (1983), Upper Bromide formation and voila group (middle and upper ordovician) in Eastern Oklahoma, *Oklahoma Geological Survey*, *Bulletin 132*, Part 3, pp. 36 - 42.

Andersen, K.H. (1994), Estimation of hydraulic fracture pressure in clay, *Canadian Geotechnical Journal*, *vol. 31,* 6*,* pp. 817 - 828, doi: 10.1139/t94-099.

Anderson, E. M. (1905), The dynamics of faulting*, Transactions of the Edinburgh Geological Society*, *vol. 8*, pp. 387- 402.

ASTM (1995), *ASTM D 4767-95, Standard Test Method for Consolidated Undrained Triaxial Compression Test for Cohesive Soils*, West Conshohocken, PA., doi:10.1520/C0033-03.

ASTM (2002), *ASTM D4767-02, Standard Test Method for Consolidated Undrained Triaxial Compression Test for Cohesive Soils*, ASTM International, West Conshohocken, PA., doi:10.1520/C0033-03.

Au, A.S.K., A.T. Yeung, and K. Soga (2006), Pressure controlled cavity expansion in clay, *Canadian Geotechnical Journal, vol. 43,* pp. 714 - 725, doi: 10.1139/T06-037.

Ayoub, J.A., J.M. Kirksey, B.P. Malone, and W.D. Norman (1992), Hydraulic fracturing of Soft formations in the gulf coast, paper presented to the SPE Formation Damage Control Symposium, Society of Petroleum Engineers, Lafayette, LA.

Baisch, S., M. Bohnhoff, L. Ceranna, Y. Tu, and H.-P. Harjes (2002), Probing the crust to 9-km depth: Fluid-injection experiments and induced seismicity at the KTB superdeep drilling hole, Germany, *Bulletin of the Seismological Society of America*, *vol. 92*, 6, pp. 2369 - 2380.

Baisch, S., and H.-P. Harjes (2003), A model for fluid-injection seismicity at the KTB, Germany, *Geophysical Journal International, vol. 152,* pp. 160 - 170.

Barenblatt, G. I. (2003), *Scaling,* 171 pp., Cambridge University Press, New York.

Barriere, J., C. Bordes, D. Brito, P. Senechal, and H. Perroud (2012), Laboratory monitoring of P waves in partially saturated sand, *Geophysical Journal International, vol. 191,* pp. 1152 - 1170.

Beeler, N. (2004), Review of the physical basis of laboratory-derived relations for brittle failure and their Implications for earthquake occurrence and earthquake nucleation, *Pure and Applied Geophysics, vol. 161,* pp. 1853 - 1876, doi: 10.1007/s00024-004-2536-z.

Behre, C. J. (1937), Bedding-plane faults and their economic importance, *Transactions of the American Institute of Mining and Metallurgical Engineers, vol. 126*, pp. 512 - 529.

Bilby, B., and Eshelby, J. (1968), Dislocations and the theory of fracture, *in Fracture: An advanced treatise*, (edited by H. Liebowitz), pp. 99 - 182, Academic Press, New York, NY.

Bohloli, B., and C. J. de Pater (2006), Experimental study on hydraulic fracturing of soft rocks: influence of fluid rheology and confining stress, *Journal of Petroleum Science and Engineering*, *vol. 53,* 1 - 2*,* pp. 1 - 12.

Bohnhoff, M., S. Baisch, and H.-P. Harjes (2004), Fault mechanisms of induced seismicity at the superdeep German continental deep drilling program (KTB) borehole and their relation to fault structure and stress field, *Journal of Geophysical Research, vol. 109,* B02309*,* doi:10.1029/2003JB002528.

Bourbie, T., O. Coussy, and B. Zinszner (1987), *Acoustics of porous media*, Editions Technip 27, Gulf Publishing Company, Houston, USA (Translated from French by Nissim Marshall).

Boyd, J.W.R., and J. Varley (2001), The uses of passive measurement of acoustic emissions from chemical engineering processes, *Chemical Engineering Science, vol. 56,* pp. 1749 - 1767.

Brace, W., and D. Kohlstedt (1980), Limits on lithospheric stress imposed by laboratory experiments, *Journal of Geophysical Research, vol. 85,* B11, pp. 6248 - 6252*.*

Broek, D. (1982), *Elementary engineering fracture mechanics,* 488 pp., Kluwer, Dordrecht, The Netherlands.

Burov, E.B. (2010), The equivalent elastic thickness, seismicity and the long-term rheology of continental lithosphere: Time to burn-out “crème brûlée”? Insights from large-scale geodynamic modeling, *Tectonophysics, vol. 484*, pp. 4 – 26.

Byerlee, J.D. (1975), The fracture strength and frictional strength of weber sandstone, *International Journal of Rock Mechanics Minining Science and Geomechanics, vol. 12,* 1, pp. 1 - 4.

Byerlee, J. (1978), Friction of rocks, *Pure and Applied Geophysics*, *vol. 116,* 4 - 5, pp. 615 - 626, doi: 10.1007/BF00876528.

Caddey, S.W., R.L. Bachman, T.J. Campbell, R.R. Reid, and R.P. Otto (1991), The Homestake gold mine, an early proterozoic iron-formation-hosted gold deposit, Lawrence County, South Dakota, U.S. Geological Survey Bulletin; 1857-J*,* Books and Open-File Reports Section U.S. Geological Survey Federal Center, Denver, CO.

Cain, R.G., N.W. Page, and S. Biggs (2001), Microscopic and macroscopic aspects of stick-slip motion in granular shear, *Physical Review*, *vol. 64*, 016413, doi: 10.1103/PhysRevE.64.016413.

Callahan, G. D. (2010), Final Report : Geotechnical Engineering Summary for the deep underground science and engineering laboratory (DUSEL), Topical report RSI-2110*,* prepared by RESPEC, Rapid City, SD, for South Dakota School of Mines and Technology, Rapid City, SD.

Callahan, T. P. (2011), Non-Newtonian fluid injection into granular media, Masters Thesis, Georgia Institute of Technology, Atlanta, GA.

Campillo, M., and I.R. Ionescu (1997), Initiation of antiplane shear instability under slip dependent friction, *Journal of Geophysical Research*, *vol. 102*, B9, pp. 20,363 - 20,371.

Carslaw, H., and Jaeger, J. (1959), *Conduction of heat in solids,* 2nd. ed. Oxford Univ. Press, Oxford, United Kingdom.

Chan, C. K. (1985), CKC E/P Cyclic loading triaxial system user's manual, soil engineering equipment company, San Francisco.

Chang, H. (2004), Hydraulic fracturing in particulate materials*,* PhD. Dessertation thesis, Georgia Institute of Technology, Atlanta, GA.

Chang, H., L.N. Germanovich, R. Wu, J.C. Santamarina, and P.E. Dijk (2003), Hydraulic fracturing in cohesionless particulate materials, *Eos Trans. AGU, 84,* 6, *Fall Meet. Suppl., Abstract H51B-03*.

Chery, J., M.D. Zoback, and S. Hickman (2004), A mechanical model of the San Andreas fault and SAFOD pilot hole stress measurements, *Geophysical Research Letters, vol. 31,* L15S13, doi: 10.1029/2004GL019521.

Chin, L. Y., and C. T. Montgomery (2004), A numerical model for simulating solid waste injection in soft rock reservoirs, paper presented at SPE Annual Technical Conference and Exhibition, Society of Petroleum Engineers (SPE), Houston, TX, United States.

Christiansen, P.P., and D.D. Pollard (1997), Nucleation, growth, and structural development of mylonitic shear zones in granitic rock, *Journal of Structural Geology*, *vol. 19,* 9, pp. 1159 - 1172.

Chudnovsky, A., A. Saada, and A.J. Lesser (1988), Micromechanisms of deformation in fracture of overconsolidated clays, *Canada Geotechnical Journal*, *vol. 25,* 2, pp. 213 - 221.

Chudnovsky, A., Y. Shulkin, E. Golovin, H. Zhang, J.W. Dudley, and G.K. Wong (2015), Observation and modeling of fluid flow under matrix and fracturing injections in unconsolidated sand, paper presented at 49th U.S. Rock Mechanics/Geomechanics Symposium, American Rock Mechanics Association, San Francisco, CA, United States.

Cornet, F. H. (2016), Seismic and aseismic motions generated by fluid injections, *Geomechanics for Energy and the Environment, vol. 5,* pp. 42 - 54, doi: 10.1016/j.gete.2015.12.003.

Coulomb, C. (1773), Sur une application des regles de maximis et minimis a quelques problemes de statique relatifs a l'Architecture, Acad. Roy, *Des sciences memories de math, Et de physique par divers savans*, *vol. 7*, pp. 343 - 382.

Cox, S., and C. Scholz (1988), Rupture initiation in shear fracture of rocks: an experimental study, *Journal of Geophysical Research, vol. 93,* B4, pp. 3307 - 3320.

Dahlheim, H., H. Gebrande, E. Schmedes, and H. Softel (1997), Seismicity and stress field in the vicinity of the KTB location, *Journal of Geophysical Research, vol. 102,* B8, pp. 18493-18506.

d'Alessio, M. A., and S. J. Martel (2005), Development of strike-slip faults from dikes, Sequoia national park California, *Journal of Structural Geology*, *vol. 27*, pp. 35 - 49, doi: 10.1016/j.jsg.2004.06.013.

Dascalu, C., I. R. Ionescu, and M. Campillo (2000), Fault fitness and initiation of dynamic shear instability, *Earth and Planetary Science Letters, vol. 177*, pp.163 - 176.

De Pater, C.J. and Y. Dong (2007), Experimental study of hydraulic fracturing in sand as a function of stress and fluid rheology, paper presented at SPE-Hydraulic Fracturing Technology Conference, Society of Petroleum Engineers, College Station, TX, United States.

De Pater C.J., and Y. Dong (2009), Fracture containment in soft sands by permeability or strength contrasts, paper presented at SPE-Hydraulic Fracturing Technology Conference, Society of Petroleum Engineers, The Woodlands, TX, United States.

Detournay, E., and Cheng, A.H.-D. (1993), Fundamentals of poroelasticity, Chapter 5, *comprehensive rock engineering: Principles, Practice and Projects,* vol. 2, Analysis and Design Method, ed. C. Fairhurst, pp. 113 - 171, Pergamon Press, Oxford, United Kingdom.

DiCarlo, D.A., J.I.G. Cidoncha, and C. Hickey (2003), Acoustic measurements of pore-scale displacements, *Geophysical Research Letters*, *vol. 30,* 17, pp. 1901, doi: 10.1029/2003GL017811.

Dieterich, J. (1978), Time-dependent friction and the mechanics of stick-slip, *Pure Applied Geophysics, vol. 116,* pp. 790 - 806.

Dieterich, J. (1979), Modelling of rock friction: 1. Experimental results and constructive equations, *Journal of Geophysics Research, vol. 84,* B5, pp. 2161 - 2168.

Dieterich, J. (1981), Constitutive properties of faults with simulated gouge, in mechanical behavior of crustal rocks, N. L. Carter, M. Friedman, J. M. Logan, and D. W. Sterns (Editors), *American Geophysical Monograph, vol. 24,* pp.103 – 120, doi: 10.1029/GM024p0103.

Doe, T.W., and G. Boyce (1989), Orientation of hydraulic fractures in salt under hydrostatic and non-hydrostatic stresses, *International Journal of Rock Mechanics Minining Sceince and Geomechanics, vol. 26,* 6, pp. 605 - 611.

Donath, F. A. (1961), Experimental study of shear failure in anisotropic rocks, *Geological Society of America Bulletin*, *vol. 72,* 6, pp. 985 - 989, doi: 10.1130/0016-7606.

Dong, Y. (2010), Hydraulic fracture containment in sand, Dissertation thesis, Delft University Technology, Netherlands.

Dong, Y., and C.J. De Pater (2007a), Closure of hydraulic fractures visualized by X-Ray CT technique in sand, paper presented at 1st Canada-US Rock Mechanics Symposium - Rock Mechanics meeting Society's Challenges and Demands, Taylor and Francis Group/Balkema, Vancouver, BC, Canada.

Dong, Y., and C.J. De Pater (2007b), Clossure of hydraulic fractures visualized by X-Ray CT Technique in sand, paper presented at 1st Canada-US Rock Mechanics Symposium - Rock Mechanics

meeting Society's Challenges and Demands, Taylor and Francis Group/Balkema, Vancouver, BC, Canada.

Dong, Y., and C.J. De Pater (2008), Observation and modeling of the hydraulic fracture tip in sand, paper presented at the 42nd U.S. Rock Mechanics Symposium (USRMS), American Rock Mechanics Association, Omnipress, San Francisco, CA, United States.

Durrheim, R.J., H. Ogasawara, M. Nakatani, Y. Yabe , H. Kawakata, M. Naoi, A.K. Ward, S.K. Murphy, J. Wienand, P. Lenegan, A. M. Milev, O. Murakami, N. Yoshimitsu, T. Kgarume, and A. Cichowicz (2012), Establishment of SATREPS experimental sites in South African gold mines to monitor phenomena associated with earthquake nucleation and rupture, Proceedings of the 6th International Seminar on Deep and High Stress Mining, Australian Centre for Geomechanics, Santiago Chile.

Durrheim, R.J., H. Ogasawara, M. Nakatani, Y. Yabe, A.M. Milev, A. Cichowicz, H. Kawakata, H. Moriya, and the SATREPS research group (2010), Observational studies to mitigate seismic risks in mines: a new Japanese - South African Collaborative research project, Proceedings of the 5th International Seminar on Deep and High stress Mining, Australian Centre for Geomechanics, Santiago Chile.

Dyskin, A.V., and L.N. Germanovich (1995), A model of fault propagation in rocks under compression, paper presented at 35th U.S. Symposium on Rock Mechanics (USRMS), American Rock Mechanics Association, Reno, Nevada.

Ellsworth, W. (2013), Injection-induced earthquakes, *Science, vol. 341,* 6142, pp. 1 - 7, doi: 10.1126/science.1225942.

Emerson, M., and P. Foray (2006), Laboratory P-wave measurements in dry and saturated sand, *Acta Geotechnica, vol. 1,* pp. 167 – 177, doi:10.1007/s11440-006-0015-7.

Emmermann, R., and J. Lauterjung (1997), The German continental deep drilling program KTB: overview and major results, *Journal of Geophysical Research, vol. 102,* B8, pp. 18,179 - 18,201.

Fischer, T., S. Hainzl, L. Eisner, S. Shapiro, and J. Le Calvez (2008), Microseismic signatures of hydraulic fracture growth in sediment formations: Observations and modeling, *Journal of Geophysical Research*, *vol. 113*, B02307, doi:10.1029/2007JB005070.

Fischer, T., S. Hainzl, and T. Dahm (2009), The creation of an asymmetric hydraulic fracture as a result of driving stress gradients, *Geophysical Journal International, vol. 179,* 1, pp. 634 - 639, doi:10.1111/j.1365-246x.2009.04316.x.

Flores, R.M., and C.W. Keighin (1989), Petrology and depositional facies of siliciclastic rocks of the midlle Ordovician Simpson group, Mazur Well, Southeastern Anadarko Basin, Oklahoma, U.S. Geological Survey Bulletin 1866-E, Books and Open-File Reports Section U.S. Geological Survey Federal Center, Denver, CO.

Folger, P., and M. Tiemann (2015), Human-induced earthquakes from deep-well injection: a brief overview, Report, Congressional Research Service, Washington D.C.

Friberg, P.A, G.M. Besana-Ostman, and I. Dricker (2014), Characterization of an earthquake sequence triggered by hydraulic fracturing in Harrison County, Ohio, *Seismological Research Letters, vol. 85,* 6*,* pp. 1295 - 1307, doi: 10.1785/0220140127.

Frohlich, C. (2012), Two-year survey comparing earthquake activity and injection-well locations in the Barnett Shale, Texas, *Proceedings of the National Academy of Sciences, vol. 109,* 35, pp. 13934 - 13938, doi: 10.1073/pnas.1207728109.

Fukuyama, E., T. Mikumo, and B. Olsen (2003), Estimation of the critical slip-weakening distance: theoretical background, *Bulletin of Seismological Society of America, vol. 93,* 4, *pp. 1835 - 1840*.

Garagash, D. I., L. N. Germanovich, L. C. Murdoch, S. Martel, Z. Reches, D. Ellsworth, T. C. Onstott, and S. D. Glaser (2009), A thermal technique of fault nucleation, growth, and slip, *Eos Trans. AGU, vol. 90,* 52*, Fall Meet. Suppl., Abstract H23E-0995*.

Garagash D. I. and L. N. Germanovich (2012), Nucleation and arrest of dynamic slip on a pressurized fault, *Journal of Geophysical Research, vol. 117,* B10310, doi:10.1029/2012JB009209.

Germanovich, L.N., D.K. Astakhov, M.J. Mayerhofer, J. Shlyapobersky, and L.M. Ring (1997a), Hydraulic fracture with multiple segments: I. Observations and model formulation, *International Journal of Rock Mechanics and Mining Science, vol. 34,* 097*,* pp. 3 - 4.

Germanovich, L.N., D.K. Astakhov, M.J. Mayerhofer, J. Shlyapobersky, and L.M. Ring (1997b), Hydraulic fracture with multiple segments: II. Modeling, *International Journal of Rock Mechanics and Mining Science*, *vol 34,* 98*,* pp. 3 - 4*.*

Germanovich, L., D. Gwaba, S. Stanchits, and J. Ayoub (2016), *Hydraulic fracturing in soft sediments: Test 4 at TerraTek,* Georgia Institute of Technology report to CAB members, Atlanta, Ga, 142 pp.

Germanovich, L. N., R. S. Hurt, J. A. Ayoub, E. Seibrits, D. Norman, I. Ispas, and C. T. Montgomery (2012), Experimental study of hydraulic fracturing in unconsolidated materials, *Society of Petroleum Engineers, SPE-151827-MS*, pp. 15 - 17.

Germanovich L.N., and L.C. Murdoch (2010), Injection of solids to lift coastal areas, *Proceedings of The Royal Society* A, *vol. 466*, pp. 3225 – 3252, doi: 10.1098/rspa.2010.0033.

Germanovich, L. N., L.C. Murdock, D.I. Garagash, Z. Reches, S.J. Martel, D.C. Gwaba, D. Ellsworth, R.P. Lowell, and T.C. Onstott (2010), A controllable earthquake rupture experiment on the Homestake fault, *Eos Trans. AGU Fall Meeting Supplement, H13F-1045.*

Germanovich, L.N., R.S. Hurt, and H. Huang (2007), Hydraulic fracturing in saturated cohesionless materials, *Eos Trans. AGU Fall Meeting Supplement, H11B-0492.*

Germanovich, L.N., R.L. Salganik, A.V. Dyskin, and K.K. Lee (1994), Mechanisms of brittle fracture of rocks with multiple pre-existing cracks in compression, *Pure and Applied Geophysics*, *vol. 143,* 1 - 3, pp. 117 - 149.

Girard, J.M., R.W. McKibbin, J.B. Seymour, and F.M. Jones (1997), Characterization of in situ stress conditions at depth-Homestake mine, Lead, South Dakota, *International Journal of Rock Mechanics and Mining Science*, *vol 34,* 104, pp. 3 - 4.

Gischig, V. S. (2015), Rupture propagation behavior and the largest possible earthquake induced by fluid injection into deep reservoirs, *Geophysical Research Letters*, *vol. 42*, pp. 7420 - 7428, doi: 10.1002/2015GL065072.

Golovin, E., A. Chudnovsky, J.W. Dudley, and G.K. Wong (2011), Injection rate effects on waterflooding mechanisms and Injectivity in cohesionless sand, paper presented at 45th U.S. Rock Mechanics Symposium (USRMS), American Rock Mechanics Association, Omnipress, San Francisco, CA, United States.

Golovani, E., H. Jasarevic, A. Chudnovsky, J.W. Dudley, and G.K. Wong (2010), Observation and characterization of hydraulic fracture in cohesionless sand, paper presented at *44th U.S.*

Rock Mechanics Symposium and 5th U.S.-Canada Rock Mechanics Symposium, American Rock Mechanics Association, Salt Lake City, UT, United States.

Goren, L., E. Aharonov, D. Sparks, and R. Toussaint (2010), Pore pressure evolution in deforming granular material: A general formulation and the infinitely stiff approximation, *Journal of Geophysical Research, vol. 115*, B09216, doi: 10.1029/2009JB007191.

Goren, L., E. Aharonov, D. Sparks, and R. Toussaint (2011), The mechanical coupling of fluidfilled granular material under shear, *Pure and Applied Geophysics, vol. 168*, pp. 2289 – 2323, doi: 10.1007/s00024-011-0320-4.

Green, C.A, and P. Styles (2012), Preese Hall shale gas fracturing: review and recommendations for induced seismicity mitigation, Induced Seismicity Mitigation Report, Keele university, Keele, United Kingdom (www.gov.uk/goverment/uploads/).

Gross, C., and M. Ohtsu (2008), *Acoustic emission testing,* Springer, Berlin, Heidelberg.

Grosse C. U., H.W. Reinhard, and F. Finck (2003), Signal-Based Acoustic Emission Techniques in Civil Engineering, *Journal of Materials in Civil Engineering*., *vol. 15,* 3, doi: 10.1061/(ASCE)0899-1561(2003)15:3(274).

Guglielmi, Y., F. Cappa, A. Jean-Philippe, P. Henry, and D. Elsworth (2015), Seismicity triggered by fluid injection-induced aseismic slip, *Science, vol. 348,* 1224, doi: 10.1126/science.aab0476.

Gwaba, D., L. Germanovich, and N. Whitney (2014), Unconsolidated sand fracturing Test 3, Georgia Institute of Technology Report to Schlumberger, Atlanta, Ga, 33 pp .

Haimson, B.C. (1972), Earthquake related stresses at Rangely, Colorado, paper presented to the 14th U.S. Symposium on Rock Mechanics (USRMS), American Rock Mechanics Association, University Park, PA, United States.

Hainey, B.W., and J.C. Troncoso (1992), Frac-Pack: an innovative stimulation and sand control technique, Paper presented at the SPE International Symposium on Formation Damage Control, Society of Petroleum Engineers, Lafayette, Loisiana, USA.

Hallbauer, D. , H. Wagner, and N. Cook (1973), Some observations concerning the macroscopic and mechanical behavior of quartzite specimens in stiff, triaxial compression tests, *International Journal of Rock Mechanics Mining Science and Geomechanics. vol. 10,* pp. 713 - 725.

Healy, J.H., W.W. Rubey, D.T. Griggs, and C.B. Raleigh (1968), The Denver earthquakes, *Science, vol. 161,* 3848, pp. 1301 - 1310.

Herschel, W.H., and R. Bulkley (1926), *Konsistenzmessungen von Gummi-Benzollösungen Kolloid Zeitschrift, vol. 39*, pp. 291 – 300.

Hickman, S., and M. Zoback (2004), Stress orientation and magnitudes in the SAFOD pilot hole, *Geophysical Research Letters, vol. 31,* L15S12, doi: 10.1029/2004GL020043.

Hickman, S., M. Zoback, W. Ellsworth, N. Boness, P. Malin, S. Roecker, and C. Thurber (2007), Structure and properties of the San Andreas fault in central California: recent results from the SAFOD experiment, *Scientific Drilling,* 1*,* pp. 29 - 32, doi: 10.2204/iodp.sd.s01.39.2007.

Hirose, T., and T. Shimamoto (2005), Slip-weakening distance of faults during frictional melting as inferred from experimental and natural pseudotachylytes, *Bulletin of the Seismological Society of America, vol. 95,* 5, pp. 1666 - 1673, doi: 10.1785/0120040131.

Holdsworth, R.E., E.W.E. Van Diggelen, C.J. Spiers, J.H.P. De Bresser, R.J. Walker, and L. Bowen (2011), Fault rocks from the SAFOD core samples: Implications for weakening at shallow depths along the San Andreas fault, California, *Journal of Structural Geology, vol. 33,* pp. 132 - 144, doi: 10.1016/j.jsg.2010.11.010.

Holland, A. (2013), Earthquakes triggered by hydraulic fracturing in South-Central Oklahoma, *Bulletin of the Seismological Society of America*, *vol. 103,* 3, pp. 1784–1792, doi: 10.1785/0120120109.

Holtz, W. G., and H.J. Gibbs (1956), Engineering properties of expansive clays: Transactions, *American Society of Civil Engineers, vol. 121*, pp. 641 - 677.

Holubec, I., and E. D'Appolonia (1973), Effect of particle shape on the engineering properties of granular soils. ASTM Spec. Tech. Publ. *vol. 523*, pp. 304 – 318.

Horton, S. (2012), Disposal of hydrofracting waste fluid by injection into subsurface aquifers triggers earthquake swarm in central Arkansas with potential for damaging earthquake, *Seismological Research Letters, vol. 83,* 2, pp. 250-260, doi: 10.1785/gssrl.83.2.250.

Huang, H., F. Zhang, P. Callahan, and J. Ayoub (2012), Granular fingering in fluid injection into dense granular media in a Hele-Shaw cell, *PRL 108,* 258001*,* doi: 10.1103/PhysRevLett.108.258001.

Huang, H., F. Zhang, P. Callahan, and J. Ayoub (2011), Fluid injection experiments in two-dimensional porous media, paper presented at the SPE Hydraulic Fracturing Technology Conference, Society of Petroleum Engineers, The Woodlands, Texas, USA.

Huck, P.J., and R.M. Koerner (1981), Acoustic emission monitoring of soil and rock grouting. Acoustic Emissions in Geotechnical Engineering Practice, ASTMSTP 750, 155-163, American Society for Testing and Materials, Philadelphia.

Hurt, R. S. (2012), Parameters controlling hydraulic fracturing and fracture tip-dominated leakoff in unconsolidated sands, paper presented at SPE Annual Technical Conference and Exhibition, *Society of Petroleum Engineers*, San Antonio, TX.

Hurt, R. S. (2012), Toughness-dominated hydraulic fractures in cohesionless particulate materials, PhD. Dessertation thesis, Georgia Institute of Technology, Atlanta, GA..

Hurt, R.S., and L.N. Germanovich (2012), Parameters controlling hydraulic fracturing and fracture tip-dominated leakoff in unconsolidated sands, paper presented at SPE Annual Technical Conference and Exhibition, *Society of Petroleum Engineers*, San Antonio, TX.

Hurt, R.S., R. Wu, L. Germanovich, H. Chang, and P.V. Dyke (2005), On mechanisms of hydraulic fracturing in cohesionless materials, paper presented at AGU Fall Meeting, Eos Trans., San Francisco, CA.

Ida, Y. (1972), Cohesive force across the tip of a longitudinal-shear crack and Griffith's specific surface energy, *Journal Geophysics Research, vol. 77,* 20, pp. 3796 - 3805.

Ishida, T. (2001), Acoustic emission monitoring of hydraulic fracturing in laboratory and field, *Construction and Building Materials, vol. 15*, pp. 283 - 295.

Jaeger, J.C., N.G. W. Cook, and R.W. Zimmerman (2007), *Fundamentals of rock mechanics,* 4th Edition, 355 pp., Blackwell Publishin, Malden, MA, United States.

Jahr, T., G. Jentzsch, A. Gebauer, and T. Lau (2008), Deformation, seismicity, and fluids: Results of the 2004/2005 water injection experiment at the KTB/Germany, *Journal of Geophysical Research, vol. 113,* B11410, doi: 10.1029/2008JB005610.

Jasarevic, H., E. Golovin, A. Chudnovsky, J.W. Dudley, and G.K. Wong (2010), Observation and modeling of hydraulic fracture initiation in cohesionless sand, paper presented at 44th US

Rock Mechanics Symposium and the 5th US/Canada Rock Mechanics Symposium, American Rock Mechanics Association, Salt Lake City, UT, United States.

Jaworski, G.W., J.M. Duncan, and H.B. Seed (1981), Laboratory study of hydraulic fracturing, *Journal of Geotechnical Engineering Division, vol. 107*, 6, pp. 713 - 732.

Ji, L., A. Settari, and R. B. Sullivan (2009), A novel hydraulic fracturing model fully coupled with geomechanics and reservoir simulation, *Society of Petroleum Engineers, vol. 14,* 3, pp. 423 - 430, doi: 10.2118/110845-PA.

Johnson, K.S. (1989), Late Cambrian-Ordovician geology of the southern Midcontinent, proceedings of a Oklahoma Geological Survey Symposium, Oklohoma Geological Survey, Norman, OK.

Johnson, J., W. Pariseau, D. Scott, and F. Jenkins (1993), In-situ stress measurements near the ross shaft pillar Homestake mine South Dakota, Report of Investigations 9446, 21 pp., United States Department of the Interior Bureau of Mines, Washington, DC.

Jones, J., and D. Soler (1999), Fracture stimulation of shallow, unconsolidated Kern River Sands, Paper presented at the SPE International Thermal Operations and Heavy Oil Symposium, Society of Petroleum Engineers, Bakersfield, CA, United States.

Keranen, K.M., M. Weingarten, G.A. Abers, and B.A. Bekins (2014), Sharp increase in central Oklahoma seismicity since 2008 induced by massive wastewater injection, *Science, vol. 345,* 6195, doi: 10.1126/science.1255802.

Khodaverdian, M., and P. McElfresh (2000), Hyraulic fracturing stimulation in poorly consolidated sand: mechanisms and consequences, Paper presented at the SPE Annual Technical Conference and Exhibition on Drilling and Completion, Society of Petroleum Engineers, Dallas, TX, United States.

Khodaverdian, M., T. G. Sorop, P. J. Van Den Hoek, S. Sathyamoorthy, and E. Okoh (2010b), Injectivity and fracturing in unconsolidated sand reservoirs: waterflooding case study, offshore Nigeria, Paper presented at 44th US Rock Mechanics Symposium and the 5th US/Canada Rock Mechanics Symposium, American Rock Mechanics Association, Salt Lake City, UT, United States.

Kim, W. -Y. (2013), Induced seismicity associated with fluid injection into a deep well in Youngstown, Ohio, *Journal of Geophysical Research-Solid Earth, vol. 118,* pp. 3506-3518, doi: 10.1002/jgrb.50247.

Kino, G. (1987), *Acoustic waves: Devices imaging and analog signal processing,* 688 pp., Prentice-Hall, Upper Saddle River, N.J.

Knopoff, L. (1964), Q, *Review of Geophysics*, *vol. 2,* 4, pp. 625 – 660.

Kochnev, V.A., I.V. Goz, V.S. Polyakov, I.S. Murtayev, V.G. Savin, B.K. Zommer, and I.V. Bryksin (2007), Imaging hydraulic fracture zones from surface passive microseismic data, *First Break, vol. 25,* pp. 77 – 80.

Koerner, R., A. Lord, and W. McCabe (1977), Acoustic-emission behavior of cohesive soils, *Journal of the Geotechnical Engineering Division – ASCE, vol. 103,* pp. 837 - 850.

Koerner, R., A. Lord, W. McCabe, and J. Curran (1976), Acoustic-emission behavior of granular soils, *Journal of the Geotechnical Engineering Division-ASCE, vol. 103,* pp. 1460 - 1461.

Koerner, R., W. McCabe, and A. Lord (1981a), Overview of acoustic emission monitoring of rock structures, *Rock Mechanics and Rock Engineering, vol. 14,* pp. 27 - 35.

Krumbein W.C., and L.L. Sloss (1963), *Stratigraphy and sedimentation,* 660 pp., Freeman, San Francisco, CA, United States.

Ladd, R. (1978), Preparing test specimens using undercompaction, *Geotechnical Testing Journal*, *vol. 1,* 1, pp. 16 - 23, doi: 10.1520/GTJ10364J.

Lei, X., K. Kusunose, M. Rao, O. Nishizawa, and T. Satoh (2000), Quasi-static fault growth and cracking in homogenous brittle rock under triaxial compression using acoustic emission monitoring, *Journal of Geophysical Research, vol. 105,* B3*,* pp. 6127 - 6139.

Leonard, M., and B.L.N. Kennett (1999), Multi-component autoregressive techniques for the analysis of seismograms, *Physics of the Earth planetary Interiors, vol. 113*, pp. 247 – 263.

Lockner, D. (1993), The role of acoustic emission in the study of rock fracture, *International Journal of Rock Mechanics Minerals Science and Geomechanics*, *vol 30,* 7, pp. 883 - 899.

Lockner, D., and N. Beeler (2002), Rock failure and earthquakes, *International Handbook of earthquake and engineering seismology, vol. 81,* A, pp. 505-537.

Lockner, D.A, and J.D. Byerlee (1993), How geometrical constraints contribute to the weaknesss of mature faults, *Nature*, *vol. 363*, pp. 250 - 252.

Lockner, D.A., J.D. Byerlee, V. Kuksneko, A. Ponomarev, and A. Sidrin (1991), Quasi-static fault growth from acoustic emissions in granite, *Nature*, *vol. 350*, pp. 39 - 42.

Loeblich, J. A. (1942), Bryozoa from the ordovician Bromide formation, Oklahoma, *Journal of Paleontology, vol. 16,* 4*,* pp. 413 - 436.

Lord, A., and R. Koerner (1974), Acoustic-emission response of dry soils, *Journal of Testing and Evaluation*, *vol. 2,* 3, pp. 159 - 162.

Lord, A., and R. Koerner (1975), Acoustic emissions in soils and their use in assessing earth dam stability, *Journal of the Acoustic Society of America*, *vol. 57,* 2, pp. 516 - 519.

Majmudar, T.S., and R.P. Behringer (2005), Contact force measurements and stress-induced anisotropy in granular materials, *Nature vol. 435*, pp. 1079 –1082, doi:10.1038/nature03805.

Marone, C. (1998), Laboratory-driven friction laws and their application to seismic faulting, *Annual Review of Earth and Planetery Sciences, vol. 26,* pp. 643 - 696.

Martel, S.J., D.D. Pollard, and P. Segall (1988), Development of simple fault zones in granitic rock, mount Abbot quadrangle, Sierra Nevada, California, *Geological Society of America Bulletin*, *vol. 100*, pp. 1451 - 1465.

Matsunaga, I., H. Kobayashi, S. Sasaki, and T. Ishida (1993), Studying hydraulic fracturing mechanism by laboratory experiments with acoustic emission monitoring, *International Journal of Rock Mechanics Mineral Science and Geomechanics*, *vol. 30,* 7, pp. 909 - 912.

McGarr, A. (1991), On a possible connection between three major earthquakes in California and oil production, *Bulletin of the Seismological Soiety of America, vol. 81,* 3, pp.948 - 970*.*

McGarr, A. (2014), Maximum magnitude earthquakes induced by fluid injection, *Journal of Geophysical Reserch*, *vol. 119*, pp. 1008–1019, doi: 10.1002/ 2013JB010597.

Michlmayr, G., D. Cohen, and D. Or (2012), Sources and characteristics of acoustic emissions from mechanically stressed geologic granular media-a review, *Earth-Science Reviews, vol. 112,* 3 - 4, pp. 97 - 114.

Mitchell, J.K., and K. Soga (2005), *Fundamentals of soil behavior*, 3rd edition, 559 pp., John Wiley and Sons, New York, NY, United States.

Montgomery, C. (2013), Fracturing fluids, paper presented to ISRM International Conference for Effective and Sustainable Hydraulic Fracturing, International Society for Rock Mechanics, Brisbane, Australia.

Murdoch, L. (1993b), Hydraulic fracturing of soil during laboratory experiments 2, Propagation, *Geotechnique*, *vol. 43,* 2*,* pp. 267 - 276.

Murdoch, L. C. (1993c), Hydraulic fracturing of soil during laboratory experiments 3. Theoretical-Analysis, *Geotechnique*, *vol. 43,* 2, pp. 277 - 287.

Murdoch, L. C. (1995), Forms of hydraulic fractures created during a field-test in overconsolidated glacial drift, *Quarterly Journal of Engineering Geology*, *vol. 28*, pp. 23 - 25, doi: 10.1144/GSL.QJEGH .

Murdoch, L. C. (2002), Mechanical analysis of idealized shallow hydraulic fracture, *Journal of Geotechnical and Geoenvironmental Engineering, vol. 128,* 6, pp. 488 - 495, doi: 10.1061/(ASCE)1090-0241(2002)128:6(488) .

Murdoch, L. C., J. R. Richardson, Q. Tan, S. C. Malin, and C. Fairbanks (2006a), Forms and sand transport in shallow hydraulic fractures in residual soil, *Canadian Geotechnical Journal, vol. 43,* pp. 1061 - 1073, doi: 10.1139/T06-063.

Murdoch, L., L. Germanovich, H. Wang, T. Onstott, D. Elsworth, L. Stetler, and D. Bout (2012), Hydrogeology of the vicinity of Homestake mine, South Dakota, USA, *Hydrogeology Journal, vol. 20,* pp. 27 - 43, doi: 10.1007/s10040-011-0773-7.

Murdoch, L. C. (1993a), *Hydraulic fracturing of soil during laboratory experiments 1. Methods and Observations,* Geotechnique, *vol. 43,* 2, pp. 255 - 265.

Murdoch, L. C., and W. W. Slack (2002), Forms of hydraulic fractures in shallow fine-grained formations, *Journal of Geotechnical and Geoenvironmental Engineering, vol. 128,* pp. 479 - 487, doi: 10.1061/(ASCE)1090-0241(2002)128:6(479).

Nakatani, M., Y. Takehara, H. Sugino, M. Matsumoto, H. Hashimoto, Y. Hasegawa, T. Murakami, A. Uezumi, S. Takeda, S. Noji, Y. Sunada, and K. Tsuchida (2007), Transgenic expression of a myostatin inhibitor derived from follistatin increases skeletal muscle mass and ameliorates dystrophic pathology in mdx mice, *The FASEB Journal, vol. 22,* pp. 477 - 487, doi: 10.1096/fj.07-8673com.

Nicholson C., and R.L. Wesson (1992), Triggered earthquakes and deep well activities, *Pure and Applied Geophysics*, *vol. 139,* 3-4*,* pp. 561 - 578.

Ogasawara, H., and the Research Group for Semi-controlled Experiment in South African Gold Mines (2002b), Microearthquake scaling relationship using near-source, redundant, wide-dynamic-range accelerograms in a South African deep gold mine, paper presented at the Southern African Institute of Mining and Metallurgy Hard Rock Safe Safety Conference, The Southern African Insitute of Mining and Metallurgy, South Africa..

Ogasawara, H., and the Research Group for Semi-controlled Experiment in South African Gold Mines (2002a), Semi-controlled earthquake generation experiment in South African Deep Gold Mines (1992-2001), *Seismogenic Process Monitoring, vol.,* pp. 119 - 150*.*

Ogasawara, H., and R.J. Durheim (2009), A Japanese-South African collaboration to mitigate seismic risks in deep gold mines, *The Southern African Institute of Mining and Metallurgy, vol. 107,* pp. 115 - 134.

Ogasawara, H., R.J. Durrheim, M. Nakatani, A. Milev, A. Cichowicz, H. Kawakata, H. Moriya, and the JST-JICA SA research group (2009), A Japanese-South African collaboration to mitigate seismic risks in deep gold mines, paper presented at the Southern African Institute of Mining and Metallurgy Hard Rock Safe Safety Conference, The Southern African Insitute of Mining and Metallurgy, South Africa.

Palmer, A.C., and J.R. Rice (1973), The growth of slip surfaces in the progressive failure of overconsolidated clay, *Philosophical Transactions of the Royal Society*, *vol. 332,* A, pp. 527 - 548.

Panah, A. K., and E. Yanagisawa (1989), Laboratory studies on hydraulic fracturing criteria in soil, *Japanese Society of Soils and Foundations, vol. 29,* 4, pp. 14 - 22.

Papanastasio, P. (1997), The influence of plasticity in hydraulic fracturing, *International Journal of Fracture, vol. 84,* 1*,* pp. 61 - 79*.*

Pariseau, W. (1985), Research study on piller design for vertical crater retreat (VCR) mining, Bureau of Mines Contract Report J0215043, 233 pp., Department of Mining Engineering, University of Utah, Salt Lake City, UT.

Pariseau, W. D. (1984), Numerical assessment of the influence of anisotropy on steeply dipping VCR stopes, Proceedings of geomechanics applications in underground Hardrock Mining, American Institute of Mining, Metallurgical, and Petroleum Engineers, New York, NY, United States.

Pariseau, W., F. Duan, and C. Schmuck, (1987), Stability analysis of the VCR stope at the Homestake mine, *Gold Mining, vol. 87,* pp. 199 - 213.

Pope, M.C. (2004), Cherty carbonate facies of the Montoya Group, southern New Mexico and western Texas and its regional correlatives: a record of late Ordovician paleoceanography on southern Laurentia, *Palaeogeography, Palaeoclimatology, Palaeoecology, vol. 210*, pp. 367 – 384.

Puckette, J., T. Halihan, and J. Faith (2009), Characterization of the Arbuckle-Simpson Aquifer, Final Report submitted to Oklahoma Water Resource Board, 60 pp., Oklahoma State University, Oklahoma City, OK.

Radjai, F., D.E. Wolf, M. Jean, and J.J. Moreau (1998), Bimodal character of stress transmission in granular packings, *Physical Review Letters, vol. 80*, pp. 61 – 64.

Rahn, P. and W. Roggenthen (2002), Hydrogeology of the Homestake Mine: Proceedings, *Academy of Science, vol. 81,* pp. 19 - 25.

Raleigh, C.B., J.H. Healy, and J.D. Bredehoeft (1976), An experment in earthquake control at Rangley, Colorado, *Science*, *vol. 191*, pp. 1230 - 1237.

Reches, Z., and H. Ito (2007), Scientific drilling of active faults: past and future, *Scientific Drilling*, pp. 235 - 258, doi: 10.1007/978-3-540-68778-8_6.

Reches, Z., and D.A Lockner (1994), Nucleation and growth of faults in brittle rocks, *Journal of Geophysical Research*, *vol. 99,* B9*,* pp. 18,159 - 18,173.

Reimer, K.L., and R.J. Durrheim (2012), Mining seismicity in the Witwatersrand basin: Monitoring, Mechanisms and Mitigation Strategies in Perspective, *Journal of Rock Mechanics and Geotechnical Engineering, vol. 4,* 3*,* pp. 228 - 249, doi: 10.3724/SP.J.1235.2012.00228.

Reiweger, I., and J. Schweizer (2013b), Measuring acoustic emissions in an avalanche starting zone to monitor snow stability, Proceedings International snow Science Workshop*,* Institute for Snow and Avalanche Research*,* Grenoble, France.

Reiweger, I, K. Mayer, K. Steiner, J. Dual, and J. Schweizer (2015), Measuring and localizing acoustic emission events in snow prior to fracture, *Cold Regions Science and Technology, vol. 110,* pp. 160 - 169, doi: 10.1016/j.coldregions.2014.12.002.

Rice, J. (1968), Mathematical analysis in the mechanics of fracture, *An Advanced Treatise*, vol. 2, edited by H. Liebowitz, chap. 3, pp. 191-311, Academic Press, New York, NY, United States.

Rice, J. (2006), Heating and weakening of faults during earthquake slip, *Journal of Geophysical Research, vol. 111*, B05311, doi:10.1029/2005JB004006.

Rioual, F., A. Valance, and D. Bideau (2000), Experimental study of the collision process of a grain on a two-dimensional granular bed, *Physical Review, vol. 62*, pp. 2450 – 2459.

Rubinstein J.L., W.L. Ellsworth, A. McGarr, and H.M. Benz (2014), The 2001 – present induced earthquake sequence in the Raton basin, *Bulletin of the Seismological Society of America, vol. 104,* 5, pp. 1 - 20, doi: 10.1785/0120140009.

Ruina, A. (1983), Slip instability and state variable friction laws, *Journal of Geophysics Research, vol. 88,* B12, pp. 10359 - 10370.

Rummel, F., H.J. Alheid, and C. Frohn (1978), Dilatancy and fracture-induced velocity changes in rock and their relation to frictional sliding, *Pure and Applied Geophysics*, *vol. 116,* pp. 743 - 764.

Santamarina, J. C., K. A. Klein, and M. A. Fam (2001), *Soils and Waves: Particulate Materials Behavior, Characterization and Process Monitoring,* 488 pp., J. Wiley and Sons, New York, NY, United States.

Schubnel, A., B.D. Thompson, J. Fortin, Y. Gueguen, and R.P. Young (2007), Fluid-induced rupture experiment on Fontainebleau sandstone: Premonitory activity, rupture propagation, and aftershocks, *Geophysical Research Letters, vol. 34,* L19307, doi: 10.1029/2007GL031076.

Scruby, C.B. (1987), An introduction to acoustic emission, *Journal of Physics E: Science Instrumentation, vol. 20*, pp. 946 – 953.

Segall, P., and D.D. Pollard (1983), Nucleation and growth of strike slip faults in granite, *Journal of Geophysical Research*, *vol. 88,* B1, pp. 555 - 568.

Shapiro, S.A., J. Kummerow, C. Dinske, G. Asch, E. Rothert, J. Erzinger, H.J. Kumpel, and R. Kind (2006), Fluid induced seismicity guided by a continental fault: Injection experiment of

2004/2005 at the German deep drilling site (KTB), *Geophysical Research Letters, vol. 33,* L01309, doi: 10.1029/2005GL024659.

Sibson, R. (1975), Generation of pseudotachylyte by ancient seismic faulting, *Geophysical Journal of the Royal Astronomical Society, vol. 43,* pp. 775-794.

Sibson, R. H. (1992), Implications of fault-valve behaviour for rupture nucleation and recurrence, *Tectonophysics, vol. 211,* pp. 283-293.

Skournal, R. J., M. R. Brudzinski, and B. S. Currie (2014), Induced earthquakes during hydraulic fracturing in Poland township, Ohio, *Bulletin of Seismological Society of America*, *vol. 105,* 1, pp. 189 - 197, doi: 10.1785/0120140168.

Soga, K., S.K.A. AU, M.R. Jafari, and M.D. Bolton (2004), Laboratory investigation of multiple grout injections into clay, *Geotechnique, vol. 54,* 2, pp. 81 - 90.

Soga, K., K. O. Gafar, M. Y. A. Ng, and S. K. A. Au (2006a), Macro and micro behavior of soil fracturing, *Proc Monogr Eng Wate*, *vol. 524*, pp. 421 - 427.

Soga, K., K. O. Gafar, M. Y. A. Ng, and S. K. A. Au (2006b), Macro and micro behavior of Soil Fracturing, paper presented at international Symposium on Geomechanics and Geotechnics of Particulate Mdia, Geomechanics and Geotechnics of Particulate Media, Taylor and Francis/Balkema, Ube, Yamaguchi, Japan.

Soga, K., S. K. A. Au, M. R. Jafari, and M.D. Bolton (2005), Laboratory Investigation of multiple grout injections into clay, *Geotechnique, vol. 55,* pp. 257 - 258.

Spetzler, H., G. Sobolev, C. Sondergeld, B. Salov, I. Getting, and A. Koltsov (1981), Surface deformation, crack formation, and acoustic velocity changes in pyrophyllite under polyaxial loading, *Journal of Geophysical Research, vol. 86,* pp. 1070 - 1080.

Stanchits, S., J. Burghardt, A. Surdi, E. Edelman, and R. Suarez-Rivera (2014a), Acoustic emission monitoring of heterogeneous rock hydraulic fracturing, paper presented to the 48th US Rock Mechanics/ Geomechanics Symposium, American Rock Mechanics Association, Minneapolis, MN, United States.

Stanchits, S., A. Surdi, E. Edelman, and R. Suarez-Rivera (2012), Acoustic emission and ultrasonic transmission monitoring of hydraulic fracture propagation in heterogeneous rock samples,

paper presented to the 46th US Rock Mechanics/ Geomechanics Symposium, American Rock Mechanics Association, Chicago, IL, United States.

Stanchits, S., A. Surdi, P. Gathogo, E. Edelman, and R. Suarez-Rivera (2014b), Onset of hydraulic fracture initiation monitored by acoustic emission and volumetric deformation measurements, *Rock Mechanics and Rock Enineeringg*, *vol. 47*, pp. 1521 - 1532, doi: 10.1007/s00603-014-0584-y.

Stein, S., and M. Wysession (2003), *An introduction to seismology, earthquakes, and earth structure*, 507 pp., Blackwell Publishing, Malden, MA, United States.

Swindlehurst, W. (1973), Acoustic emission - 1 introduction*, non-destructive testing, vol. 6,* 3*,* pp. 152 - 158.

Tesarick, D. J. (2002), Initial stability study of large openings for the national underground science laboratory at the Homestake mine, Lead, SD, Proceedings of the 5th North American Rock Mechanics Symposium and the 17th Tunnelling Association of Canada Conference, Tinnelling Association of Canada, Toronto, Ontario, Canada.

Thompson, B.D., R. P. Young, and D.A. Lockner (2005), Observations of premonitory acoustic emission and slip nucleation during a stick slip experiment in smooth faulted westerly granite, *Geophysical Research Letters, vol. 32,* L10304, doi:10.1029/2005GL022750.

Tiab, D., J. Lu, H. Nguyen, and J. Owayed (2010), Evaluation of fracture asymmetry of finite-conductivity fractured wells, *Journal of Energy Resources Technology, vol. 132,* 012901-1, doi: 10.1115/1.4000700.

Tordesillas, A., and M. Muthuswamy (2009), On the modeling of confined buckling of force chains, *Journal of the Mechanics and Physics of Solids*, *vol. 57,* pp. 706 – 727, doi: 10.1016/j.jmps.2009.01.005.

Tullis, T., and J. Weeks (1986), Constitutive behavior and stability of frictional sliding of granite, *Pure and Applied Geophysics, vol. 124,* 3, pp. 383 - 414.

Uenishi, K., and J.R. Rice (2003), Universal nucleation length for slip-weakening rupture instability under nonuniform fault loading, *Journal of Geophysical Research*, *vol. 108,* B1, pp. 2042-2056, doi: 10.1029/2001JB001681.

Vallejo, L.E. (1993), Shear Stresses and the hydraulic fracturing of earth dam soils, *Soils and Foundations, vol. 33,* 3*,* pp. 14 – 27.

Van den Hoek, P. J. (1993), New 3-D model for optimised design of hydraulic fractures and simulation of drill-cutting reinjection, paper presented at Offshore Europe 93 Proceedings, Society of Petroleum Engineers, Aberdeen, Scotland.

Viesca-Falguieres, R.C., and J.R. Rice (2010), Landsliding as the progressive growth of a slipping region: Initiating dynamic rupture propagation by local pore-pressure increase and its potential for arrest, *Eos Trans., AGU Fall Meeting supplement, Abstract OS21H-05*.

Viesca, R.C., and J.R. Rice (2012), Nucleation of slip-weakening rupture instability in landslides by localized increase of pore pressure, *Journal of Geophysical Research, vol. 117*, B03104, doi: 10.1029/2011JB008866.

Wallace, R.E. (1970), Earthquake recurrence intervals on the San Andreas fault, *Geological Society of America Bulletin, vol. 81,* 10, pp. 2875 – 2889.

Wang, H. (2000), *Theory of linear poroelasticity with applications to geomechanics and hydrogeology*, 304 pp., Princeton University Press, Princeton, NJ, United States.

Wang, Y., X. Li, B. Zheng, S.D. Li, and Y.T. Duan (2016), A laboratory study of the effect of confining pressure on permeable property in soil-rock mixture, *Environmental Earth Science, vol. 75*, pp. 284, doi: 10.1007/s12665-015-5193-x.

Warpinski, N.R., P.T. Branagan, and R.E. Peterson (1998a), Mapping hydraulic fracture growth and geometry using microseismic events detected by a wireline retrievable accelerometer array, paper presented at the SPE Gas Technology Symposium, Society of Petroleum Engineers, Calgary, Alberta, Canada.

Webby, B.D., Cooper, R.A., Bergstrom, S.M., and Paris, F. (2004), Stratigraphic framework and time slices, *in The Great Ordovician Biodiversification Event*, (edited by Webby, B.D., Paris, F., Droser, M.L., and Percival, I.G.), pp. 41 - 47, Columbia University Press, New York, NY, United States.

Wedman, M. L., K. W. Lynch, and J. W. Spearman (1999), Hydraulic fracturing for sand control in unconsolidated heavy oil reservoirs, paper presented at the SPE Western Regional Meeting, Society of Petroleum Engineers, Anchorage, Alaska, United States.

Wibberley, C.A.J., and T. Shimamoto (2003), Internal structure and permeability of major strike-slip fault zones: the medium tectonic line in mie prefecture, Southwest Japan, *Journal of Structural Geology*, *vol. 25*, pp. 59 - 78.

Wong, T. (1986), On the normal stress dependance of the shear fracture energy, *in Earthquake source mechanics*, (edited by S. Das, J. Boatwright, C.H., Scholz), American Geophysical Union, Washington DC, United States, doi: 10.1029/GM037p001.

Wright, W.F. (1965), Petroleum geology of the Simpson group, West Texas and Southeast New Mexico, Proceedings of the Symposium on the Simpson, Tulsa Geological Society Digest, Tulsa, OK, United States.

Wu, R. (2006), Some fundamental mechanisms of hydraulic fracturing, *Dissertation thesis, Georgia Institute of Technology, Atlanta GA.*

Wu, R., L.N. Germanovich, P.E Van Dyke, and Lowell, R.P. (2007), Thermal technique for controlling hydraulic fractures, *Journal of Geophysical Research*, *vol. 112*, B05209, doi: 10.1029/2005JB003815.

Yabe, Y. (2008), Evolution of source characteristics of AE events during frictional sliding, *Earth, Planets and Space, vol.* 60, pp. 5 – 8.

Yeck, W.L., L.V. Block, C.K. Wood, and V.M. King (2014), Maximum magnitude estimations of induced earthquakes at Paradox Valley, Colorado, from cumulative injection volume and geometry of seismicity clusters, *Geophysical Journal International*, *vol. 200*, pp. 322 - 336, doi: 10.1093/gji/ggu394.

Zhang, F. (2012), Pattern formation in fluid injection into dense granular media, Dissertation thesis, Georgia Institute of Technology, Atlanta GA.

Zhang, F., B. Damjanac, and H. Huang (2013), Coupled discrete element modeling of fluid injection into dense granular media, *Journal of Geophysical Research – Solid Earth, vol. 118,* 6*,* pp. 2703 – 2722.

Zhang, F., and H. Huang (2011), Coupled DEM-CFD modeling of fluid injection into granular media, Proceedings of 45th U.S. Rock Mechanics Symposium, American Rock Mechanics Association, San Francisco, CA, United States.

Zhou, J., Y. Dong, C. J. De Pater, and P. L. J. Zitha (2010b), Experimental study of the impact of shear dilation and fracture behavior during polymer injection for heavy oil recovery in unconsolidated reservoirs, Paper presented at Canadian Unconventional Resources and International Petroleum Conference, Society of Petroleum Engineers, Calgary, AB, Canada.

Zoback, M. D., and S. Hickman (1982), In situ study of the physical mechanisms controlling induced seismicity at monticello reservoir, South Carolina, *Journal of Geophysical Research, vol. 87,* B8*,* pp. 6959-6974.

Zoback, M., Hickman, S., W. Ellsworth, and the SAFOD Science Team (2011), Scientific drilling into the San Andreas fault zone - an overview of SAFOD's first five years, *Science Drilling, 11,* doi:10.2204/iodp.sd.11.02.2011.

Zoback, M.D., and H.-P. Harjes (1997), Injection-induced earthquake and crustal stress at 9 km depth at the KTB deep drilling site, Germany, *Journal of Geophysical Research, vol. 102,* B8*,* pp. 18477 - 18491.